



UNIVERSIDADE DE
COIMBRA



Nuno Cláudio Ferreira Rosa

STUDY OF STRUCTURAL AND
THERMAL PERFORMANCE OF
LIGHTWEIGHT STEEL FRAMING (LSF)
MODULAR CONSTRUCTION

PhD thesis in Steel and Composite Construction
supervised by Professor Paulo Santos, Professor Helena Gervásio, and
Professor José Joaquim da Costa and submitted to the Department of Civil
Engineering, Faculty of Sciences and Technology of the University of Coimbra

September 2018

STUDY OF STRUCTURAL AND THERMAL PERFORMANCE OF LIGHTWEIGHT STEEL FRAMING (LSF) MODULAR CONSTRUCTION

by

Nuno Cláudio Ferreira Rosa

M.Sc. in Mechanical Engineering in the specialization area of Energy and
Environment by the University of Coimbra (2013)

Thesis submitted to the Department of Civil in partial fulfilment of the
requirements for the degree of

Doctor of Philosophy in Steel and Composite Construction

by the

**FACULTY OF SCIENCES AND TECNOLOGY
UNIVERSITY OF COIMBRA**

Thesis Supervisors

Professor Paulo Fernando Antunes dos Santos
Department of Civil Engineering of the University of Coimbra

Professor Helena Maria dos Santos Gervásio
Department of Civil Engineering of the University of Coimbra

Professor José Joaquim da Costa
Department of Mechanical Engineering of the University of Coimbra

Coimbra, 2018



This PhD thesis is framed in the context of the Steel and Composite Constructions focus area of the Institute for Sustainability and Innovation in Structural Engineering (ISISE) and Cool-Haven research projects, the FP7 European project ModCons (FP7-SME-201 2-1) and *EcoSteelPanel* (IDI 2012. 24804). The work was also supported by the Development of Industrial Aerodynamics (ADAI), by FEDER funds through COMPETE 2020 – POCI, and by Portuguese funds through FCT in the framework of the project "PCMs4Buildings – Systems with PCM-filled rectangular cavities for the storage of solar thermal energy for buildings", refs. POCI-01-0145-FEDER-016750 | PTDC/EMS-ENE/6079/2014, and the following companies: Urbimagem; Fachaimper; Forbo flooring systems; Weber (Saint-Gobain); Termolan; Bifase, Sociveda, Falper and FibroPlac.

ABSTRACT

Lightweight Steel Framing (LSF) construction is recognized as a sustainable construction system, not only because steel is one of the most recyclable materials in the world but also due to the advantages of this type of construction. The panelised method is one of the construction processes of pre-fabrication of walls, floors and roofs. These panels, which are produced in factory, are constituted by steel profiles and oriented strand boards (OSB) connected by screws, and then transported and assembled at the construction site. Screw connections fit perfectly in the industrialized production and they are highly used due to its efficiency, fast application and suitability for load bearing. Although the screws are easy to install, it is exceedingly difficult to quantify their stiffness and strength contributions to the structural system due to their complex behaviour. Moreover, the contribution from the OSB panels is usually omitted in the LSF structure design as structural element. Finally, the panelised method is one of the fastest and most efficient methods for LSF modular construction. However, due to the low mass of the construction elements and the high number of thermal bridges, one of the drawbacks of this construction system is having low thermal inertia. Over the years new technologies have been developed to increase buildings thermal inertia, such as Earth-to-Air Heat Exchangers (EAHE) and Trombe Walls. Although EAHE system are already well known, its design is always difficult to carry out due to the high variation of physical, thermal and geometric parameters. On the other hand, the application of the Trombe Walls in a LSF modular construction system has not yet been developed. In this context, the main objectives of this thesis are: (1) to analyse and give better understanding of screw connection in LSF panels and to analyse the contribution of OSB boards to the lateral stiffness of the steel frame; (2) to provide design guidelines for suitable design, and operation control, of an efficient EAHE; (3) to develop a new Trombe Wall system that can be easily assembled in a LSF construction. Therefore, this thesis is divided into four parts, where the first one is introductory and the remaining three are dedicated to the development of the aforementioned objectives.

The first part of this thesis presents some structural concepts and discusses the thermal performance of LSF buildings focusing on thermal inertia. The mechanical and thermal properties of structural and non-structural materials are experimentally evaluated. To provide deeper understanding of screw connections in LSF structures and their impact on the response of the structure, the second part of this thesis presents experimental, numerical and analytical studies on screw connections (steel-to-steel and steel-to-OSB) and wall panels. Therefore, the main objectives of these

part are: (i) to analyse the behaviour of steel-to-steel screw connections using experimental, numerical and analytical approaches (EN 1993-1-3 and AISI S100); (ii) to investigate experimentally the steel-to-OSB boards connection and to assess analytically their behaviour using formulae proposed by EN 1995-1-1 (2004); (iii) to characterize the behaviour of LSF panels using screw connections subjected to lateral loading and to analyse the OSB contribution; (iv) to develop a reliable numerical model for a parametric study in which the performance of the unbraced panel frame, OSB braced panel frame and panel frame braced using diagonal steel strips is compared.

An extensive study on EAHE systems is presented in the third part of the thesis. The main research goals are: (i) to analyse the ground temperature variation with depth using analytical and experimental approaches; (ii) to develop a simple steady-state one-dimensional model for design and for prediction of the overall thermal performance of the system; (iii) to investigate the thermal performance of an EAHE system pilot installation located in Coimbra, during all four seasons of the year; (iv) to understand the influence of the system automation control; (v) to analyse the geometric (pipe diameter and length) and physical/thermal parameters (air velocity, pipe and ground thermal conductivity) and their impact on the thermal performance of the system; (vi) to analyse the influence of pipe spacing and diameter, and air velocity in transient conditions using Computational Fluid Dynamics (CFD) software (Ansys CFX 18.0).

The fourth part of the thesis is fully dedicated to the development of a Water Trombe Wall that can be assembled in a LSF modular construction. The development of this system is divided in four parts: (i) to analyse the Thermal Energy Storage (TES) wall during four seasons of the year by means of experimental, analytical and numerical approaches; (ii) a parametric study where the influence of orientation, colour and thermal capacity of the TES are investigated; (iii) to analyse the influence of promoting heat exchanges between TES assemble on different façades using CFD modelling; (iv) to experimentally evaluate the thermal performance of a full-scale WTW prototype in a LSF construction located in Coimbra.

Finally, the last chapter of this thesis presents the main conclusions of this work and a few recommendations for the future researches.

Keywords: LSF, Screw connections, LSF panels, Lateral Load, Thermal Inertia, EAHE, Trombe Walls, TES

RESUMO

A construção leve em aço (LSF, do inglês *Lightweight Steel Framing*) é atualmente reconhecida como um sistema construtivo sustentável, não só porque o aço é um dos materiais mais recicláveis do mundo, mas também devido às vantagens deste sistema construtivo. Um dos processos de pré-fabricação de paredes, lajes ou coberturas é a utilização do método construtivo da painelização. Neste método, painéis constituídos por perfis metálicos e placas de OSB (do inglês *Oriented Strand Board*) conectados através de parafusos, são construídos e montados em fábrica e depois transportados e assemblados em obra. A utilização de ligações aparafusadas demonstram ser as mais adequadas e eficientes garantindo maior resistência mecânica. O efeito das ligações aparafusadas no sistema estrutural é difícil de quantificar, devido à complexidade do comportamento dos parafusos. Além disso, a contribuição das placas de OSB na rigidez dos painéis é usualmente desprezado durante a fase de projeto. O método da painelização é considerado um dos métodos mais rápidos e eficazes da construção modular em LSF. No entanto, devido à reduzida massa dos elementos construtivos e ao elevado número de pontes térmicas, estas construções apresentam o inconveniente de ter uma baixa inércia térmica. Já existem várias tecnologias capazes de colmatar a baixa inércia térmica, tais como a utilização de sistemas EAHE (do inglês, *Earth-to-Air Heat Exchangers*) e as paredes de Trombe. Apesar dos sistemas EAHE já estarem bem presentes no mercado, o seu dimensionamento é sempre difícil de realizar/prever devido à enorme variação dos parâmetros físicos, térmicos e geométricos. Em relação às paredes de Trombe, a sua aplicação específica em uma construção modular em LSF ainda não foi desenvolvida. Neste contexto, os principais objetivos desta tese são: (1) avaliar o comportamento das ligações aparafusadas em painéis LSF e verificar a influência do OSB na rigidez dos painéis; (2) fornecer informações de dimensionamento e desempenho térmico de um sistema EAHE, (3) desenvolvimento um sistema de parede de Trombe que possa ser aplicado numa construção em LSF. Esta tese é dividida em quatro partes. Após a primeira parte, que é introdutória, as três restantes partes são dedicadas ao desenvolvimento dos objetivos acima indicados.

Assim primeira parte da tese apresenta uma visão geral da construção modular a nível estrutural e térmico. É também apresentado um estudo experimental da caracterização mecânica e térmica de alguns materiais utilizados em construção LSF. De forma a permitir uma melhor compreensão do comportamento das ligações aparafusadas e o seu impacto na estrutura, a segunda parte da tese apresenta estudos experimentais, numéricos e analíticos realizados em ligações aparafusadas (aço-aço

e aço-OSB) e em painéis em LSF. Os objetivos principais da segunda parte são os seguintes: (i) avaliar o comportamento de ligações do tipo aço-aço através de modelos experimentais, numéricos e analíticos (EN 1993-1-3 e AISI S100); (ii) avaliar experimentalmente o comportamento de ligações do tipo aço-OSB e comparar com o modelo analítico da EN 1995-1-1 (2004); (iii) avaliar experimentalmente o comportamento de painéis em LSF quando sujeitos a uma carga horizontal e verificar qual a contribuição do OSB e das ligações aparafusadas na sua desempenho estrutural; (iv) desenvolver um modelo numérico calibrado e validado com base em dados experimentais que será utilizado para comparar a contribuição do OSB com a utilização de uma chapa metálica de contraventamento estrutural.

Na terceira parte da tese é apresentado um estudo sobre sistemas EAHE. As principais linhas de investigação são: (i) avaliar a temperatura do solo em profundidade; (ii) desenvolvimento de método analítico unidimensional e estacionário que possa ser utilizado para dimensionamento e previsão, em evolução transiente hora-a-hora, do desempenho térmico de um sistema EAHE; (iii) avaliar o desempenho térmico de um sistema EAHE instalado num edifício, localizado em Coimbra, durante quatro estações do ano; (iv) análise do controlo domótico do sistema; (v) avaliação analítica da influência dos parâmetros geométricos (diâmetro, comprimento de tubos) e físicos/térmicos (velocidade do ar, condutividade térmica dos tubos e do solo); (vi) verificar a influência da distância entre tubos, diâmetro e velocidade do ar em regime transiente através de modelação CFD (do inglês, *Computational Fluid Dynamics*) em ANSYS CFX 18.0.

A quarta parte da tese é dedicada ao desenvolvimento de um sistema de parede de Trombe com água (WTW do inglês *Water Trombe Wall*) que possa ser integrado numa construção modular em LSF. O desenvolvimento do sistema é realizado em várias fases: (i) estudo experimental, analítico e numérico do acumulador de energia térmica durante as quatro estações do ano; (ii) estudo paramétrico do acumulador de energia térmica, onde é avaliada a sua orientação, cor e capacidade térmica; (iii) avaliação numérica (CFD) de permutação de calor entre painéis colocados em diferentes fachadas; (iv) avaliação experimental do desempenho térmico do protótipo WTW numa construção em LSF situada em Coimbra (Portugal). No capítulo final são apresentadas as principais conclusões do trabalho e recomendações para trabalhos futuros.

Palavras-chave: LSF, Ligações Aparafusadas, Painéis, Carga Lateral, Inércia Térmica, EAHE, Parede de Trombe, Acumulador de Energia Térmica

AGRADECIMENTOS

Esta dissertação só foi realizada graças à colaboração e apoio incondicional de professores, colegas, amigos e família. A todos o meu eterno agradecimento!

Ao Professor Paulo Santos por todos os conhecimentos transmitidos e ajuda durante estes anos. Eu sei que não deve ter sido nada fácil aguentar a minha teimosia...Professor, apesar de todos os contratempos ocorridos, expresso o meu maior agradecimento por tudo...

Ao Professor José Costa pela sua disponibilidade, pela sua confiança e por todo o apoio, em particular na dedicação incansável nestas últimas semanas. Muito obrigado por ter acreditado em mim em todos os momentos.

À Professora Helena Gervásio, por toda a ajuda, conhecimentos transmitidos e pela sua compreensão em fases menos motivantes.

Ao Professor Luís Simões da Silva, por toda a sua ajuda e compreensão durante o doutoramento. Muito obrigado por tudo Professor, principalmente pela sua amizade!

A todos os meus colegas de gabinete, em especial ao Tiago Manco por estes trinta e nove meses alucinantes, foram muitas as horas que passamos juntos amigo...Ao meu amigo Filip Ljubinkovic, apesar de cantares mal como tudo, és uma excelente pessoa e um excelente amigo para a vida. Ao meu amigo Eduardo Roque, ninguém imagina o quanto me aturaste estes últimos meses, o teu apoio foi incondicional. Vocês são umas máquinas!

Ao meu grande amigo Cláudio Martins, por toda a ajuda em todos os momentos bons e menos bons. Sem ti era mesmo impossível, não preciso falar muito... tu sabes que estás no meu coração.

Aos membros do ISISE, agradeço toda a disponibilidade durante todas as fases deste doutoramento e pela vossa amizade.

A todas as empresas envolvidas neste trabalho, sem elas nada disto teria sido possível.

A todos os meus amigos, são tantos e tão especiais que todas as páginas desta dissertação não seriam suficientes para descrever o meu agradecimento!

Aos meus pais e à minha irmã por toda a paciência durante os meus momentos menos motivantes, sem vocês nada disto teria sido possível.

CONTENTS

CHAPTER I	Introduction	1
I.1.	Framework and motivation	1
I.2.	Research background and objectives.....	3
I.3.	Thesis outline	6
PART A: LIGHT STEEL FRAMING MODULAR CONSTRUCTION.....		9
CHAPTER II	Modular construction systems	11
II.1.	Introduction.....	11
II.2.	Overview of LSF modular construction.....	13
II.2.1.	Normative documents for structural design.....	13
II.2.2.	Structural design	14
II.2.3.	Construction materials	16
II.2.4.	Classification of LSF construction	17
II.2.5.	Thermal performance	18
II.2.5.1.	Thermal bridges	18
II.2.5.2.	Thermal inertia	20
II.3.	Materials mechanical and thermal properties of the materials	21
II.3.1.	Steel mechanical properties characterization.....	21
II.3.2.	Oriented strand board properties characterization	22
II.3.3.	Characterization of thermal properties.....	25
II.4.	Final remarks	27
PART B: STRUCTURAL PERFORMANCE OF LSF MODULAR CONSTRUCTION.....		29
CHAPTER III	Structural performance of light steel framing panels using screw connections subjected to lateral loading.....	31
III.1.	Introduction.....	31
III.2.	Behaviour of screw connections in shear in light steel framing panels.....	34
III.2.1.	Steel-to-steel screw connections.....	34
III.2.1.1.	Assessment of the response of single shear screw connections	37

III.2.1.2.	Experimental test on single shear screw connection	42
III.2.1.2.1.	Test programme and layout	42
III.2.1.2.2.	Tests results	44
III.2.1.3.	Numerical modelling of single shear screw connection	47
III.2.1.3.1.	Development of FE model for simulation of screw connection in shear	47
III.2.1.3.2.	Model validation and calibration	48
III.2.1.3.3.	Numerical results.....	50
III.2.2.	OSB-to-steel screw connection.....	51
III.2.2.1.	Assessment of the resistance of a OSB-Steel screw connection	51
III.2.2.2.	Experimental behaviour on single shear screw connection	53
III.2.2.2.1.	Test program and layout	53
III.2.2.2.2.	Test results	54
III.3.	Analytical determination of the response of LSF wall panels to lateral loading	56
III.3.1.	LSF wall braced with steel straps	57
III.3.2.	Sheathed LSF walls.....	58
III.4.	Experimental tests on light steel framing panels subject to lateral loading	60
III.4.1.	Experimental campaign.....	61
III.4.1.1.	Experimental programme	61
III.4.1.2.	Experimental procedure	62
III.4.1.3.	Experimental layout	64
III.4.1.4.	Results and discussion	65
III.5.	Numerical evaluation of LSF panels subject to lateral loading	68
III.5.1.	Validation and calibration of the FEM model	69
III.5.2.	Structural performance of LSF panels to lateral loading	70
III.6.	Conclusions.....	72
PART C: EARTH-TO-AIR HEAT EXCHANGERS		75
CHAPTER IV Earth-to-air heat exchangers overview and a simple design approach based on ϵ-NTU method		77

IV.1. Introduction.....	77
IV.2. Overview of previous scientific researches	80
IV.2.1. Experimental analysis	80
IV.2.2. Analytical and numerical modelling.....	83
IV.2.2.1. Analytical modelling	84
IV.2.2.2. Numerical modelling	86
IV.2.3. Guidance overview.....	90
IV.2.3.1. Geometric parameters	90
IV.2.3.2. Physical and thermal parameters	91
IV.3. Ground temperature – Analytical Approach.....	93
IV.4. Heat transfer in heat exchangers the ϵ -NTU approach	95
IV.5. EAHE design and energy performance	100
IV.6. Final remarks	102
CHAPTER V Modelling and performance analysis of an earth-to-air heat exchanger pilot installation in Csb climate	103
V.1. Introduction.....	103
V.2. Experimental approach	104
V.2.1. Experimental setup.....	106
V.2.2. Monthly average recorded values	107
V.2.3. Energy performance analysis.....	108
V.2.3.1. Heating season	112
V.2.3.2. Cooling season.....	113
V.2.3.3. Mid seasons.....	114
V.3. Analytical approach.....	115
V.3.1. Mathematical modelling	115
V.3.2. Model validation.....	117
V.3.2.1. Heating season	118
V.3.2.2. Cooling season.....	119
V.3.2.3. Mid seasons.....	119

V.4. Parametric study	121
V.4.1. Pipe length.....	121
V.4.2. Pipe diameter	123
V.4.3. Air velocity	125
V.4.4. Pipe material.....	126
V.4.5. Soil typology.....	127
V.5. Conclusions.....	129
CHAPTER VI Computational fluid dynamic modelling of an earth-to-air heat exchanger	131
VI.1. Introduction	131
VI.2. CFD models.....	131
VI.2.1. Mathematical model.....	133
VI.2.2. Initial and boundary conditions	135
VI.2.3. Validation of CFD models	136
VI.2.3.1. Geometry of the EAHE pilot installation (Model 01).....	136
VI.2.3.2. Single pipe (Model 02)	138
VI.3. Parametric Study	140
VI.3.1. Effect of pipe diameter operating with different air velocities	141
VI.3.2. Space between adjacent pipes.....	144
VI.4. Conclusions.....	149
PART D: TROMBE WALL TECHNOLOGY	151
CHAPTER VII Trombe walls review and design methods	153
VII.1. Introduction	153
VII.2. Trombe wall technologies	154
VII.2.1. Trombe wall typologies	156
VII.3. Overview of previous scientific researches	159
VII.3.1. Experimental analysis	159
VII.3.2. Analytical and numerical modelling	163
VII.3.2.1. Analytical modelling.....	163

VII.3.2.2. Numerical modelling	166
VII.3.3. Guidance overview	168
VII.4. Heat transfer fundamentals for a double glass Trombe Wall system.....	171
VII.4.1. Energy performance analysis	175
VII.5. Final remarks	181
CHAPTER VIII Development of a Water Trombe Wall system for LSF modular construction	183
VIII.1. Introduction.....	183
VIII.2. Brief review of Water Trombe Walls	184
VIII.3. Development of the Thermal Energy Storage system for the Water Trombe Wall	185
VIII.3.1. Thermal storage system design	186
VIII.3.2. Experimental small-scale prototype.....	188
VIII.3.3. Analytical approach.....	189
VIII.3.4. Numerical approach.....	191
VIII.3.5. Analytical model validation	192
VIII.3.6. Thermal behaviour of TES Wall.....	193
VIII.3.6.1. Clear sky conditions	194
VIII.3.6.2. Cloudy conditions.....	196
VIII.3.7. Parametric study	197
VIII.3.8. Computational fluid dynamics modelling of a dynamic water wall ..	200
VIII.4. Design and thermal performance analysis of a Water Trombe Wall prototype	203
VIII.4.1. Pre-design	204
VIII.4.2. Experimental set-up and instrumentation	208
VIII.4.3. Experimental Modules Verification	213
VIII.4.4. Methodology	215
VIII.4.5. Preliminary results.....	216
VIII.5. Conclusions and future developments	220

CHAPTER IX	Conclusions and future developments	223
IX.1.	Overview	223
IX.2.	Conclusions and contributes of this thesis	224
IX.3.	Forthcoming work and future research	228
REFERENCES	231
ANNEX A.	249
A1.1	Grid and time-step convergence.....	249
A1.1.1	First cell height calculation.....	250
A1.2	Unstructured grid analysis	250
A1.3	Hybrid grid analysis.....	252
A1.4	Numerical convergence control	253

LIST OF FIGURES

Figure I.1 – Experimental test with non-braced wall panels.	4
Figure I.2 – Earth-to-air heat exchanger and Water Trombe Wall in a LSF building.	6
Figure I.3 – Thesis outline.....	7
Figure II.1 – Illustration of 2D and 3D modules from ModCons project.	12
Figure II.2 – Cross section of steel cold-formed steel profiles for beams and columns 1993-1-1, (2005).....	14
Figure II.3 – Design steps of cold-formed steel structures.....	15
Figure II.4 – Example of a cross-section of a LSF wall.	17
Figure II.5 – Classification of LSF walls and respective temperature distribution/thermal transmittance values (Santos, 2017).	18
Figure II.6 – LSF wall model used in parametric study (Martins <i>et al.</i> (2015).....	19
Figure II.7 – Results of the parametric study (Martins <i>et al.</i> 2015).....	19
Figure II.8 – Illustrative example of building thermal mass effect.	20
Figure II.9 – S280GD+Z mechanical characterization according with EN 10002-1. .	22
Figure II.10 – Experimental layout for OSB tensile tests.....	23
Figure II.11 – Experimental results of OSB mechanical properties.	23
Figure II.12 – Force – displacement for tensile experimental and numerical analysis.	24
Figure II.13 – Stress – extension and yield stress for compression tests.....	25
Figure II.14 – Hot disk experimental layout.	26
Figure II.15 – Experimental vs theoretical values of material thermal conductivity.	26
Figure III.1 – ModCons experimental layout.....	34
Figure III.2 – Failure modes in screw connection subject to shear.	35
Figure III.3 – Examples of stud-stud screw connection in LSF panels.....	37
Figure III.4 – Spring mechanical model reproducing a screw connection.	37
Figure III.5 – Evaluation of tearing and bearing failure of screw connection in shear according to the EN 1993-1-3, (2006) and the AISI S100, (2007) ($f_u = 360 \text{ N/mm}^2$; $d =$ 4.8).....	40
Figure III.6 – Comparison EN 1993-1-3, (2006) and AISI S100, (2007) analytical expressions for determination of tearing and bearing resistance.....	41
Figure III.7 – System of forces due to the eccentricity of loading in the screw connection between panel studs (horizontal and vertical).	42
Figure III.8 – Self-drilling screws used in the screw connection tests.....	43

Figure III.9 – Screw connection test specimen's dimensions and experimental layout.	44
Figure III.10 – Force-deformation of the screw connection.	45
Figure III.11 – Screw rotation observed in the screw connection test.	45
Figure III.12 – a) Additional bending moment generated by the eccentricity of the loading on the screw connections; b) ratio between screw connection resistance and test results.	47
Figure III.13 – Finite element model of the screw connection tested.	48
Figure III.14 – Comparison between the force-deformation curves of the numerical model and screw connection tests.	49
Figure III.15 – Comparison between the deformation pattern of experimental and numerical model.	49
Figure III.16 – Comparison of the yield lines in horizontal profile both in the screw connection test and in the numerical model.	49
Figure III.17 – Comparison of force-deformation curve between connection and global test configuration.	50
Figure III.18 – Detail results of the screw connection simulation.	51
Figure III.19 – OSB to Steel screw connection.	52
Figure III.20 – Test specimen of steel-OSB connection with ST 4.8.	54
Figure III.21 – Experimental results for steel-OSB connection with ST 4.8 x32 screw.	55
Figure III.22 – Force-displacement OSB-steel connection.	56
Figure III.23 – LSF wall braced with steel straps.	57
Figure III.24 – LSF wall braced with steel sheet or panel.	59
Figure III.25 – Frame braced by OSB with steel frame connection spacing – 300 mm.	62
Figure III.26 – Frame braced by OSB with steel frame connection spacing – 150 mm.	62
Figure III.27 – Representation of the experimental layout (ASTM 564 – 06, 2012).	63
Figure III.28 – Experimental layout.	65
Figure III.29 – LSF panels test specimens.	66
Figure III.30 – Failure on the LSF panels tests.	66
Figure III.31 – Force-deformation results of the experimental tests on LSF panels subject to lateral loading.	67
Figure III.32 – Comparison between literature tests, performed tests and analytical model.	68
Figure III.33 – Comparison between experimental and numerical results.	70

Figure III.34 – Model with steel bracing system against test report results by Branston <i>et al.</i> (2006).....	71
Figure III.35 – Force-deformation curves comparing numerical simulations and experimental tests of LSF panels subjected to lateral loading.....	71
Figure IV.1 – Ground Coupled Heat Exchangers systems.	78
Figure IV.2 – EAHE loop configurations.....	80
Figure IV.3 – Underground soil temperature in Coimbra (PT) for 2014.	95
Figure IV.4 – Differential heat balance and thermal resistance network in a heat exchanger pipe.	99
Figure V.1 – EAHE buried pipes and inlet filter.	104
Figure V.2 – Buried pipes layout of the EAHE system and building location.	105
Figure V.3 – Longitudinal vertical cross section scheme of the EAHE system.	105
Figure V.4 – Ground temperature sensors.....	106
Figure V.5 – Monthly average temperatures (2014): environment air, ground (1.9 m deep), and respective differences.	107
Figure V.6 – Seasonal operation of the EAHE (2014).	108
Figure V.7 – Average COP for the EAHE operation over 2014.....	110
Figure V.8 – Hourly results in heating season for cloudy (a) and sunny days (b).	112
Figure V.9 – Hourly results in cooling season.....	114
Figure V.10 – Hourly results in the spring season.	114
Figure V.11 – Hourly results in the autumn season.	115
Figure V.12 – Measured and predicted outlet air temperatures in heating season for cloudy (a) and sunny (b) days.	119
Figure V.13 – Measured and predicted outlet air temperature for cooling season	119
Figure V.14 – Measured and predicted outlet air temperature for mid seasons.	120
Figure V.15 – Outlet air temperature variation for different pipe lengths ($\dot{V} = 213 \text{ m}^3/\text{h}$ in cooling and $\dot{V} = 455 \text{ m}^3/\text{h}$ in heating).....	122
Figure V.16 – Variation of the mean efficiency and COP with the pipes' length... ..	123
Figure V.17 – Outlet air temperature evolution for different commercial pipe diameters.....	124
Figure V.18 – Evolution of mean efficiency and COP according with the pipe diameter.	125
Figure V.19 – Outlet air temperatures evolution for different air velocities.....	126
Figure V.20 – Variation of the mean efficiency and COP with the airflow velocity.	126
Figure V.21 – Outlet air temperatures for different pipe materials.....	127
Figure V.22 – Outlet air temperatures for different soil thermal conductivities.	128

Figure VI.1 – Mean ground temperature profiles in cooling and heating operation modes (measured values).....	135
Figure VI.2 – CFD validation against measured values.	136
Figure VI.3 – Air temperature distribution along the EAHE at $t = 9$ hours ($T_{a, in} = 4.5^{\circ}\text{C}$) of simulation.	137
Figure VI.4 – Temperature contour for $t = 9$ hours at a 12 m length (sensors location).	138
Figure VI.5 – Numerical results for grid refining in air domain.	139
Figure VI.6 – CFD and analytical air outlet temperature for cooling and heating ($\dot{V} = 210 \text{ m}^3/\text{h}$ in cooling and $\dot{V} = 433 \text{ m}^3/\text{h}$ in heating).	140
Figure VI.7 – Temperature distribution of the soil and flowing air domain in a vertical plane at the pipe mid-length for $t = 17 \text{ h}$ in cooling operation.	142
Figure VI.8 – Results from one-pipe simulation.	143
Figure VI.9 – Mean heat rate for different pipe diameter and air velocities.	144
Figure VI.10 – Results for different pipe spacing and diameter, and air velocity.	146
Figure VI.11 – Variation of the heat transfer rate per pipe with decreasing pipe spacing, relatively to $d_p = 1.0 \text{ m}$	147
Figure VII.1 – Trombe wall operation modes.....	155
Figure VII.2 – Composite and water Trombe Wall.....	157
Figure VII.3 – Zigzag Trombe wall and TransWall (Saadatian <i>et al.</i> 2012).	158
Figure VII.4 – PV and Fluidised Trombe walls.	158
Figure VII.5 – Chen <i>et al.</i> (2006) experimental layout.	159
Figure VII.6 – Liu <i>et al.</i> (2013) experimental Trombe wall system.	161
Figure VII.7 – Hu <i>et al.</i> (2015) schematic of experimental layout.	162
Figure VII.8 – Rabani <i>et al.</i> (2015) experimental layout.....	163
Figure VII.9 – Energy balance in a double glass Trombe wall system.	171
Figure VII.10 – Thermal resistance of the Trombe wall system.....	176
Figure VII.11 – Heat balance in the Trombe wall system.	177
Figure VIII.1 – Water wall horizontal cross-section (<i>EcoSteelPanel</i>).....	186
Figure VIII.2 – Screw connection of the <i>EcoSteelPanel</i> water wall.	186
Figure VIII.3 – 2D isothermal lines of the <i>EcoSteelPanel</i> water wall joint connection.	187
Figure VIII.4 – Thermal transmittance results for the <i>EcoSteelPanel</i> water walls....	188
Figure VIII.5 – 3D model of the water TES small-scale prototype.	188
Figure VIII.6 – Experimental tests of the water TES small-scale prototype.....	189
Figure VIII.7 – Illustration of the studied variables applied in the thermal balance of the prototype.	190

Figure VIII.8 – Numerical results for the exterior surface of the small-scale prototype.	192
Figure VIII.9 – Experimental and analytical results comparison.....	193
Figure VIII.10 – Weather conditions for three days of clear and cloudy sky.....	194
Figure VIII.11 – Analytical prediction of the external surface temperature for different orientations during a clear sky day.	195
Figure VIII.12 – Analytical prediction of the heat flux for different orientations during clear sky.	196
Figure VIII.13 – Analytical prediction of the external surface temperature for different orientations during a cloudy day.....	196
Figure VIII.14 – Analytical prediction of the heat flux for different orientations during cloudy sky.....	197
Figure VIII.15 – Measured daily average temperatures of the prototype for different orientations.	198
Figure VIII.16 – Experimental prototypes for the parametric study.....	199
Figure VIII.17 – Temperatures measured on the water-filled prototypes.....	199
Figure VIII.18 – Schematic representation of the CFD models.	200
Figure VIII.19 – CFD module for permanent conditions and transient south temperature.	201
Figure VIII.20 – Temperature and velocity vectors of water flow between south panels (natural convection).	202
Figure VIII.21 – Temperature distribution for model 03.....	202
Figure VIII.22 – Temperature distribution for model 04.....	203
Figure VIII.23 – Steel frames used in analytical and numerical study.....	205
Figure VIII.24 – Heat transfer decrease results for the WTW with noggings.	206
Figure VIII.25 – Analytical and CFD results.....	207
Figure VIII.26 – Tri-dimensional WTW module design.....	208
Figure VIII.27 – Tri-dimensional rendering of the water Trombe wall with six modules in a LSF construction (Cool Haven).....	208
Figure VIII.28 – Experimental set-up: WTW module (1) and reference module (2).	209
Figure VIII.29 – Construction details of the experimental modules.	209
Figure VIII.30 – Water Trombe Wall prototype assemblage and sensors location.	210
Figure VIII.31 – Example of sensors map for south wall, roof and slab.	211
Figure VIII.32 – Example of some experimental instrumentation.....	212
Figure VIII.33 – Experimental results with CO ₂ concentration decay method.....	213
Figure VIII.34 – Infrared thermographic inspections (<i>e.g.</i> doors).....	214

Figure VIII.35 – Temperature and relative humidity verification between experimental modules.	214
Figure VIII.36 – Outdoor air temperature and solar radiation.	215
Figure VIII.37 – Indoor and outdoor conditions from 6 th of May to 14 th of May of 2018 (first period).	217
Figure VIII.38 – Indoor and outdoor conditions from 14 th of May to 22 th of May of 2018 (second period).	218
Figure VIII.39 – Indoor and outdoor conditions from 26 th of May to 05 th of June (third period).	218
Figure VIII.40 – WTW and experimental modules temperatures and heat rate.	219
Figure A.1 – Number of elements with unstructured grid mesh.	251
Figure A.2 – Numerical results for grid refining in ground domain.	251
Figure A.3 – Numerical results for grid refining in air domain.	252
Figure A.4 – Hybrid grid in Ansys CFX.	253
Figure A.5 – Numerical convergence.	254
Figure A.6 – Numerical results for grid refining in air domain.	255
Figure A.7 – Yplus contour at 17 hours of numerical simulation.	255
Figure A.8 – Temperature contour in transient conditions for t = 17 hours of simulation.	256

LIST OF TABLES

Table III.1 – Screw connection test specimens.....	42
Table III.2 – Geometrical properties of the self–drilling screws used in the screw connections tests.	43
Table III.3 – Summary of the results on steel-to-steel screw connections.	46
Table III.4 – Main properties of the test specimens of the OSB-steel screw connection.	54
Table III.5 – Summary of the experimental force-deformation curve of the OSB-steel screw connection.....	55
Table III.6 – Experimental programme on LSF panels subject to lateral loading.....	61
Table III.7 – Summary of the results of the experimental tests on LSF panels subject to lateral loading.	67
Table IV.1 – Summary of researcher’s achievements in experimental, analytical and numerical analysis for EAHE systems, according with the main design parameter focused (1 st column).....	92
Table V.1 – Monthly average values for the EAHE energy performance evaluation.	109
Table V.2 – Monthly average values for the EAHE energy performance evaluation, only during operation time.	111
Table V.3 – Thermophysical properties used in model validation (Çengel, 2009).	118
Table V.4 – EAHE geometric features used in model validation.	118
Table V.5 - Analytical model accuracy overview.....	121
Table V.6 – Scheme of the parametric study for different pipe length and diameter, air velocity, pipe material and soil typology topology.	121
Table V.7 – Pipe diameters used in the sensitivity analysis ⁽¹⁾	124
Table V.8 – Mean efficiency and COP according with the pipe material and season.	127
Table V.9 – Soil typologies and thermal conductivities used in the sensitivity analysis.....	128
Table V.10 – Mean efficiency and COP according with the soil thermal conductivity.	129
Table VI.1 – Thermo-physical properties of materials used in simulation.	133
Table VI.2 – Parametric study with a single pipe EAHE for different air velocities and diameters.....	141

Table VI.3 – Parametric study for different pipe diameters, air velocities and pipe spacing.	145
Table VI.4 – Maximum difference in outlet air temperature with the decrease of pipe space, relatively to $d_p = 1.0$ m in cooling mode.....	148
Table VI.5 – Maximum difference in outlet air temperature with the decrease of pipe space, relatively to $d_p = 1.0$ m in heating mode.....	148
Table VI.6 – Maximum difference in heat loss rate per pipe with the decrease of pipe spacing, relatively to $d_p = 1.0$ m in cooling.	149
Table VI.7 – Maximum difference in heat loss rate per pipe with the decrease of pipe spacing, relatively to $d_p = 1.0$ m in heating.....	149
Table VII.1 – Summary of researcher’s achievements in experimental, analytical and numerical analysis of Trombe walls, according with the main design parameter focused (1 st column).	169
Table VIII.1 – Boundary conditions of the 2D models for both panel generation. .	187
Table VIII.2 – Input parameters.....	191
Table VIII.3 – Numerical results and experimental measurements.....	192
Table VIII.4 – Wall materials thermal properties and thickness.....	193
Table VIII.5 – CFD boundary conditions.	201

NOMENCLATURE

Uppercase Letters

A	Effective area of the opening (Trombe Wall air vents) [m ²]
A_1	Cross section area of OSB boards [m ²]
A_{bottom}	Area of the Trombe wall bottom vent [m ²]
A_g	Area of the double glass [m ²]
A_i	Inner surface area of the pipe (s) [m ²]
A_n	Net cross-section area of the sheet (accounting for the screw hole) [m ²]
A_{net}	Cross-section area of the plate (accounting for the screw hole) [m ²]
A_{st}	Area of the storage wall front surface [m ²]
A_{top}	Area of the top vent [m ²]
$A_{sol,k}$	Effective collecting area of the Trombe wall [m ²]
B_s	Amplitude of the annual variation of the soil surface [°C]
C	Heat capacity [J/(°C)]
COP	Coefficient of performance [-]
C_r	Capacity ratio [-]
E_c	Elasticity modulus [MPa]
EB	Energy balance [kWh]
EP	Equivalent power [W]
E_t	Total Energy [J]
F_0	Shading reduction factor from the horizontal elements overlapping the glazing [-]
F_1	10% of the ultimate load [N]
F_2	40% of the ultimate load [N]
$F_{ax, RK}$	Characteristic withdrawal capacity of the screw [N]
$F_{external}$	Force applied with an eccentricity [N]
F_b	Connection resistance [N]
$F_{contact}$	Contact force developed by steel profiles [N]
$F'_{b, test}$	Resistance of the screw connection obtained on the test [N]
$F_{b, Rd}$	Bearing resistance [N]
$F_{b, Rk}$	Screw-steel bearing [N]
F_h	Reduction factor for obstacles from other building exterior elements [-]

F_f	Shading reduction for obstacles from the vertical elements overlapping the glazing [-]
F_F	Glazed fraction [-]
F_{max}	Maximum force achieved in steel-to-steel connections [N]
$F_{n, Rd}$	Net-section resistance [N]
$F_{n, Rk}$	Steel net-section [N]
F_{u2}	Ultimate tensile strength of the steel sheet not in contact with screw head [MPa]
F_{ul}	Ultimate tensile strength of the steel sheet in contact with screw head [MPa]
$F_{sh, ob, k}$	Shading reduction factor for external obstacles [-]
$F_{r, k}$	View factor between the Trombe wall and the sky [-]
$F_{v, Rd}$	Shear resistance [N]
$F_{v, Rk}$	Characteristic shear resistance of the screw determined by testing [N]
$F_{v, Rk, screw}$	Shear failure of the screw [N]
$F_{v, Rk, wood}$	Wood-screw bearing [N]
G	Shear stiffness of LSF wall panel [N/mm]
$G_{R,L}$	Grashof number [-]
G_{sul}	Monthly-average solar radiation incident on South surface [kWh/m ² month]
H	Heat transfer coefficient of the Trombe wall surface [W/°C]
H_0	Heat transfer coefficient of non-ventilated wall surface [W/°C]
Hor_IR	Infrared radiation flux emitted by the sky [W/m ²]
I	Solar radiation intensity [W/m ²]
I_r	Solar irradiance, the mean energy of the solar irradiation in the cooling season [kWh/m ²]
$I_{sol, k}$	Mean energy of solar irradiation in the heating season [W/m ²]
I_w	Solar irradiance, the mean energy of the solar irradiation in the heating season [(W Mseg)/m ²]
$K_{B-S, Con}$	Brace-stud connection [kN/m]
K_i	Coefficients of local pressure drop [-]
$K_{ini, H, Wall}$	Initial lateral stiffness of the wall panel [kN/m]
$K_{T, Anchorage}$	Wall overturning [kN/m]
$K_{T, Brace}$	Diagonal steel strap tension [kN/m]
L	Pipe (s) length [m]
M	Heating season duration [days]

$M_{add,con}$	Additional bending moment on the connection [kN.m]
$M_{add,prof}$	Additional bending moment on the profile [kN.m]
$M_{y, RK}$	Characteristic screw yield moment [N.m]
N	Opaque sky cover [-]
$N_{C,Stud}$	Wall stud compression [N]
$N_{C,Track}$	Wall track compression [N]
N_{ED}	Axial force [kN]
$N_{T,Brace}$	Diagonal steel strap tension [N]
$N_{T,Track}$	Wall track tension [N]
Nu	Nusselt number [-]
$P_{\epsilon b}$	Buoyancy dissipation term [-]
P_k	Turbulence production due to viscous forces [-]
P_{kb}	Buoyancy production term [-]
P_{load}	Hydraulic jack load [kN]
Pr	Prandtl number [-]
P_{ss}	Shear resistance of the screw determined by testing [N]
\dot{Q}	Heat transfer [W]
Q_c	Cooling sensible heat [Wh]
\dot{Q}_{conv}	Heat transfer rate by convection [W]
$\dot{Q}_{gn,sw}$	Rate of solar heat gains in the air cavity [W]
Q_h	Heating sensible heat [Wh]
$\dot{Q}_{ht,al}$	Heat loss rate of the air cavity [W]
\dot{Q}_l	Heat loss rate through the glass [W]
\dot{Q}_{rad}	Heat transfer rate by radiation [W]
\dot{Q}_{sol}	Solar gains [MJ]
\dot{Q}_{trans}	Heat transfer rate by conduction [W]
R_1	Convective thermal resistance inside the pipe [K/W]
R_2	Thermal resistance to conduction through the pipe's wall [K/W]
R_3	Thermal resistance to conduction through the ground [K/W]
R	Reduction factor for the influence of a "group effect" of screws [-]
R_{air}	Thermal resistance of the Trombe wall air cavity/layer [(m ² .°C) /W]
$R_{B-S,Con}$	Brace-stud connection [N]
Re_d	Reynolds number [-]
R_e	Unit thermal resistance (<i>R</i> -value) of exterior layers [(m ² . °C) /W]

R_i	Unit thermal resistance of interior materials [(m ² .°C)/W]
R_j	Unit thermal resistance of elements [(m ² .°C)/W]
R_{se}	Unit thermal resistance on the outdoor surface [(m ² .°C)/W]
R_{si}	Unit thermal resistance on the internal surface [(m ² .°C)/W]
$R_{S-S, Con}$	Sheet-to-Stud connection [N]
R_{steel}	Unit thermal resistance of steel layer [(m ² .°C)/W]
$R_{S-T, Con}$	Sheet-to-Track connection [N]
$R_{T, Anchorage}$	Hold-down connection to the ground [N]
R_{VR}	Equivalent thermal resistance of the Trombe wall air cavity/layer [(m ² .K)/W]
R_{water}	Unit thermal resistance of water layer [(m ² .°C)/W]
R_{xps}	Unit thermal resistance of XPS [(m ² .°C)/W]
S_{ini}	Initial stiffness [N/m]
$Sky_{emissivity}$	Sky emissivity [-]
T_0	Dew point temperature [°C]
T_a	Outdoor air temperature [°C]
T_{air}	Air temperature in Trombe wall air cavity [°C]
$T_{a,in}$	Inlet air temperature [°C]
$T_{a,out}$	Outlet air temperature [°C]
T_i	Indoor air temperature [°C]
T_{g1}	Temperature of the first glass surface [°C]
T_{g2}	Temperature of the second glass surface [°C]
T_{g3}	Temperature of the third glass surface [°C]
T_{g4}	Temperature of the fourth glass surface [°C]
T_m	Average soil temperature [°C]
$T_{si,1}$	Average surface temperature of the storage wall surface [°C]
$T_{si,2}$	Average surface temperature of the glass [°C]
T_s	Soil/Ground temperature [°C]
T_{sky}	Sky temperature [°C]
T_{st}	Temperature of the storage wall surface [°C]
$T_{surface}$	Temperature of the TES - <i>EcoSteelPanel</i> surface [°C]
T_w	Water temperature [°C]
U_0	Heat transfer coefficient of the Trombe Wall [W/(m ² .°C)]
U_{ext}	Overall heat transfer coefficient for the exterior materials [W/(m ² .°C)]
U_i	Overall heat transfer coefficient referred to the pipes' inner surface [W/(m ² .°C)]

U_{int}	Overall heat transfer coefficient for the interior materials [W/m ² .°C]
\dot{V}	Air flow rate [m ³ /h]
V_{Sheet}	Non-steel sheet or panel shear [N]
\dot{W}	Electric power consumed by the fan [W]
Z	Vertical distance between top and bottom air vents [m]

Lowercase letters

a	Height of LSF wall test specimen [m]
b	Width of LSF wall test specimen [m]
$b_{tr, l}$	Reduction factor for adjacent unconditioned space with internal heat source [-]
C_d	Discharger coefficient [-]
C_p	Specific heat [J/(kg.°C)]
e_1	Edge distance in the direction of the loading [m]
e_2	Edge distance in the perpendicular direction to the loading [m]
e_{air}	Thickness of the air cavity [m]
e_{cont}	Eccentricity originated by the contact force between steel profiles [m]
e_{ext}	Eccentricity distance [m]
e_{fluid}	Thickness of air layer in a double-glass glazing [mm]
e_g	Thickness of glass [mm]
d	Nominal diameter of the screw [mm]
d_a	Overturning deformation [mm]
d_b	Bending deformation [mm]
d_f	Sheet-to-track and sheet-to-stud deformation [mm]
d_{Fmax}	Deformation at maximum force [mm]
d_i	Internal pipe diameter [m]
d_s	Sheet or panels shear deformation [mm]
d_p	Pipe spacing [m]
d_u	Ultimate deformation [mm]
f	Friction coefficient [-]
$f_{ax, k}$	Characteristic point-side withdrawal strength [N/mm ²]
$f_{head, k}$	Characteristic head-side pull-out strength [N/mm ²]
$f_{h, K}$	Characteristic embedment strength in the OSB boards [N/mm ²]
f_{yb}	Yielding tension without blending [N/mm ²]
f_u	Ultimate tensile strength of the steel sheet [N/mm ²]

f_{ub}	Ultimate tension [N/mm ²]
g	Gravity acceleration [m/s ²]
g_a	Ratio of the accumulated internal-external temperature difference when the ventilation is on [-]
g_{\perp}	Glazing factor [-]
h_{air}	Convection heat transfer coefficient in Trombe wall air cavity [W/(m ² °C)]
h_e	Convection heat transfer coefficient of exterior surface [W/(m ² °C)]
$h_{e,g}$	Convection heat transfer coefficient due to wind [W/(m ² °C)]
h_i	Convection heat transfer coefficient of interior surface [W/(m ² °C)]
h_r	Radiation heat transfer coefficient through the air layer [W/(m ² °C)]
$h_{r,g1}$	Radiation heat transfer coefficient for the outdoor conditions [W/(m ² °C)]
$h_{r,g2}$	Radiation heat transfer coefficient from the third surface to the second surface of the double glass [W/(m ² °C)]
h_{rg3}	Radiation heat transfer coefficient from the storage wall to the fourth surface of the glass [W/(m ² °C)]
k	Turbulence kinetic energy per unit mass [J/kg] or [m ² /s ²]
k_{fluid}	Thermal conductivity of fluid [W/(m°°C)]
k_g	Thermal conductivity of glass [W/(m°°C)]
k_{soil}	Thermal conductivity of ground [W/(m°°C)]
k_{pipe}	Thermal conductivity of pipes' wall [W/(m°°C)]
k_{stv}	Dimensionless parameter function of the air flow rate through the ventilated layer [-]
l_1	Measuring length for tensile tests [mm]
\dot{m}	Mass air flow rate [kg/s]
n	Number of screws used in the connection [-]
n_p	Number of pipes [-]
p	Fluid pressure [Pa]
q	Heat flux [W/m ²]
\dot{q}	Diffuse and direct radiation flux from the sky to an azimuth of 90° [W/m ²]
r_1	Pipe internal radius [m]
r_2	Pipe external radius [m]
r_3	Radius of the thermally affected zone of the ground around the pipe [m]
t	Time [h]

t_0	Day with lower annual environment temperature [-]
t_1	Plate thickness in contact with the screw head [mm]
t_2	Plate thickness without contact with the screw head [mm]
t_d	Current day [day]
$t_{d,1}$	Heating season duration [h]
$t_{d,2}$	Cooling season duration [h]
t_{pen}	Point-side penetration length or the length of the threaded part in the point side member [mm]
p	Pressure of the airflow [Pa]
p_1	Pitch distance in the loading direction [m]
p_2	Pitch distance perpendicularly to the loading direction [m]
u	Air velocity component in x direction [m/s]
u_1	Total displacement for 10% of the ultimate load [mm]
u_2	Total displacement for 40% of the ultimate load [mm]
u_w	Wind velocity [m/s]
v	Fluid velocity [m/s]
v	Fluid velocity component in y direction [m/s]
v_s	Steel volume [m ³]
v_w	Water volume [m ³]
w	Fluid velocity component in z direction [m/s]
z	Vertical distance below or above the ground [m]

GREEK LETTERS

α_s	Thermal diffusivity of the ground [m ² /day]
α	Thermal diffusivity of the fluid [m ² /s]
α_g	Absorptivity of the glass [-]
α_{st}	Solar absorption coefficient of the storage wall exterior surface
β	Coefficient of thermal expansion [K ⁻¹]
γ_{al}	Ratio between the solar gains and heat loss of the air [-]
ϵ	Heat Exchanger Effectiveness [-]
ϵ_d	Rate of dissipation of k [m ² /s ³]
ϵ_{g1}	Emissivity of the first surface of the glass cover [-]
ϵ_{g2}	Emissivity of the second surface of the glass cover [-]
ϵ_{g3}	Emissivity of the third surface of the glass cover [-]

ε_{ge}	Emissivity of the fourth trombe wall surface layer [-]
ε_s	Emissivity of the storage wall [-]
η_{fan}	Fan efficiency [%]
η_{mean}	Mean efficiency of the earth-to-air heat exchanger [%]
σ	Stefan-Boltzmann constant [W/(m ² .K ⁴)]
μ	Fluid viscosity [N.s/m ²]
μ_t	Turbulent viscosity [N.s/m ²]
ν	Kinematic viscosity [m ² /s]
ρ	Domain/material density [kg/m ³]
τ	Stress tensor [N/m ²]
τ_g	Transmissivity of the double glazing [-]
Φ	Resistance factor for LRFD and LSD [-]
$\Phi_{sol,mm,k}$	Time-average heat flow rate from solar heat source [W]
$\Phi_{r,k}$	Extra heat flow due to thermal radiation to the sky from the Trombe wall [W]
Ω	Safety factor for ASD
$\Delta\theta$	Average difference between the external air temperature and the sky temperature [°C]
ΔH	Additional heat transfer coefficient [W/ °C]
Δ_{int}	2D LSF wall panel displacement [mm]
Δt	Time step or period [h]
ΔT	Temperature difference between inlet and outlet [°C]
ΔT_1	Difference between inlet air and ground temperatures [°C]
ΔT_2	Difference between outlet air and ground temperatures [°C]
ΔT_{ml}	Logarithmic mean temperature difference [°C]
Δp	Pressure drop [Pa]

ABBREVIATIONS

AISI – American Iron and Steel Institute

ASD – Allowable Strength Design

ASPHP – Air Source Heat Pump

CFD – Computational Fluid Dynamics

COP – Coefficient of Performance

DHW – Domestic Hot Water

DX-GCHP – Direct Expansion Ground Couple Heat Pump

EAHE – Earth-to-Air Heat Exchanger

EB – Energy Balance

EP – Equivalent Power

EPS – Expanded Polystyrene

ETICS – External Thermal Insulation Composite Systems

FEM – Finite Element Method

GCHE – Ground Couple Heat Exchangers

GHG – Greenhouse Gas

GSHP – Ground Source Heat Pump

HDPE – High-Density Polyethylene

HRV – Heat Recovery Ventilation

HVAC – Heating, Ventilation and Air Conditioning

LMTD – Logarithmic Mean Temperature Difference

LSD – Limit State Design

LSF – Lightweight Steel Framing

LRFD – Load and Resistance Factor Design

LVDT - Linear Variable Differential Transformer

MBI – Modular Building Institutes

NSF – Net Section Failure

NTU – Number of Transfer Units

OSB – Oriented Strand Board

PCMs – Phase Change Materials

PMC – Permanent Modular Construction

PVC – Polyvinyl Chloride

SHESS – Soil-Heat-Exchangers Storage Systems

TES – Thermal Energy Storage

UAT – Underground Air Tunnel

WTSW – Water Thermal Storage Wall

WTW – Water Trombe Wall

CHAPTER I

Introduction

I.1. Framework and motivation

The scarcity of certain non-renewable energy sources and the effects on climate caused by CO₂ emissions is nowadays one of the biggest global concerns, leading to the need to reduce energy consumption (Vijayavenkataraman *et al.* 2012), reflected by new standards, laws, norms, policies and regulations. Half of the EU's final annual energy consumption (1102 Mtoe) used for heating and cooling, is distributed among the following sectors: 45% (248 Mtoe) for the residential sector (mainly households building), followed by 37% (202 Mtoe) for industry and 18% (96 Mtoe) used for services (EU, 2016). Buildings are responsible for 30 to 40% of the primary energy consumption and approximately 33 % of greenhouse gas (GHG) emissions worldwide (Díaz *et al.* 2013). This consumption is based on several building typologies and measures over a long period of time. It includes the embodied energy, or the energy required for the fabrication and transport of materials, the operation energy used for Heating, Ventilation and Air Conditioning (HVAC) systems, lighting and Domestic Hot Water (DHW); and the energy in the final stage of demolition or recycling energy. Due to the increase in occupants' comfort demands the operation energy required by active heating and cooling systems is the major cause of the increase of primary energy consumption.

Energy efficiency is one of the priorities of current policies, especially in the European Union. In December 2008, under the Kyoto Protocol (1997), and after months of tough negotiations, the European Parliament adopted the "Climate Energy Package", highlighting some targets for the year 2020. This legislation implements the 20-20-20 targets for 2020: to reduce by 20% the emission of greenhouse gases, to increase by 20% the energy efficiency in the EU and to reach 20% of renewable in total energy consumption (EU, 2008). To regulate the energy consumption in the building sector, the EU published the 2010/31/EU European Directive (EU, 2010) requiring that all new building to be constructed in the EU starting in 2020 should be nearly zero energy building (nZEB). The European

Commission has taken the construction methodology “*Passivhaus*” (from the Germany, Passive House) developed in Germany by *Passivhaus-Institut Dramstadt*, as a reference for nZEB (Griffiths and Nolte, 2011). Recently, a new directive (EU) 2018/844 of the European Parliament and Council of 30 May 2018 amending Directive 2010/31 EU (energy performance of buildings) and directive 2012/27/EU (energy efficiency) was published. The union is committed to developing a sustainable, competitive, secure and decarbonised energy system by 2050 (EU, 2018). The reduction of primary energy consumption can be achieved by using more efficient thermal systems and by improving the buildings construction methodologies therefore reducing the energy needs for space heating and cooling and the embodied energy. Sustainable construction of buildings plays a crucial role for reaching the EU’s long term 80-95% GHG reduction objective and also plays an important role in the European economy (European Commission, 2012). Sustainability takes into account the entire life cycle of the building, from design to construction, operation, maintenance, renovation and demolition, and it aims to find the right balance between homebuilding and the sustainable environment (Vilcekova *et al.* 2016).

Every year, new technologies are developed to complement current practices in creating “greener structures”, trying to reduce the overall impact of buildings on human health and natural environment. Light steel framing (LSF) is an alternative to buildings structures made by hot rolled structural steel, wood, masonry and other conventional materials (Mahdavinejad *et al.* 2011). LSF structures can reduce construction costs and they are also recognized as an environment friendly and sustainable construction system. Also, this kind of structures can be easily used for modular construction, showing a great possibility as an alternative to traditional *in-situ* approaches and could be a means of providing affordable housing in the dense and land deprived urban areas (Jellen and Memari, 2013). Nowadays, LSF modular constructions systems are being competitive used due to the speed of production and assemblage. The assemblage of a wall panel can be done very quickly usually using screws for the assemblage of structural and non-structural elements, fitting perfectly in the industrialized production. However, despite the economic, social and environmental advantages offered by this type of construction there are some characteristics that lead to some disadvantages. Namely, the mass of a LSF building, which is usually lower due to the reduced mass of the material in the envelope of the building. This means that this kind of construction has some difficulty in storing heat and providing inertia against outdoor temperature fluctuations. Thermal mass property is effective in improving building comfort in any climate zone that

experience daily temperature fluctuations, during heating and cooling season. Therefore, the use of renewable energies (active or passive systems) can play an important role in the achievement of major reductions in the energy consumption for space heating and cooling.

Over the last years, new technologies (active, passive and hybrid energy systems) have been developed and presented with the main objective to increase buildings thermal inertia. Walls are usually the largest portion of the building envelope, creating a route for thermal transmission because of their large surface area. This allows thermal/solar radiation to pass through the building during sunlight and the possibility to store this energy, working as a diurnal Thermal Energy Storage (TES). New innovative solutions have been developed aiming to improve the energy performance of building façade components such as *Trombe Walls*, *Autoclaved Aerated Concrete Wall*, *Double Skin Wall* and *Green Walls* (Omrany *et al.* 2016).

Another way of increasing buildings thermal inertia is the use of ground as a heat source or as a heat sink. Ground has a huge thermal inertia and can be considered as a seasonal TES, where the temperature variation at the surface is reduced deeper in the ground. In addition, a time lag occurs between the variation of the ground and surface temperatures. One technology that is able to promote heat exchanges between buildings indoor and ground is the Earth-to-Air Heat Exchangers. The number of installations of this type of systems increased 10% during the last 10 years (Singh *et al.* 2013). An EAHE system consists of a subterranean network of pipes that forces outdoor air for ventilation to flow within the pipes by means of a fan.

I.2. Research background and objectives

The research work presented in this thesis addresses the study of structural and thermal systems for LSF modular construction comprehending different research fields and projects. Three research projects served as the main background of this thesis: (1) ModCons (FP7-SME-2012-1); (2) EcoSteelPanel (IDI 2012, 204804); and (3) Earth-to-Air Heat Exchangers (Cool Haven company research project).

LSF wall panels produced by Cool Haven company were developed within the scope of FP7 European project ModCons (FP7-SME-2012-1). LSF wall panels are one of the main construction methods of modular construction and many studies have been performed over the last years. These wall panels are usually assembled using screw connections, which are responsible of fixing the steel-to-steel and steel-to-non-structural elements. The second part of the thesis provides a detail study of screw connections by means of experimental campaigns, followed by analytical and

numerical analysis. European and American design codes, and numerical models with finite element method were used to complement the experimental campaign.

The main objectives of this part of the thesis are: (1) to give better understanding of steel-to-steel connection behaviour with self-drilling screws; (2) to study of the connection between steel-to-OSB; (3) to analyse the structural behaviour of braced and unbraced LSF wall panels (Figure II.1) using screw connections subjected to lateral loading; (4) to study the influence of the distance between screw connections.



Figure I.1 – Experimental test with non-braced wall panels.

As already mentioned, LSF construction provides great potential when compared with other types of construction systems. However, the mass of this type of construction is lower than traditional construction systems leading to a drawback in terms of building thermal inertia. As already mentioned, the ground has a huge inertia compared with a building and EAHE systems are one alternative way to improve buildings inertia by ventilation. However, the behaviour of these systems depends on the climate and ground characteristics where they are installed. Also, physic and geometric parameters have an important influence on the overall thermal performance and they should be well known before design. For a better understanding of these kind of systems, an EAHE with open loop was installed in a low-rise residential building in Coimbra (Portugal). The system was properly monitored and assessed for one year. This building (Figure I.2) was constructed using LSF structures combined with modular construction produced by Cool-Haven company. The monitored system is based on the KNX protocol and programmed with ETS5 software, which allows the total control of the EAHE based on indoor

temperatures and CO₂ levels. The main objectives of this study are: (1) experimental tests of the pilot installation over the four seasons of the year; (2) to study the importance of the EAHE operation control; (3) to develop a simple analytical tool for EAHE design and to validate it against data taken from the *in-situ* monitoring system for cooling and heating operation times; (4) to use the proposed model to perform a parametric study to understand the system behaviour exchanging physical and dynamical parameters; (5) to use computational fluid dynamic modelling to analyse the thermal performance of the heat exchanging under transient conditions for different pipe diameters and air velocities; and (6) to analyse the influence of distance between pipes under transient conditions during two days of cooling and heating conditions.

Focusing on building façades and within the scope of the project EcoSteelPanel (IDI 2012, 204804), the final part of this thesis presents the development of a new sustainable LSF solution that could be used as a rain water harvesting and simultaneously can improve the thermal behaviour and energy efficiency of LSF modular construction buildings. After some preliminary studies the final solution of this wall is based on a standard Trombe Wall system. However, in this case the heat storage wall is basically a steel panel filled with water (*EcoSteelPanel*) which will be directly connect to the LSF structure of the building. The Water Trombe Wall (Trombe Wall with a TES) solution was developed to be easily implemented in a LSF house. This wall absorbs diffuse and direct solar radiation during the day and transfer the heat to the building interior by controlled convection during the night. *EcoSteelPanel* filled with water can be used as TES and can be incorporated in a normal modular construction building. Also, in the future, this Water Trombe Wall could be work as a hybrid system to produce or pre-heat of DHW using internal heat exchangers pipes. Another objective of this kind of system is to mitigate the heat losses mainly at night and to increase thermal inertia. The traditional Trombe Walls have low thermal resistance during night or prolonged cloudy periods, the heat flux is transferred from inside to the outside of a building. On the other hand, the Water Trombe Wall in this study has a high thermal resistance and controlled the usual inverse thermosyphon that occurred in typical Trombe Wall. Hence, the main objectives of this study are: (1) to assess the TES potential of the panel by experimental prototypes exposed over one year to outdoor conditions and measured surfaces and water temperatures when exposed to solar radiation; (2) to develop numerical and analytical models to predict the steady-state/transient thermal behaviour of the TES wall, including changing the water between panels integrated in different façades; (3) in order to evaluate the thermal performance of the Water

Trombe Wall (WTW) two identical experimental modules (One module is used as a “reference” and while the other has the WTW system in the south façade) in LSF (cubic houses) with the same inner dimensions (2.75x2.75mx2.8m) were designed, constructed and monitored; finally (4) the WTW thermal performance will be evaluated during a few days with natural and forced convection.



Figure I.2 – Earth-to-air heat exchanger and Water Trombe Wall in a LSF building.

I.3. Thesis outline

The content of this thesis is indicated in Figure I.3. This thesis is divided into four parts and nine chapters. Part A provides a general overview of lightweight steel framing for modular construction in terms of structural and thermal performances. Part B presents a study of the structural performance of LSF modular construction. Due to the low thermal inertia of LSF construction the two final parts (C and D) present two thermal systems (Earth-to-Air Heat Exchangers and Trombe Walls) that can reduce this drawback.

The first two parts (A and B) of this thesis comprise Chapters II and III. Chapter II is divided into three sections. The first two sections present some structural concepts and discuss the thermal performance of LSF buildings focusing on thermal inertia. The mechanical and thermal properties of structural and non-structural materials are experimentally evaluated, to later numerical and analytical calculations. To provide a deeper understanding of screw connections in LSF structures and their impact on the response of the structure, Chapter III (Part B) provides numerical, analytical and experimental studies on screw connections (steel-to-steel and steel-to-OSB) and wall panels.

Part C comprises Chapter IV to Chapter VI. In Chapter IV the fundamentals of the heat transfer in EAHEs are presented, including the development of an analytical design methodology based on the effectiveness-number of transfer unit's (ϵ -NTU) relationships for heat exchangers. Additionally, a literature review on experimental,

CHAPTER I

Introduction

analytical and numerical studies with EAHE systems is provided. The thermal properties of a sandy and clayey soil are investigated using analytical and measured data for later analytical and CFD models. Chapter V focusses on the experimental and analytical assessment of an EAHE pilot installation performance in the Csb climate over one year. A parametric study is carried out based on the analytical model previously developed.

In Chapter VI, transient 3D models were developed to evaluate the heating and cooling performance of an EAHE combining different pipe diameters, air velocities and distance between pipes. Part D comprises Chapter VII and Chapter VIII. Chapter VII provide a literature review of Trombe Wall technologies and heat transfer fundamentals for design and energy evaluation. The development of a new Water Trombe Wall system (WTW) for LSF modular construction is presented in Chapter VIII. In addition, in this chapter, the thermal performance of the thermal storage layer is analysed with experimental, numerical and analytical approaches. Preliminary studies on the full-scale WTW system are discussed. The final conclusions and future work are given in Chapter IX.

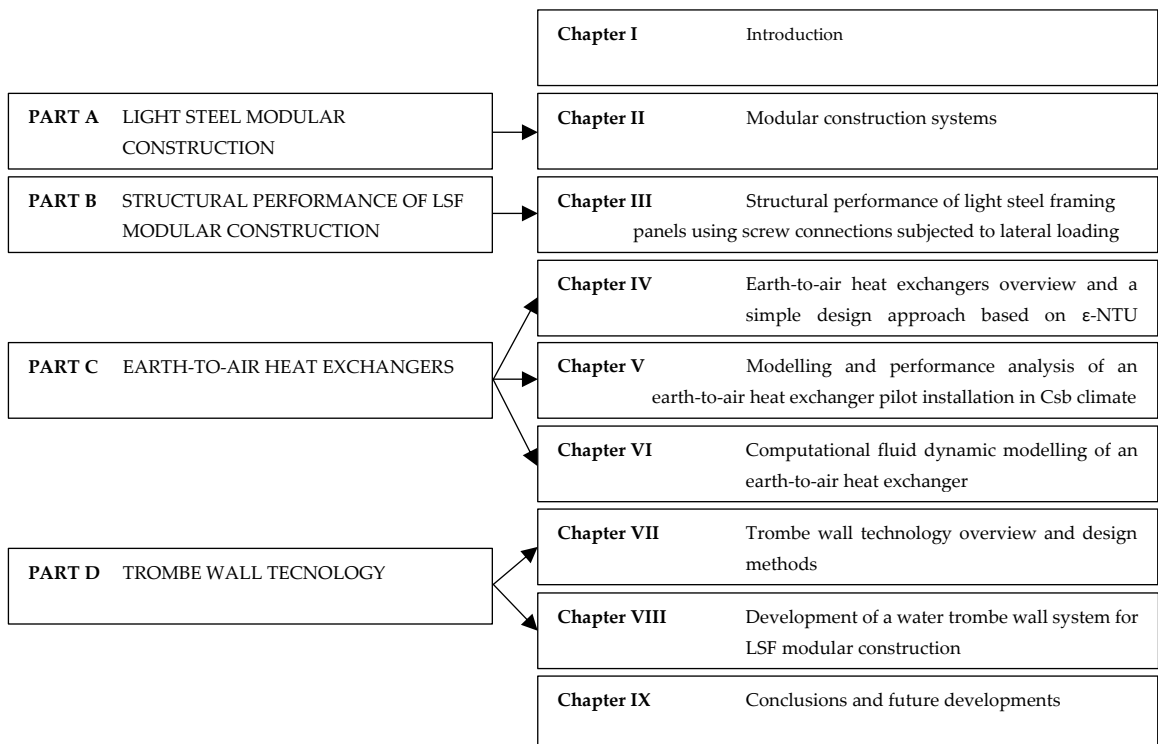


Figure I.3 – Thesis outline.

PART A

LIGHT STEEL FRAMING MODULAR CONSTRUCTION

CHAPTER II

Modular construction systems

II.1. Introduction

Light Steel Framing (LSF) construction is recognized as a sustainable construction system that has been gaining popularity, not only because steel is one of the most recyclable materials in the world, but also due to the advantages of light weight construction. A LSF designation comes up from the fact that profiles are fabricated from steel plates with reduced thickness that are cold formed. The most common sheathing in LSF for low-rise residential building are made of OSB (Oriented Strand Boards) and gypsum plasterboards for the outer and inner layers of external walls, respectively (Soares *et al.* 2017). In this type of construction, steel profiles are the main structural elements; however, it is important to consider the bracing effect of OSB and gypsum plasterboard which have an important role mainly for horizontal loads (*e.g.* wind) in the plane of the walls (Davies, 2006). In some seismic regions, it is usual to use a steel plate bracing also known as *Saint Andrew Cross*.

Modular construction methods show great potential as an alternative to traditional construction ‘in situ’ methods and could be a means of providing the much-needed affordable housing, *e.g.* in urban areas. The Modular Building Institutes (MBI) define modular construction as: “Modular describes a construction method or process where individual modules stand alone or are assembled together to make up larger structures”. MBI classifies modular construction in two categories: Permanent Modular Construction (PMC) and Relocatable Buildings. PMC is subdivided into 2D panelised (*e.g.* in Figure II.1a) and 3D modular construction systems (*e.g.* Figure II.1b). 2D panelised modular construction is based on the assemblage and production of light steel framing (LSF) panels that can be transport to the construction site. These panels are increasingly being used in modular construction methods, not only due to its lightness and speed of assemblage but also due to its easy adaptability to most architectural and structural requirements.

3D modular construction refers to 3D modules composed by an assemblage of 2D panelised components, *e.g.* walls and floors. Usually, these 3D modules are completely assembled off site and then transported and connected with other 3D modules on site. However, they may also work as a stand-alone module system.

The main advantage of the 2D penalised method consists in the increased flexibility of the connection between pre-fabricated elements, economy of material (3D modular construction requires doubling of profiles), lightness of the construction elements to move on site and optimization of the transport (3D modular construction requires a higher volume to be transported).

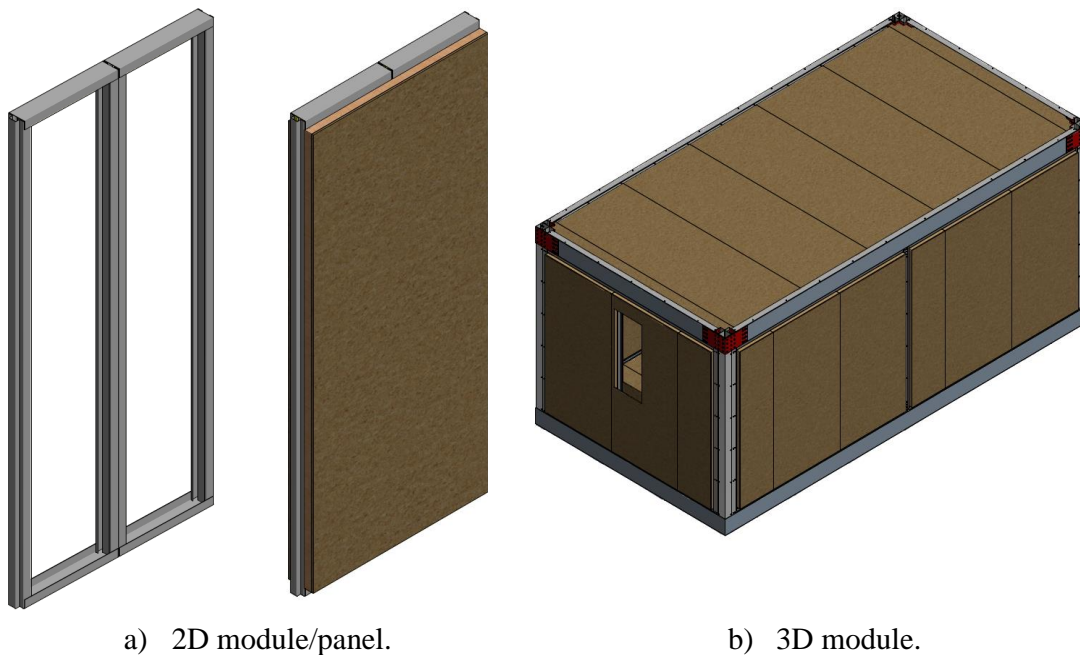


Figure II.1 – Illustration of 2D and 3D modules from ModCons project.

Some of the main advantages of LSF modular construction are the following: (1) 100% recycling material without losing its properties; (2) lightness; (3) speed of fabrication and erection with an increase of productivity and cost savings; (4) reduction of resources necessary for the construction; (5) adaptability to new requirements over the service life of the structure; (6) structure dismantling ;(7)built off-site (in the factory) with controlled environment; (8) clean construction without the usual community disturbance of typical constructions. However, there are a few inconvenient with the usage of cold – formed steel profiles: (1) susceptibility to instability phenomena; (2) steel profile web crushing by concentrated loads; (3) high torsional deformability; (4) steel hardening; (5) the calculation steps for this kind of construction are very complex; and (5) cold – formed profiles are expensive due to the galvanization process.

The use of light steel framing in housing and low-rise multi-storey buildings is well established in regions as North America (AISI, 1999). In Europe, only in the northern countries this type of structures has a relevant presence in the construction market (LSK, 2005). Over the last decades, the interest on this type of construction has been growing; however, the market is still dominated by other structural solutions, such as reinforced concrete and masonry. However, one of the challenges of LSF modular construction market is overcoming social stigmas from the past, where many people associate this kind of construction with unattractive, low quality and industrialized structures. To further expand the market and the share of light steel framing, its competitiveness must be improved. The reduction of construction time and cost, combined with a safe and durable construction, are major advantages (Soares *et al.* 2017). In Portugal there are several factors that are delaying the construction with LSF methods (Jos *et al.* 2016): (1) the current economic situation; (2) lack of disclosure; (3) lack of training professionals responsible for the assemblage; (4) cultural barriers; and (5) the final prices are still very high comparing to the tradition construction.

In this chapter an overview of LSF construction is presented. The structural design, the construction materials and the thermal performance are discussed. The final section of this Chapter presents an experimental campaign carried out to characterize the mechanical and thermal properties of materials used in LSF construction in particular the mechanical properties of steel grade S280GD+Z and OSB3 boards are presented. The thermal conductivity of the materials is also measured. These values are important for the numerical and analytical studies carried out in the later stages of the research work.

II.2. Overview of LSF modular construction

II.2.1. Normative documents for structural design

In the last century, in the United States the standard for the design of light gage steel structural members was published by the American Iron and Steel Institute (AISI). The AISI aims to: (1) defend public policies that support the competitive environment to the domestic factory; (2) provide high quality products and added additional values for a range of customer; (3) produce steel in a safe and environmentally friendly way; (4) raise the North American Steel Market in both applications, traditional and innovated solutions.

As a leader in the cold formed industry, AISI plays an important role in the development and expansion of this market. AISI developed the specification for the Design of Cold – Formed Steel Structural Members, the original technical document

for LSF industry. Over the years, they have developed and published several other technical documents, including guides and manuals for calculation and construction of LSF. All this work has laid the foundation for the deployment and growth of the LSF industry in the US and around the world. The “North American specification for Design of Cold – Formed Structural Members” is a regulatory document for this type of construction, which is also valid in Canada, United States and Mexico. This standard replace the previous edition of the standards in the previous editions of the regulation for the design of cold formed structural steel elements published by AISI, and the previous edition of the CSA (Canadian Steel Association) S136 “Structural elements of cold – formed steel -2 published by the Canadian Standards Association(AISI S100, 2007). In Europe, the introduction of the Eurocodes has changed the way steel structures are designed, where a common European standard should be used. In past, due to the lack of specific guides and regulations the LSF system was not well known and used as a structural system in Europe. However, with the introduction of new normative documents, LSF structures design methods can be found in the Eurocode 3 - Design of Steel Structures: Part 1- 3 Supplementary rules for cold – formed members and sheeting (EN1993-1-3, 2006).

II.2.2. Structural design

The EC3-1-3 and part of EC3-1-5, deal with the specific design of cold-formed steel structures. The type of cross sections used for LSF construction can be classified as: (1) Simple open sections; (2) opened coupled sections; and (3) closed coupled sections. Figure II.2 shows an example of the typical cross section used in LSF construction.

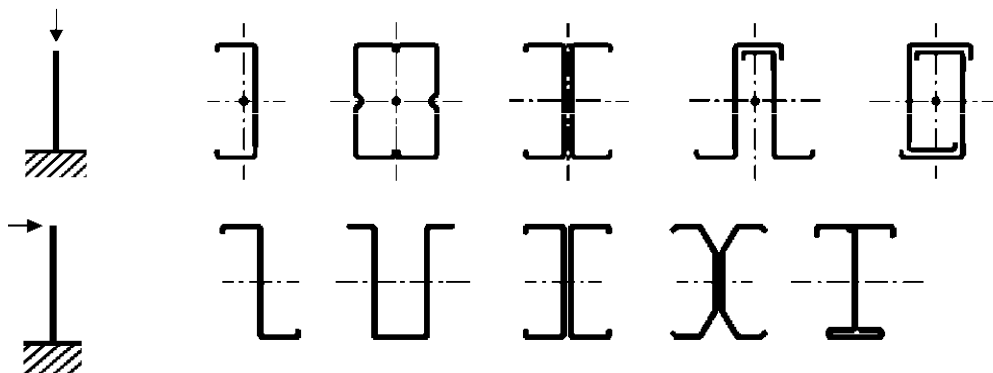


Figure II.2 – Cross section of steel cold-formed steel profiles for beams and columns 1993-1-1, (2005).

The most common commercial profiles are the opened sections “C” and “U”. The “C” and “U” can be assembled “back to back” and also a “C” profile can be coupled with a “U” section. Normally, the coupled “C” profiles are closed by two “U”

profiles. Usually, the thickness of the steel sheet for LSF profiles is in a range of 0.45 to 6 mm (Santos *et al.* 2012). It is important to define the partial factors adopted for ultimate limit states and serviceability limit states. EC3-1-3 gives the partial safety factors for each verification. For the design of structures made of cold formed profiles, it is important to verify the “structural classes” associated with failure consequence according to EN 1990 – Annex B. The material selection is also a very important step of the design process. It is important to evaluate the mechanical properties of steel, the manufacturing process, the limits of steel thickness and the connections. A special attention should be given to the material durability. EC3-1-3 presents a few documents: (1) EN – ISO 12944-2, for corrosion resistance of fasteners for the environmental class; (2) EN 508-1, for roofing products; and (3) EN 1993, for other products.

Figure II.3 summarises the design steps of cold-formed steel structures. The design and safety verification of one structure can be done with analysis leading to the ultimate load. However, this analysis can be complex. The traditional method of EN 1993-1-1 (2005), uses the reduction of the mechanical properties of the cross-section (effective cross-section). In this case, the safety verification of the resistance and stability is not done based on the real properties of the cross-section. But on an effective cross-section when the steel profiles have class 4 cross-section. Screw connections in LSF modular construction (Point 6 of Figure II.3) are discussed in detail in Chapter III. Experimental, numerical and analytical studies are performed to have a better understanding of this important stage of LSF design.

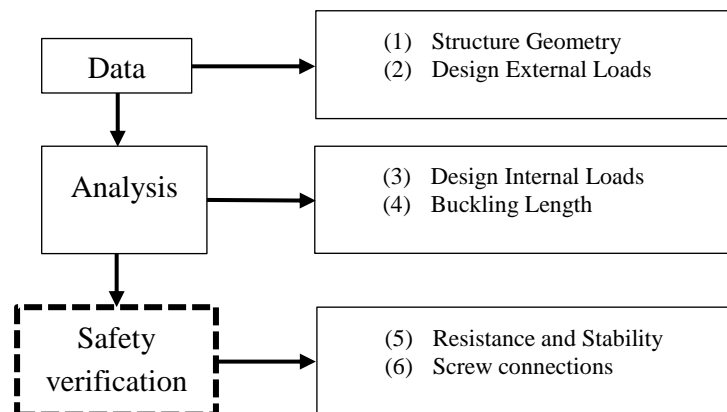


Figure II.3 – Design steps of cold-formed steel structures.

II.2.3. Construction materials

The right choice of materials can increase the total value of a property/building. Materials provide thermal and acoustic insulations and help to brace structural steel profiles. In a LSF construction, material layers can be divided in three parts: (1) exterior layer, with insulation material; (2) inner layer between steel profiles flanges, with an air cavity and thermal insulation; and (3) internal layer, usually us plasterboard and with or without thermal insulation. Usually, the exterior layer is composed by an External Thermal Insulation Composite Systems (ETICS). These systems are thermal insulations coatings of expanded polystyrene (EPS) boards fixed to the exterior OSB panels with glue and mechanical fixings. EPS is a rigid cellular plastic and is an excellent material for construction as it is light, yet rigid foam with good thermal insulation and high impact resistance (EPS Packaging Group, 2012). EN 13499 (2003) provides specific requirements, procedures for testing, marking and labelling for thermal insulation products for buildings. Finally, the EPS boards can be bonded or mechanically fixed to the wall.

Most construction companies use OSB boards to brace the steel structure. These boards are formed by adding adhesives and then compressing layers of wood strand (flakes) in specific orientations. The OSB is a material with good mechanical properties making this material suitable for load-bearing applications in LSF construction. There are four grades of OSB defined in EN 300 (2006) in terms of their mechanical performance and resistance to moisture: (1) OSB1, general purpose boards and boards for interior fitments for use in dry conditions; (2) OSB2, load bearing boards for use in dry conditions; (3) OSB3 load bearing boards for use in humid conditions; and finally (4) OSB4, heavy duty load bearing boards for use in humid conditions. However, the mechanical behaviour of OSB panels is very unpredictable due to the fibre direction. In the next section, the mechanical properties of this material are described.

The inner layer or inside layer of the steel panel is usually divided into two parts: (1) an air cavity; and (2) *e.g.* a mineral wool, which is the common thermal insulation material in LSF construction. Stone wool insulation is mostly used between the steel studs. This insulation allows to fulfil three fundamental requirements: thermal insulation, acoustic insulation and fire protection. The requirements for mineral wool insulation are specified in EN 13162:2012+A1 (2015). There are other materials that can be used, such as fibreglass insulation and injected polyurethane. Finally, the interior layer is finished with pasteboard that can be glue to the OSB panels or fixed using steel profiles. Plasterboard is basically an inner layer of gypsum sandwich

between two outer layers of lining paper including various additives in the gypsum layer and varying the weight and strength of the lining paper. Because gypsum has crystals with small amount of water, the layer can resist fire and helps the temperature of the fire to go, thus preventing the rapid-fire spread. Also, these boards provide good acoustic insulation and have low thermal conductivity. An example of a LSF wall is illustrated in Figure II.4.

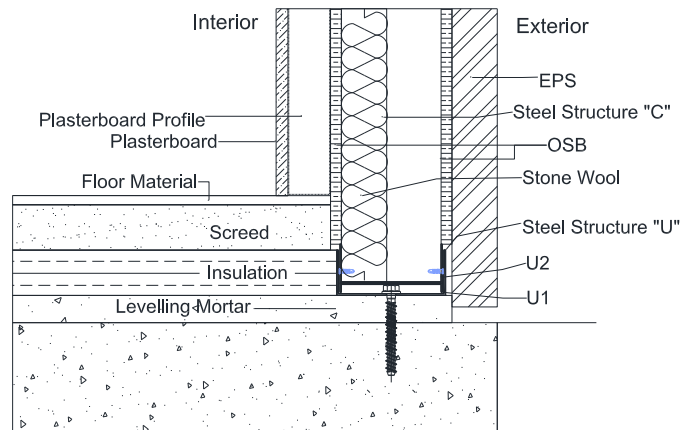


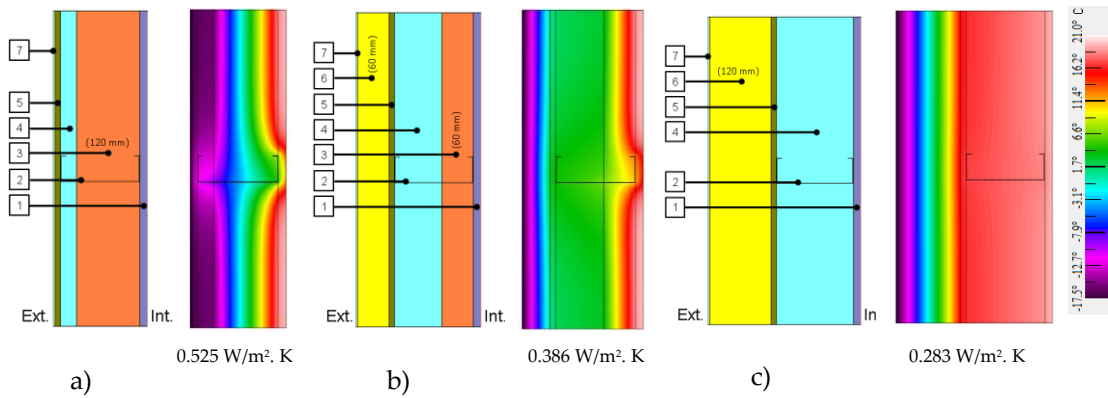
Figure II.4 – Example of a cross-section of a LSF wall.

II.2.4. Classification of LSF construction

Light steel framing construction is classified according to the location of the thermal insulation (Santos, 2017). Figure II.5 illustrates the three types of LSF construction: (a) Cold frame construction; b) Hybrid construction; and c) Warm frame construction. In cold frame construction, the thermal insulation is placed inside the wall between the steel studs. This leads to two drawbacks: (1) this construction may suffer of some interstitial condensation due to the low temperature of the steel elements in colder climates; and (2) the thermal bridges are higher leading to an increase of thermal transmittance value which leads to higher heat gains/losses.

In hybrid construction type the thermal insulation is distributed between wall air cavity (between steel profiles) and outer surface. This construction type is the most used in LSF construction.

Finally, in the warm frame construction all the thermal insulation is placed on the outer wall surface. This type of construction allows a higher reduction of the thermal bridges effect which leads to a better overall thermal performance. However, the high thickness of the thermal insulation leads an increase of wall thickness, which may lead to smaller net floor area (Soares *et al.* 2017).



1 – Gypsum; 2 – LSF steel profile; 3 – Stone wool; 4 – Air cavity; 5 – OSB; 6 – EPS; 7 – ETICS.

Figure II.5 – Classification of LSF walls and respective temperature distribution/thermal transmittance values (Santos, 2017).

II.2.5. Thermal performance

The thermal efficiency of a building depends on several factors such as climate conditions region, building envelope, human behaviour and finally HVAC systems. Climate is an external key factor with an impact on thermal behaviour and energy efficiency where the main parameters are: air temperature, solar radiation; relative humidity, wind speed and direction; ground temperature and daylight hours (Santos, 2017). The design of the building envelope, should consider the following aspects: (1) building shape coefficient; (2) building orientation; (3) air tightness; (4) construction materials for walls, roofs and floors considering the thermal bridges; (5) thermal mass; (6) glassing; (7) shading devices. The occupant's behaviour and the HVAC system have a direct relation and they should be considering during the design phase for the perfect control of the systems and for their correct selection. Lightweight steel framing construction has great advantages in terms of structural behaviour and sustainability. However, due to the high thermal conductivity of the structural steel and low mass, this kind of construction has a few disadvantages in terms of thermal bridges and lower thermal inertia. However, there are some strategies to mitigate thermal bridges and to increase thermal inertia.

II.2.5.1. Thermal bridges

Thermal bridges in the building envelope may increase the total energy demand for space heating and cooling. Erhorn-Kluttig and Erhorn (2009) concluded that thermal bridges could increase the heating energy needs by up to 30%. However, they also concluded that the cooling energy need is significantly lower. Ge and Baba (2015) investigated the dynamic effect of the thermal bridges and the results show that the inclusion of different thermal bridges junctions increases the annual heating energy

CHAPTER II

Modular construction systems

load by 37.4-42.2%. Also, in LSF construction the high number of steel profiles can be very tricky to consider on the total thermal performance of the building. In modular construction this problem can be worse, due to the increase of steel connections between LSF 2D panels. However, some studies present mitigation strategies. Martins *et al.* (2015) in a parametric study of LSF thermal bridges presented some mitigation strategies for modular construction (wall module). Figure II.6 presents the 3D wall module used for their parametric study.

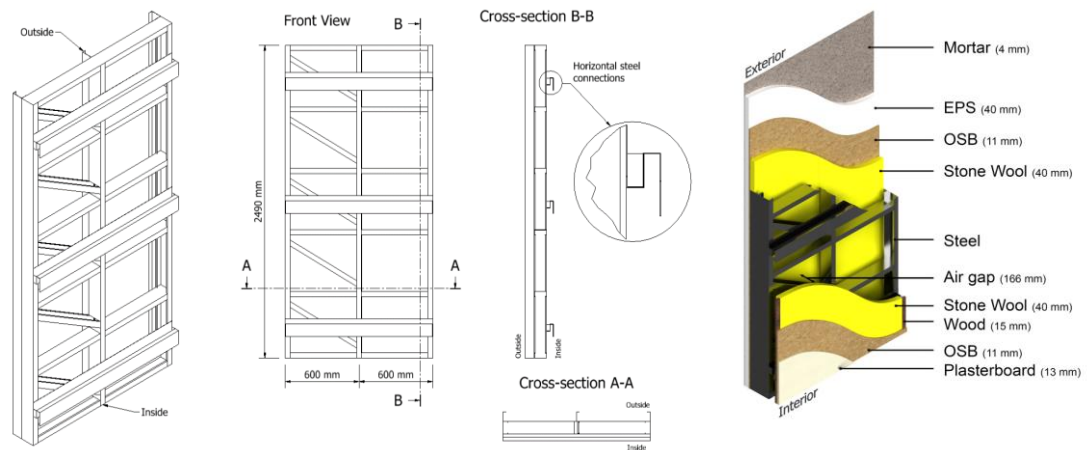


Figure II.6 – LSF wall model used in parametric study (Martins *et al.* (2015)).

The above study was developed using tri-dimensional software (Ansys CFX) necessary to evaluate the U-Value for different wall configurations. Several models were developed: Model B uses thermal break rubber strips; Model C uses vertical male or female studs; Model D has stotted steel studs and model “E” fixing bolts instead of horizontal steel plate connection. In this study it was conclude that the thermal transmittance of the wall could be reduced by up to 8.3%, (Model G) which is around 75% of the total impact of the steel thermal bridges (Figure II.7).

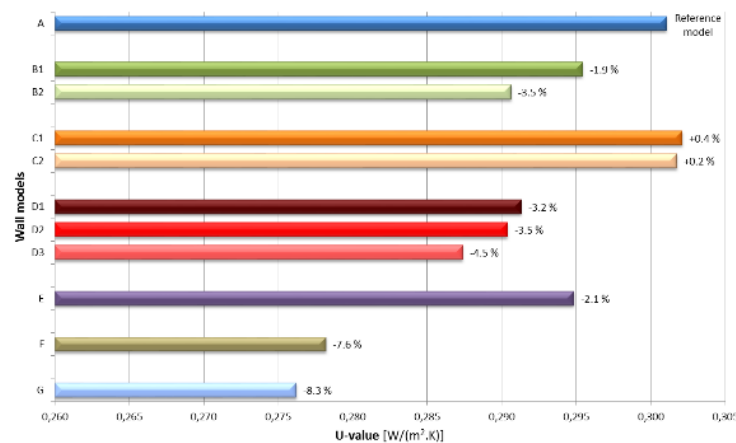


Figure II.7 – Results of the parametric study (Martins *et al.* 2015).

The authors also presented a design guidance: (1) Introduce at least one-third of continuous thermal insulation; (2) If the previous condition is verified, then some proposed thermal bridges mitigations could be reduced; (3) Also, thermal profiles with higher number of narrow slots are more efficient; (4) Use two layers of perpendicular steel studs to avoid trespassing the entire wall module cross section with two parallel steel profiles; (5) The air cavity between steel profiles can be partial filled with insulation. Finally, it was concluded that the U-Value could be reduced by 68% with all the proposed mitigations strategies that includes new insulation materials such as aerogel and vacuum insulation panels.

II.2.5.2. Thermal inertia

Thermal inertia is a bulk material property related to thermal conductivity and volumetric heat capacity. Thermal inertia term is used for modelling heat transfer and measuring the capacity of a bulk material to conduct and store/release heat over time. In buildings design, the thermal conductivity of materials is used to measure the thermal resistance (R-value) and the transmittance (U-value) of construction elements. On the other hand, in buildings the heat capacity, which is also known as thermal mass, is a property that measures the building capacity to store heat and provide inertia against outdoor temperature fluctuations. A building with high thermal inertia/thermal mass is usually composed by materials with high specific heat capacity and high density (low thermal diffusivity). This property allows dampening and retarding of temperature peaks and decrease cooling and heating need of the building. A comparison between the internal temperature of a building with low (lightweight construction) with a building with high thermal mass (heavyweight construction) is illustrated in Figure II.8.

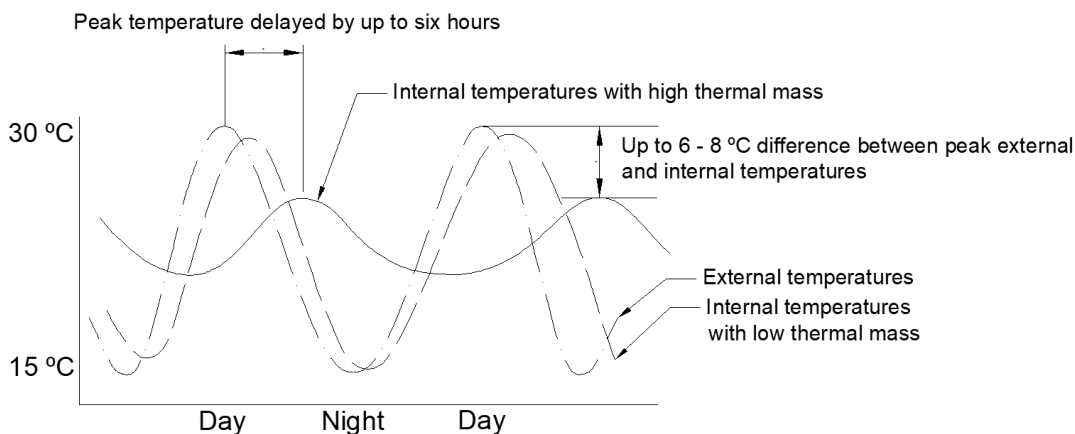


Figure II.8 – Illustrative example of building thermal mass effect.

During hot summer days, a high thermal mass allows to absorb the excess of heat caused by the use of the building and its solar gains. During night time, the exterior temperature drops and with natural ventilation the storage heat can be release to the outside. In hot and humid climates, it is not recommended to build houses with high thermal inertia due to their capacity to maintain the heat gains. During winter, the energy storage of the thermal mass of the building can be used during night periods, when the outside temperature drops. In buildings with sporadic occupancy a low thermal mass can be more advantageous, due to its smaller capacity to store heat, it is possible to heat and cool the interior faster with less power consumption.

In the case of buildings with permanent occupation, the lack of thermal mass may lead to a substantial increase in the energy consumption by air condition systems. One drawback of LSF systems is the low thermal mass, leading to higher daily indoor temperature fluctuations. This is more evident for climates with higher outdoor temperature fluctuations such as the Mediterranean climates (Martins *et al.* 2015). Several strategies were proposed by Santos *et al.* (2017) that can be used to improve the thermal inertia of LSF buildings, such as the use of massive construction materials (*e.g.* Trombe Walls), the use of PCMs (Phase change materials) and the use of ground thermal mass (Ground Source Heat Exchangers). The first two strategies operate as a solar passive heating, which are assemble on the façade of buildings and can store solar thermal energy during the day and release it during the night. The last strategy takes advantage of the huge ground thermal inertia to promote heat exchange between ground and buildings indoor.

Chapter IV and VII presents a review of Ground Source Heat Exchangers and Trombe Walls, respectively.

II.3. Materials mechanical and thermal properties of the materials

II.3.1. Steel mechanical properties characterization

Steel used in cold rolling process is supplied in grades S220GD+z, S250GD+Z, S280GD+Z, S350GD+Z or S550GD+Z (EN10326, 2004). The yield strength changes from 220 to 550 N/mm² and there is a minimum G275 coating with a thickness of zinc coating of 0.04 mm (275 g/m²) usually the steel used for this type of construction is the S280GD, which in EC3-1-3, represent a S280GD+Z steel (structural carbon steel sheet with continuous immersion of hot zin) with a yielding tension without blending (f_{yb}) of 280 N/mm² and ultimate tension (f_{ub}) of 360 N/mm².

The assessment of the mechanical properties of the steel used in the tests was made according to EN 10002-1 (2001). Figure II.9a shows the geometric characteristics of

S280GD+Z specimen for the tensile tests and the results of the tests are indicated in Figure II.9 by the extension-force plot until 2% of steel extension. The experimental tests were done according to EN 10002-1 (2001), which represents different velocities.

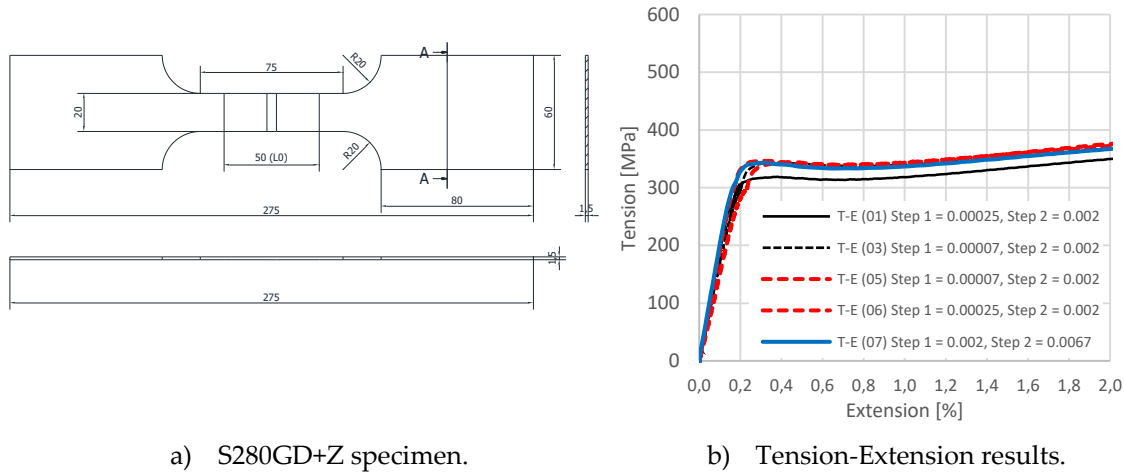


Figure II.9 – S280GD+Z mechanical characterization according with EN 10002-1.

II.3.2. Oriented strand board properties characterization

To investigate the mechanical properties of OSB boards, an experimental campaign is performed. The main objective of these tests is to understand the material behaviour in tensile and compression. These tests are performed according with the British Standard EN 789 (1996) Test Methods – “*Determination of mechanical properties of wood-based panels*” referred by EN 300 (2006). According with the British Standard EN 789 , at least ten OSB specimens must be test under tensile and compression forces. Bending tests were not performed at this stage. The OSB boards must be cut in two different directions to consider the different fibre directions. The OSB mechanical properties experimentally achieved are also compared with the values present in EN 12369-1 (2001) – “*Characteristic values for structural design – Particleboard and fibreboard*”.

A transducer is fixed in the middle of the OSB board and measures the total displacement of the board in a range of 100 mm (l_1). These experimental tests allow the measuring of the elasticity modulus, the tensile strength and the stiffness of a OSB specimen. A steel support was developed and used to make the connection between the OSB specimens and the electromechanical press machine without any eccentricities. Figure II.10 shows main the characteristics of the steel support and test specimen used in the experimental tests. To fix the steel support in the OSB board six M10 bolts in stainless steel were used to ensure stability of the specimen during the tensile test.

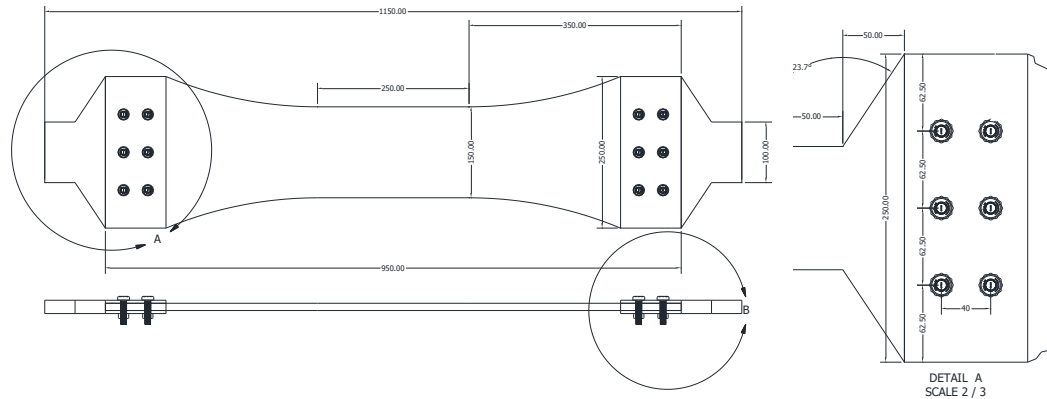


Figure II.10 – Experimental layout for OSB tensile tests.

Initially, ten specimens were used, however it was found an error in LVDT sensor (linear variable differential transformer). Due this, the total displacement of obtained five specimens was not considered in the experimental tests. These five specimens (specimen 5 to 10) were not considered for calculation of the elasticity modulus. The elasticity modulus (E_c) can be obtained using the following expression given by BS EN 789, 1996:

$$E_c = \frac{(F_1 - F_2) \times l_1}{(u_2 - u_1) \times A_1} \quad (1)$$

where, F_2 and F_1 represents 40% and 10% of the ultimate force occurred during the test, respectively; u_2 and u_1 represents the total displacement obtained for F_2 and F_1 . The area of the cross section (A_1) was measured in all specimen with a value of 0.001836 m². Figure II.11a and b show the yield stress and the elasticity modulus results, respectively.

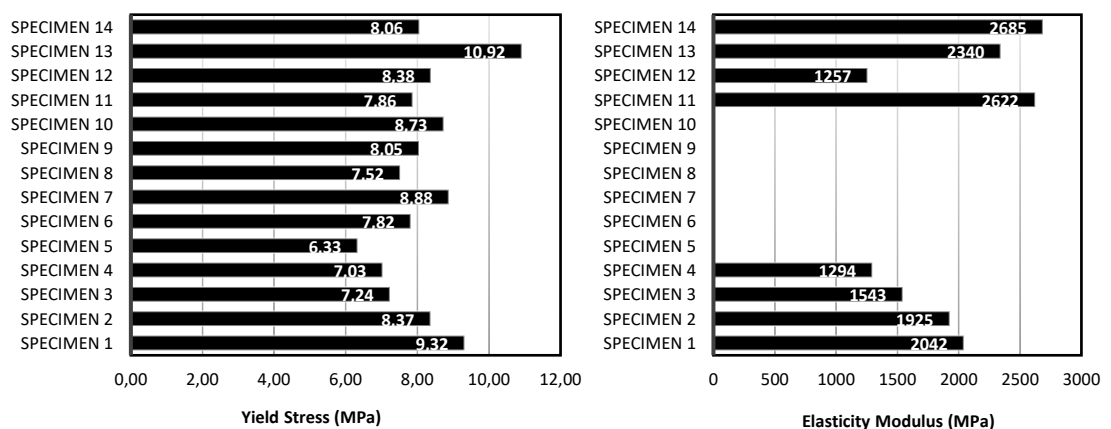
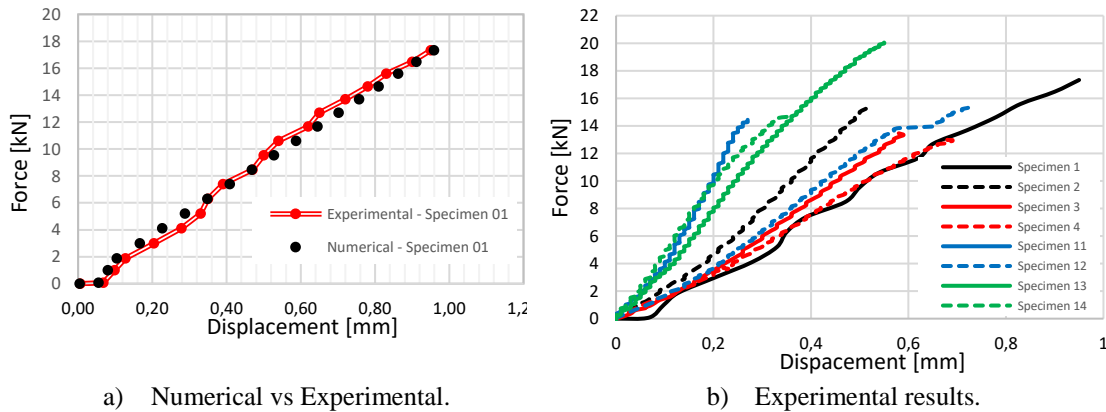


Figure II.11 – Experimental results of OSB mechanical properties.

Experimental results are clear, and it can be concluded that OSB boards have a very unpredictable mechanical behaviour especially during the analysis of the E_c . The main reason of this unpredictable behaviour is due to the OSB fibres direction, especially when the OSB board has fibres on the perpendicular direction of the applied load. The average yield strength obtained is 8.18 N/mm² with a minimum and maximum value of 6.33 and 9.32 N/mm², respectively. The theoretic value presented in EN 12369-1 (2001) is 9.4 N/mm² in X and Y direction and 7.0 N/mm² in Z direction. The elastic modulus achieved is lower than the value specified in the EN 12369-1 (3800 MPa) and EN300 (3500 MPa). The mean value is 1949 MPa. Figure II.12a presents the comparison between numerical and experimental force-displacement curves. Figure II.12b presents the force-displacement curves from experimental results.



a) Numerical vs Experimental. b) Experimental results.
Figure II.12 – Force – displacement for tensile experimental and numerical analysis.

The first test specimen is used to validate the numerical model developed in Ansys Workbench (structural analysis model). The first specimen was selected for the numerical validation due to the proximity between experimental result of the yield strength (9.3 MPa) and the predicted value (9.4 MPa). The mechanical properties given by EN 12369-1 (2001) are used in this numerical model. The 3D model considers the orthotropic properties of OSB boards. This allows better results for the achievement of yield strength and elasticity modulus. Results shown a good agreement between experiment and numerical model (Figure II.12a). It is found that the total displacement achieved in the numerical model was 1.1 mm against 0.95 mm obtained in the experimental test. It can be concluded that the values given by EN 12369-1 (2001) can be used for future and more complex models.

BS EN 789 (1996) presents the experimental requirements for the compression tests in OSB boards. According the standard, the specimens should have a thickness lower than 40 mm and a width equal to 5 to 6 times the specimen thickness. The total length must be 200 mm and the l_1 is equal to 100 mm, considering the Annex A from BS EN

789 (1996). Figure II.13 a) and b) displays the experimental results of yield stress and the extension-stress curves, respectively.

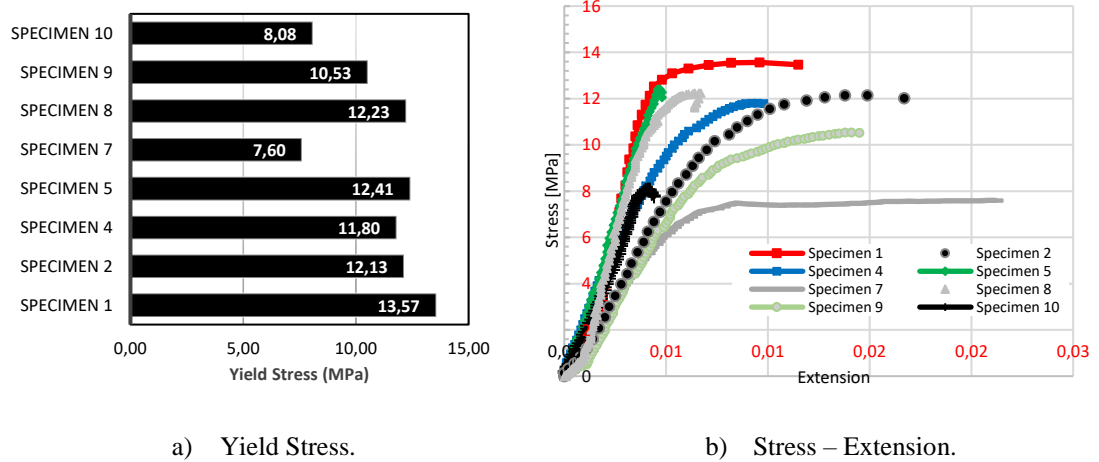


Figure II.13 – Stress – extension and yield stress for compression tests.

The average yield strength is 11.18 N/mm^2 , with a minimum and maximum values of 8.1 N/mm^2 and 13.57 N/mm^2 , respectively. The theoretical values present in EN 12369-1 (2001) are 15.4 N/mm^2 and 12.7 N/mm^2 for the load and thickness directions, respectively. The elasticity modulus is calculated using Equation (1). It is found a big difference between the theoretical value of elasticity modulus given by the standard (3800 MPa) and the mean value achieved experimentally (2311 MPa). However, for better results a larger sample size would give more accurate results.

The stress-extension curves are not perfectly straight at the first time-steps of tests (Figure II.13b). The reason of this happens is due to the contact between the specimen cross section and the mechanical press. This contact is not perfect due the irregular surface of OSB specimens.

II.3.3. Characterization of thermal properties

In the previous section the mechanical properties of steel and OSB panels were presented. However, it is also important to understand the thermal properties of the main materials used in LSF construction. Hence, the aims of this section is to provide experimental information about the thermal properties of these material, specifically the thermal conductivity.

The thermal conductivity [$\text{W}/(\text{m} \cdot ^\circ\text{C})$] is experimentally achieved for isotropic and anisotropic materials. To measure these values a Hot Disk TPS2500S system was used. The thermal diffusivity and specific heat were not considered in this experimental campaign. However, it is recommended for future works the

measurement of these two parameters, because they are important for transient modelling.

Figure II.14 illustrates the experimental system during the experiments on steel plates. The experimental specimens have 6 cm width 6 cm length and different thickness.

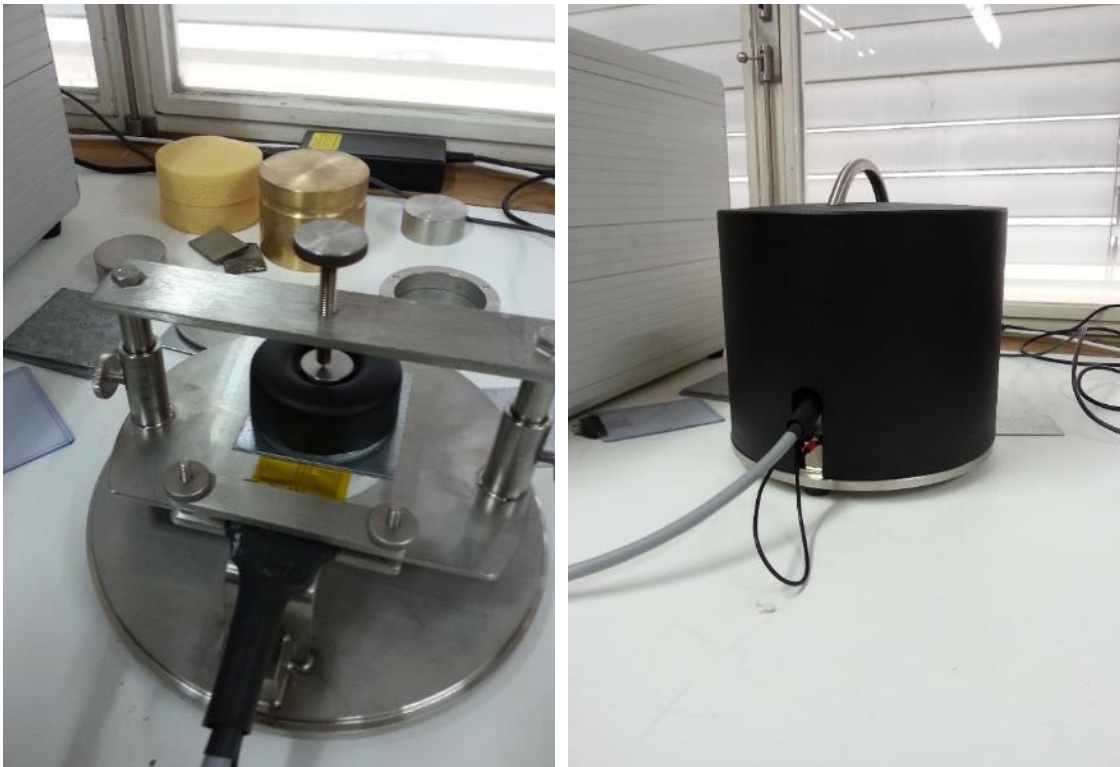


Figure II.14 – Hot disk experimental layout.

The thermal conductivity achieved experimentally and the corresponding values provided by the standard ISO 10456 (2007) – “Building materials and products – hydrothermal properties are indicated in Figure II.15.

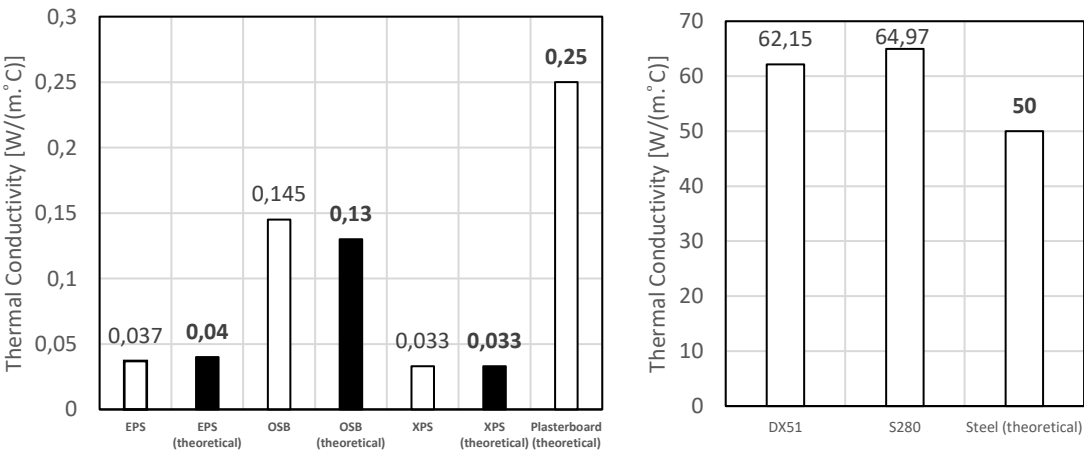


Figure II.15 – Experimental vs theoretical values of material thermal conductivity.

As observed in Figure II.15, the experimental thermal conductivity of the material is similar to the one provided by ISO 10456 (2007), except for steel. Two of the most common in LSF construction types of steel were study; DX51 and S280,. ISO 10456 (2007) provides a value of 50 W/(m.°C) for the thermal conductivity of steel. However, the experimental results showed a higher value, within a mean thermal conductivity of 62.15 W/(m.°C) and 64.97 W/(m.°C), for DX51 and S280, respectively. Other references, *e.g.* Çengel (2009), referred the value of 60.5 W/(m.°C). It is observed that the humidity and the air temperature during the experimental tests have influence in the final results. For higher humidity values the thermal diffusivity of the materials increases, and the thermal conductivities increase.

II.4. Final remarks

A brief overview of LSF modular construction systems and some structural concepts and thermal performance were presented in this chapter. The mechanical and thermal properties of the main materials used in LSF buildings were investigated. The mechanical properties of the steel (S280GD+Z) were measured for later numerical models. The mechanical properties of OSB boards were analysed according to the test method proposed by EN 789 (1996). Results were compared with the ones given by EN 12369-1 (2001) and EN 300 (2006). Results have shown that OSB boards have a very non-uniform behaviour under tensile and compression forces. A larger sample of test specimens is recommended for future development. The thermal properties of the materials were measured and compared with the ones given by ISO 10456 (2007). Experimental results showed a higher value of steel thermal conductivity between 62 W/(m.°C) and 64.97 W/(m.°C) for DX51 and S280, respectively. For later numerical and analytical models and based on measured values, the steel thermal conductivity will be considered equal to 60.5 W/(m.°C) (Çengel, 2009).

PART B

STRUCTURAL PERFORMANCE OF LSF MODULAR CONSTRUCTION

CHAPTER III

Structural performance of light steel framing panels using screw connections subjected to lateral loading

III.1. Introduction

Light steel framing wall panels are increasingly being used in modular construction, not only due the lightness and speed of production and assemblage but also due to its easy adaptability to most architectural and structural requirements. During the assemblage of LSF wall panels, screws are highly used given, its efficiency, fast application and suitability for load bearing. Screw connections fits perfectly in the industrialized production, for being simple to design, faster to install and with low cost (Lee *et al.* 2014). However, for higher load bearing cases they are not suitable due to its limited load capacity. In LSF structures screw connections are mostly subjected to shear load. The main reasons for this type of application are: (1) majority of connection consider this type of behaviour and it is suitable for LSF connections; (2) the very limited resistance to tension forces of connections using screws, as the connecting layers are clamped only by the screw threads.

In LSF construction screws are also used for the connection between non-structural elements (*e.g.* derived wood boards) to structural frames. Usually these non-structural elements are not considered during the LSF structure design as structural element. However, the contribution of these boards should not be neglected. Some previous studies had proved the contribution of these non-structural elements. Serrette and Ogunfunmi (1996) performed a monotonic test with cold-formed steel framed walls to analyse the influence of gypsum board and flat-strap X-bracing. The results shown that the gypsum board has significant contribution to the shear strength, but under seismic loading the static values should be reduced.

Tian, Wang and Lu (2004) performed monotonic tests with flat strap X-bracing. They concluded that the strength of a frame with thin flat steel straps is almost the same as that of a frame braced with *e.g.* OSB boards. They also concluded that the failure of using boards as bracing system, occurred near to the screw connections. Also, if the board thickness increases and screw spacing decreases, the racking strength increases.

Vieira and Schafer (2012) investigated the stiffness and strength features in cold-formed steel framing walls with sheathing. Experimental results revealed that the lateral stiffness with OSB sheathing is 3 times greater than using gypsum boards, and the shear capacity in OSB is almost 7 times greater than gypsum board and the displacement at peak load is 2 times greater with OSB boards. They also studied the influence of fastener spacing and concluded that neither the initial stiffness nor the strength varied significantly as a function of fastener spacing. Results show that using studs braced with OSB boards and overdriving the fasteners could increase 32% the initial stiffness and decrease 45% the strength and deformation capacity. The full test scale show that the sheathing bracing derives from local and diaphragm stiffness.

The lateral behaviour of sheeted cold-formed steel panels is dependent on the complex behaviour that occurs at each fastener location (Buonopane *et al.* 2015) and several studies were conducted showing the primordial role of connection in the overall performance of LSF panels. Over the time a few experimental and analytical studies were presented showing the primordial role of the connection in the overall performance of lightweight steel panels.

Serrette *et al.* (1997) investigate the performance of sheathed gauge steel framed shear walls subjected to a static lateral load. The tests were conducted in accordance with the basic test criteria defined in ASTM E-72-80. Results from the tests showed that failure of the walls resulted from rotation (tilting) of the fasteners about the plane of the stud flange followed by either the head of the screw pulling through the panel or the screw breaking the edge of the panel.

Branston *et al.* (2006) developed a shear wall design method that could be used in conjunction with 2005 National Building Code of Canada. The authors conducted an extensive experimental study to provide information on the response of single-storey shear walls.

Casafont *et al.* 2007 presented an experimental research on tensile screwed joints straps. The dominant failures modes were identified: (1) tilting and net section (T+

NSF) failure and (2) tilting, bearing and pull out (T+B+PO). They concluded that T+NSF joints are suitable for seismic design because the straps yield before the connection fail. The T+B+PO joints are not suitable because the connection fails before the straps can yield.

Lange and Naujoks, (2007) presented a study of the behaviour of cold-formed steel walls with sheathing under horizontal and vertical loads and developed a design procedure based on the results. Fiorino *et al.* (2007) present experimental results on screw connections between wood-or gypsum-based panels and cold-formed steel stud profiles aiming the selection of the main parameters that affects the shear behaviour of this type of connections. In addition, the authors present a procedure for prediction of the lateral load-displacement response of steel panels systems. Two year later Fiorino *et al.* (2009) presented an approach for the seismic design of sheathed CFS frame structures. The approach consists in a preliminary definition of the wall geometry and materials, and a successive evaluation of the sheathing fasteners exterior spacing through linear dynamic or nonlinear static seismic analysis.

Baran and Alica, (2012) studied the behaviour of LSF wall panels with Oriented Strand Board sheathing. The researchers conducted static lateral load tests on a total of thirteen full scale wall panels specimens. Results shown that the geometry of hold-down has a major effect on the overall behaviour of the panels. The major damages were observed in the hold-down attachment and adjacent parts. Tilting of screws connection between OSB and Steel frames and the separation between the OSB panels from the framing were observed as deformation modes. The existence of diagonal struts causes a slight increase of load capacity and initial stiffness of the panels.

Screw fasteners are easy to install, however their stiffness and strength contributions to the structural system are exceedingly difficult to quantify, this is due to complex kinematics related to, for example, screw head to plate contact and screw thread-plate interaction (Corner, 2014). It is therefore very important to characterize and to control the response of this type of connections for predicting wind and seismic drift. To provide a better understanding of the behaviour of screw connections and their impact on the frame, this chapter presents experimental and numerical studies performed on screw connections and wall panels. In the first part of this chapter, the behaviour of screw steel-to-steel and steel-to-OSB connections is presented. The analytical evaluation of the screw connection behaviour based on EN 1993-1-3 and AISI S100 design standards is discussed and experimental and numerical models of single screw steel-to-steel connection are analysed. Focusing in the connection

between steel-to-OSB board, this type of connection is analysed experimentally and with analytical formulae proposed by EN1995-1-1, (2004). In the second part of the chapter, the behaviour of cold-formed steel panels using screw connections subjected to lateral loading is investigated experimentally, numerically and with one analytical approach. The numerical model was calibrated and validated against experimental data. Then this model is used parametrically to evaluate the impact of additional bracing systems. Therefore, the contribution of the bracing system is assessed by comparing the performance of the unbraced panel with the OSB braced panel frame and panel frame braced using diagonal steel stripes.

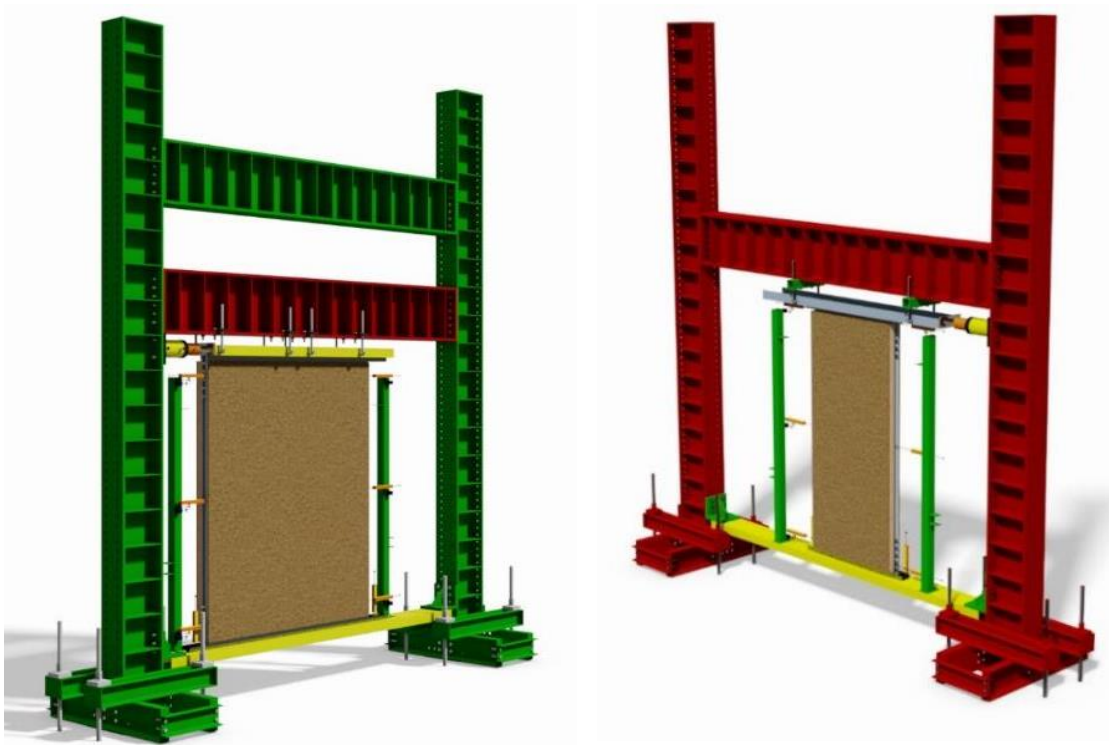


Figure III.1 – ModCons experimental layout.

III.2. Behaviour of screw connections in shear in light steel framing panels

III.2.1. Steel-to-steel screw connections

In LSF the behaviour of the connection is influenced by the thickness of the thin-walled, which is characterized by a small stiffness (Davies, 1991). Therefore, design equations are different from those used in connections with thicker elements. Also, screw connection work without nut, which provides a restraint. This implies that this type of connection depends on the mechanical interface between the thread and the connected plates. Also, in this type of connection there is significant screw rotation, especially using a single screw, because the restraint provided by nuts is not present.

However, using more than one row of screw, can prevent this rotation depending on the pitch distance (Corner, 2014). In terms of load transfer mechanism, screw connections are very like shear bolted connections. The load is transfer between the connected members (here denominated as plate) through shearing of the screw. The failure modes that may develop are:

- a) **Tilting and Tearing:** screws rotation occurs combined with plate tearing occurring pure shear deformation and damage of the plate and elongation of the screw hole (Figure III.2a);
- b) **Tilting and Bearing:** screw rotation occurs with screw plate bearing, occurring an elongation of the screw hole and yielding of the plate also occurs due to the pressure induced by the screw (Figure III.2b);
- c) **Shear of the Screw:** The shear resistance of the screw is exceeded, and the screw is split in two parts. The failure occurs in the shear plane (Figure III.2c);
- d) **Net Section:** The tension resistance of the plate is exceeded due to the reduction of the cross section. Concentration of stresses occurs around the holes which exceed the yield strength of the material. The failure crack is perpendicular to the loading (Figure III.2d).

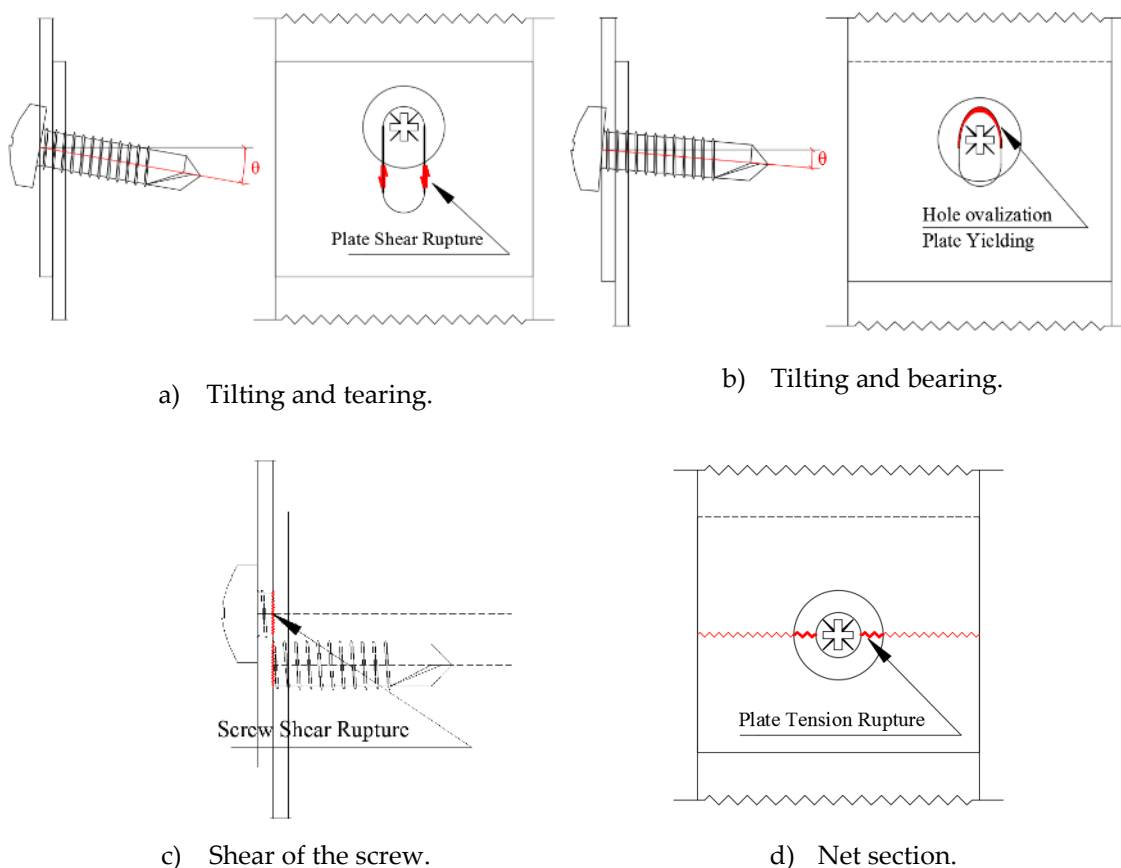


Figure III.2 – Failure modes in screw connection subject to shear.

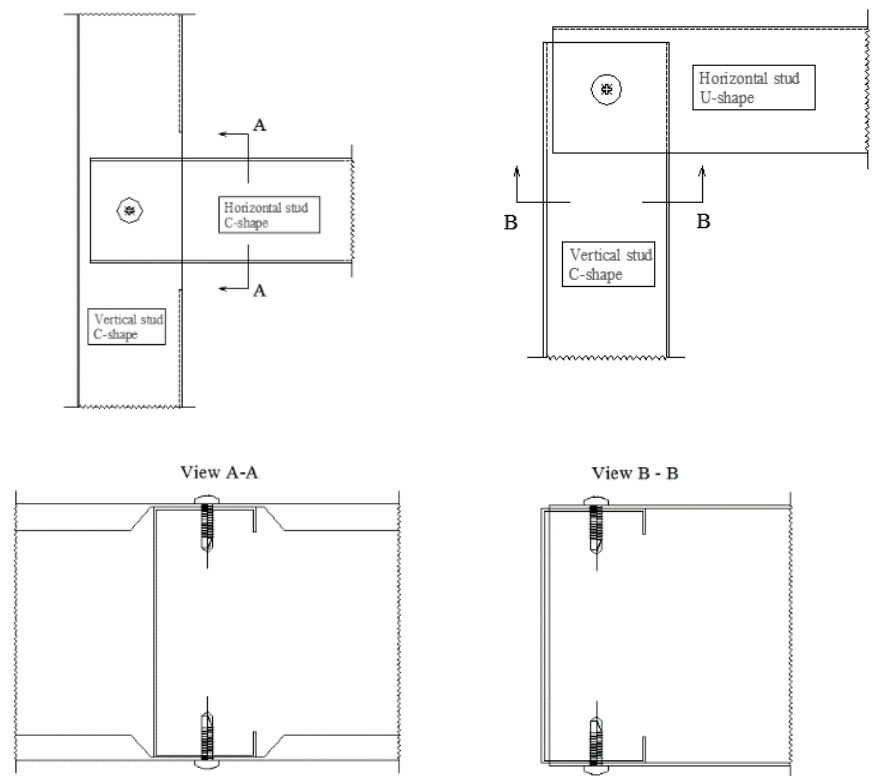
The modes of failure are clearly identified, the behaviour of the screw connections is complex due to the screw rotation. In single shear plane connections, the eccentricity of the loading leads to a rotation of the screw (tilting), as the screw rotation leads to a pull-out force on the screw. This pull-out force is then compensated by the screw head pressure against the steel plate and consequently local bending develops on the plate. The higher the flexibility of the steel plate leads to a higher rotation. Corner, (2014) developed a model to predict the fastener tilting based on the plate thickness and on the pitch distance.

In the shear connections with eccentricity, as single shear plane connections, fastener tilting, tearing and bearing are usually coupled and therefore, in the codes no distinction is made between these modes of failures being characterized/identified as a unique mode of failure. The shear failure of the screw occurs only in the case where thicker plates are used. As in light steel framing, thin elements are often used, this failure mode do not occur so often. In relation to the net section failure, it mainly occurs in the case of connections with thin and narrow plates, for example when using extra plates to connect members. In most of the connections in light steel framing, this mode of failure does not occur as connections are performed often between members directly, where the cross-section is considerably resistant in comparison to the resistance of other modes of failure.

In the construction of panels, the screw connection between the members, vertical and horizontal studs, is often performed inserting the vertical studs (C or Ω shape type) in the horizontal studs also known as noddings (U shape type or C shape type with a notch), as illustrated in Figure III.3. This configuration is a shear connection type and failure may occur from one of the modes previously described. In the case of braced panels, this type of connection is also used to connect the diagonal bracings or the OSB boards to the panel members (vertical and horizontal studs). Subsequently, the bearing capacity and the stiffness of the panels to lateral loading depend on the behaviour of this type of connections. Therefore, the characterization of the connection behaviour is important to evaluate the panel performance. In the next sections, the behaviour of shear screw connections in LSF is discussed based on analytical, experimental and numerical investigations.

CHAPTER III

Structural performance of light steel framing panels using screw connections subjected to lateral loading



a) Connection within the panel.

b) Connection at the edge of the panel.

Figure III.3 – Examples of stud-stud screw connection in LSF panels.

III.2.1.1. Assessment of the response of single shear screw connections

The design of a screw connection is based on the evaluation of the individual failure previously shown. In practical terms, the principles of the component method (Simões da Silva, 2008) are applicable. The connection may be represented by the mechanical spring model illustrated in Figure III.4.

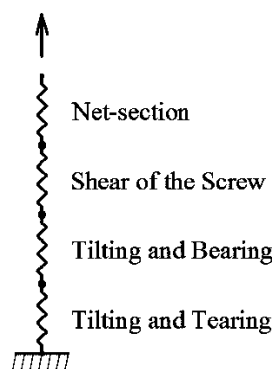


Figure III.4 – Spring mechanical model reproducing a screw connection.

Each mode of failure is identified as a component and reproduced by a translational spring. The connection response results then from the assembly of four springs in series. In practice, the deformation of such connection is completely neglected and therefore the model is only used to evaluate the load capacity. The below expressions present the design rules for screw connection according with Eurocodes (EN 1993-1-3, 2006). For tilting and tearing/bearing failure mode,

$$F_{b,Rd} = \frac{\alpha f_u d t_1}{\gamma_{M2}} \quad (2)$$

$$\left\{ \begin{array}{l} t_1 = t_2 \rightarrow \alpha = 3.2 \sqrt{t_1 / d} \leq 2.1 \\ t_2 \geq 2.5 t_1 \text{ and } t_1 < 1.0 \text{ mm} \rightarrow \alpha = 3.2 \sqrt{t_1 / d} \leq 2.1 \\ t_2 \geq 2.5 t_1 \text{ and } t_1 \geq 1.0 \text{ mm} \rightarrow \alpha = 2.1 \\ t_1 \leq t_2 \leq 2.5 t_1 \rightarrow \alpha \text{ obtained by linear interpolation} \end{array} \right\} \quad (3)$$

where t_1 is the plate thickness in contact with the screw head [m], t_2 the plate thickness without contact with the screw head [m], d is the screw nominal diameter, f_u the ultimate tensile strength of the steel sheet [N/mm²], γ_{M2} is the partial safety factor (1.25). For the failure mode of shear of the screw,

$$F_{v,Rd} = \frac{F_{v,Rk}}{\gamma_{M2}} \quad (4)$$

where $F_{v,Rk}$ is the characteristic shear resistance of the screw determined by testing. In the case deformation capacity is required:

$$F_{v,Rd} = 1.2 F_{b,Rd} \quad (5)$$

Finally, for the net section,

$$F_{n,Rd} = \frac{A_{net} f_u}{\gamma_{M2}} \quad (6)$$

where A_{net} is the net cross-section area of the plate (accounting for the screw hole).

The range validity is given by:

$$\begin{aligned} 0.45 &\leq t_1, t_2 \leq 4 \text{ mm} \\ e_1 &\geq 1.5d; e_2 \geq 1.5d; p_1 \geq 3d; p_2 \geq 3d \\ 2.6 \text{ mm} &\leq d \leq 6.4 \text{ mm} \\ f_u &\leq 500 \text{ N/mm}^2 \end{aligned} \quad (7)$$

CHAPTER III

Structural performance of light steel framing panels using screw connections subjected to lateral loading

where e_1 is the edge distance in the direction of the loading; e_2 is the edge distance in the perpendicular direction to the loading, p_1 is the pitch distance in the direction of the loading, p_2 is the pitch distance in the perpendicular direction to the loading. The thinnest sheet is next to the head of the screw (t_1). The other cases are not contemplated by the code.

The design rules for screw connection according to North American Standard (AISI S100, 2007) are given below. For the failure mode of tilting and tearing/bearing,

$$\begin{aligned}
 \text{AISI S100: } F_{b,Rd} &= \frac{P_{ns}}{\Omega} \\
 \text{AISI S100 LRFD: } F_{b,Rd} &= \phi P_{ns} \\
 \text{AISI S100 LSD: } F_{b,Rd} &= \phi P_{ns} \\
 &\left\{ \begin{aligned} t_2 / t_1 \rightarrow P_{ns} &= \text{Min} \left(4.2 \sqrt{t_2^3 d F_{u2}}; 2.7 t_1 d F_{u1}; 2.7 t_2 d F_{u2} \right) \\ t_2 / t_1 \geq 2.5 \rightarrow P_{ns} &= \text{Min} \left(2.7 t_1 d F_{u1}; 2.7 t_2 d F_{u2} \right) \\ 1.0 \leq t_2 / t_1 \leq 2.5 \rightarrow P_{ns} &\text{ obtained by linear interpolation} \end{aligned} \right\} \quad (8)
 \end{aligned}$$

Limitation due to end distance (e_1)

$$P_{ns} \leq t_1 e_{1,1} F_{u1} \text{ or/and } t_2 e_{1,2} F_{u2}$$

d is the screw nominal diameter, F_{u1} is the ultimate tensile strength of the steel sheet in contact with screw head, F_{u2} is the ultimate tensile strength of the steel sheet not in contact with screw head, $e_{1,1}$ is the edge distance in the direction of the loading of the sheet not in contact with screw head and $e_{1,2}$ is the edge distance in the direction of the loading of the plat in contact with the screw head. Ω is the safety factor for ASD – Allowable Strength Design (recommended value is 3.00) and Φ is the resistance factor for LRFD – Load and Resistance Factor Design and LSD – Limit State Design (recommended value is 0.50 and 0.40, respectively). For the failure of shear of the screw,

$$\begin{aligned}
 \text{AISI S100 ASD: } F_{v,Rd} &= \frac{P_{ss}}{\Omega} \\
 \text{AISI S100 LRFD: } F_{v,Rd} &= \Phi P_{ss} \\
 \text{AISI S100 LSD: } F_{v,Rd} &= \Phi P_{ss}
 \end{aligned} \quad (9)$$

where P_{ss} is the shear resistance of the screw determined by testing. For the net section,

$$\begin{aligned}
\text{AISI S100 ASD: } F_{n,Rd} &= \frac{A_n F_u}{\Omega} \\
\text{AISI S100 LRFD: } F_{n,Rd} &= \Phi A_n F_u \\
\text{AISI S100 LSD: } F_{n,Rd} &= \Phi A_n F
\end{aligned} \tag{10}$$

where A_n is the net cross-section area of the sheet (accounting for the screw hole), Ω is the safety factor for ASD (recommended value is 2.0); Φ is the resistance factor for LRFD and LSD (recommended value is 0.75). The range of validity is given by,

$$\begin{aligned}
e_1 &\geq 1.5d; e_2 \geq 1.5d; p_1 \geq 3d; p_2 \geq 3d \\
\text{AISI S100: } 2.0 \text{ mm} &\leq d \leq 6.4 \text{ mm}
\end{aligned} \tag{11}$$

The main difference between the design rules is the evaluation of the bearing and tearing failure. The EN1993-1-3, (2006) methodology is limit when the plate near to the head of the screw is thinnest, where the AISI S100, (2007) covered all the possibilities. Figure III.5 and Figure III.6 shows the comparison between the two methodologies to evaluate the two modes of failure, considering a single screw, one grade, the same screw diameter and no influence of edges and variation of plate thick. It can be observed from Figure III.5 a) that with EN1993-1-3, (2006), only for higher thickness of steel plate, bearing becomes the governing mode. For the AISI S100, (2007) method, failure depends on the thickness of both sheets. It can be seen in Figure III.5 b) that when the thickness of the latter is increased the bearing of the sheet in contact with screw head becomes governing. Figure III.6 display the direct comparison between both methods where can be seen that for EN1993-1-3, (2006) the characteristic resistance is smaller than those obtained using AISI S100, (2007).

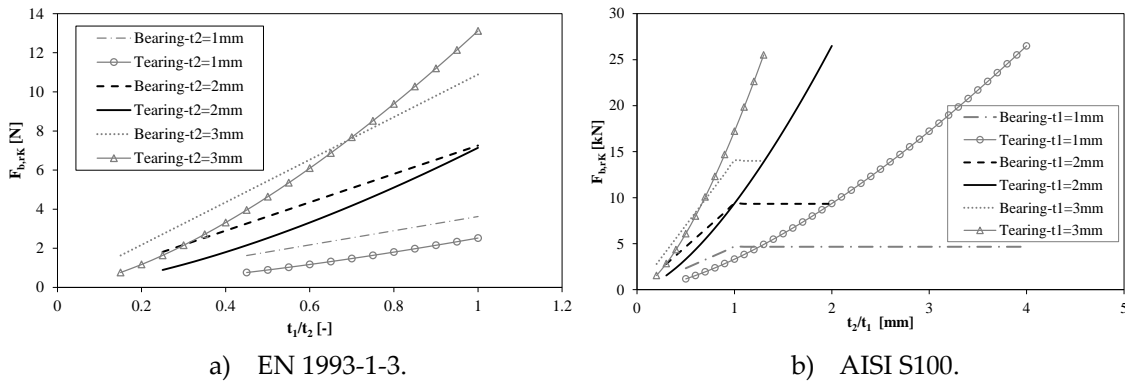
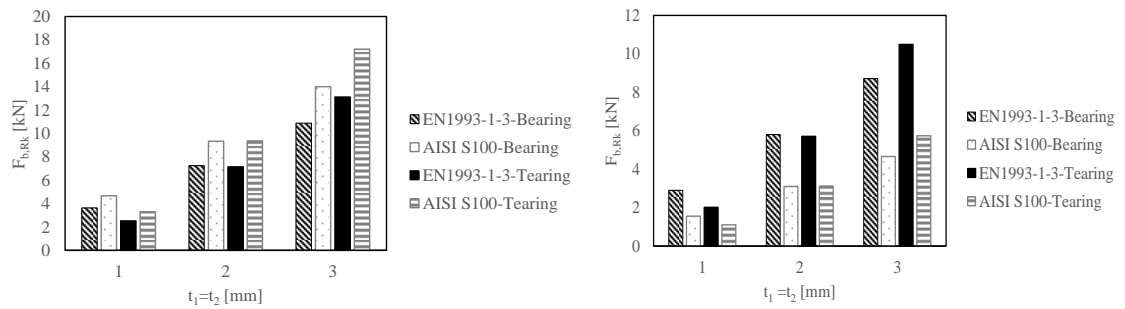


Figure III.5 – Evaluation of tearing and bearing failure of screw connection in shear according to the EN 1993-1-3, (2006) and the AISI S100, (2007) ($f_u = 360 \text{ N/mm}^2$; $d = 4.8$).

CHAPTER III

Structural performance of light steel framing panels using screw connections subjected to lateral loading



a) Characteristic values.

b) Design values.

Figure III.6 – Comparison EN 1993-1-3, (2006) and AISI S100, (2007) analytical expressions for determination of tearing and bearing resistance.

The connection resistance is obtained according to:

$$F_b = \text{Min}(F_{b,Rd}; F_{v,Rd}; F_{n,Rd}) \quad (12)$$

LaBoube and Sokol, (2002) concluded that for multiple screw connection, the screw pattern did not significantly influence the strength of the connection. A design equation that reflects the influence of a “group effect” of screws was developed to calculate the reduction factor.

$$R = (0.535 + 0.467 / \sqrt{n}) \leq 1.0 \quad (13)$$

where n is the number of screws used in the connection. The connection resistance is then calculated by the following expression:

$$F_{b,total} = F_b n R \quad (14)$$

In relation to the deformation of the screw connection subjected to shear load, as referred above, it is usually disregarded and consequently, no model is found in the literature. The connection illustrated previously in Figure III.3 (with one screw in each side), has eccentricities between the loading and the connection. If this connection works as a perfect hinge, the axis of rotations is the line defined by the two screws. Using as example the connection in Figure III.3a, the free body rotation (θ) ends when the profiles come into contact, as represented by the deformed connection in Figure III.7. The equilibrium is then established: the force applied ($F_{external}$) with eccentricity (e_{ext}) originates a secondary bending moment, which is balanced by the contact force ($F_{contact}$) developed between the profiles. This contact force has an eccentricity (e_{cont}) to the rotation point. The friction forces that may

develop between the profile flanges were completely neglected in this model, as this depend on the tightening forces which are very limited in this type of connection.

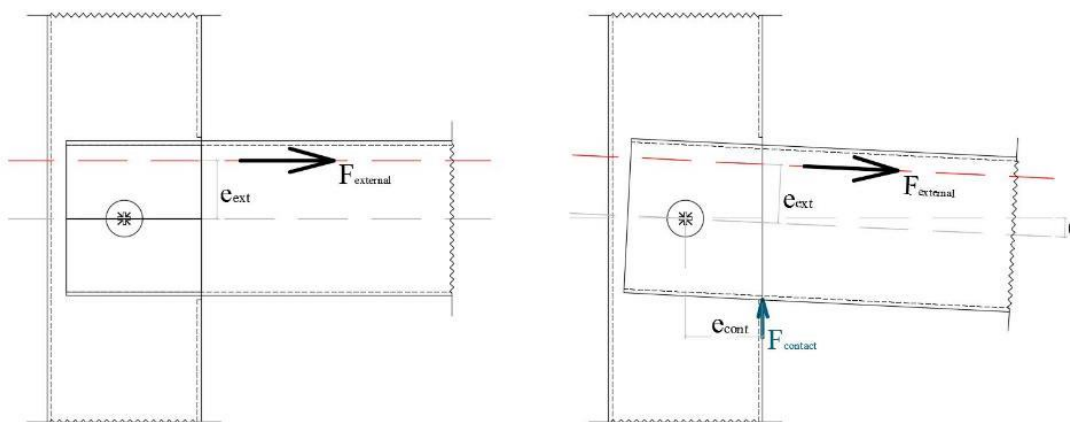


Figure III.7 – System of forces due to the eccentricity of loading in the screw connection between panel studs (horizontal and vertical).

III.2.1.2. Experimental test on single shear screw connection

III.2.1.2.1. Test programme and layout

To characterize a single shear screw connection behaviour with the configuration illustrated in Figure III.3a, experimental tests were performed. For these experimental tests two cold-formed profiles were connected using self-drilling screws. As represented in Figure III.3a a channel profile was inserted into a U profile, and the connection was achieved by screwing each flange of the U-profile to the flanges of the channel profile. The screws that were used are Fabory and SFSintec. Six experimental tests were performed, three for each type of screw (Table III.1). All the tests were static monotonic.

Table III.1 – Screw connection test specimens.

Nº	Test ID	Profiles	Screws	Test Type	
1	FAB T1	C-100x40x10x1	Fabory®	Static Monotonic	
2	FAB T2		U-100x40x1		Φ4,8
3	FAB T3				
4	SFS T1	both S320GD+Z			
5	SFS T2				
6	SFS T3				

The geometry of the self-drilling screws used in the tests is illustrated in Figure III.8. The main difference between them is in the head of the screw. The SFSintec screw

CHAPTER III

Structural performance of light steel framing panels using screw connections subjected to lateral loading

has a square flat head with lower head thickness allowing better fixation of non-structural panels to the frame. However, the application of this screws requires special tools and the main issue in the terms of performance, as the head-plate contact surface is smaller given the reduce dimension of the head. On the other hand, the Fabory screw as a standard configuration of a drilling screw with a pan head.



SFSintec® SL3-F Fabory® ST4.8

Figure III.8 – Self-drilling screws used in the screw connection tests.

Table III.2 shows the geometrical characteristics of both screws. The technical information of the screws was obtained from the technical documents (SFS Intec, 2002), (Fabory, 2013).

Table III.2 – Geometrical properties of the self—drilling screws used in the screw connections tests.

Screw Designation	Screw Type	Head Type	Head Dimension	Shaft diameter	Shaft length
ST4.8	Self-drilling	Circular pan head	d=9,5mm	4,8mm	13mm
SL3-F-4.2	Self-drilling	Square flat head	b=6,0mm	4,2mm	15mm

The nominal dimension of the tests specimens used in the experimental campaign is presented in Figure III.9a. The experimental tests were performed in a testing press machine and the specimens were fixed with additional steel pieces (Figure III.9b). The horizontal profile web was bolted to the auxiliary steel plates using eight bolts. These bolts are loaded in tension during the tests. The web of the vertical profile was connected to an auxiliary steel plate through a double overlap shear connection using four bolts. These steel plates were connected to the testing machine. The load applied with this layout has a small eccentricity previously explained. Also, it is usual the presence of an eccentricity on this type of connections due the screwing process that cannot guarantee that it is executed at the level of the profile gravity centre. The loading of the test specimens was monotonic and consisted of an

imposed controlled displacement with a test speed of 0.02 mm/s applied up to failure. The displacement was measured by LVDT's fixed at both sides of the vertical profile web.

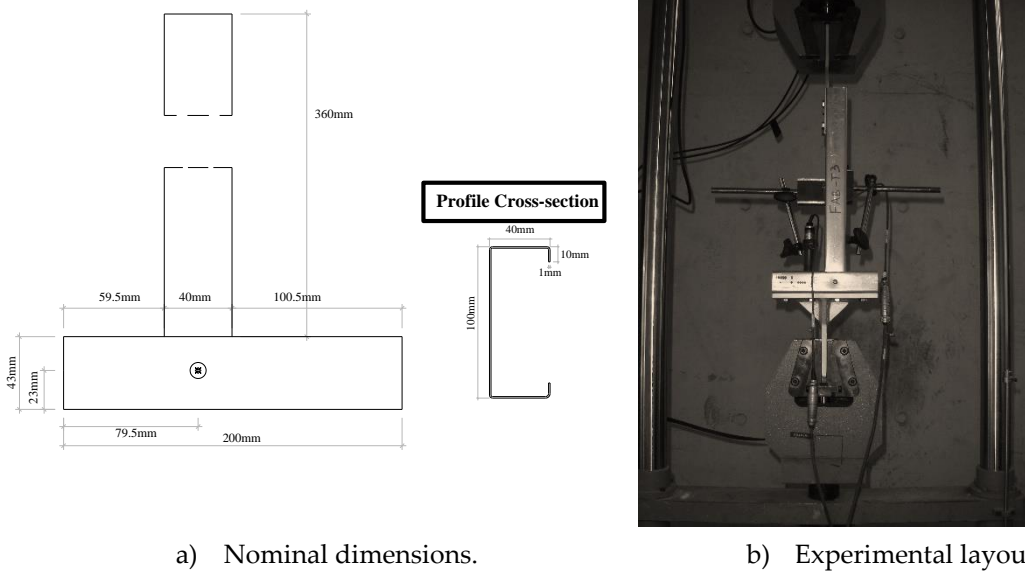


Figure III.9 – Screw connection test specimen's dimensions and experimental layout.

III.2.1.2.2. Tests results

The force-deformation curves obtained from the tests are represent in Figure III.10. Due to a problem of the fixation system, test results from specimen number 4 were not considered. The difference between the designation of LVDT1 and LVDT2 is related to the position of the LVDT. LVDT1 and LVDT2 were positioned between the flanges of the vertical profile in opposite sides of the profile web. It can be seen a very similar response between both plots. Test specimen SFS T2 showed some deviations, especially in what concerns to the stiffness. This may happen due to installation imperfections. The response is characterized by a force-deformation relation with nonlinearity up to the maximum force, which is governed by the local deformation of the plate in front of the screw (bearing). It is observed that with the increase of the deformation, the screw rotates (tilting) and the screw head penetrates the steel plate. This phenomenon can be better observed with the SL3-F screws due the smaller screw head (Figure III.11a). At the maximum load, it is observed an instable behaviour due to the screws threads. When the screw rotates the force transferred is no longer pure shear, tension is developed. The screw is then pull through steel-plate near the screw head. The instability behaviour observed in the curves represents the thread crossing the plates.

CHAPTER III

Structural performance of light steel framing panels using screw connections subjected to lateral loading

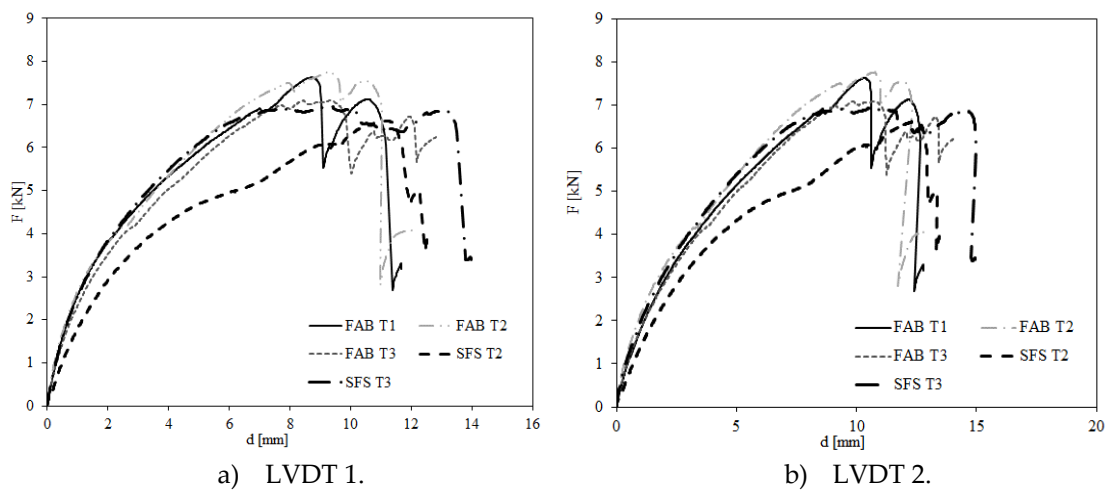


Figure III.10 – Force-deformation of the screw connection.

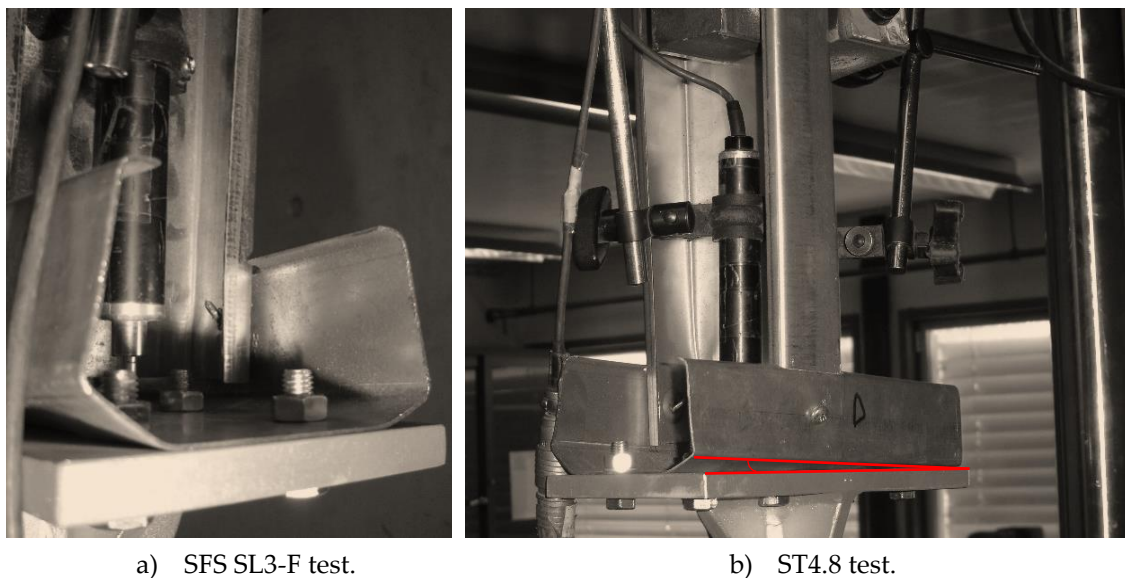


Figure III.11 – Screw rotation observed in the screw connection test.

Test results on steel-to-steel screw connections are presented in Table III.3. F_{max} represent the maximum force achieved; S_{ini} the initial stiffness determined based on the deformation at $2/3$ of F_{max} ; d_{Fmax} the deformation at maximum force and d_u the ultimate deformation (deformation at failure of the connection). It was found a good agreement in terms of the average maximum resistance and the screw diameter. The ratio (ST4.8/SF3-L) between diameter is 1.14 while the ratio between the average maximum resistance is 1.12. It is observed that the connection with FAB screw are slightly stiffer than with SFS screws which have higher deformation capacity, indicating a direct relation between this parameter and the screw diameter.

Due the eccentricity of the loading, an additional bending moment develops at the level of the connection which must be transferred to the horizontal profile through the equilibrium, as illustrated in Figure III.7. In this case, the rotation occurs on the

horizontal profile flange until contact is achieved. The rotation of the horizontal profile flange was observed during experimental tests and can be noticed in Figure III.11b. This rotation may be happened due to the plastic deformations that developed in the horizontal profile web around the bolts connecting the horizontal profile to the support plate.

Table III.3 – Summary of the results on steel-to-steel screw connections.

Test ID	F_{max} [kN]	S_{ini} [kN/m]	d_{Fmax} [mm]	d_u [mm]
FAB T1	7.63	1407.53	8.69	11.68
FAB T2	7.84	1133.77	10.64	14.03
FAB T3	7.12	1093.70	9.55	14.44
Average FAB	7.53	1211.67	9.63	13.38
SFS T2	6.73	890.21	12.29	13.48
SFS T3	6.99	1273.22	10.39	14.91
Average SFS	6.86	1081.72	11.34	14.20

As already mentioned the testing machine applies a load to the vertical profile with an eccentricity on the connection. Consequently, bending moments are developed in this profile. To quantify the magnitude of this bending moments, the eccentricities considered for the calculation of the additional bending moment on the connection ($M_{add,con}$) and on the profile ($M_{add,prof}$) were 19.5 mm and 11.54 mm, respectively. The first was obtained from the nominal dimensions of the test specimens and the later results from the calculation of the effective properties of the connections according to EN1993-1-3, 2006 (Figure III.12a). Due to the similar response of specimens, only the results of FAB T2 were used in this calculation. The additional bending moment at the level of the connection and on the profile represents approximately 40% and 25% of the resistance bending capacity, respectively. Figure III.12b presents the ratio between the screw connection resistance estimated according to the design codes EN1993-1-3, (2006) and AISI S100, (2007), and the tests results. In the computation of the ratio, the characteristic values of the resistance were used. According to the model described in previous section, and based on the configuration of the connection, tearing/tilting is the governing failure. The reduction factor R for the group effect was not considered because the screws are in different sides of the profile. It was assumed two single screw connections. To compare these values with the experimental results, the real force on the screw was achieved considering the referred rotation at the level of the connection in order to achieve the contact. The rotation was calculated based on the nominal clearance between the profiles flanges

which was 3 mm. The resistance of the screw connection ($F'_{b,test}$) obtained on the test is obtained using the following expression:

$$F'_{b,test} = F_{b,test} (1 - \text{Sen}\theta) \quad (15)$$

It is observed that the AISI S100 results are less conservative than the EN 1993-1-3 model. However, the american standard has more conservative safety factors used for the calculation of the design values.

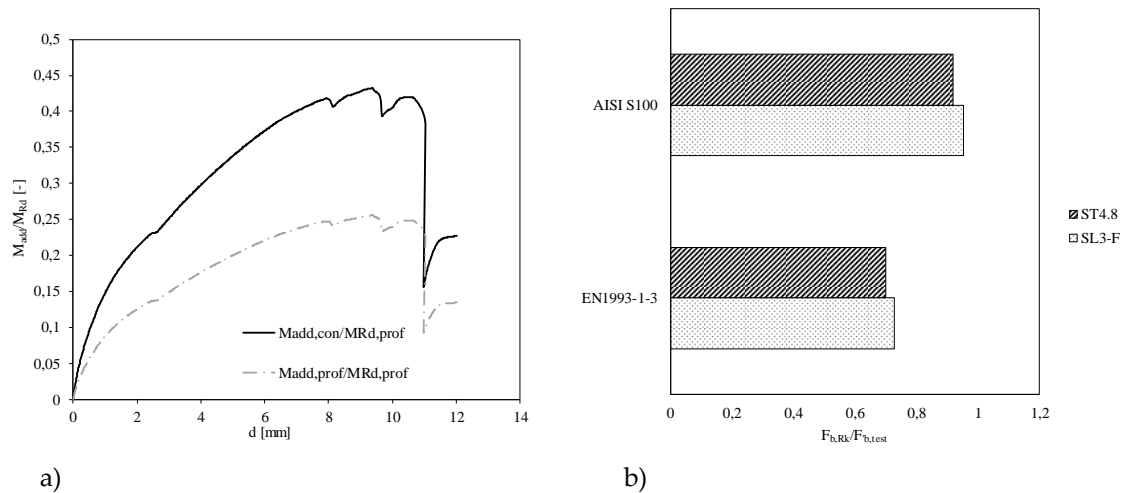


Figure III.12 – a) Additional bending moment generated by the eccentricity of the loading on the screw connections; b) ratio between screw connection resistance and test results.

III.2.1.3. Numerical modelling of single shear screw connection

III.2.1.3.1. Development of FE model for simulation of screw connection in shear

The screw connection tested and described in section III.2.1.2 was numerically study using the finite element software ABAQUS. The model was developed using three-dimensional solid elements for modelling both steel profiles and screws (Figure III.13). Taking in consideration previous research works conducted by Henriques (2013) the continuum stress/displacement 3D solid element C3D8R was chosen for better computation efficiency (time and accuracy). The analysis considered the geometrical and material nonlinearities. The initial imperfections were not considered, and the simulation was performed using the nominal dimensions. The screws were modelled as perfect cylinders with the diameter of the screws (nominal diameter). To avoid rigid body mechanism, the extremities of the cylinders screws head (Figure III.13b) were modelled to avoid the loss of the screw. These simplifications imply a difference between the real screw-profile interaction and

numerical model. This simplification may affect the response of the connection after the first load peak when the screw thread passes through the vertical profile flange. The interaction between screw-plate consisted in the use of the “hard” contact model with frictionless behaviour to get better numerical convergence. The contact between the two parts occurs with transmission of pressure, without penetration and without development friction forces. The same interaction model was used for the interaction between profiles. The boundary conditions of the models try to simulate the real test conditions. Supports were applied on the horizontal profile fully restraining the nodes that were in contact with the bolt nut of the fixation system. The load was applied on the top of the vertical profile until the failure of the connection. The load was also applied only on the web of the profile to obtain the same eccentricity in the experimental.

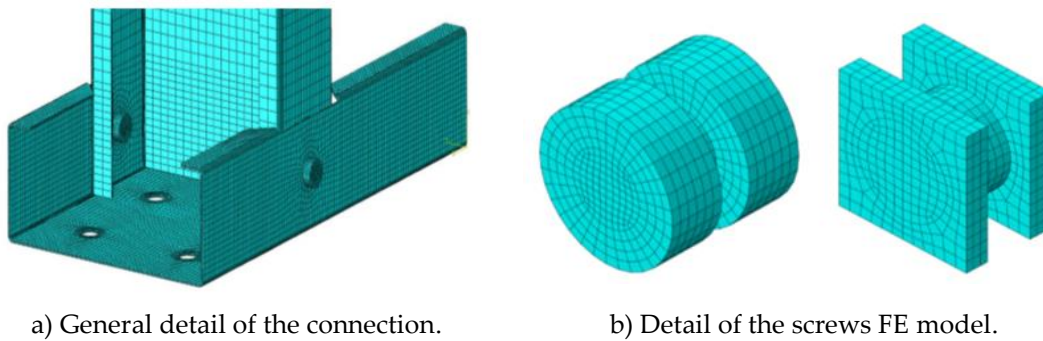


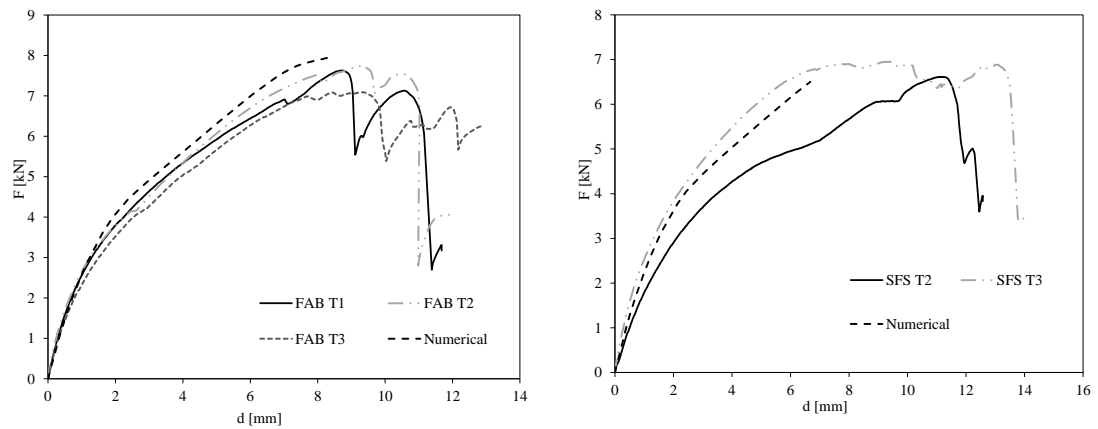
Figure III.13 – Finite element model of the screw connection tested.

III.2.1.3.2. Model validation and calibration

The validation of the numerical models was conducted by comparing the experimental force-deformation curves with those achieved numerically. Figure III.14 presents the force-deformation curves for both screws. The deformation on the numerical models was obtained using nodal displacements between nodes at the same location of the LVDTs. Due to the simplifications already mentioned, these numerical models attempt to reproduce the experimental tests only up to the maximum force-deformation. It can be observed a very good agreement between numerical and experimental results. The little difference between results is mainly due to the imperfections on the tests specimens, that were not considered in the numerical models. Figure III.15 presents the comparison between the deformation pattern obtained experimentally and numerically. It can be observed a very good reproduction by the numerical model, except for the screw rotation. The accuracy of the model is also demonstrated in Figure III.16 through the comparison between yield lines developed in the horizontal profile. These plastic deformations had a significant impact in the measured deformation.

CHAPTER III

Structural performance of light steel framing panels using screw connections subjected to lateral loading



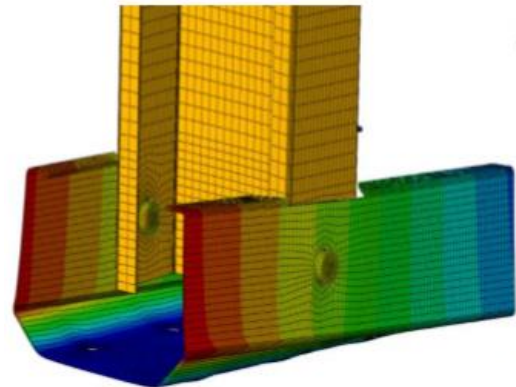
a) Connections using ST4.8 screws.

b) Connections using SL3-F-4.2 screws.

Figure III.14 – Comparison between the force-deformation curves of the numerical model and screw connection tests.



a) Experimental model.

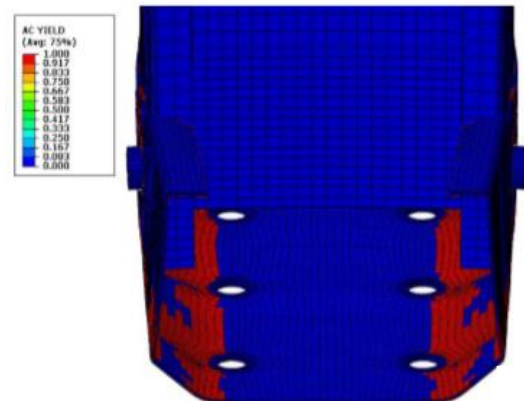


b) Numerical model.

Figure III.15 – Comparison between the deformation pattern of experimental and numerical model.



a) Experimental model.



b) Numerical model.

Figure III.16 – Comparison of the yield lines in horizontal profile both in the screw connection test and in the numerical model.

III.2.1.3.3. Numerical results

With the experimental tests it is not possible to measure the pure connection deformation. The force-deformation curves presented in Figure III.17 represent the total deformation of the test configuration including the plastic deformations on the horizontal profile. However, after the numerical validation the model can be used to predict the screw connection deformation. It was assumed that the connection deformation corresponds to the local deformation within the vicinity of the connection. Figure III.17a presents the position of the nodes. The node N1 is placed at the axis of the connection and N2 is at approximately $3d$. This value was considered because is the limited of the area affected by stresses transferred from the screw to the plates. This limit is also given by EN1993-1-3, (2006) as the minimum distance between the screws, the screw and the edge, and between the screw and the end plate.

The plot presented in Figure III.17b shows the force-deformation curves for the connection and global test connection. It can be observed that the behaviour of the connection is a lot stiffer. As illustrated in Figure III.18, deformation becomes relevant only after the profile flange attained yielding due to the pressure between screw and plate. Figure III.18b shows the stresses on the screw and it can be observed that higher values are achieved on the screw shaft. This happens due to the screw flange bearing. It is also observed a non-symmetric pattern on the screw heads indicating the rotation of the screw already observed experimentally. However, due to the simplifications considered, the numerical model cannot reproduce the post-peak behaviour and the considerable rotation of the screws.

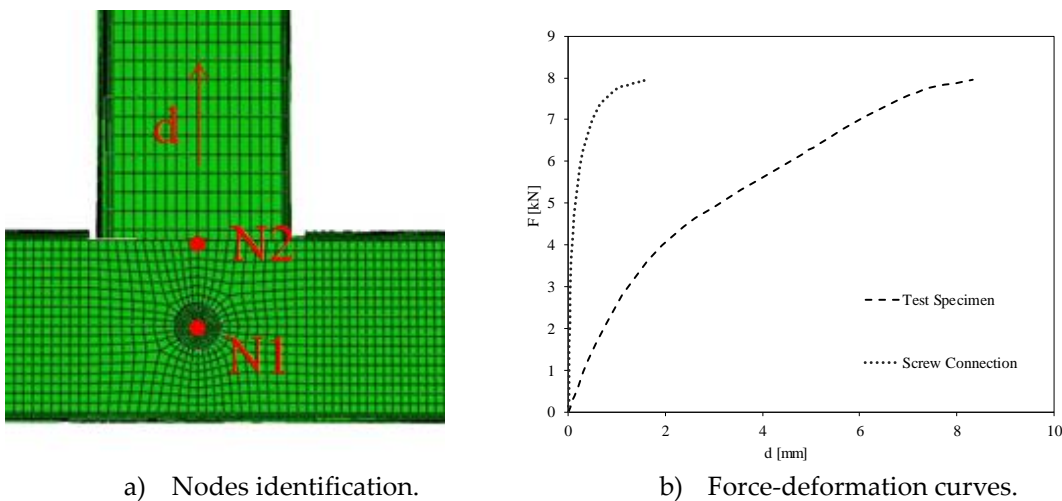


Figure III.17 – Comparison of force-deformation curve between connection and global test configuration.

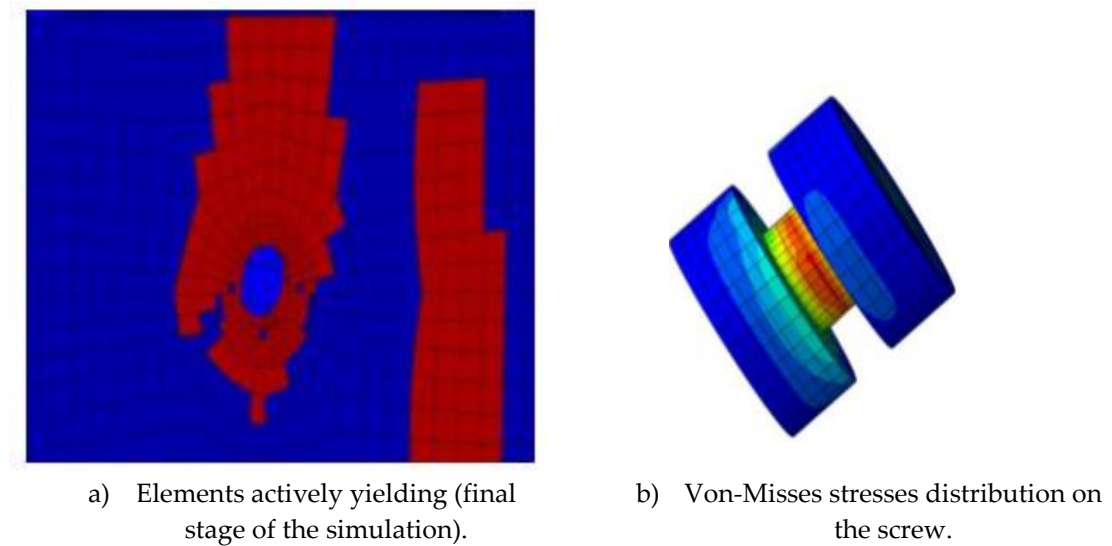


Figure III.18 – Detail results of the screw connection simulation.

III.2.2. OSB-to-steel screw connection

The contribution of the OSB boards to the lateral stiffness of the steel frame is dependent on the connection between the OSB boards and the frame. The behaviour of this connection is neglected in EN 1993-1-3, (2006), where the contribution of OSB boards or any other non-structural material is not covered by the standard. The resistance of these connections has then to be assessed using EN1995-1-1, (2004). The North American standard AISI S400-15, (2015) considers the contribution of these non-steel elements to the lateral behaviour of LSF structures. The approaches available in these standards, for the evaluation of the OSB-Steel connections, are hereafter presented and discussed; however, emphasis is given to the European standard. Nevertheless, in general there is still a lack of information on such type of connections. Thus, experimental tests on OSB-Steel connections were conducted and these tests are analysed.

III.2.2.1. Assessment of the resistance of a OSB-Steel screw connection

The load transfer mechanism in a single shear screw connection between OSB board and a steel profile is similar to the mechanism discussed in section III.2.1. The load is transferred from the OSB board to the steel plate through the screw shank in shear as illustrated in Figure III.19. As already mentioned, the Eurocode 3 does not address this type of connection or any other issue related to a non-steel material. However, the Eurocode 5 addressed these connections. The connection resistance has to take into account the different modes of failure: on the OSB board; on the screw and on the steel-plate described in section III.2.1.1. Therefore, the resistance associated to the OSB component is presented.

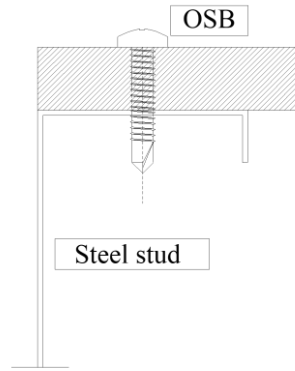


Figure III.19 – OSB to Steel screw connection.

The referred code makes a first different between thin and thick plates. Thin plates are those which the thickness is smaller or equal to $0.5d$, and thick plates are those which the thickness is greater than d . Where d represent diameter of the screw. For intermediate values, a linear interpolation should be used for calculation of the characteristic capacity of the connection. In this presented investigation, only thin plates are considered. Then, as only single shear connections are used, the characteristic load-carrying capacity ($F_{v,Rk}$) for the screwed connection is given by:

$$F_{v,Rk,wood} = \min \left\{ \begin{array}{l} 0.4 f_{h,k} t_1 d \\ 1,15 \sqrt{2 M_{y,Rk} f_{h,k} d} + \frac{F_{ax,Rk}}{4} \end{array} \right\} \quad (16)$$

where: $f_{h,k}$ is the characteristic embedment strength in the OSB board, t_1 is the thickness of the OSB board; d is the diameter of the screw (nominal diameter), $M_{y,Rk}$ is the characteristic screw yield moment and finally $F_{ax,Rk}$ is the characteristic withdrawal capacity of the screw. For the determination of the characteristic embedment strength ($f_{h,k}$) the following expression applies:

$$f_{h,k} = 0.65 d^{-0.7} t_1^{0.1} \quad (17)$$

The first term in Eq. 16 is related to the OSB board and represents the bearing resistance for the OSB screw contact. The second term incorporates also the screw response. The bending capacity of the screw is given by the following expression:

$$M_{y,Rk} = 0.3 f_u d^{2.6} \quad (18)$$

A minimum tensile strength of 600 N/mm^2 is required by EN1995-1-1, (2004). The pull-out component is determined by the minimum of the resistance to pull-out at the head at the point side of the screw:

$$F_{ax,Rk} = \text{Min} \left\{ \begin{matrix} f_{ax,k} dt_{pen} \\ f_{head,k} d_h^2 \end{matrix} \right\} \quad (19)$$

where $f_{ax,k}$ is the characteristic point-side withdrawal strength, $f_{head,k}$ is the characteristic head-side pull-out strength; t_{pen} is the point-side penetration length or the length of the threaded part in the point-side member. As in configuration illustrated in Figure III.19, on the point-side of the screw connection has a steel plate, this resistance can be neglected. Consequently, the shear resistance of the connection can be achieved by:

$$F_{v,Rk} = \min(F_{v,Rk,wood}; F_{v,Rk,screw}; F_{b,Rk}; F_{n,Rk}) \quad (20)$$

where $F_{v,Rk,wood}$ represents the wood-screw bearing, $F_{v,Rk,screw}$ the shear failure of the screw, $F_{b,Rk}$ the screw-steel bearing and $F_{n,Rk}$ the steel net-section.

The AISI S400-15, (2015) also considers the resistance of this type of connections for the design of cold-formed steel structures subjected to lateral loads. However, the approach is not based on the determination of the resistance of the screw connection, but on the overall configuration of the panel. Nominal strengths for diaphragms made of timber are given based on the panel configuration and imposing maximum screw spacing and size of the screws. The prequalified connection between the timber panel and the steel frame were not addressed; however, further information may be found in AISI S400-15, (2015). Finally, it should be observed that in both approaches, the minimum edge distance should be respected. In the next section, the estimation of the connection resistance according to the European code is compared with the results of experimental data.

III.2.2.2. Experimental behaviour on single shear screw connection

III.2.2.2.1. Test program and layout

The tests performed, consisted on single shear screw connection between OSB board and steel plates. The connection between both materials was performed using a self-drilling screw type ST 4.8, as the one used in the steel-to-steel connection described before. The main objective of these tests was the characterization of the connection behaviour, the attainment of the force-displacement curve. A total of five tests were performed. Within the five tests, no variations were performed on the geometrical and material properties. The test specimen's geometry is illustrated in Figure III.20 and the main characteristics are summarized in Table III.4 . The test specimens were loaded up to the failure.

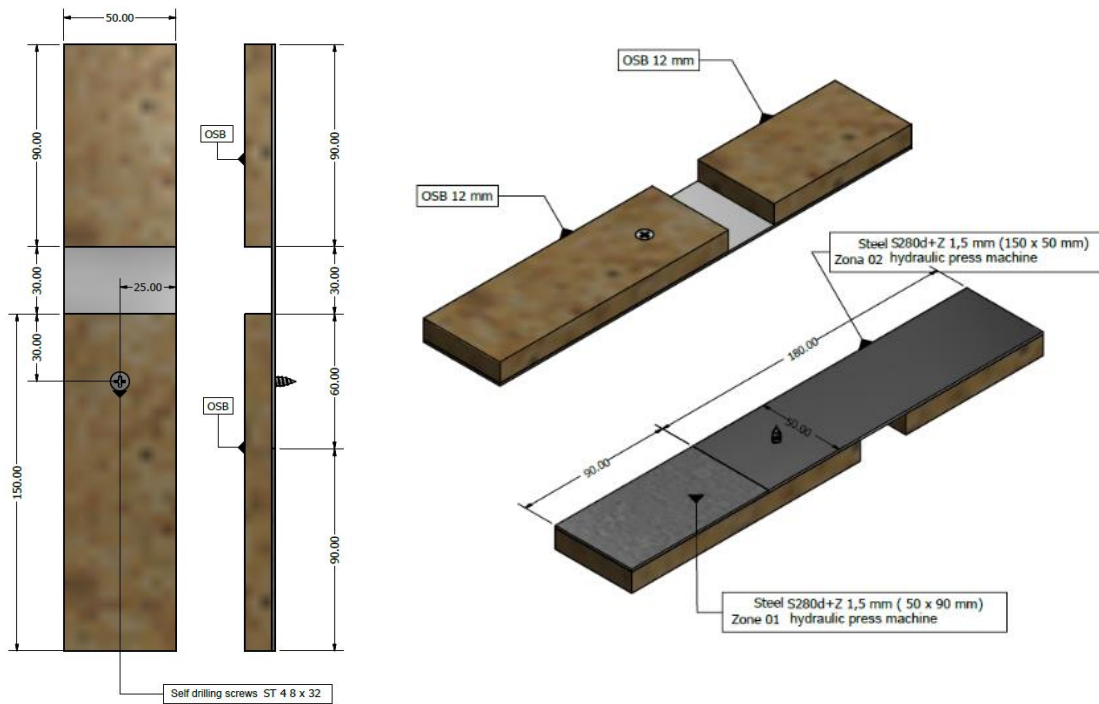


Figure III.20 – Test specimen of steel-OSB connection with ST 4.8.

Table III.4 – Main properties of the test specimens of the OSB-steel screw connection.

Steel plate	OSB	Screw	Edge distances
$t = 1.5$ mm Steel	$t = 12$ mm	$d = 4.8$ mm	$e_1 = 30$ mm
S280GD+Z	OSB3	$d_h = 9.5$ mm	$e_2 = 25$ mm

III.2.2.2.2. Test results

Similarly, to the steel-to-steel connection, this connection showed significant screw rotation, as illustrated in Figure III.21. The load-displacement curve is characterized by a significant non-linear response from the beginning of loading. Figure III.22a shows the curves for the five test specimens. These curves show a very similar response, which is consistent with the fact that no variations were performed. Consequently, these curves are assumed to represent this type of connection with confidence. Table III.5 summarizes the test results using the same parameters used for steel-to-steel connections. The average maximum load observed was 2.5 kN.

CHAPTER III

Structural performance of light steel framing panels using screw connections subjected to lateral loading



Figure III.21 – Experimental results for steel-OSB connection with ST 4.8 x32 screw.

Table III.5 – Summary of the experimental force-deformation curve of the OSB-steel screw connection.

Variable	Test A	Test B	Test C	Test D	Test E
F [kN]	2.44	2.90	2.19	2.29	2.93
S_{ini} [kN/m]	893.77	947.71	829.55	820.79	626.07
d_{Fmax} [mm]	5.80	5.68	7.79	8.13	7.63
d_u [mm]	7.49	8.73	8.63	8.76	8.6

The experimental results were compared with the analytical resistance obtained from the application of the method described in the previous section (Figure III.22 b). The analytical resistance is approximately four times smaller than the average resistance of the experimental results. In the analytical calculation, the wood component governs the resistance of the connection. This was also observed experimentally. The reason for the considerable conservative result from the code relies on the fact that wood is a material that has a great variability on its properties.

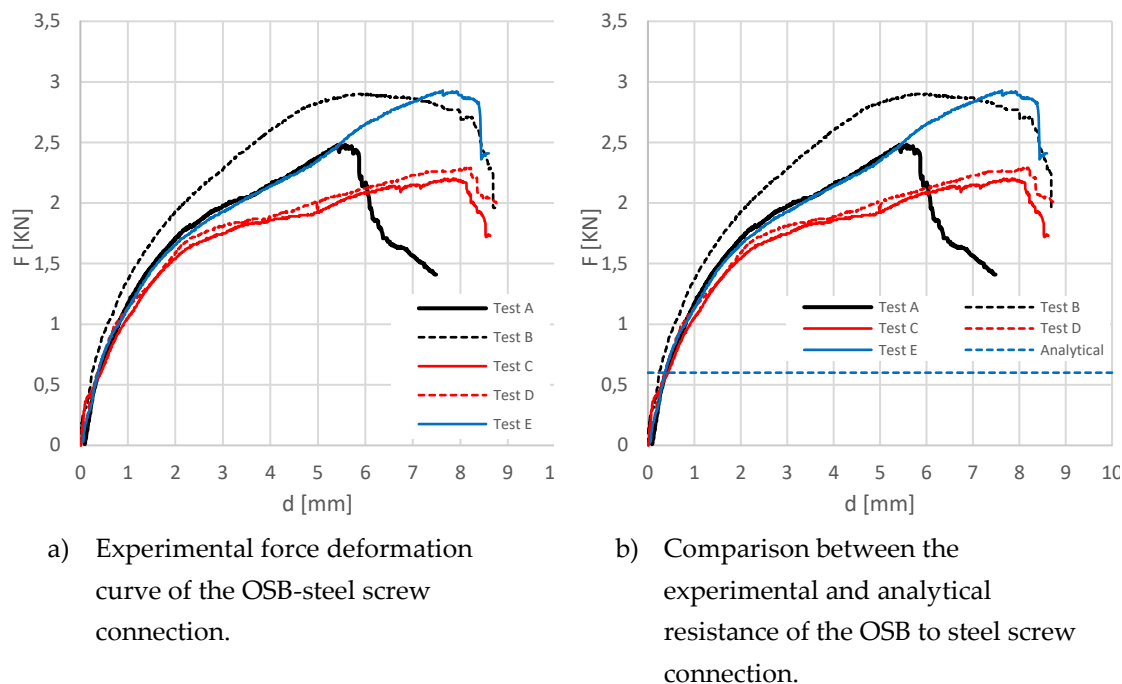


Figure III.22 – Force-displacement OSB-steel connection.

III.3. Analytical determination of the response of LSF wall panels to lateral loading

In LSF walls subjected to lateral loading, European and the American code design approaches are distinct reflecting the different mentality towards this type of construction in both continents. AISI S213-07 w/D1-09, (2012) is totally dedicated to the design of LSF walls subjected to lateral loading. In Europe a few authors such as Fülöp and Dubina, (2004) and Landolfo *et al.* (2007) have dedicated their research interests to the subject. In order to design a LSF structure subjected to lateral loading, the designer has to refer to different design prescriptions from the different structural Eurocodes as EN1993-1-3, (2006), EN1992-4, (2017); EN1995-1-1, (2004) and EN1998-1, (2005), and establish a design procedure making the link between the different codes.

The use of non-steel elements in LSF structures is completely neglected. In particular case of housing, LSF construction implies the use of non-steel elements such as wood-boards which have a strong influence on the overall structural performance of these LSF panels. The lateral stability of LSF structures may be assured by traditional bracing systems such as: diagonal steel straps, LSF vertical trusses, steel sheets and finally non-steel/panels. A common configuration is the use of diagonal steel straps and OSB boards. Therefore, in the following sections the design approach for both type of systems is presented and discussed.

III.3.1. LSF wall braced with steel straps

In LSF walls braced with steel straps, the resistance and stiffness to lateral loads is entirely provided by steel elements. Accordingly, the design approach for these structural systems is usually denominated “all steel” design approach. The EN1993-1-3, (2006) cover this type of systems, excepted for the anchoring to the concrete foundation, and complemented by the design prescriptions for the seismic condition (EN1998-1, 2004). The American code has a standard dedicated to LSF structures design when subject to a lateral load which complements the general design rules for the design of LSF structures given in AISI S100, (2007). The American standard approach is a direct design method based on prescribed design solutions for the different design situations. The principles behind both codes have the same theoretical base. The load capacity of a LSF wall when subjected to a lateral load results from the bearing capacity of two groups: the members and the connections. Figure III.23a illustrates the different components of a LSF wall. These components contribute for the lateral stiffness of the wall and can limit the resistance in a single storey frame. Figure III.23b shows the load path in the structure.

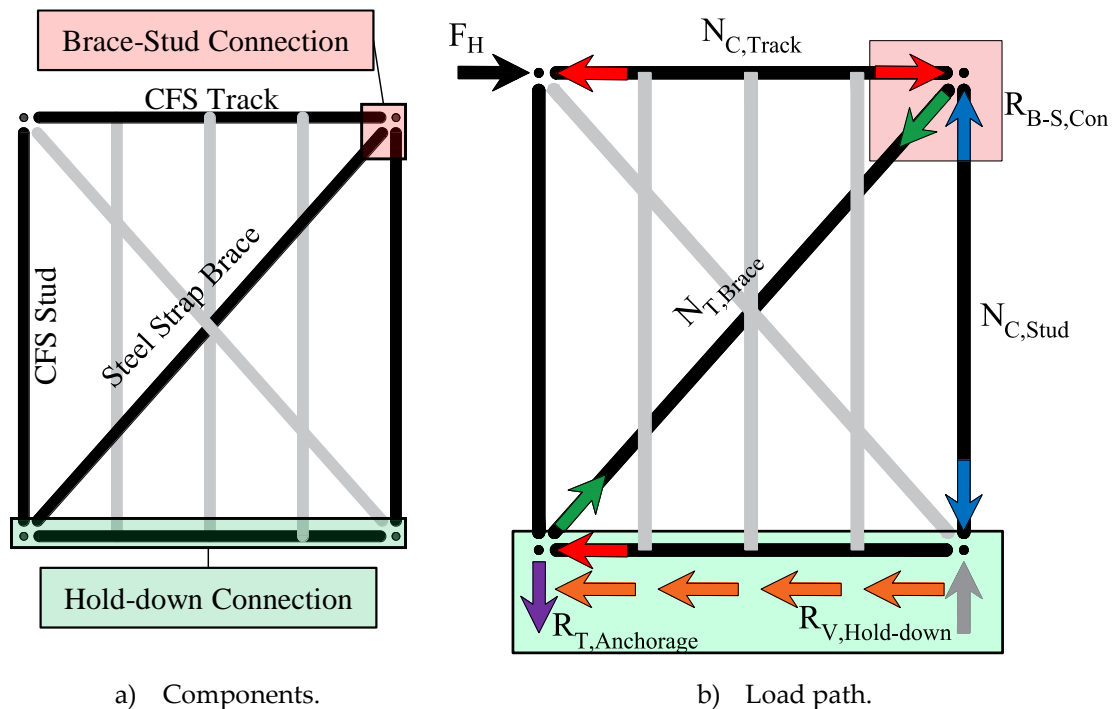


Figure III.23 – LSF wall braced with steel straps.

The components of the wall are the following ones: (1) wall stud in compression ($N_{C, Stud}$); (2) wall track in compression ($N_{C, Track}$); (3) diagonal steel strap in tension ($N_{T, brace}$); (4) brace-stud connection ($R_{B-S, Con}$); (5) hold-down connection to the ground ($R_{T, Anchorage}$ and $R_{V, Hold-down}$); (6) hold-down connection between floors. Another component is added which is the connection between two consecutives floors.

Usually, in multi-storey LSF building the columns are interrupted at the floor level. This connection can be a limitation to the load path to the foundations. The design of the components listed is covered by both standards, AISI S100, (2007) and EN1993-1-3, (2006). The load capacity of the wall subject to lateral loading is obtained by the smallest resistance of the listed components, when there is equilibrium between external and internal forces, as expressed by:

$$F_{H,max} \leftrightarrow \min(N_{C,Stud}; N_{C,Track}; N_{T,Brace}; R_{B-S,Con}; R_{T,Anchorage}; R_{V,Hold-down}) \quad (21)$$

Macillo *et al.* (2014) addressed this approach in detail and was investigated and verified against experimental data by Fiorino *et al.* (2016) and Iuorio *et al.* (2014). The results from the authors had showed that the model accurately estimate the strength of the wall to lateral loading. The authors also adopted the design prescriptions from the EN1998-1, (2004) for concentric brace frames and applied the principle of the capacity design approach. However, the EN1998-1, (2004) does not address specifically LSF structures. On the other hand, AISI S213-07, (2012) addresses the seismic design of LSF walls and behaviour factors are provided.

However, Fiorino *et al.* (2016) and Iuorio *et al.* (2014) estimated behaviour factors and concluded that the values obtained were higher than those proposed by AISI S213-07, (2012). The authors propose the use of the same behaviour factors used for concentric brace frames given in EN1998-1, (2004), for European territories. For the lateral stiffness of the LSF wall with diagonal steel straps, the model proposed by Macillo *et al.* (2014) consists in considering the deformation of: (1) diagonal steel strap in tension ($N_{T,Brace}$); (2) brace-stud connection ($K_{B-S,Con}$); and (3) wall overturning ($K_{T,Anchorage}$).

In this model, the slip between wall and foundation can be neglected. The contribution of these components to the initial lateral stiffness of the wall consist in a system of elastic springs in series and can be obtained by:

$$K_{ini,H,Wall} = \frac{1}{\frac{1}{K_{T,Brace}} + \frac{1}{K_{B-S,Con}} + \frac{1}{K_{T,Anchorage}}} \quad (22)$$

III.3.2. Sheathed LSF walls

As above mentioned, the EN1993-1-3, (2006) neglected the contribution of non-structural elements on the lateral stability of LSF walls. However, Branston *et al.*

(2006) demonstrated that these non-structural elements can provide adequate strength and stiffness to the structure when subjected to lateral loadings. Therefore, in AISI S213-07, (2012) these components are considered to resist to lateral loading arising from wind or earthquake actions. The response of sheathed LSF walls using non-structural elements, in particular wood derivate sheets or panels, is dependent of the response of different parts of the system (Branston *et al.* (2006) and Fiorino, (2009)): (1) wall stud in compression ($N_{C, Stud}$); (2) wall track in tension ($N_{T, Track}$); (3) non-steel or panel in shear (V_{Sheet}); (4) sheet-to-track connection ($R_{S-T, Con}$); (5) sheet-to-stud connection ($R_{S-S, Con}$); hold-down connection ($R_{T, Anchorage}$ and $R_{V, Hold-down}$); (6) hold-down connection between floors. These are illustrated in Figure III.24 for a wall panel with two segments. This principle can be considered for walls with any number of segments.

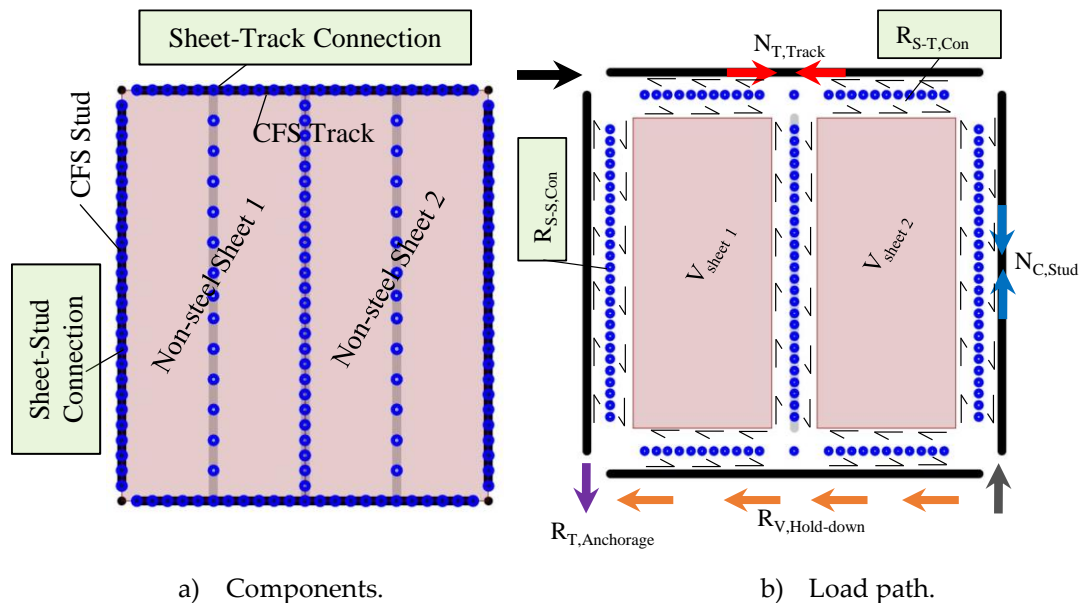


Figure III.24 – LSF wall braced with steel sheet or panel.

The evaluation of the system components, excepted the non-steel or panel and sheet-to-stud/track connection, can be performed using the design rules presented in section III.3.1, the EN1995-1-1, (2004) provides the design rules for non-steel components, such as wood derivate. The EN1993-1-3, (2006) and EN1995-1-1, (2004) provides design guidance's that can be used in this case, for example the steel-to-timber connection presented in section III.2.2. The AISI S213-07, (2012) covers not only "all-steel" LSF braced walls, but also the LSF walls braced with non-steel sheet or panels. Similar to the previous case, the resistance of the wall to lateral loading is given by the smallest value of the listed components where there is equilibrium between the external and internal forces:

$$F_{H,max} \leftrightarrow \min(N_{C,Stud}; N_{T,Track}; V_{Sheet}; R_{S-S,Con}; R_{S-T,Con}; R_{T,Anchorage}; R_{V,Hold-down}) \quad (23)$$

In the case of cyclic loading, the best structural response obtained with failure of the Sheet-to-Stud/Track connection (Branston *et al.* (2006) and Fiorino, (2009)) as these connections fail in a ductile manner. Branston *et al.* (2006) noticed that in the experimental tests on walls governed by the connection response, no distinction in failure is noticed between monotonic and cyclic tests. In terms of behaviour factor of the LSF wall braced with wooden boards, no analogy can be done with the structural systems covered in EN1998-1, (2004). Different values are found in literature. A value of 4 is proposed by Fiorino, (2009), while in AISI S213, the value proposed for LSF wall with shear panels of other materials is 2. Fiorino, (2009) concluded that latter values are conservative. To improve the accuracy of the behaviour factor more studies on extensive dynamic nonlinear analysis are still required.

The lateral deformation of the LSF wall panel is obtained adding the contribution of different parts of the system (Branston *et al.* (2006) and Fiorino, (2009)): (1) sheet or panels shear deformation (d_s); (2) bending deformation (d_b); (3) sheet-to-track and sheet-to-stud deformation (d_f); (4) overturning deformation (d_a). The best performance of the wall panel is obtained when the governing component is the sheet-to-stud/track connection. Only this member is assumed entering to non-linear range (Fiorino, 2009). The determination of force-deformation of the LSF wall subjected to a lateral loading is complex and normally is achieved by experimental tests. In this case, the load-displacement curve can be derived using the relation proposed by R.M. Richard, (1975). This approach is able to provide accurate estimate of the response of the wall to lateral loading (Branston *et al.* (2006) and Fiorino, (2009)), however, it is required experimental tests. This approach is suitable for numerical studies, for example, to assess the seismic performance of LSF structures accounting for the contribution of non-steel sheets/panels.

III.4. Experimental tests on light steel framing panels subject to lateral loading

To characterize the behaviour of LSF panels subject to lateral loading, full-scale experimental tests were conducted. These were limited to the testing of bare steel panels (unbraced) and steel panels braced with OSB boards. The main objective of these experimental tests is the achievement of the contribution of OSB board to the stiffness of LSF panels. The panels configuration used in these experimental tests are produced by a modular construction company, Cool Haven. In this configuration, the vertical studs have different cross-section from the usual channel section ("C profiles") due to the particularly of the on-site panels assembling system.

Nevertheless, the main purpose was to characterize the lateral response of the panels, which is mainly influenced using OSB board and not by the shape of the cross-section.

II.4.1. Experimental campaign

III.4.1.1. Experimental programme

The behaviour of LSF panels subject to lateral loading was experimentally assessed. Monotonic static load tests were conducted on a total of six full scale wall panels as indicated in Table III.6. To characterize the lateral behaviour of the panels, the main variables are: (1) panels with bare steel frame or frames braced by OSB boards; and (2) OSB board-frame screw connections spacing. Three series of two tests were considered. The monotonic load is a static monotonic lateral load applied at the top of the panel.

Table III.6 – Experimental programme on LSF panels subject to lateral loading.

Test ID	Type	Variable
Test 01 Test 02	Bare steel frame	No OSB board
Test 03 Test 04	Frame braced by OSB board	OSB board – steel frame screw connection spacing → 300 mm (Figure III.25)
Test 05 Test 06		OSB board – steel frame screw connection spacing → 150 mm (Figure III.26)

Figure III.25 and Figure III.26 illustrates the panels configurations with the main dimensions. The panels under study have 1.2 m wide and 2.8 m high, corresponding to a ratio of 2.33. Each panel is composed by two smaller panel modules (600 mm wide) assemblage of with back-to-back screw connections (ST 5.5 x 19) and top and bottom tracks connected by ST 4.8 x 15. The OSB/3 is the same previously tested and presented in Chapter 2, with 12 mm of thickness. These OSB boards brace both sides of the steel frames. In the “exterior” side of the wall panel the OSB is directly connect to the frame using ST 4.8 x 32 screw connections. On the exterior side of the wall panel OSB is connect to a wood-frame with 50 x 50 mm. This wood frame is usually filled with an insulation material (rockwool). The wood frame is connected to the steel frame by ST 6.3 x 100 screws. On this side of the wall panel, OSB boards are connected to the wood frame with 3.5 x 35 screws.

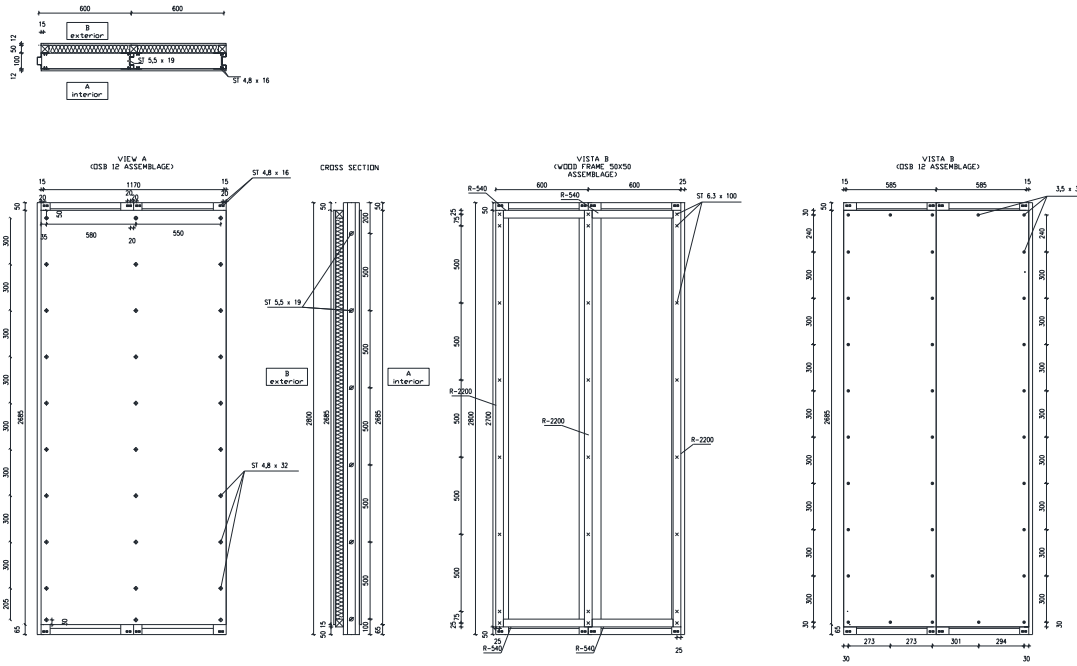


Figure III.25 – Frame braced by OSB with steel frame connection spacing – 300 mm.

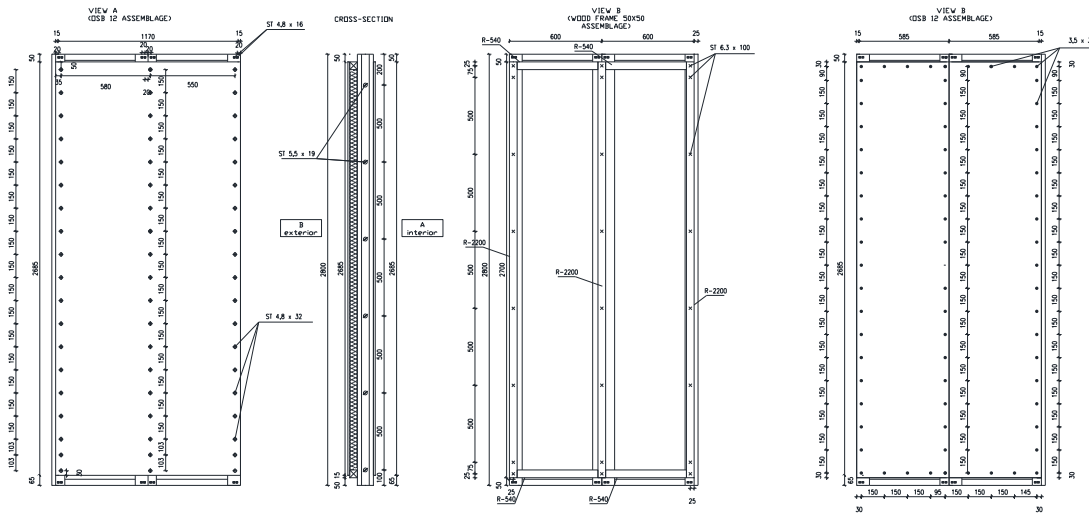


Figure III.26 – Frame braced by OSB with steel frame connection spacing – 150 mm.

III.4.1.2. Experimental procedure

The experimental procedure used in this experimental campaign is based in two American standards: ASTM E564-06, (2012) – “Static Load Test for Shear Resistance of Framed Walls for Buildings” and ASTM E72-15, (2015) – “Conducting Strength Tests of Panels for Building Construction”. According with these standards at least two tests for wall should be performed to determine the resistance capacity of the wall panel. The global load should be applied on the top of the wall panel, at the

CHAPTER III

Structural performance of light steel framing panels using screw connections subjected to lateral loading

centre of the steel frames using a hydraulic jack able to maintain a displacement rate constant until the ultimate force. This must be accomplished within a minimum time interval of five minutes. For these monotonic static tests, a pre-load of 10% of the estimated ultimate force should be applied for five minutes. After this five minutes the load must be removed. After five minutes all sensors must be set to its original condition.

The second step of the procedure consists in applying 1/3 and 2/3 of the estimated ultimate load, remove the load and wait another five-minute giving time for the wall panel recovery. The third step consists in applying the load (0.07 mm/s) until the collapse of the wall panel. The applied load should be monitored with a load cell with an accuracy of $\pm 1\%$. The displacement sensors must have an accuracy of 0.25 mm for horizontal/vertical displacements. Figure III.27a illustrates the displacement points that should be measured according with ASTM E564-06, (2012). Figure III.27b illustrates the horizontal measurements.

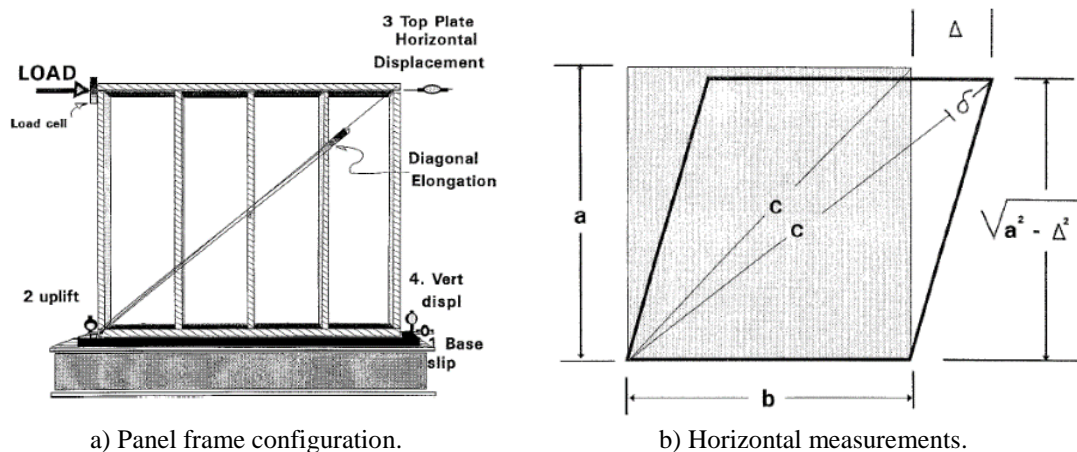


Figure III.27 – Representation of the experimental layout (ASTM 564 – 06, 2012).

According with Figure III.27a at least four transducers must be used to directly measure the deformation in four fundamental points. The measurements are quite complex because the wall assembly may tend to suffer translations or rotation out of the plane. To measure the vertical displacement of the wall a transducer is placed at point 4 (Figure III.27a). On the other side of the wall panel (point 2) a transducer measures the uplift of the wall panel. The transducer placed at point 3 will measure the horizontal displacement of the wall. Finally, at point 1 the transducer will measure the horizontal displacement at the wall panel bottom. The angular displacement of the wall panel is calculated based on the diagonal elongation with the following expression:

$$(c + \delta)^2 = (b + \Delta)^2 + (a^2 - \Delta^2) \frac{(F_2 - F_1) \times l_1}{(\mu_2 - \mu_1) \times A} \quad (24)$$

Substituting,

$$a^2 + b^2 = c^2 \quad (25)$$

$$2c\delta + \delta^2 - 2b\Delta = 0 \rightarrow \Delta = \frac{2c\delta + \delta^2}{2b} \quad (26)$$

The value obtained, can be also calculated based on the horizontal and vertical displacement measurements of the four transducers. The internal shear displacement (Δ_{int}) is determined by the following expression:

$$\Delta_{int} = \Delta_a - \Delta_1 - (\Delta_2 - \Delta_4) \times \frac{a}{b} \quad (27)$$

Then the internal shear stiffness (G) of the wall panel is given by expression:

$$G = \frac{P}{\Delta_{int}} \times \frac{a}{b} \quad (28)$$

Since the behaviour of the wall panel is non-linear, for the calculation of the internal shear stiffness a reference load of 33% of the ultimate load (P_u) is considered.

III.4.1.3. Experimental layout

The details of the test layout are provided in Figure III.28. The test specimens were fixed to a support beam in the bottom and load beam on the top through two hold-downs and two fixing plates with M20 bolts. These hold-downs were responsible for resisting the uplift and shear force effects introduced on the panels during the load tests. Loading was provided by a hydraulic jacket with a 900 kN capacity and a load cell with a capacity up to 1000 kN. To measure the deformation of the panel several transducers were used (LVDT300 on the load beam and LVDT200 to measure the horizontal and top displacements of the wall). To prevent displacements out of the plane of the panel, the load beam was braced with roller bearings on both sides of the panel, as indicated in Figure III.28.

CHAPTER III

Structural performance of light steel framing panels using screw connections subjected to lateral loading

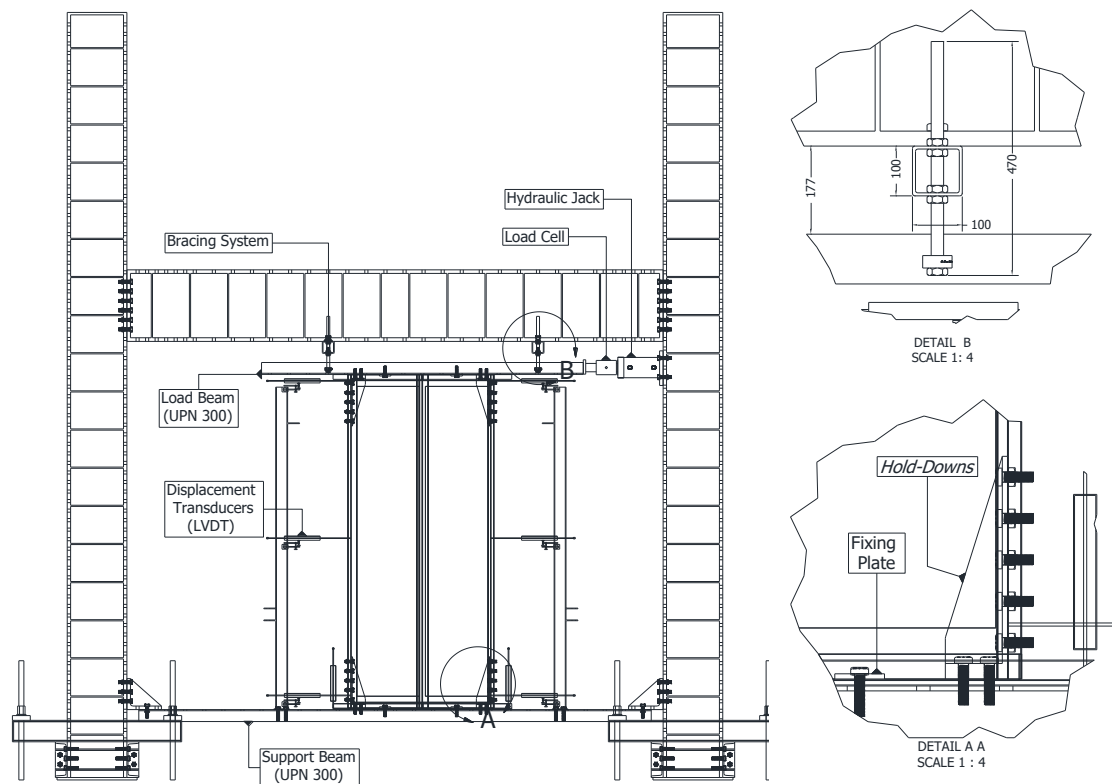
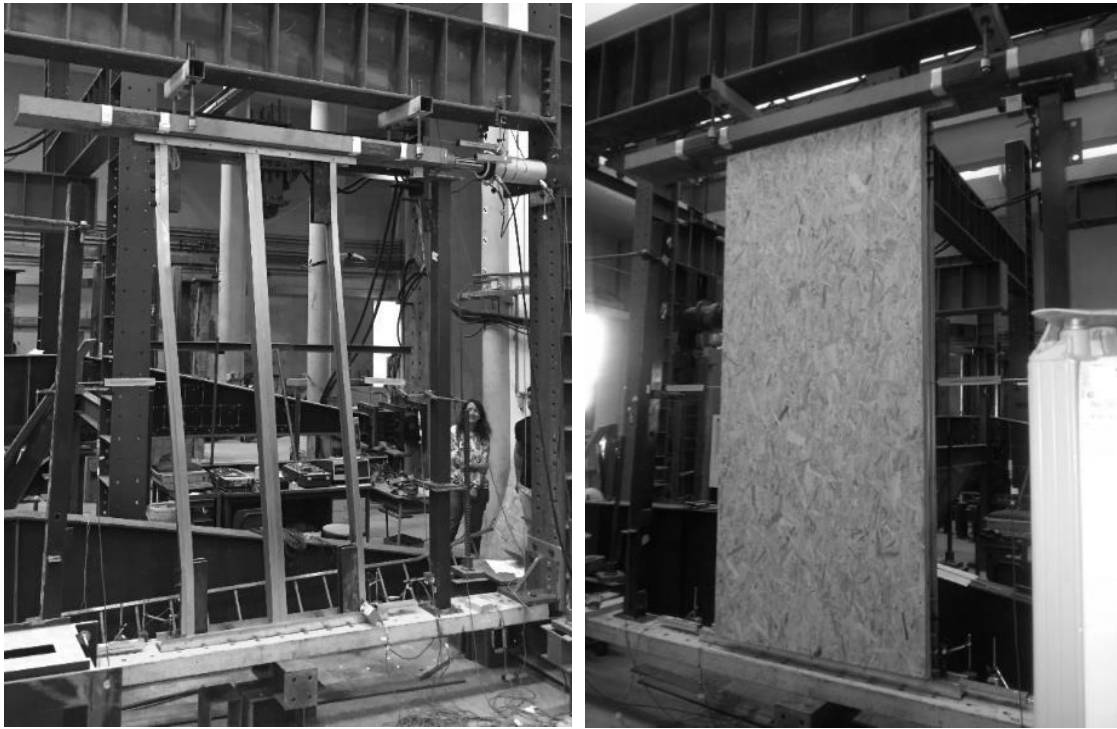


Figure III.28 – Experimental layout.

III.4.1.4. Results and discussion

The experimental tests of all specimens (Figure III.29) were conducted up to failure. In the bare steel panel, failure occurred in the vertical stud by local instability of the profile (Figure III.30a). In the braced panels, failure was observed in the connection between the OSB board and the steel profile (Figure III.30b). The test results are summarized in Table III.7. The shear stiffness was determinate based on a load corresponding to 33% of the ultimate load (P_u). The beneficial of the OSB board is evident. The latter was quantified using as reference the bare steel panel results (Figure III.31a).

The deformability of the panels, especially of the bare steel panel is highly dependent on the shear screw connection between profiles. It was observed from the bared steel panel tests that screw connections did not limited the resistance of panel, as failure occurred with instability of the steel profile. However, this depend on the number of screws used in the connection between steel profiles, but in this case study, it depends on the hold-down system at the corners required by the test standards. The screw connections between the OSB board and the steel profile contributes significantly to the lateral resistance of the panel. This is evident, as with the increase of the number of screws the lateral resistance also increases.



a) Bared Steel Panel.

b) Braced panel with OSB boards.

Figure III.29 – LSF panels test specimens.



a) Bared Steel Panel.

b) Braced panel with OSB boards.

Figure III.30 – Failure on the LSF panels tests.

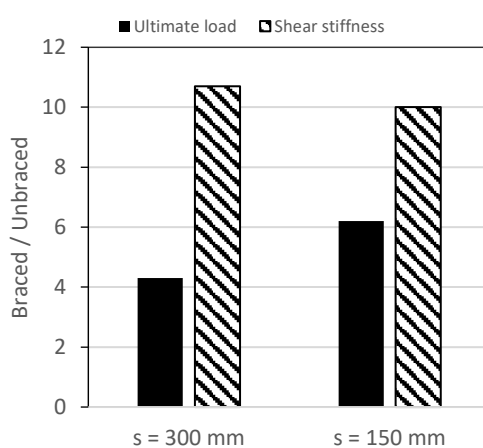
CHAPTER III

Structural performance of light steel framing panels using screw connections subjected to lateral loading

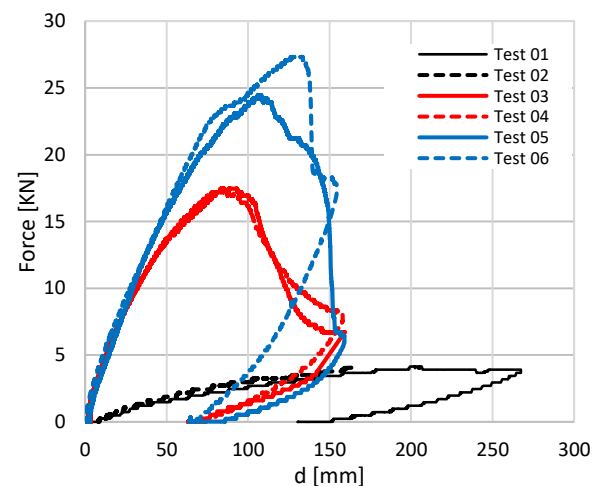
Table III.7 – Summary of the results of the experimental tests on LSF panels subject to lateral loading.

Test ID	Ultimate load [kN]	Average ultimate load [kN]	Panel shear stiffness G [N/mm]	Average panel shear stiffness G [N/mm]
Test 01	3.91	3.99	79.00	90.68
Test 02	4.06		102.35	
Test 03	17.47	17.47	965.10	960.45
Test 04	17.46		955.80	
Test 05	24.40	25.85	904.00	900.50
Test 06	27.30		897.00	

Figure III.31b shows the force-displacement curves obtained in the tests. The force represents the total lateral load applied at the top of the wall panels and the displacement corresponds to the horizontal displacement measured at the top of the panel. Results show a clearly difference between the test specimens. The tests done with bare steel frames (Test 01 and Test 02) show a very flexible behaviour with low load capacity and high deformation capacity. The specimens with OSB boards (Test 03 to 06) show a higher lateral stiffness and load capacity in comparison to the bare steel frame. The increase is in order of 4-5 times the value obtained for the bared steel frame. Therefore, the OSB board has a non-negligible impact on the frame. Furthermore, these two series of specimens confirm that the number screws fixing the OSB board to the steel frame is directly related with the lateral load capacity. The higher the number of screws, the higher the load capacity.



a) Quantification of the contribution of the OSB boards.



b) Force-deformation curves.

Figure III.31 – Force-deformation results of the experimental tests on LSF panels subject to lateral loading.

Figure III.32 shows a global comparison between the experimental results obtained by Branston *et al.* (2006), the experimental results in this experimental campaign and the analytical method previously described. The dimensions, material and geometric properties of the walls are different; however, the comparison was performed using the ultimate resistance ratio and the corresponding screw spacing ratio.

As observed in Figure III.32, there is a deviation between these experimental tests and the ones performed by Branston *et al.* (2006). This difference is not noticed between the two types of walls reported by the author. This means, that the difference is not related to the size of the wall but due to the different construction system used. In relation to the analytical values, it is observed a higher deviation. This was expected mainly because of the conservative results already observed previously in Section III.2.2. Also, the analytical model cannot consider the frame effect observed in the experimental tests (Figure III.31b). However, the failure mode is the same: the sheet-to-track connection.

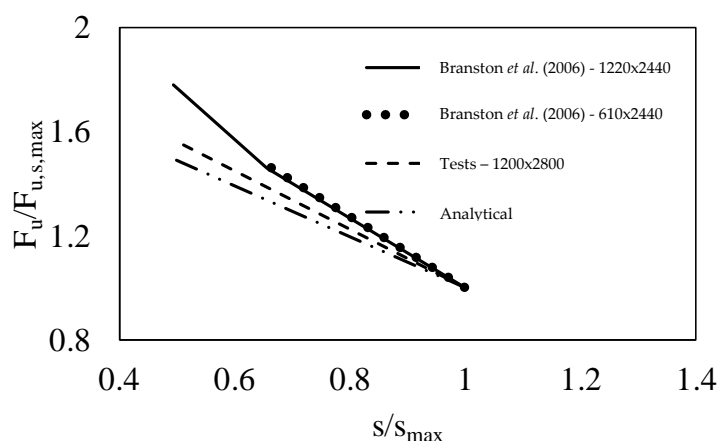


Figure III.32 – Comparison between literature tests, performed tests and analytical model.

III.5. Numerical evaluation of LSF panels subject to lateral loading

Due to limited number of experimental tests and to further investigation of the contribution of the OSB boards in comparison with steel-braced and non-braced panel, numerical simulations were performed. The numerical models were developed in finite element software Abaqus. Two models were developed: (1) a model that reproduces the experimental test on the bare steel frame for validation purpose; and (2) use the previous model incorporating a steel frame bracing using flat strips. The main characteristics of the model are:

- The steel cold-formed profiles, including bracing are simulated by means of shell elements (S4R);
- No initial imperfections, local and global, were considered;
- The simulations reproduce the experimental tests (push-over analysis), where the load was applied at the top of the frame;
- The analysis considered geometric and material non-linearities;
- The material behaviour used for steel profiles is an elastic-perfectly plastic law;
- The screw connections used to assemble the steel profiles are considered fully rigid in the screw position;
- The screw connections used to connect the diagonal steel straps to the profiles is also considered fully rigid, however the number of screws was assumed so that the connection is not a limitation;
- The anchorage of the panel is assumed rigid.

The developed numerical model has two limitations: (1) cannot reproduce the complete response of the panel to lateral loading when the behaviour is governed by the connections; and (2) accuracy can only be obtained while the connections remain in the elastic range. However, the proposed models were developed to analyse the influence of OSB boards on the lateral response of the panel in comparison with a common brace system with flat straps. In the sub-sections, the model is validated, and the efficiency of the difference systems is discussed.

III.5.1. Validation and calibration of the FEM model

Figure III.33b presents the comparison between the force-displacement curves obtained experimentally and numerically. The force and the displacement represent the total applied load and the displacement at the top of the frame in direction of the applied load, respectively. The numerical model shows a good agreement against measured values for the initial stiffness. However, after 1.5 kN load, a deviation is justified by the screw connection modelling which is assumed more rigid in the numerical model. It was noticed that in experimental tests with the increasing load a rotation of the screws occurred. With this rotation, the plates (member flanges) are blocked by the screw threads. Whenever a thread traverses the plate there is a slip in the structure response until the next thread starts working effectively. Because of this a more deformable structure is found. The mechanism is observed in experimental tests. In terms of maximum load, an excellent agreement was achieved. Figure III.33a presents the experimental and numerical deformation of the bare steel frame. The

global behaviour of the test is well reproduced numerically. From these results, it can be concluded that the numerical model provides an accepted accuracy to perform more analysis of different bracing solutions.

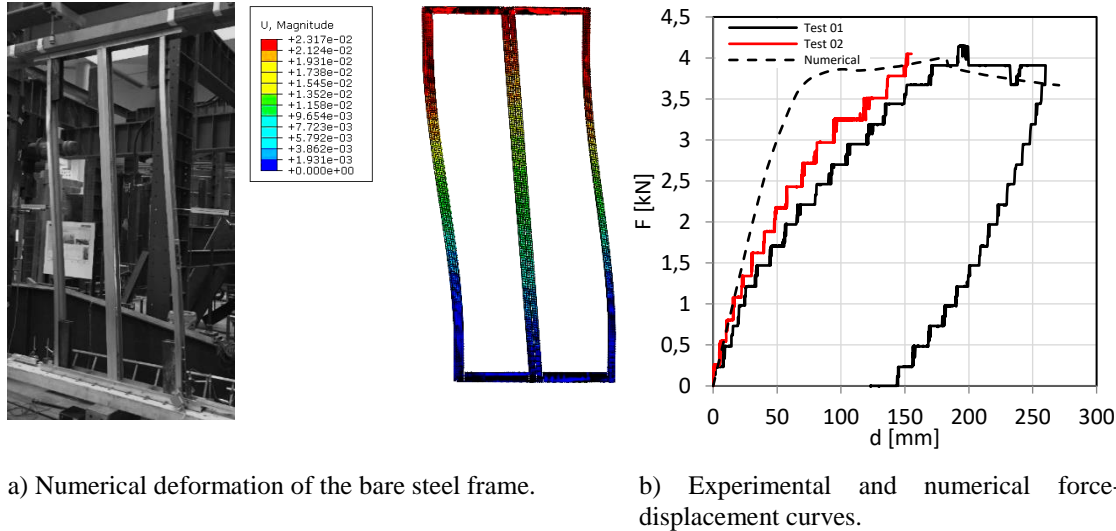


Figure III.33 – Comparison between experimental and numerical results.

III.5.2. Structural performance of LSF panels to lateral loading

In LSF structures, it is usual to use bracing systems with steel elements. A common solution is the use of flat steel strips. To compare the traditional bracing systems with the OSB boards, a second numerical model was developed. The model is illustrated in Figure III.34a and consists in the previous model braced with a steel flap stripes. According with the company that produces this modular construction system (Cool Haven), the standard solution relies in flat stripes of 100 mm x 1.5 mm. However, this depends on the design situation.

The load capacity of the panels is often governed by the connection between brace and stud and the number of screw connections. However, the number of screws will not affect the initial stiffness of the braced system and can be considered fully rigid. Figure III.34b illustrates the model validation against results obtained by Branston *et al.* (2006). To make this comparison, the initial lateral stiffness of the tests was modified using the following factors: (1) diagonal steel strap cross-section area (A_{Num}/A_{Test}); (2) length of the diagonal steel strap (L_{Test}/L_{Num}); (3) and the angle of the diagonal with the horizontal ($\cos^2\alpha_{Num}/\cos^2\alpha_{Test}$). Only the described factors were used for the normalization of test results, because the initial stiffness is mainly affected by the deformation of the diagonal steel strap, and therefore, the other components presented in Section III.3.1 can be neglected. Even with this simplification, it can be observed a good accuracy of the model.

CHAPTER III

Structural performance of light steel framing panels using screw connections subjected to lateral loading

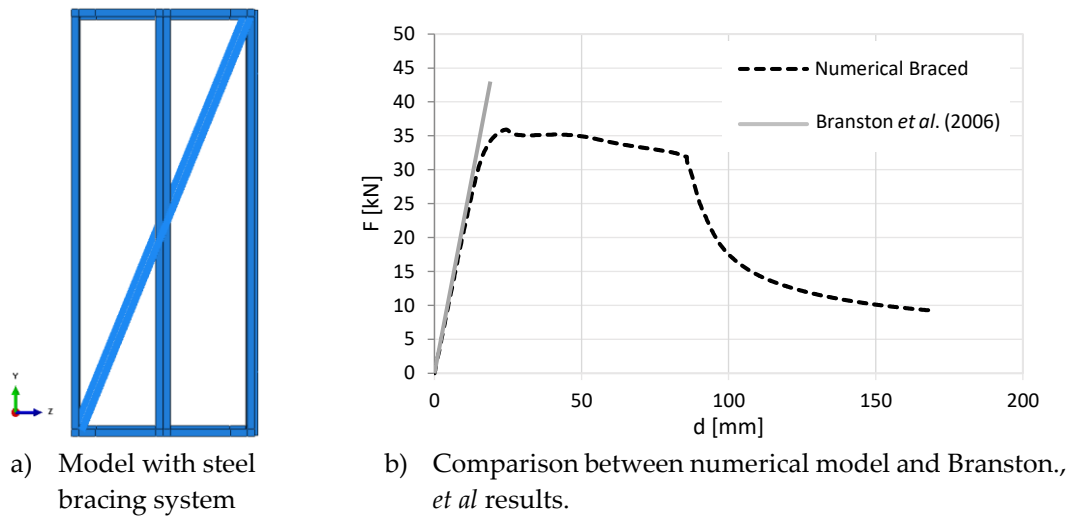


Figure III.34 – Model with steel bracing system against test report results by Branston *et al.* (2006).

Figure III.35 presents the force-deformation curves for the numerical models (braced and unbraced structure) and all the experimental tests. It can be seen, that the LSF panel with steel bracing system provides the highest stiffness. However, it also can be seen the contribution of OSB boards which contributes significantly for the lateral stiffness of the panels. The same trend was also observed in studies made by Vieira and Schafer (2012) and Baran and Alica, (2012).

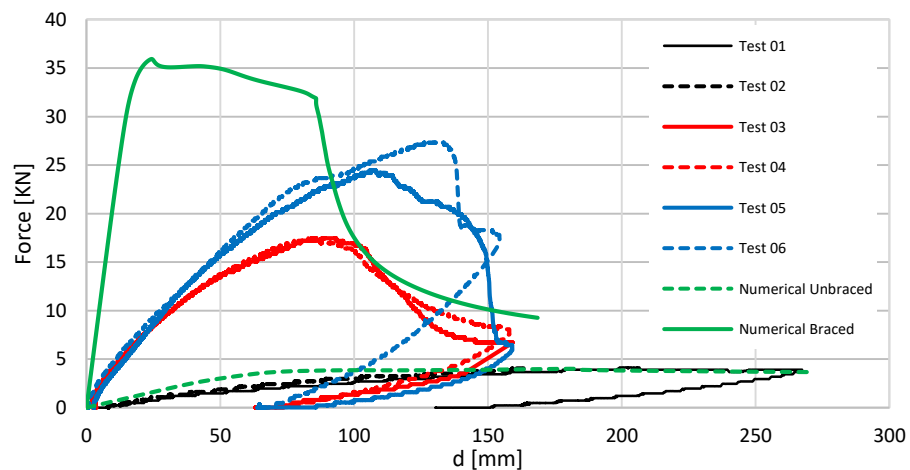


Figure III.35 – Force-deformation curves comparing numerical simulations and experimental tests of LSF panels subjected to lateral loading.

The results may not be compared as different panel configurations and connections were used. The differences of the lateral stiffness between the three solutions (bare steel framed panel, steel braced panel and OSB braced panel) are the following:

- The ratio between steel braced panel ($S_{ini} = 2127 \text{ N/mm}$) and the unbraced steel panel ($S_{ini} = 60 \text{ N/mm}$) is approximately 35.5;

- The ratio between the steel braced panel ($S_{ini} = 2127 \text{ N/mm}$) and steel panel braced by the OSB board ($S_{ini} = 332 \text{ N/mm}$) is approximately 6.4.

III.6. Conclusions

An integrated approach for assessing the behaviour of LSF panels subjected to a lateral load using screw connection was presented in this chapter. The behaviour of steel-to-steel, OSB-to-steel screw connections and the global behaviour of LSF panels subjected to lateral load was evaluated. The stiffness and resistance of the LSF panels, subjected to lateral loading are influenced by the response of these connections. The first part of this chapter presents a numerical, analytical and experimental research of the behaviour of steel-to-steel screw connections. It was concluded that the analytical approach given by AISI provides more accurate results than the EN 1993-1-3 comparing against experimental results.

The numerical calculations showed that the deformation only due to the connection is negligible in comparison to the deformations that may arise in other parts or due to eccentricities. It was concluded that assuming this connection as rigid is a reasonable approach. The experimental investigations on OSB-steel screwed connections show some variability on the post-elastic resistance. This variability is since the failure is governed by the OSB part of the connection which presents a high variability on the mechanical properties. This relevant in an ultimate strength of the material, which is governed by the highly non-uniform microstructure of the material. This non-uniform microstructure of the material was investigated in Chapter II.

The comparison between analytical approach provide in EN1995-1-1, (2004) and the experimental tests shows a conservative approach of the code, and can be justified by the high variability on the material properties of the OSB board (Chapter II). The comparison between the panel using flat steel strips and the panel using OSB board, for the lateral bracing, showed that the contribution of OSB boards is significant and therefore it is a consistent solution for the lateral stability of LSF structures. Currently, the EN1993-1-3, (2006) neglects this type of construction element in LSF construction. This is not the case of the AISI that addresses the use of these elements for the lateral stability of LSF structures.

The experimental results showed that the connection between timber or timber derived boards and steel frame influence the lateral capacity and latera stiffness of the panel. It is concluded that the contribution of OSB boards is an effective way for

CHAPTER III

Structural performance of light steel framing panels using screw connections subjected to lateral loading

increase the panel resistance. A revision of the EN1993-1-3, (2006) in order to address the contribution of timber derived boards on the lateral stiffness of LSF is therefore recommend.

PART C

EARTH-TO-AIR HEAT EXCHANGERS

CHAPTER IV

Earth-to-air heat exchangers overview and a simple design approach based on ϵ -NTU method

IV.1. Introduction

Heating, Ventilation and Air Conditioning (HVAC) systems have an important role in ensuring indoor air quality and comfort and are among the major components of energy consumption in buildings. The development of energy efficient HVAC systems is essential to ensure lower energy costs and to protect the environment from GHG emissions. A technological reference is the use of geothermal energy; since the 1920s (Pintaldi *et al.* 2015), ground coupled technologies have been developed that use the thermal energy stored in earth crust. At depth, the Earth has constant temperature that is colder than the environment air temperature in summer and warmer than air temperature in winter. This temperature difference can be also used for pre-heating and pre-cooling by installing suitable systems. Ground Coupled Heat Exchanger systems have the advantages of being environmentally friendly and easy to control, presenting stable capacity and low maintenance cost.

Most of such systems consist of a set of horizontal or vertical plastic pipes, in series and/or parallel configurations, to carry a heat transfer fluid (glycol, water or air) that will exchange heat with the ground. The total pipes' surface area (length and diameter), the temperature difference between ground and environment, the fluid thermophysical properties and the flow rate have high influence on the system's overall thermal performance. There are three types of GCHE: Ground Source Heat Pumps (GSHP), Direct Expansion Ground-Coupled Heat Pump (DX-GCHP) and, for pre-conditioning of ventilation air, Earth-to-Air Heat Exchangers (EAHE). GSHP systems (Figure IV.1a) are a reference technology for HVAC that use heat pump systems. Normally these systems have vertical boreholes with high density heat

exchanger pipe loops where the water, an anti-freezing fluid or a mixture of them, flows. These systems have high thermodynamic efficiency for space heating and cooling: the power consumption required to produce thermal energy for air conditioning can be 45% lower than in a conventional Air Source Heat Pump (ASHP) system and 97% lower than in a conventional boiler-based system (Zhai *et al.* 2012). In cooling mode, comparing to a conventional air-to-water ASHP and a water-to-water, the reduction is 28% and 55%, respectively. GSHP systems are electrically powered; however 75% of the total energy is obtained by the heat exchangers and only 25% is given by electric network (Ochsner, 2007).

GSHP systems can be categorized as regular and Direct Expansion Ground Coupled Heat Pumps systems (Figure IV.1 b). DX-GCHP systems use refrigerants as heat transfer fluid, which flows through buried cooper pipes. Compared with conventional GSHP systems, these systems require less land area for heat transfer and are more efficient, because they dispense circulation pumps, the thermal resistance in heat exchanger pipes is lower and, due to the condensing/evaporating temperature in cooling or heating modes, they work with higher thermal potential for heat transfer (Omojaro and Breitkopf, 2013).

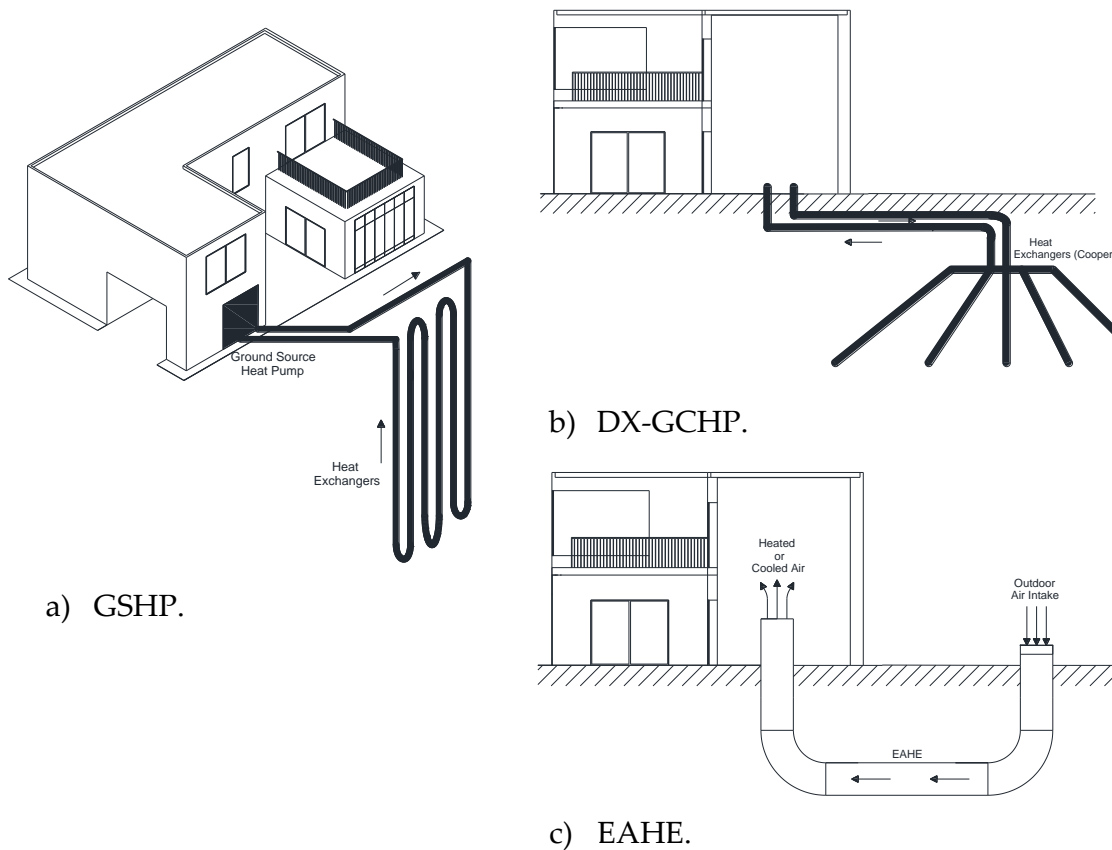


Figure IV.1 – Ground Coupled Heat Exchangers systems.

EAHE systems (Figure IV.1 c) are exclusively used for building ventilation, when the outdoor air temperature fluctuations are high when compared with ground temperatures. Such systems are composed by buried pipes in PVC or HDPE with open or closed loops. In cooling mode (summer), the ventilation air can be cooled because the ground temperature is lower. During the heating season (winter), the outdoor air can be warmed up or pre-heated in the heat exchanger whenever the environment air is significantly cooler than the ground.

Back to 3000 B.C., Iranian architects used underground air tunnels (UAT) for passive cooling (Goswami and Ileslamlou, 1990). Such systems are nowadays known as earth-to-air heat exchangers (EAHEs). An EAHE system consists of a network of pipes (the heat exchanger itself) buried deep in the ground, through which the ventilation airflow is forced by a fan. The air intake device is a small “tower” containing a pre-filtration section that arrests the larger-size particulate matter suspended in the outdoor air, to prevent contamination and minimize fouling inside the buried pipes.

The heat exchanger can be installed in open fields or below the foundation slab as a parallel network, or in series at a depth of 2.5 – 3 meters where the ground temperature stays nearly constant due to the high thermal inertia of the ground. The pipe circuit can be configured as an open or a closed loop (Figure IV.2). In the closed loop, the indoor air is conducted through the network of buried pipes and supplied again to the building at a temperature close to the ground temperature. During periods when the environment air temperature is too high or too low, the close loop proves to be more effective than an open loop. However, the closed loop does not allow the renewal of indoor air. One solution for this problem is using a Heat Recovery Ventilation (HRV) strategy, based on an air-to-air cross-flow heat exchanger that promotes heat transfer between the incoming and exhaust air flows. The HRV can improve climate control, while also saving energy by reducing heating and cooling energy requirements.

The next sections describe in more detail the EAHE system, the main advantages and disadvantages during operation periods, and the thermal performance assessment by experimental, analytical and numerical methodologies.

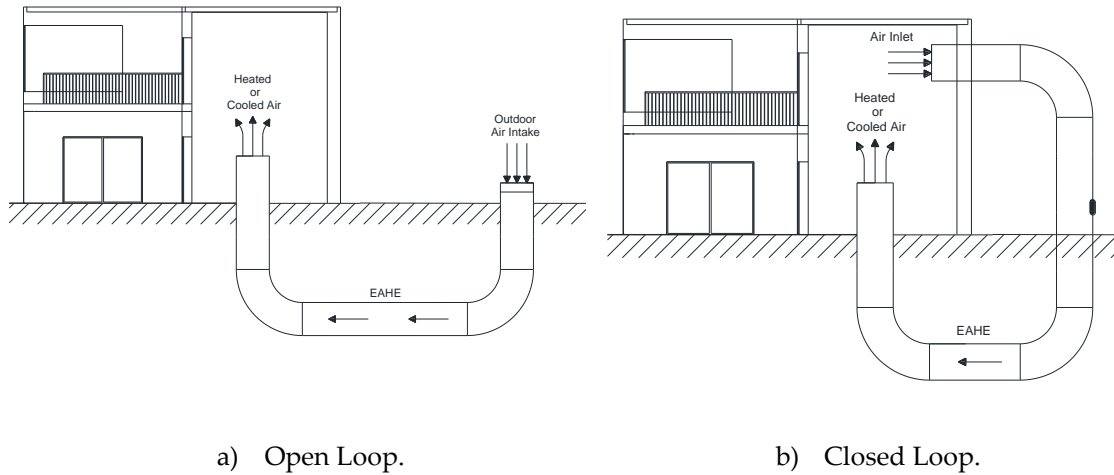


Figure IV.2 – EAHE loop configurations.

IV.2. Overview of previous scientific researches

IV.2.1. Experimental analysis

During the past years quite some experimental studies were published on this subject. Mavroyanopoulos and Kyritsis (1986) studied an EAHE with aluminium pipes installed at a depth of 2 meters in a greenhouse. They concluded that the energy consumption of the EAHE fan was only 20% of the total energy supplied and the ground temperature was sufficient to heat up and cool down the greenhouse, showing the potential of this systems. In 1993, a paper based on underground air tunnels for heating and cooling agricultural and residential buildings showed that both open and closed loop systems can operate with Coefficient of Performance (COP) as high as 12 (Goswami, 1993). The COP equation is presented later in this Chapter. Although they concluded that a smaller pipe diameter led to higher temperature drops, it also increases the required fan power. In 1994, Baxter presented a detailed performance analysis of an EAHE system. The results revealed that the ground temperature gradient on the axial direction is not homogeneous.

Hollmuller and Lachal (2001) studied the fundamental difference between winter preheating and summer cooling potential of a buried pipe system under Central European Climate. They concluded that in Central Europe stress between climate dynamics and comfort thresholds induces a fundamental asymmetry between heating and cooling potential of the ground, which can be used as a seasonal energy buffer. During winter, the EAHE system can be used for preheating, but the air conditioning (AC) systems still are fundamental for space heating. In summer, the EAHE alone is suitable for space cooling.

Bansal *et al.* (2010) studied the thermal performance of an EAHE installed in India for summer cooling and winter heating. The experimental installation comprises two horizontal cylindrical pipes with 23.42 m length and 0.15 m inner diameter buried at 2.7 m in a dry soil, one made of polyvinyl chloride (PVC) and the other of steel, connected to a common intake and outlet for airflow. They concluded that the performance of the EAHE was not affected by the pipe material and a cheaper material could be used. Also, they observed that in cooling mode the air temperature increased from 8.0 up to 12.7 °C, and the COP increased from 1.9 to 2.9, when the air velocity was increased from 2 to 5 m/s. In heating mode, they concluded that when the air velocity rises from 2 to 5 m/s, the air temperature rises from 4.1 to 4.8 °C (Bansal *et al.* 2009).

Abbaspour-fard *et al.* (2011) investigated the influence of the buried pipe depth and length, air velocity and pipe material on the performance of an EAHE installed in the north-east of Iran. They made 72 experiments in a EAHE test-system with two parallel horizontal pipes with 0.1 m diameter and 18 m length. The pipes were buried in a flat land with unsaturated soil at 2 m and 4 m depth, and they were made of PVC and galvanized mild steel, respectively. They concluded that the highest differential temperature was obtained in the galvanized pipe buried at 4 m and with lower air velocity (4 m/s). It was also observed that the pipe material had the lowest effect on the thermal performance of the EAHE. It was observed that the EAHE system had better performance during cooling mode, when the COP achieved a value of 5.5. In heating mode, the COP is lower with the value of 3.5. In the same year, Ascione *et al.* (2011) had concluded that 3.0 m is the optimum buried depth.

Woodson *et al.* (2012) presented a paper where they studied an EAHE system installed in Burkina Faso. The experimental setup comprised a horizontal open-loop PVC pipe system with 25 m length and 0.125 m diameter, buried at a 1.5 m depth. They showed that the EAHE system could cool down the outdoor air by more than 7.5 °C, for outdoor temperatures between 25 °C and 43 °C.

Mogharreb *et al.* (2014) performed experimental tests of an EAHE system that comprised a horizontal pipe with 0.1 m diameter, 18 m length and made with galvanized mild steel. The pipe was buried at 4 m depth in a flat land with unsaturated soil. It was observed that the COP of the system was higher in cooling mode (4.32) than during the heating mode (1.01). They also studied the influence of vegetation on the soil surface and they conclude that this variable has negative effects on the thermal performance of the system.

Bisoniya *et al.* (2015) performed experimental tests in a EAHE system in cooling mode with parallel pipes in India. The experimental setup had two cylindrical PVC pipe with 0.1016 m diameter and 9.114 m length. Both pipes were connected in series by elbows and a pipe of 1 m length of the same diameter, and the total pipe assembly had a 19.23 m length which was buried at 2 m depth. It was concluded that with the increase of airflow velocity, the air outlet temperature is lower during cooling season. They also concluded that EAHE system can be used effectively to reduce cooling load of buildings in hot and dry summer weather conditions, where a considerable amount of electrical energy can be saved comparing to a conventional AC system.

Several researchers studied the combination of an EAHE with other technologies, like Phase Change Materials (PCMs), HVAC systems, evaporation systems and solar systems *e.g.* Solar Photo Voltaic systems (PV). Rodrigues and Gillott (2013) presented an experimental study of an EAHE system with PCMs which uses “the space” surfaces as sources of heating and cooling the space. The combination of both technologies tries to provide cool air to discharge the PCM. They made a series of experimental tests in a space where the EAHE system and the PCMs worked together, and the space performance was compared to a reference room. They concluded that combining these two technologies could decrease temperature fluctuations in the room by up to 47 %.

Misra *et al.* (2012) investigated the thermal performance of an EAHE and an AC system with an air-cooled condenser. The experimental layout comprises a 60 m long PVC pipe of 0.10 m of inner diameter, buried at 3.7 m in a flat land with dry soil. The test procedure comprises four different arrangements/modes of the system. The first arrangement considered only the AC working. In the second one, the air condition supplied air to the room and 100% conditioned air from EAHE is also delivered. In third mode, the AC supplied the conditioned air to a room and 100% air from the EAHE is used for cooling the condenser tube of the air conditioner. In the last mode, the AC system supplied (part of the required) conditioned air to the room, while 50% conditioned air from the EAHE was directly taken into the room and the other 50% used for the AC condenser. It was found that electric energy consumption got reduced by 18% in the third mode of the EAHE combined with an AC, comparing with the first mode.

Bansal *et al.* (2012) showed that an EAHE system combined with an evaporative system could improve 69% the cooling effect in hot and dry climates. However, they

said that the replacement of AC units or heaters depends on electric tariffs and on the efficiency of the fan.

Recently, Jakhar *et al.* (2015) presented a study of the thermal performance of an EAHE system with a solar air heating duct installed in north-western India. The EAHE with the solar duct was connected to a room. The experimental test comprised a horizontal PVC pipe with 0.1 m diameter and 60 m long in a flat land with dry soil at 3.7 m depth. The system had integrated a U-shaped duct of 12.2 m length and 0.0645 m² cross-section area, made of galvanized iron. This U-shaped duct was exposed to solar radiation for solar heating only during winter. During winter, the absolute minimum outdoor temperature was close to 4 °C and the mean value was 9 °C. They concluded that, in heating mode, the heating capacity, the COP and the room temperature increased by 1217.6 – 1280.8 kWh, 4.57, and 1–3.5 °C, respectively. Also, they stated that the total cost of the installation could be reduced by reducing the total length of the buried heat exchanger/pipes. Another solution to increase the COP of these systems is using a photovoltaic system to deliver the necessary electric energy for the EAHE fan (Chel and Tiwari, 2010).

IV.2.2. Analytical and numerical modelling

Over the years, numerous analysis models of Earth-to-Air Heat Exchangers were developed for buildings' and greenhouses' applications. The models are today available for evaluating the thermal performance of EAHE systems. They can be divided into analytical and numerical methods where the thermal performance of this kind of systems can be estimated using different approaches based on (a) the specific energy supply [kWh/(m².y) and W/m²], (b) heat transfer NTU and h_{mean} , (c) temperature behaviour, and (d) energy efficiency (COP). Normally, analytical methods are more simple to use comparing with numerical methodologies. The modelling of EAHE systems can be classified as one-dimensional (1D), two-dimensional (2D) and three-dimensional (3D). 1D modellings are used to derive a relation between air inlet temperature and air outlet temperature. Usually, analytical models are 1D and more simple and quicker to use. However, analytical methods have more assumptions such as steady-state conditions, negligible gradients of soil temperature in the axial direction and of the soil thermal properties. 2D numerical models are more advanced than 1D, considering the ground temperature gradient between surface to a specific depth. 3D models using computational fluid dynamics (CFD) are costly and normally take much more time to solve. However, they are more dynamic, and allow solving problems with complex geometries. Commercial

software like ANSYS Fluent and CFX, STAR, ADINA, ABAQUS and Autodesk CFD Simulation are available and popular for EAHE design. The thermal modelling can be also evaluated in transient conditions using dynamic building simulations software like TRNSYS or EnergyPlus.

IV.2.2.1. Analytical modelling

Several analytical models were developed to predict the thermal behaviour of the EAHE. One analytical model was proposed to determine the thermal performance and the seasonal cooling potential of an underground air pipe system, assuming that the thermal properties of the ground were constant and homogeneous, and analysing the effect of length, pipe radius and airflow rate (Sodha *et al.* 1993). Bojic *et al.* (1997) presented the technical and economic evaluation of an EAHE system using numerical procedures. The problem was solved using a steady-state energy equation for soil layers for each time step. They concluded that the EAHE system could provide a portion of the daily building needs for space heating or cooling. Also, the cost of the EAHE energy is lower for summer than for winter. Based on this model, the evaluation of a EAHE system performance for space heating and cooling indicated that the system covered a portion of the daily needs of a building.

Mihalakakou *et al.* (1995) developed a new accurate parametric model to predict the thermal performance of a heat exchanger system by analysing temperature data of circulated air at the pipes' outlet. A parametric study was performed to verify the thermal performance of the EAHE system with the variation of the pipe length, pipe radius and air velocity and the depth of the buried pipes. It was found that the proposed simplified model enabled simple and accurate calculation of the outlet air temperature.

Gauthier *et al.* (1997) developed a transient three-dimensional heat transfer model based on the coupled conservation equations of energy for the soil and the circulating air, for studying the thermal behaviour of soil heat exchange-storage systems (SHESs). The model considers the non-homogeneous properties of the soil, the heat storage and heat recovery rates inside the pipes. A mathematical model, based on the representation of temperature in the form of the Fourier integral, was developed to calculate the air and soil temperature in an EAHE (Kabashnikov *et al.* 2002). The thermal behaviour of the heat exchanger was studied for different lengths and diameter of the pipes, airflow rate, spacing between pipes and pipe depth, and an analytical expression was obtained for the optimum length of the tube. De Paepe and Janssens (2003) developed a one-dimensional analytical model to analyse the

influence of the design parameters of the heat exchanger on the thermo-hydraulic performance. They used a relation to formulate a design method which can be used to determine the characteristic dimensions of the EAHE in a form that optimal thermal effectiveness is reached with acceptable pressure drop. They concluded that the thermal performance and the pressure drop increase with the pipe length, and that the thermal performance is improved for smaller pipe diameters. They also concluded that, using a higher number of parallel pipes, the pressure drop is lower, and the thermal performance increases.

Ghosal *et al.* (2004) developed a simple analytical model to evaluate the thermal performance in terms of thermal load levelling and COP of an EAHE connected to a greenhouse located in IIT Delhi, India, in a tropical climate. The experimental and model-predicted temperatures exhibited fair agreement. It was concluded that the EAHE system is more effective in winter than in summer, during a complete day.

Al-Ajmi *et al.* (2006) presented a theoretical model to predict the outlet air temperature and cooling potential of an EAHE in an arid climate. This model considered that the soil has homogenous thermal conductivity and the thermal resistance of the pipe wall was neglected. The model was validated against other available models and showed good agreement. It was concluded that the EAHE system could reduce the cooling energy demand in a typical house by 30%, over the peak summer season.

Cucumo *et al.* (2008) proposed a 1-D transient analytical model to predict the EAHE's performance at different depths for space heating and cooling. The model predicted the temperature fields of the fluid flowing in the pipe and of the ground in the proximity of the buried pipe, considering the contribution of heat from the ground surface, the overheating of the pipe walls and the latent heat exchanges (condensation) in the buried pipes. The agreement between the model and experimental data was proved very satisfactory.

Benhammou and Draoui (2015) presented a transient 1-D model used to study an EAHE for summer cooling. After the model validation against theoretical and experimental data, obtained in Ajmer (India) on an April day by other researchers (Bansal *et al.* 2010), a parametric study was done to investigate the influence of the geometrical and dynamical parameters on the thermal performance of the EAHE.

Niu *et al.* (2015) developed a 1-D steady-state control volume model that considered both sensible and latent heat transfer. This model was used to simulate the performance of an EAHE and was calibrated by comparing against experimental

data. The air temperature and relative humidity, the air velocity at the inlet of the EAHE, the pipe surface temperature, the pipe length and diameter were analysed. They concluded that the cost of using sophisticated programs for EAHE design is high and this developed tool can predict the cooling capacities, including total, sensible and latent capacity, with high accuracy.

Belatrache *et al.* (2016) presented the modelling and simulation of an EAHE in the climate conditions of south Algeria. The model was based on the energy balance when the soil temperature is constant. The equation that describes the variation in the air temperature along the pipes takes into account the outdoor temperature, the thermophysical properties of the soil, the geometry of the pipes and air velocity of the air. The analytical model was validated against experimental data from Bansal and Mishra *et al.* (2012), with 9.5% of absolute relative deviation between analytical and experimental results. For lower air velocities, the relative error reported was lower. The results for the performance and overall energy savings showed that the daily cooling capacity of the EAHE was 1.76 kWh.

IV.2.2.2. Numerical modelling

During the past years, several numerical methodologies were developed to evaluate the thermal performance of EAHE systems. The use of numerical or computation tools can predict the thermal performance of this system in transient conditions with several boundary conditions or considerations. For instance: (a) the energy transfer can be considered two-dimensional, (b) the ground temperature gradient between surface and pipes depth, (c) evaporation of water, (d) condensation and evaporation inside the pipes, (e) transient heat convection, (f) turbulent and laminar flow regimes. However, the use of these methodologies can be tricky and very complex. Several researchers presented their studies with numerical models.

Mihalakakou *et al.* (1994) presented a numerical model to calculate the performance of multiple, parallel EAHE systems. The transient, implicit numerical model was based on coupled and simultaneous transfer of heat and mass through the soil and in the pipes, and it was validated against experimental data. They concluded that the model shows a very good agreement between the observed and predicted values. The governing equations were discretized by the control-volume formulation (similar to the finite-difference methods) in TRNSYS. After model calibration, the researchers made a study of the system sensitivity to different design parameters such as pipe lengths, depths of buried pipes below the surface, distance between adjacent pipes and the pipe radius. Bojić *et al.* (1999) developed a numerical model

of the EAHE with two buried pipes. The mathematical model of the EAHE was obtained by dividing the domain of soil and pipes into elementary volumes, using steady-state energy equations, and applying a time-marching method. They showed how the season, the soil thermal conductivity and the pipe spacing influence the energy transfer from the ground to the EAHE.

Hollmuller and Lachal (2001) developed an explicit numerical model which considers the latent and sensible heat exchanges, as well as the frictional losses, water infiltration and flow along the pipes. This allows the control of the airflow direction as well as for flexible geometry. After the algorithms' development, the model can be used and adapted to TRNSYS (dynamic systems' simulation software). The validation was performed against analytical solutions and experimental data from their monitored systems.

A numerical model to predict the energy conservation potential of an EAHE was developed by Kumar *et al.* (2003). This model considers the ground temperature gradient, surface conditions, moisture content and other design aspects of the EAHE. The model was based on the heat and mass transfer in the pipes and was developed within the scope of numerical techniques of finite-difference and FFT (Matlab). The numerical model was validated against experimental data with an error range around 1.6 % and used to predict the air outlet temperature for different parameters, such as humidity, airflow rate and ambient temperature.

Pfafferott (2003) presented the study of the performance of three EAHE systems for mid-European office buildings in service. The temperature of the soil surrounding the pipes was considered as a design input parameter. The time variation curves for inlet and outlet air temperatures and for the ground temperature were analysed using a regression function of the mean temperature, a temperature amplitude and a phase shift. The outlet air temperature is calculated knowing the ground temperature, the inlet air temperature and estimating the number of transfer units (NTU). It was concluded that thermal recovery of the soil was adequate to retain the performance level.

Badescu (2007) developed a model based on a numerical transient 2-D approach that allowed to compute the ground temperature at the surface and at various depths. The ground was divided into several sections perpendicular to the pipes. For each section, the heat equation was solved with the control-volume formulation method and the interaction between sections was done with the energy balance for the pipe.

Thiers and Peuportier (2008) presented a study of the thermal performance of a passive building equipped with an EAHE system installed in France. The researchers modelled the building using the software COMFIE for dynamic building simulation. However, in order to take into account the EAHE system that includes a heat recovery unit, they developed algorithms able to simulate the ground and EAHE thermal behaviours. Tittlein *et al.* (2009) developed a numerical model where the heat flux entering the pipe was expressed as a function of the temperature of the air crossing the pipe and the external solicitations. The model was based on the response factors method that reduces the physical problems and was validated against two other models.

Gan (2014) developed a computer program for simulating the thermal performance of an EAHE for preheating and precooling of ventilation supply air, considering the dynamic variation of climatic, load and soil conditions. The program solves equations for coupled heat and moisture transfer in the soil, with boundary conditions for convection, radiation and evaporation/condensation that change with the climatic conditions and the heat exchanger. The computer program can be used for assessing the effect of several parameters of the EAHE. The program can also be used for predicting the dynamic thermal performance of hygroscopic building elements as well GCHE with heat pump systems and heat recovery units.

Xamán *et al.* (2015) investigated the numerical simulations of pseudo thermal behaviour of an EAHE for three cities in Mexico. They developed a code based on finite-volume methods and carried out several hourly simulations for different Reynolds number through one day. The model considered boundary conditions such as surface radiation, long wave radiation and solar radiation absorbed on the ground surface, environment air temperature, heat convection on the surface and inside the pipes, and the latent heat flux from the ground surface due to evaporation. They considered that the ground temperature was constant at a 10 m depth, and the left and right boundaries of the domain were assumed as adiabatic. The inlet air temperature is the environment air temperature and the values of the outlet air temperature are obtained after the simulation.

Khabbaz *et al.* (2016) present an experimental and numerical study of an EAHE system for cooling, installed in a residential building in Morocco. The numerical study was carried out with TYPE 460 of the TRNSYS software, and a finite-element model was developed. The model combined the sensible and latent heat transfer with transient 3-D thermal diffusion in the soil. The simulation was made for two consecutive years, the first of which serves only for thermal conditioning of the soil,

in relation with environment air fluctuations. They conclude that a good agreement was found between TRNSYS simulations and experimental data.

Three-dimensional finite-volume CFD simulation tools have also been used to evaluate the thermal performance of EAHE systems. Zhang and Haghighat (2009) investigated the thermal behaviour of air flowing in horizontal buried ducts using a finite-volume method (Ansys Fluent 6.2). The main objective was the employment of the stored soil thermal capacity to decrease the temperature variations of the external outdoor air. The numerical results were compared with those from the literature.

Vaz *et al.* (2011) presented their experimental and numerical study of an EAHE installed in Brazil. The experimental results were used to validate a CFD model (Ansys Fluent) of the heat exchanger using numerical solutions of the conservation equations. The researchers compared the numerical and experimental results of air temperature inside the pipes, and the maximum difference was less than 15%. With this numerical model, it was possible to visualise the behaviour of the thermal field along the ground, especially near the pipes, where the ground temperature is affected. They also concluded that the use of CFD models is better to understand the physical phenomena involved.

Misra *et al.* (2013) studied the thermal performance of an EAHE under transient conditions, using CFD (Ansys Fluent) and experimental data. The main objective of the study was to evaluate the effect of time duration of continuous operation, thermal conductivity of the soil, pipe diameter and air flow rate. The CFD model takes into account the transient temperature field around the horizontal pipe, the heat transfer and airflow turbulence.

Mathur *et al.* (2015) investigated the thermal performance of an EAHE for three operation modes, using a three-dimensional transient CFD model (Ansys). The first operation mode consists of the EAHE working continuously for 12 h, and in second and third modes, the EAHE operates intermittently. They assumed that the thermophysical properties of solids and fluids are constant over the soil and air temperature ranges, and that the inlet air velocity was constant. They concluded that CFD model shows a good agreement with experimental data.

Rodrigues *et al.* (2015) performed a numerical investigation on different geometrical configurations of an EAHE using Constructal Design to obtain the highest thermal potential. The numerical simulations were performed using Ansys Fluent. They concluded that for the same area occupied by the pipes and a fixed airflow rate, the

increase of the number of pipes can improve the EAHE thermal performance by 73% for cooling and 115% for heating. Serageldin *et al.* (2016) developed a mathematic model based on unsteady, one-dimensional and quasi-steady state energy conservation equations. Additionally, an explicit finite-difference numerical method was used to solve the mathematical problem using MATLAB. The researchers also developed a three-dimensional CFD model in Ansys Fluent to predict the air and soil temperatures. They achieved a good agreement between experimental, numerical and CFD models with an average error and correlation coefficient of 2.09, 97% and 3.3 and 95.5%, for CFD simulation and mathematical model, respectively. The CFD model was used to perform a parametric research to study the influence of different parameters, such as pipe diameter, pipe material, pipe space, pipe length and air velocity.

IV.2.3. Guidance overview

Based on the main conclusions of the published research (listed below in Table IV.1), the following subsections summarize some relevant considerations for EAHE design. They are mainly addressed to dynamical and geometrical design parameters that have influence on the overall thermal performance of an EAHE. The control mode of an EAHE system is not included in these considerations, because it depends on the building operation, climate, soil characteristics and EAHE performance. However, during this research thesis, experimental and analytical approaches were used to verify the influence of the EAHE control based on set-points of air temperature and CO₂ concentration.

IV.2.3.1. Geometric parameters

Benhammou and Draoui (2015) and Niu *et al.* (2015) concluded that the difference between inlet and outlet air temperature in the EAHE is smaller when the pipe diameter is increased. This happens because, for given airflow rate and pipes' length and number, the convective heat transfer coefficient decreases, leading to lower outlet air temperature (in heating mode) and lower COP. Typical diameters are 0.1 to 0.3 meters, but it always depends on the energy needs (*e.g.* a commercial building has larger energy needs).

Benhammou and Draoui (2015) concluded that, when the pipe length increases, the temperature difference between inlet and outlet air increases. Niu *et al.* (2015) also made a parametric study and they concluded that, above a 50 m length, the COP decreases due to increase of the system pressure drop. The use of a parallel configuration is the best solution for higher energy needs, using higher number of

pipes (Bojic *et al.* 1997) and total length of the circuit. However, the optimum value depends on the airflow rate, soil and climatic conditions. Kabashnikov *et al.* (2002) studied the decrease in energy efficiency of the heat exchanger with decrease in the space between tubes. They concluded that it is possible to ignore the thermal interactions of the pipes and the influence of the ground-atmosphere interface, for spacing distances of 1 – 2 meters.

IV.2.3.2. Physical and thermal parameters

Ground temperature depends on the thermophysical properties of the ground and on the climatic conditions aboveground. Researchers concluded that underground temperature fluctuations are lower between 2 m (Kusuda and Achenbach 1965) and 4 meters depths (Khatry *et al.* (1978). Abbaspour-fard *et al.* (2011) concluded that, for a 4 m depth, the outlet air temperature has a higher temperature differential. However, Badescu (2007) says that, at a 2 m depth, there is a good compromise between small annual temperature fluctuations and excavation costs. Ascione *et al.* (2011) concluded that 3.0 m is the optimum burying depth. Taking into consideration the researchers, the optimum depth for these systems is between 2 to 4 meters, depending on the soil thermal properties and environment conditions.

The ground surface is also important. Mogharreb *et al.* (2014) concluded that the presence of vegetation on the soil surface has negative effects on the thermal performance of these systems. Also, Mihalakakou *et al.* (1997) concluded that a bare soil surface can increase the system's heating capacity comparing to a short-grass-covered soil. Ascione *et al.* (2011) studied the influence of the climate and of the soil composition. They concluded that the best energy performances were obtained for wet and heavy soil and cold winter climates, for a 3 m depth EAHE system. However, taking into account the material surrounding the buried pipes, a good contact between soil and pipes must be ensured by using clay or sand. They also concluded that the high water content of some soil typologies improves the EAHE performance.

The coefficient of performance and temperature differential drops when the air velocity increases (Benhammou and Draoui, 2015). Niu *et al.* (2015) conclude that for smaller air velocities the outlet air temperature is lower during cooling mode. The pipe material has a small influence on the overall thermal performance of EAHE systems. Bansal *et al.* (2010) and Hossein *et al.* (2011) concluded that the EAHE thermal performance was not affected by the pipe material and a cheaper pipe can be used.

Table IV.1 – Summary of researcher's achievements in experimental, analytical and numerical analysis for EAHE systems, according with the main design parameter focused (1st column).

EAHE Parameter	Authors	Methodology	Description	Major Achievement
Ground	(Kusuda and Achenbach, 1965)	Analytical / Numerical	Development of a methodology to predict the ground temperature with depth	Underground temperature fluctuations are lower from 2 to 4 m depth
	(Mogharreb <i>et al.</i> 2014)	Experimental	Influence of the ground surface and pipe materials	Vegetation on the ground surface has negative effects on the EAHE thermal performance
	(Mihalakakou <i>et al.</i> 1997)	Numerical	Development of a model to predict the daily and annual variation of ground surface temperature	Bare soil surface can increase the system's heating capacity
	(Ascione <i>et al.</i> 2011)	Dynamical / Numerical	Influence of the climate and soil composition on the EAHE thermal performance	Best performance was obtained for wet and heavy soil composition. It is important that the contact between soil and pipes should be "perfect"
Air velocity	(Benhammou and Draoui, 2015)	Analytical	Parametric study of an EAHE system	For smaller air velocities, the outlet air temperature is lower during cooling, The COP decreases with the increase of air velocity
Pipe length	(Benhammou and Draoui, 2015)	Analytical	-	When the pipe length increases, the temperature differential between inlet and outlet air increases
	(Niu <i>et al.</i> 2015)	Analytical	-	After 50 m length, the COP decreases due to increase system pressure drop
Pipe Diameter	(Benhammou and Draoui, 2015; and Niu <i>et al.</i> 2015)	Analytical	Both studies present parametric studies of EAEH thermal performance	The differential between inlet and outlet air temperature is smaller when the pipe diameter is increased.
Pipe Disposal	(Bojic <i>et al.</i> 1997)	Numerical	Technical and economic evaluation of an EAHE system using numerical procedures	Parallel configuration is the best solution for higher energy needs, using higher number of pipes and total length of the circuit.

CHAPTER IV

Earth-to-air heat exchangers overview and a simple design approach based on ϵ -NTU method

EAHE Parameter	Authors	Methodology	Description	Major Achievement
Pipe spacing	(Kabashnikov <i>et al.</i> 2002)		Studied the decrease in energy efficiency of the heat exchanger with decrease in the space between tubes	Spacing distances of 1 – 2 meters
Pipe Material	(Bansal <i>et al.</i> 2010)	Experimental	Thermal performance of an EAHE for summer cooling and winter heating installed in India	Pipe material has negligible influence on the EAHE thermal performance

IV.3. Ground temperature – Analytical Approach

Ground temperature is one of the most important parameters that affects heat transfer in EAHE systems. The evaluation of the soil temperature in depth is essential to calculate the EAHE cooling and heating potential. The ground temperature varies with latitude, weather conditions, time of the year, altitude, landscape, shading, surrounding buildings, ground surface conditions and soil properties. The best approach to achieve exact values of the ground temperature is direct measurement *in-situ*. However, it is not always possible to measure this parameter for different depths, and only a few weather stations provide measured data of ground surface temperature. Therefore, analytical and numerical methodologies were developed to predict ground temperature with depth. In 1965, Kusuda and Achenbach presented a study of ground temperature. They analysed data from 63 stations located in fifty different areas in the United States. They developed a simple heat conduction methodology based upon the simple harmonic representation of the ground temperature variation. The results showed acceptable approximation of the monthly averaged ground temperature at different depths. Equation (29) represents the developed model where the thermal diffusivities must be computed using information from the ground thermal properties. This equation can be found in several commercial softwares (*e.g.* EnergyPlus) and in the ASHRAE handbook for HVAC systems and equipment.

$$T(z, t_d) = T_m - B_s \times \exp \left[-z \left(\frac{\pi}{365 \alpha_s} \right)^{1/2} \right] \cos \left[\left(\frac{2\pi}{365} \right) \left(t_d - t_0 - \frac{z}{2} \left(\frac{365}{\pi \alpha_s} \right)^{1/2} \right) \right] \quad (29)$$

where T_m represents the average soil temperature [$^{\circ}\text{C}$], B_s the amplitude of the soil surface temperature variation [$^{\circ}\text{C}$], z the ground depth [m], t_d the current day, t_0 the day with lower annual environment temperature, and α_s represents the thermal diffusivity of the ground [m^2/day]. Figure IV.3 a) plots a comparison between experimental data obtained in Coimbra (PT) and analytical values using the Kusuda and Achenbach equation, for 1.05 m and 1.9 m depths in a sandy/clayey soil. This soil has a thermal conductivity of $1.5 \text{ W}/(\text{m}\cdot^{\circ}\text{C})$, density of $2700 \text{ kg}/\text{m}^3$ and thermal diffusivity of $0.034 \text{ m}^2/\text{day}$ (VDI 4640). The data was measured in 2014, where the average temperature amplitude was around 9.7°C . Analytical values have a good agreement with experimental data. Figure IV.3 b) shows the underground temperature distribution with depth using Equation (29). It can be seen that the ground temperature is constant for depths above 10 m.

Kusuda and Achenbach (1965) also present some recommendation guides about underground soil temperature: (a) ground temperature sites should be close to a local weather station; (b) surface should be bared or covered with short grass; (c) soil thermal properties should be determined; (d) the temperature at 3ft depth (0.9 meters) should be observed; (e) underground temperatures should be measured at least for three years; (f) temperature should be observed at five or more different depths. Kusuda and Achenbach (1965) still is one of the most cited references. However, other studies have been conducted over the years. Khatry *et al.* (1978) presented an analysis of the periodic variation of ground temperature with depth, based on an energy balance at surface that considers the periodicity of solar radiation and atmospheric temperature.

The equation for the temperature as a function of time and depth was used to investigate the daily and annual variations for Kuwait. Bharadwaj and Bansal (1981) presented an analysis for the calculation of the daily and annual variations of the ground temperature distribution for various surface conditions. They concluded that the temperature becomes constant at a depth of about 0.15 m for daily variations, while the annual variations become negligible at a depth of 4 m. Mihalakakou *et al.* (1997) also presented a model to predict the daily and annual variation of the ground surface temperature. It is based on the transient heat conduction differential where the energy balance equation at the ground surface is used as boundary condition. This energy balance considers the latent heat flux due to evaporation at the ground surface, long wave radiation, convective heat transfer between the air and the ground surface, and the radiation absorbed on the surface. The model was validated against measured data and it was used in an investigation of the ground temperature

CHAPTER IV

Earth-to-air heat exchangers overview and a simple design approach based on ϵ -NTU method

sensitivity to different energy balance factors. All these previous studies were the base of new advanced numerical algorithms implemented in commercial softwares.

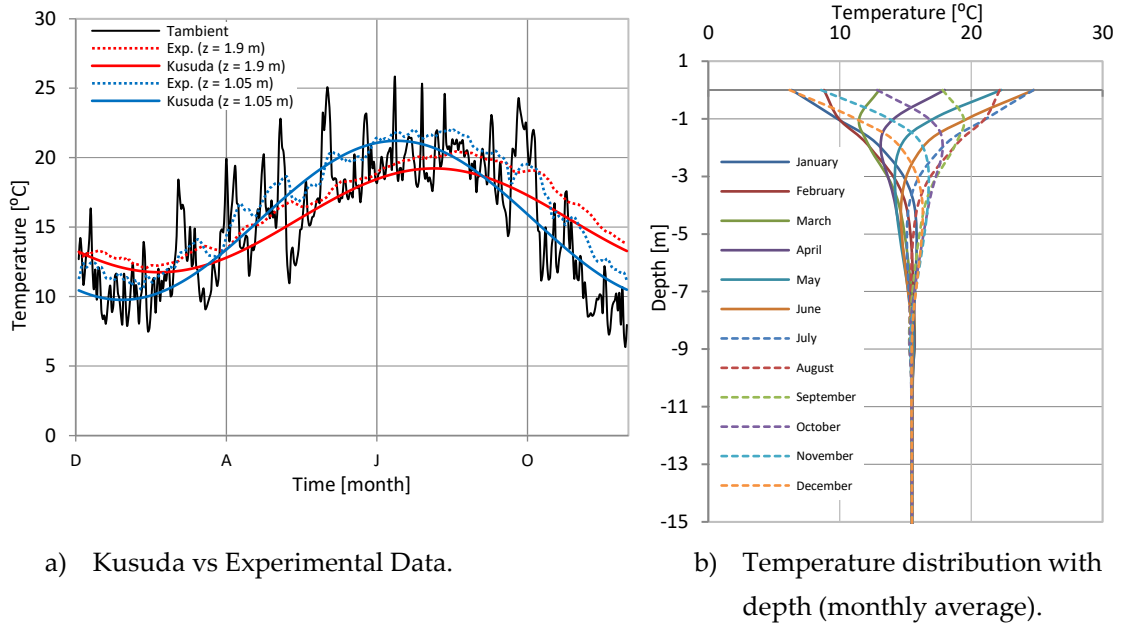


Figure IV.3 – Underground soil temperature in Coimbra (PT) for 2014.

IV.4. Heat transfer in heat exchangers the ϵ -NTU approach

The heat transfer in an air-ground heat exchanger considers the heat convection between the fluid and the pipes' inner surface, and the heat conduction through the pipe walls and the ground. In the analysis of heat exchangers, it is appropriate to use an overall heat transfer coefficient U_i that accounts for the influence of all these effects on the heat transfer rate. U_i [$W/(m^2 \cdot ^\circ C)$] is obtained using the following expression:

$$U_i A_i = \frac{1}{\sum_j R_j} \quad (30)$$

where A_i is the total internal surface area of pipes [m^2] and R_j are the elemental thermal resistances [$(m^2 \cdot ^\circ C)/W$]. There are three thermal resistances to be considered in earth-to-air heat exchangers (Figure IV.4 b). The first one (R_1) is the convective thermal resistance associated with the internal airflow, the second (R_2) represents the thermal resistance to heat conduction through the pipe walls, and finally the thermal resistance of the ground (R_3). These thermal resistances are given by the following expressions:

$$R_1 = \frac{1}{A_i h_i} \quad R_2 = \frac{\ln\left(\frac{r_2}{r_1}\right)}{2\pi L k_{pipe}} \quad R_3 = \frac{\ln\left(\frac{r_3}{r_2}\right)}{2\pi L k_{ground}} \quad (31)$$

where r_1 and r_2 are the internal and external pipe radius [m], r_3 is the radius of the thermally affected zone of the ground around each pipe, and L represents the heat exchanger total length [m]. k_{pipe} and k_{ground} represent the thermal conductivity [W/(m.°C)] of the pipes' wall material and of the ground, respectively. The heat convection coefficient h_i [W/(m².°C)] for a forced flow inside the pipe is obtained by:

$$h_i = \text{Nu} \frac{k_{fluid}}{d_i} \quad (32)$$

where d_i and k_{fluid} represent the internal pipe diameter [m] and the thermal conductivity of the fluid [W/(m.°C)], respectively. The Nusselt number (Nu) can be estimated using appropriate empirical correlations. For turbulent internal flows, the Gnielinski correlation is commonly used, having a wide validity range of values (Çengel, (2009)):

$$\text{Nu} = \frac{(f/8)(\text{Re}_d - 1000)\text{Pr}}{1 + 12.7(f/8)^{1/2}(\text{Pr}^{2/3} - 1)} \quad (33)$$

where Pr and Re_d are the Prandtl and Reynolds numbers, and f is the Darcy friction factor. These values can be obtained by the expressions (with the validity ranges of Re_d and Pr values for Eq. (33)):

$$f = [0.79 \ln(\text{Re}_d) - 1.64]^{-2} \quad 3000 \leq \text{Re}_d = \frac{v d_i}{\nu} \leq 5 \times 10^6 \quad 0.5 < \text{Pr} = \frac{\nu}{\alpha} \leq 2000 \quad (34)$$

where ν , α and v represent the fluid velocity [m/s], thermal diffusivity [m²/s] and kinematic viscosity [Pa.s]. The Nusselt number for turbulent flow could also be approached using the simpler Dittus-Boelter correlation:

$$\text{Nu} = 0.023 \text{Re}_d^{4/5} \text{Pr}^n \quad \begin{array}{ll} n = 0.4 \text{ (heating)} & \text{Re}_d \geq 10000 \\ \text{or } n = 0.3 \text{ (cooling)} & 0.6 \leq \text{Pr} \leq 160 \end{array} \quad (35)$$

which however is not so accurate and is valid only for fully turbulent flow regimes.

In Equations (32) to (35), all thermophysical properties of the fluid should be evaluated at an average temperature between inlet and outlet.

Having estimated the overall heat transfer coefficient U_i , the heat transfer rate of the heat exchanger could be calculated using the method of the *logarithmic mean temperature difference* (LMTD), Çengel, (2009):

$$\dot{Q} = U_i A_i \Delta T_{ml} \quad (36.a)$$

$$\Delta T_{ml} = \frac{\Delta T_1 - \Delta T_2}{\ln\left(\frac{\Delta T_1}{\Delta T_2}\right)} \quad (36.b)$$

where $A_i = \pi d_i L$ is the total internal surface area of pipe, ΔT_{ml} is the LMTD, $\Delta T_1 = T_s - T_{a, in}$ is the temperature difference between the soil and the inlet air, and $\Delta T_2 = T_s - T_{a, out}$ is the temperature difference between the soil and the outlet air. The problem with this method is that it is more appropriate for dimensioning a heat exchanger. When the goal is the analysis of its thermal performance, both \dot{Q} and $T_{a, out}$ are unknown *a priori* and an iterative procedure is required. Alternatively, the effectiveness-NTU (Number of Transfer Units) can be used. In this method, the effectiveness ϵ is defined as the ratio between the heat transfer rate in the heat exchanger (\dot{Q}) and the maximum possible heat transfer rate (\dot{Q}_{max}):

$$\epsilon = \frac{\dot{Q}}{\dot{Q}_{max}} \quad (37)$$

while the Number of Transfer Units is defined as:

$$NTU = \frac{U_i A_i}{\dot{m}_a c_{p,a}} \quad (38)$$

where \dot{m}_a [kg/s] is the mass airflow rate and $c_{p,a}$ [J/(kg.°C)] is the air specific heat, estimated at an average temperature between inlet and outlet. Note that, for a network of parallel pipes (in similar conditions), A_i and \dot{m}_a should represent the total inner surface area and mass airflow rate of the whole set.

The heat transfer rate by convection to the air flowing inside the pipes, expressed by Equation (36.a), is equal to the rate of change of the air internal energy between inlet and outlet, given by:

$$\dot{Q} = C_a (T_{a,out} - T_{a,in}) \quad (39)$$

where $C_a = \dot{m}_a c_{p,a}$ is the so-called the *heat capacity rate* [W/°C] of the airflow rate.

As for the maximum heat transfer rate (\dot{Q}_{\max}), it is defined as the product of the minimum heat capacity rate, C_{\min} , by the maximum temperature difference occurring in the heat exchanger, which, in a EAHE, is that between the soil and the inlet air:

$$\dot{Q}_{\max} = C_{\min} (T_s - T_{a,in}) \quad (40)$$

In the case of a common heat exchanger – a device operating the heat transfer between two different fluid flows –, the particular ε -NTU relation depends on the geometric configurations of the heat exchanger itself and of the fluid flows, as well as on the *capacity ratio* C_r , defined by:

$$C_r = \frac{C_{\min}}{C_{\max}} \quad (41)$$

In the present case of a EAHE, there is no second fluid flow: the airflow exchanges heat with the soil, whose heat capacity is comparatively infinite (its temperature variations at a daily scale are negligible when compared with those of the internally flowing air, and of the ambient air itself). Therefore, $C_{\max} \rightarrow \infty$, $C_{\min} = C_a$, and $C_r = 0$. The effectiveness can then be given just by:

$$\varepsilon = \frac{T_{a,out} - T_{a,in}}{T_s - T_{a,in}} \quad (42)$$

and the ε -NTU relation is [Çengel (2009)]:

$$\varepsilon = 1 - e^{-NTU} \quad (43)$$

Thus, for a given EAHE configuration and knowing the airflow rate (and, thus, the NTU value), this method allows finding directly the effective heat rate \dot{Q} , on an instantaneous or steady-state basis (through Eq. (37)), and likewise the estimation of $T_{a,out}$ using Equations (39) or (42).

Anyway, whichever method is used – LMTD or ε -NTU –, an expression can be derived to directly calculate the outlet air temperature, after knowing the U_i value in a given/installed EAHE. The rationale is based on a heat rate balance applied to a differential length of a pipe, which, after integration to the whole pipes' length (or surface area), would give rise to Equations (36.a) and (36.b).

CHAPTER IV

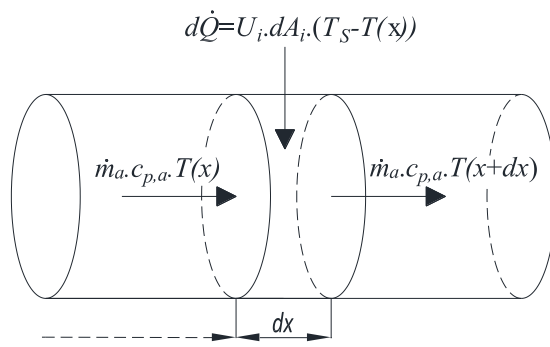
Earth-to-air heat exchangers overview and a simple design approach based on ϵ -NTU method

Considering a differential control volume of length dx and located at a distance x from the pipe inlet, where the bulk air temperature is $T(x)$, the energy balance is written as:

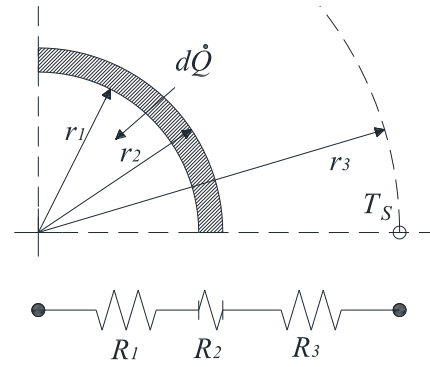
$$\dot{m}_a c_{p,a} T(x) + U_i dA_i (T_S - T(x)) = \dot{m}_a c_{p,a} T(x + dx) \quad (44.a)$$

where $dA_i = \pi d_i dx$. This balance equation can be rearranged into:

$$\dot{m}_a c_{p,a} dT = U_i \pi d_i (T_S - T(x)) dx \quad (44.b)$$



a) Heat balance in a differential control volume.



b) Thermal network.

Figure IV.4 – Differential heat balance and thermal resistance network in a heat exchanger pipe.

and integrated over the whole pipes' length L :

$$\int_{T_{a,in}}^{T_{a,out}} \frac{1}{T_S - T(x)} dT = \frac{U_i \pi d_i}{\dot{m}_a c_{p,a}} \int_0^L dx \quad (45.a)$$

$$\left[\ln(T_S - T(x)) \right]_{T_{a,in}}^{T_{a,out}} = - \frac{U_i \pi d_i}{\dot{m}_a c_{p,a}} [x]_0^L \quad (45.b)$$

$$\frac{T_S - T_{a,out}}{T_S - T_{a,in}} = e^{-\frac{U_i A_i}{\dot{m}_a c_{p,a}}} \quad (45.c)$$

Finally, by solving Equation ((45.a)c) for $T_{a, out}$, the outlet air temperature can be calculated by:

$$T_{a,out} = T_s - (T_s - T_{a,in}) \cdot e^{-NTU} \quad (46)$$

Equation (46) is the basis for the *analytical model* used to evaluate the thermal performance evaluation of the installed EAHE, as described later in section IV.5. Since it derives from a steady-state energy balance, the transient behaviour of the EAHE is simulated as a sequence of steady-state energy balances (valid for every one-hour period), and the boundary conditions (T_s and $T_{a,in}$ in Equation (42)) are updated at the beginning of every time step. Further assumptions are involved in both the LMTD and ε -NTU methods: (a) the airflow inside the pipes is dynamically and thermally developed, (b) the soil surrounding the pipes is homogenous with constant thermal properties and (c) the soil temperature gradients are neglected in the axial direction.

IV.5. EAHE design and energy performance

The design of an EAHE is based on the ventilation requirements. For a given airflow rate, it is important to choose the internal pipe diameter, d_i , to ensure a turbulent flow regime and thus enhance the convection heat rate. In this phase, it is important to choose between a series or a parallel pipe arrangement considering the mass airflow rate and the available land area. Likewise, it is important to ensure a significant value for the EAHE NTU, which should lie in the range of 1.5 to 3. In a parallel pipe arrangement, the total pipe length of heat exchanger for a specific pipe diameter is then calculated by:

$$L = \frac{-NTU \dot{m}_a c_{p,a}}{\pi d_i U_i} \times n_p \quad (47)$$

where n_p represents the total number of pipes. This process leads to an interactive calculation to achieve the best design consisting of a suitable combination of number of pipes, pipe length and diameter.

The energy performance of an EAHE system can be influenced by several physical and dynamical parameters, which include the heat exchanger design, the circulating fan and the ground thermal properties. The energy performance of such systems can be evaluated in terms of a *coefficient of performance* (COP) estimated by the flowing equation (Benhammou and Draoui, 2015):

CHAPTER IV

Earth-to-air heat exchangers overview and a simple design approach based on ϵ -NTU method

$$\text{COP} = \frac{\dot{m}_a C_{p,a} \left[\int_0^t (T_{a,in} - T_{a,out}) dt \right]}{\frac{\Delta p \dot{V}}{\eta_{fan}} \Delta t} \quad (48)$$

where, η_{fan} refers to the fan electric efficiency, [%], \dot{V} is the volume airflow rate [m^3/h] and Δp the pressure drop in the system [Pa]. The denominator of the equation represents the electric energy consumed (W) by the fan [in Wh].

The upper term of Equation (48) represents the heating or cooling sensible heat (Q), expressed in Wh, during a finite period Δt (e.g., one hour) and can be estimated as:

$$Q_h = \dot{m}_a C_{p,a} (T_{a,in} - T_{a,out}) \Delta t \quad (49)$$

$$Q_c = \dot{m}_a C_{p,a} (T_{a,out} - T_{a,in}) \Delta t \quad (50)$$

A COP greater than 1 indicates that the thermal energy obtained through the EAHE is greater than the electric energy used for its operation, for a given Δt . When the COP is lower than 1, it means that energy is being wasted. In such occasions, it is preferable to switch off the ventilation system for pre-heating and cooling proposals. However, based on the measured outdoor temperature (e.g. in heating mode, when the outdoor temperature is higher than the ground temperature), a by-pass can be added to the circuit and the indoor air quality in the building can be better than just by natural ventilation. It can be seen from Equations (49) and (50) that, for the correct system design, the ground temperature and climatic parameters should be well known, in order to predict the overall performance of the system. However, in both equations the outlet air temperature should converge as possible to the ground temperature, in which case the heat exchanger would have the maximum efficiency. The mean efficiency can be calculated by the following equation (Benhammou and Draoui, 2015):

$$\eta_{mean} = \frac{\left[\int_0^t (T_{a,in} - T_{a,out}) dt \right]}{\left[\int_0^t (T_{a,in} - T_{soil}) dt \right]} \quad (51)$$

Based on the electrical power consumed by the fan (W , in kW) and the thermal rate for heating or cooling, the energy balance (EB, in kWh) and the equivalent power (EP) can be calculated using the flowing equations:

$$EB = \sum (\dot{Q} - \dot{W}) \cdot 1h / 1000 \quad (52)$$

$$EP = \frac{\sum (\dot{Q} - \dot{W}) \cdot 1h / 1000}{\Delta t} \quad (53)$$

IV.6. Final remarks

This chapter of the thesis presents a literature overview of EAHEs, an analytical approach to calculate the soil temperature and a steady-state one-dimensional analytical model based on the effectiveness-number of transfer unit's (ϵ -NTU) which can be used for system design. The thermal properties of a sandy and clayey soil were investigated using an analytical formula and compared against measured values. These properties are used in later analytical and numerical studies. A guidance overview was presented based on the main conclusions of the published research. The control mode of an EAHE is not included in these considerations, because it depends on the building operation, climate, soil typology and EAHE performance. Chapter V addresses the control mode of an EAHE pilot installation located in Coimbra (Portugal). The analytical model presented in this chapter and the CFD model developed in Chapter VI is used to investigate the influence of geometrical, physical and thermal parameters.

CHAPTER V

Modelling and performance analysis of an earth-to-air heat exchanger pilot installation in Csb climate

V.1. Introduction

Earth-to-air heat exchangers (EAHE's) are sustainable and efficient systems suitable for space heating and cooling in buildings, and they can be alternative or complementary to conventional air conditioning systems. In this chapter, the performance of an EAHE installed in an LSF single-family residential building located in Coimbra (Portugal) is assessed. The thermal performance of this pilot installation is analysed along the four seasons of a year and the influence of the EAHE operation control is assessed. An analytical model developed in Chapter IV to predict the thermal performance of the EAHE is validated against data obtained from the *in-situ* monitoring system for both cooling and heating operation periods. The proposed model is used to estimate the air temperature at the outlet of the heat exchanger and a parametric study is conducted to assess how the overall thermal performance of the system is influenced by different variables, namely: pipe length and diameter, air velocity, pipe wall material and type of soil. It is concluded that the difference between outlet and inlet air temperature rises with the increasing of the pipe length and ground thermal conductivity, and with the decrease of pipe diameter and air velocity. However, due to the pressure drop inside the pipes, the thermal performance of the system, evaluated in terms of a coefficient of performance (COP), decreases when the pipe length, pipe diameter and the air velocity are increased. Due to the low thermal resistance of the pipe wall, it is also observed that the pipe material has a small influence on the system energy performance. The most relevant parameter is the air velocity, given its influence on the convection heat rate and on the head loss of the airflow.

V.2. Experimental approach

The pilot Earth-to-Air Heat Exchanger (EAHE) system was installed next to a single-family residential building, located in the city of Coimbra, which is currently used as an office by a local company, Cool Haven. According with Köppen Geiger climate classification, the city of Coimbra is located in Csb climatic region (Kottek *et al.* 2006). This climatic region is characterized by a tempered climate with rainy winter and slightly hot, dry summer (Santos *et al.* 2011). The building is constructed with light steel framing modular-construction methods, as projected by Cool Haven company. The installation was executed on a sandy and clayey soil. The groundwater level is deep enough not to interfere with the system's thermal behaviour. Figure IV.1 illustrates the burying operation of the parallel pipes during the construction works of this EAHE and sketches the most relevant dimensions. Outdoor air is taken into the EAHE system through an inlet "tower" b) provided with a gross particle filter (F5filter, according with EN779:2012).

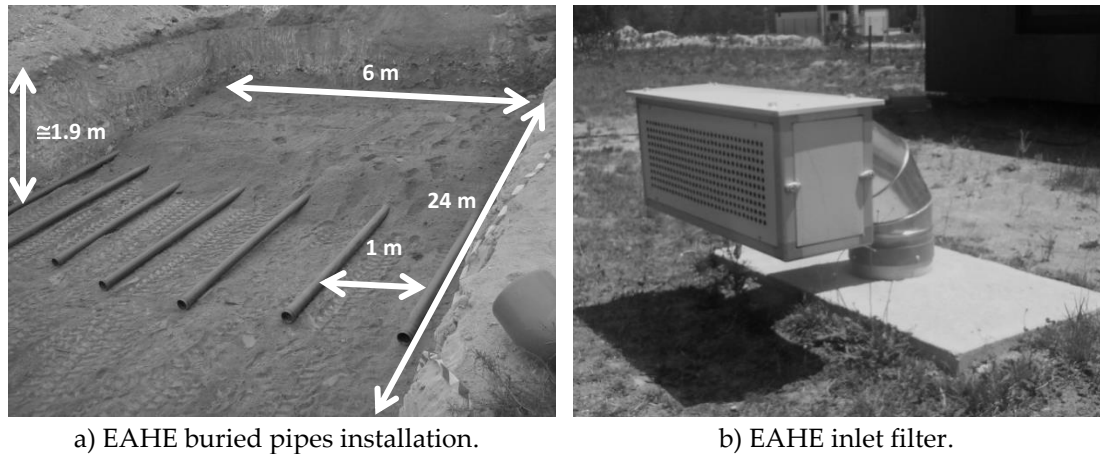


Figure V.1 – EAHE buried pipes and inlet filter.

The PVC pipes were arranged in a parallel configuration, as represented in Figure V.2. Before entering the building, the ventilation air passes through a heat recovery system, located in point O of Figure V.2. which is activated during the winter months. The mechanical ventilation heat-recovery system unit consists of a horizontal *Power Box 60* with double entry and direct coupling fan and static heat exchanger crossed flows. To enable the drainage of condensate and/or infiltrated water, the pipes where placed with a 2% minimum inclination towards a drainage ditch (D), as illustrated in Figure V.2.

CHAPTER V

Modelling and performance analysis of an earth-to-air heat exchanger pilot installation in Csb climate

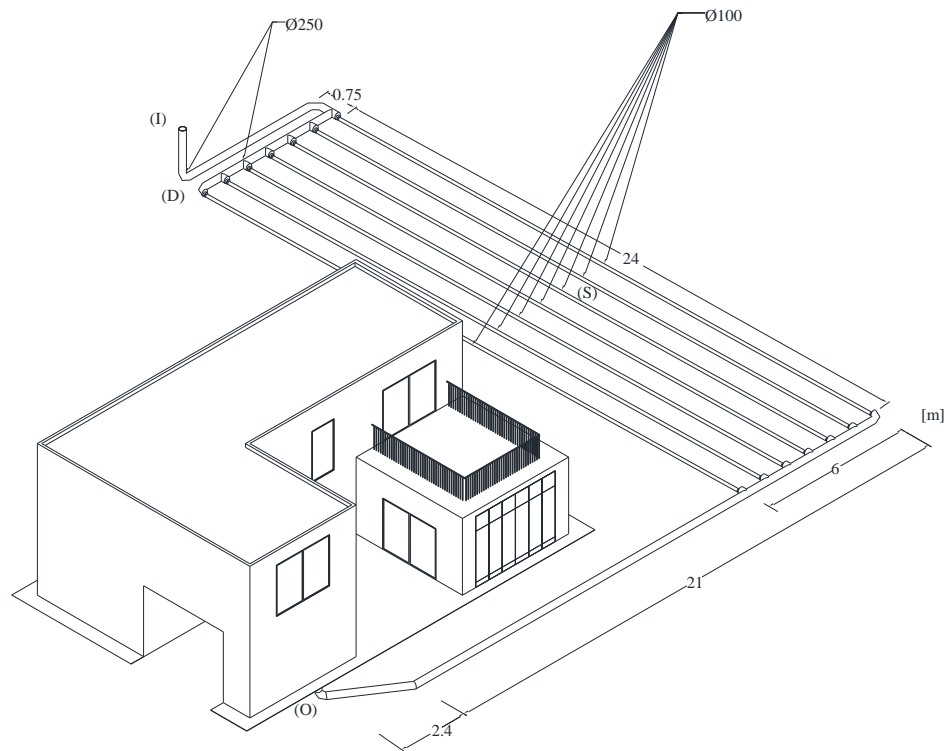


Figure V.2 – Buried pipes layout of the EAHE system and building location.

The system was designed to deliver a maximum air flow rate of $600 \text{ m}^3/\text{h}$, providing globally 1.6 air changes per hour within the house. The air flow rate [m^3/h] was measured with a TROX[®] VMR airflow meter with 200 mm of diameter, located before the heat recovery unit.

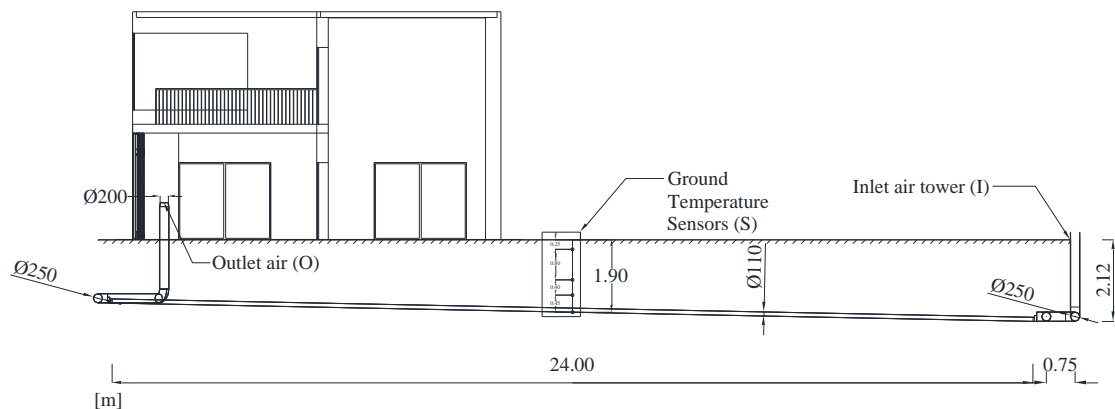


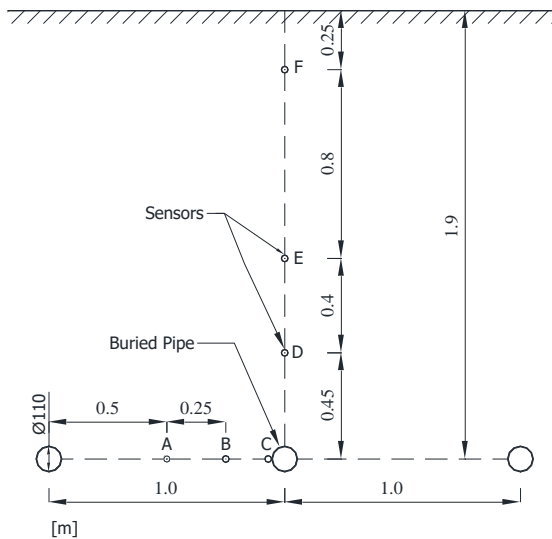
Figure V.3 – Longitudinal vertical cross section scheme of the EAHE system.

The building cooling and heating are primarily provided by a split type air conditioning system. The EAHE was programmed using KNX protocol to ensure indoor air quality (activated when the indoor carbon dioxide concentration exceeds

the recommended limits) and/or when the indoor air temperature rises above 25 °C (cooling mode) or is lower than 20 °C (heating mode).

V.2.1. Experimental setup

To evaluate the thermal behaviour of the EAHE, a monitoring system (Campbell CR800) was installed that enables to measure: (i) soil temperatures at six different points (A to F as illustrated in Figure V.4a; (ii) inlet and outlet air temperatures (points I and O in Figure V.3); (iii) outlet airflow rate, and (iv) electricity consumed by the fan. The environment air temperature is measured by a weather station installed on the roof of an adjacent industrial hall. For ground monitoring, five PT100 temperature probes with a polynomial linearization error of ± 0.5 °C and one probe unit for measuring temperature and humidity (sensor F), with a precision of ± 0.02 °C, were installed, as illustrated in Figure V.4b.



a) Vertical cross section of buried sensors and pipes.

b) PVC pipes to insert the ground temperature probes at different depths.

Figure V.4 – Ground temperature sensors.

The inlet air temperature was measured by a thermo-hygrometer (accuracy of $\pm 3\%$) positioned inside the air intake tower. A PT100 sensor (with an accuracy of ± 0.5 °C) was introduced inside the pipe, right after it emerges from the ground, providing the reading of the outlet air temperature. A air flow meter (accuracy of $\pm 3\%$) was also placed next to this sensor. The EAHE system is controlled using KNX protocol that communicates with five thermostats and CO₂ sensors placed in different areas inside the building.

V.2.2. Monthly average recorded values

The monthly-averaged temperatures of the ground recorded in Sensor A are illustrated in Figure V.5a, and of the outside environment air (recorded in the nearby weather station) over the year of 2014 are plotted in Figure V.5.

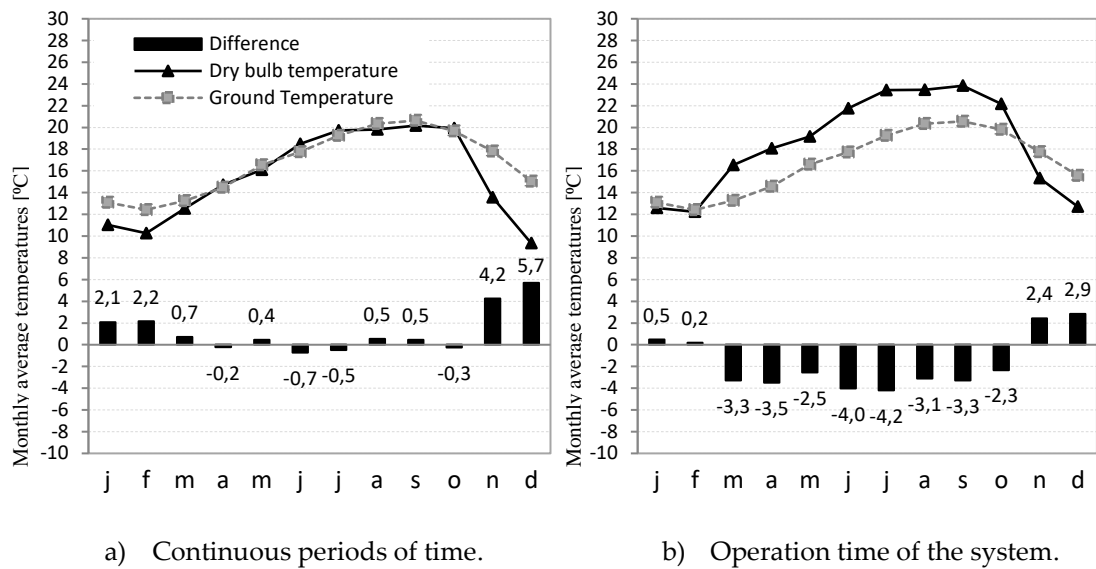


Figure V.5 – Monthly average temperatures (2014): environment air, ground (1.9 m deep), and respective differences.

During the year of 2014, the usually lower annual thermal amplitude of the ground when compared with ambient air, due to the huge thermal inertia of the ground, is not well visible. The highest differences between ground and dry bulb air temperatures (monthly averages) occurred in the heating season. To evaluate the importance of the working schedule, Figure V.5b indicates the temperatures and the respective differences between ground and dry bulb temperatures, averaged only for the operation periods of the EAHE in every month over 2014.

The average difference between ground and dry bulb temperature for the EAHE operation time during the cooling season is greater because the system operates mostly during day time when the temperature difference is higher. An example of this occurred during May-August of 2014, where the average difference between the two charts is 4.2 °C. In the heating season, the average differences are lower due to the proximity between the dry bulb environment air and the ground temperature. For instance, during December 2014, the average difference between the dry bulb temperature and the ground temperature was 5.7 °C for all periods of time and 2.9 °C considering only the system operation periods.

V.2.3. Energy performance analysis

The recorded values were used to evaluate the energy performance of the EAHE system. It is observed that the system did not operate continuously. Since the building is used as an office, the system was mainly active during day time, and the following analysis was based only on data collected during periods of the system operation. The sum of operation time of the system for the four seasons of the year (in 2014) is presented in Figure V.6 over the 24 hours of a day. It can be observed that the main working hours of the system are between 09:00 to 17:00.

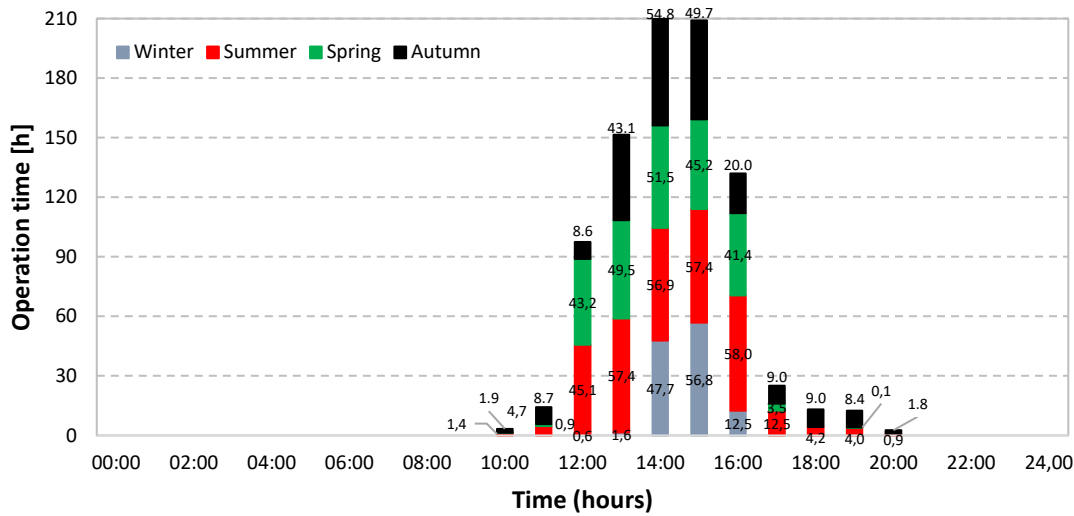


Figure V.6 – Seasonal operation of the EAHE (2014).

For the evaluation of the system performance the following variables were considered: (i) inlet and outlet air temperatures, (ii) airflow rate and (iii) electric energy consumed by the fan. This analysis was performed between January/2014 and December/2014 where the system operating time was higher.

The monthly average values of the most relevant parameters for the evaluation of the energy performance of the EAHE system are indicated in Table V.1. The average dry bulb/environment temperature (T_a), the ground temperature (T_s) and the respective difference are computed only for the operation periods of the system. The instantaneous coefficient of performance (COP) is the ratio between the heat rate in the EAHE (\dot{Q}) and the electric power consumed by the fan (\dot{W}). The energy balance (EB) and the equivalent power (EP) indicated in Table V.1, were calculated on an hourly basis using the following equations:

$$EB = \sum (\dot{Q} - \dot{W}) \times 1h / 1000 \quad (54)$$

CHAPTER V

Modelling and performance analysis of an earth-to-air heat exchanger pilot installation in Csb climate

$$EP = \frac{\sum(\dot{Q} - \dot{W}) \times 1h / 1000}{\Delta t} \quad (55)$$

where Δt is the operating time of the system, in hours.

It can be observed that the highest monthly averaged COP (1.2) does not occur in the month of higher temperature differences: July 2014 (COP = 1.1). This is explained by the fact that, in some periods, the system works with negative values of COP losing thermal energy due to the unfavourable difference between ground and outdoor temperatures. In addition, it may happen when the periods of working time are shorter than the time step considered (1 hour); for instance, when the EAHE system stops working due to the drop of CO₂ levels indoors. This means that the heating or cooling sensible heat (Q), is lower for a given Δt .

Table V.1 – Monthly average values for the EAHE energy performance evaluation.

	T_a	T_s	$T_s - T_a$	Δt	\dot{W}	\dot{Q}	COP	EB	EP
	[°C]	[°C]	[°C]	[h]	[W]	[W]	[-]	[kWh]	[W]
January	12.6	13.1	0.5	44.7	253.0	76.1	0.4	-12.2	-273.3
February	12.2	12.4	0.2	38.1	246.8	57.9	0.4	-11.2	-292.8
March	16.6	13.3	-3.3	36.4	233.8	139.5	0.6	-5.7	-155.5
April	18.1	14.6	-3.5	55.6	245.2	28.7	0.3	-18.8	-338.9
May	19.2	16.6	-2.6	89.4	265.8	244.2	0.8	-2.7	-30.4
June	21.8	17.7	-4.0	90.4	268.6	268.1	0.9	-0.1	-0.7
July	23.4	19.2	-4.2	115.6	280.3	363.2	1.1	11.6	100.5
August	23.5	20.3	-3.1	102.6	249.8	182.4	0.6	-8.6	-84.1
September	23.8	20.6	-3.3	84.2	272.9	299.3	1.0	2.7	31.6
October	22.2	19.8	-2.3	123.0	277.2	354.8	1.2	12.0	97.1
November	15.3	17.8	2.4	53.0	234.7	211.3	0.9	-1.9	-34.8
December	12.7	15.6	2.9	39.0	254.1	223.0	0.9	-1.7	-43.1
Annual	18.4	16.7	-1.7	72.7	256.9	204.0	0.8	-3.0	-85.4

By analysing the values indicated in Table V.1, it is observed that, from the point of view of energy efficiency, the operation of the EAHE was profitable only during the months of July and October when the COP was greater than 1 and the energy balance

and equivalent power were effectively positive. These results suggest that, for an office-like occupancy schedule, the system is more efficient during the cooling season due to the higher temperature difference between ground and outdoor air temperatures. Figure V.7 plots the monthly averaged COP of the EAHE system per time of the day for the four seasons of the year.

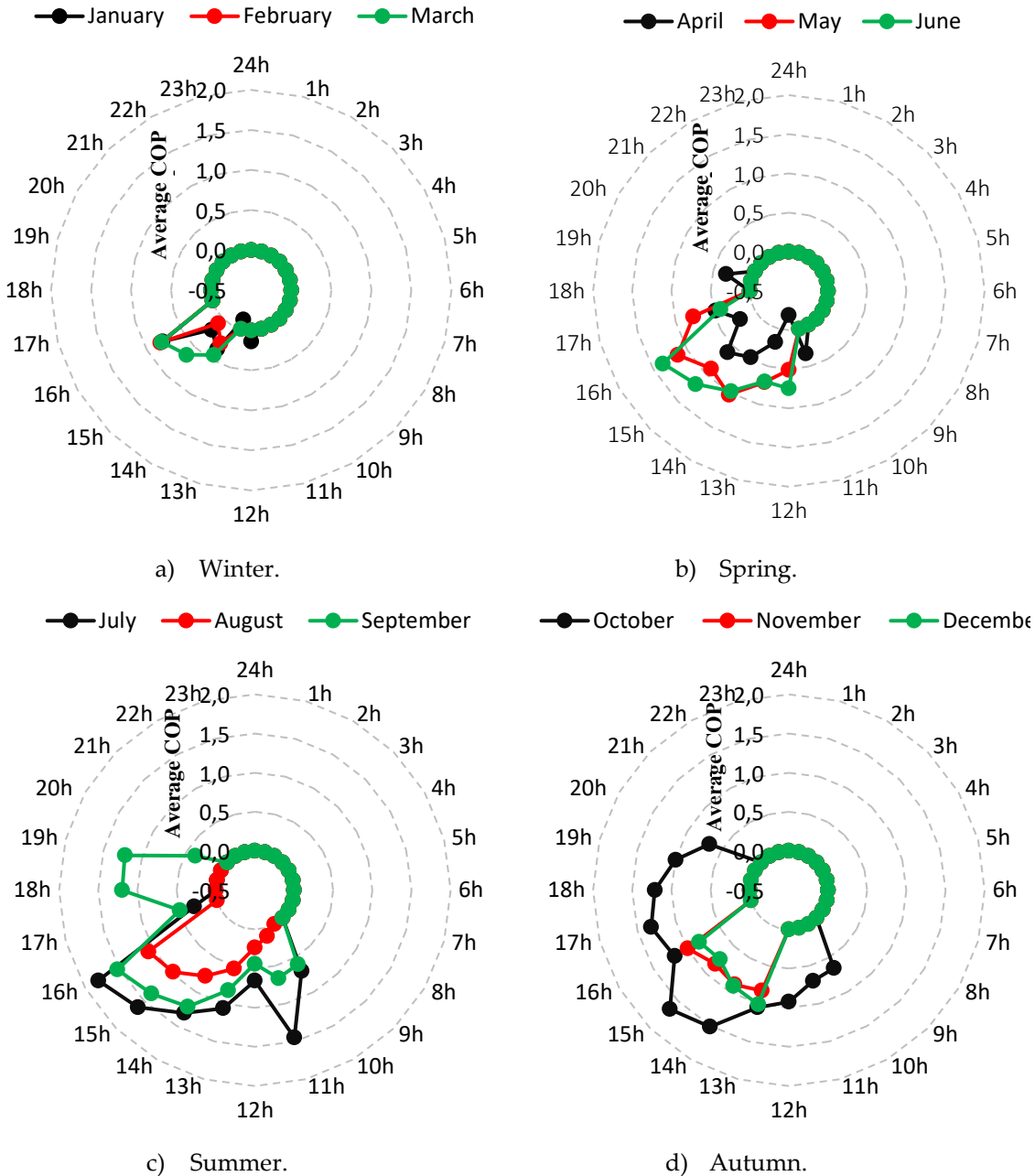


Figure V.7 – Average COP for the EAHE operation over 2014.

The graphs show that the main working hours of the system were during day-time with the greatest average COP value of 1.6 obtained between 14:00 and 15:00 in July. The lowest average COP of -0.2 was obtained for April between 11:00 to 12:00. Furthermore, winter is the season with lower COP values given the diurnal

operation schedule of the EAHE system, which is the least favourable for heating mode (lower temperature difference between the ground and the outdoor air). The global yearly performance of the system indicates that the average COP and the equivalent power were 0.8 and -85.4 W, respectively. During this period, the global difference between the thermal energy collected in the EAHE (\dot{Q}) and the power consumed by the fan (\dot{W}) was 52.8 W. These results enable to highlight the importance and need of a correct control of the operation of the EAHEs to avoid unnecessary energy consumption. During the heating season, it was found that in some periods the temperature of the ground was lower than outdoors. Thus, the EAHE system had negative COP: it was cooling even more the outdoor cold air, thus increasing the energy needs for space heating. Table V.2 displays the monthly averaged values of the COP, the heat rate (\dot{Q}), the energy balance (EB) and the equivalent power (EP) values for the system optimized to work only when the temperature difference between ground and ambient ($T_s - T_a$) is favourable.

Table V.2 – Monthly average values for the EAHE energy performance evaluation, only during operation time.

	T_a	T_s	$T_s - T_a$	Δt	\dot{W}	\dot{Q}	COP	EB	EP
	[°C]	[°C]	[°C]	[h]	[W]	[W]	[-]	[kWh]	[W]
January	11.8	13.1	1.3	31.4	238.8	143.7	0.7	-4.9	-108.6
February	11.6	12.4	0.8	23.7	216.7	114.9	0.6	-4.3	-112.3
March	16.1	13.3	-2.8	25.9	227.3	274.9	1.1	2.1	57.6
April	18.3	14.3	-4.0	23.6	177.2	225.2	1.0	2.4	43.2
May	19.4	16.6	-2.7	68.2	254.6	336.0	1.1	8.1	91.1
June	22.3	17.8	-4.6	72.3	260.4	340.1	1.1	8.2	90.9
July	23.5	19.3	-4.3	111.6	277.8	375.9	1.2	13.3	115.4
August	23.5	20.3	-3.1	102.4	249.8	182.4	0.6	-8.6	-84.1
September	23.8	20.6	-3.3	84.2	272.9	299.3	1.0	2.7	31.6
October	22.2	19.8	-2.3	122.0	277.2	357.5	1.2	12.4	100.6
November	14.9	17.8	2.9	45.0	234.7	253.9	1.1	1.8	32.9
December	12.7	15.6	2.9	39.0	254.1	223.0	0.9	-1.7	-43.1
Annual	18.3	16.7	-1.6	62.4	245.1	260.6	1.0	2.6	17.9

Table V.2 shows an improvement of the annual average COP value from 0.8 to 1.0. It may also be observed the positive energy balance (2.6 kWh) and the equivalent power (17.9 W). The average monthly COPs would be above unity for six months of the year, showing the importance of an adequate working control of the EAHE system. To better understand the variation of the system's performance throughout the year, three typical periods of operation (heating, cooling and mid seasons) are detailed in the following sections.

V.2.3.1. Heating season

The performance characteristics of the EAHE in the heating mode were analysed based on data collected during cloudy and sunny days. Figure V.8a shows the hourly variation of the COP, ground temperature, air inlet and outlet temperatures during two cloudy days (14th and 15th of February) when the system was operated continuously.

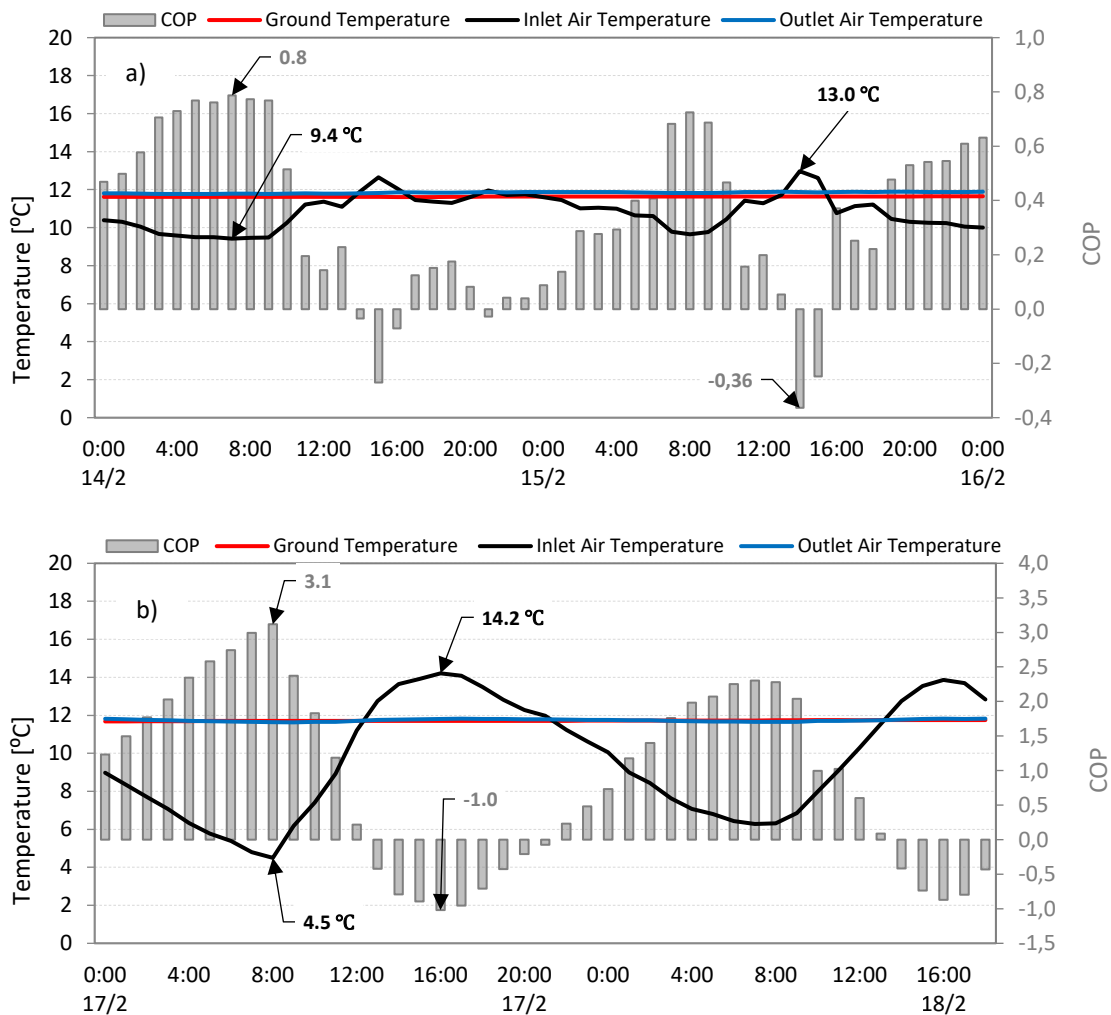


Figure V.8 – Hourly results in heating season for cloudy (a) and sunny days (b).

As expected, the EAHE outlet air temperature is too low to provide by itself comfort conditions ($\sim 20^{\circ}\text{C}$) during the heating season. This situation occurred often throughout the winter confirming that during this season the building must be heated primarily by the air conditioning system. Thus, for this season the main purpose of an EAHE system should be to reduce heating energy requirements, by pre-heating the outdoor air required for ventilation (to ensure indoor air quality).

The system behaves differently during day and night-time. During the night, due to the significant cooling of the outdoor air, there is an increased temperature difference between the ground and incoming air which enabled the EAHE to warm up the outdoor air by as much as 2.2°C . In these conditions, the system's COP at night is higher than during the day, when it can become negative: the ground is colder than the outdoor air for ventilation, which is then cooled down by the EAHE, instead of being heated up. In the heating season, the performance profile of the EAHE system is not adequate for the actual type of occupation of this building (office) since it is mostly used during the day. However, such profile would be more suitable for a real residential building in which the occupation period matches the highest heating potential of the system during the winter season. This fact explains why, although temperature differences between the ground and ambient air are greater during the winter, the average COP here obtained is lower than 1.

Figure V.8b shows two sunny days during the heating season (17th and 18th of February). In this case, the outdoor temperature fluctuations and the difference between ground and outdoor temperature are now much higher. As before, the night COP values (up to 3.1) are much higher than the daytime ones, being the lowest values negative (-1.0). During daytime, the system needs to be optimized in terms of operation set-points, since the outdoor temperature is higher than ground temperature, originating a negative efficiency (in heating mode). For an inlet temperature of 14.2°C and outlet temperature of 11.8°C , the COP value is -1.0 (February 17 at 16:00).

V.2.3.2. Cooling season

Figure V.9 displays the EAHE system behaviour on two summer days (6th and 7th of July) during which it was continuously operated. The thermal amplitude of the outdoor air was quite high (10.7°C) and the average difference between ground and inlet temperature is 12.1°C , which led to an average COP greater than unity (2.0). During day-time, the higher inlet air temperature enabled the EAHE to reach a COP of 3.2 and cool down the warm air by almost 19°C (June 6 at 15:00). At night, given

the cooler outside environment air there is a decrease around 38% of the system performance, reaching a minimum value of 1.3 (June 6 at 04:00 am). Unlike what occurred during winter, in summer the period in which the system reaches its greatest potential matches the occupation schedule of the building (day-time). This feature explains why, although temperature differences between the ground and ambient air are greater during winter, the highest COP was recorded in summer.

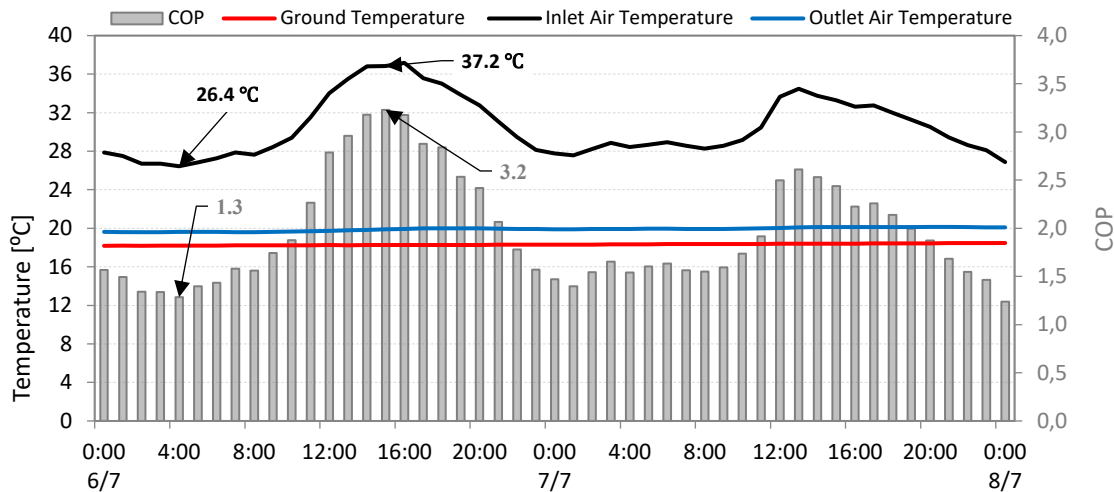


Figure V.9 – Hourly results in cooling season.

V.2.3.3. Mid seasons

Figure V.10 displays the thermal performance of the EAHE system during two days of the spring season (April 9 and 10, continuous operation), being the difference between air inlet and outlet temperatures lower, in comparison with winter and summer, as well as the thermal performance of the EAHE. The average COP for these two days was 0.4 with a maximum value of 0.9.

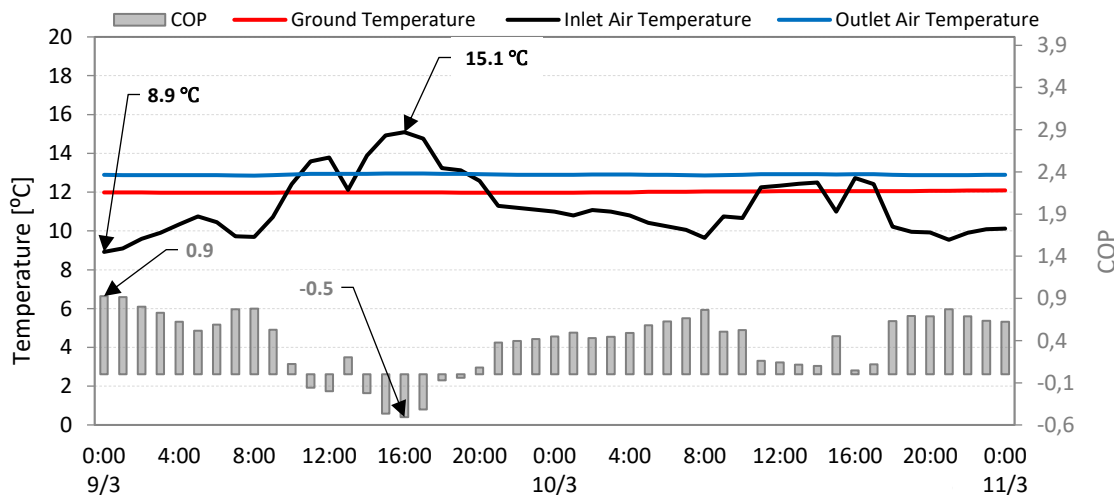


Figure V.10 – Hourly results in the spring season.

Figure V.11 represents the temperature evolution during autumn (November 19 and 20) where the average inlet/outside temperature ($9.8\text{ }^{\circ}\text{C}$) is much lower than the average ground temperature ($16.6\text{ }^{\circ}\text{C}$). Notice that due to the huge thermal inertia and heat storage capacity of the soil, the ground temperature almost keeps the same values as in the summer season, with a difference of $1.7\text{ }^{\circ}\text{C}$ between November and July. Therefore, the average COP for these *in situ* measurements was relatively high (1.9). As expected, the highest COP values were obtained during night-time when the inlet air temperature is lower. The maximum temperature difference between inlet air and ground is $10.5\text{ }^{\circ}\text{C}$ ($\text{COP} = 2.7$).

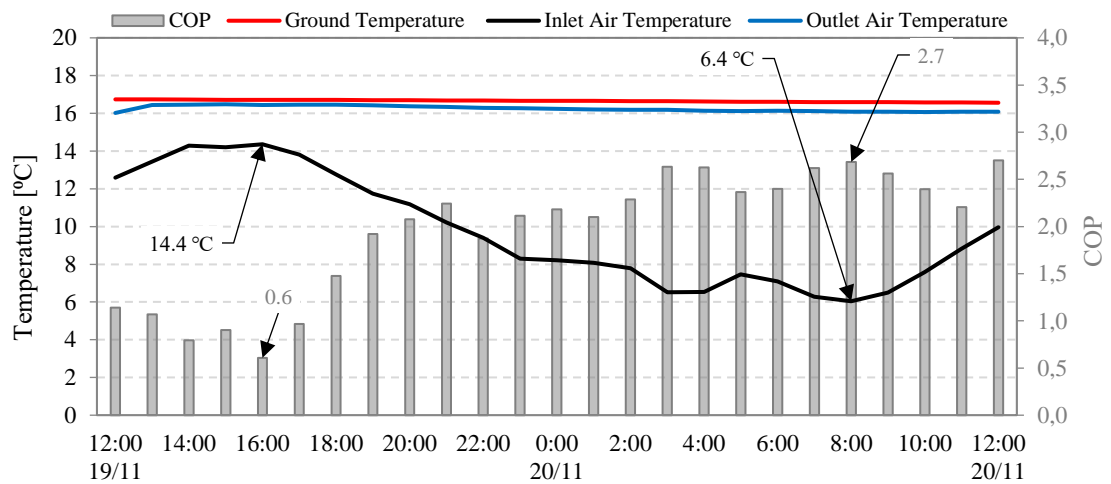


Figure V.11 – Hourly results in the autumn season.

V.3. Analytical approach

V.3.1. Mathematical modelling

A one-dimensional analytical model of a EAHE system was developed for predicting the outlet air temperature as a function of the soil and air intake temperatures. The model was presented in detail Chapter IV. This model is assumed to be valid for simulating a time evolution considered as a step sequence of steady-state balances, with maximum time intervals of 1 hour, as the input temperatures of the soil and of the inlet air are updated with hourly registered values. In this model, the main assumptions are:

- Steady-state conditions during each 1-hour period;
- The airflow inside the pipes is dynamically and thermally developed;
- The soil surrounding the pipes is homogeneous, with constant thermal conductivity;

- Negligible gradients of the soil temperature (T_{soil}) in the axial direction.

Consequently, the physical model is that of internal heat convection combined with one-dimensional heat conduction through a multi-layer cylindrical system (Figure IV.4a, Chapter IV). The steady-state assumption strictly neglects the thermal inertia of the soil layer; however, the error associated with this simplification is minimized since (i) the transient inlet air temperature and soil temperature (measured or predicted) are specified as inputs at every time step; and (ii) the time steps (of 1 hour) are short enough compared with the daily cycle and with overall period of the transient process.

The energy balance applied to a differential control volume of the airflow located at a certain position x in the pipe is expressed (Figure IV.4a, Chapter IV) is present in Equation (44b). U_i represents the overall heat transfer coefficient [$\text{W}/(\text{m}^2 \cdot ^\circ\text{C})$] between the air and the ground, given by:

$$U_i = \frac{1}{\frac{1}{h_i} + r_1 \left(\frac{\ln \left(\frac{r_2}{r_1} \right)}{k_{\text{pipe}}} \right) + r_1 \left(\frac{\ln \left(\frac{r_3}{r_2} \right)}{k_{\text{ground}}} \right)} \quad (56)$$

where r_2 and r_1 represents the exterior and internal radius [m] of the pipe, and r_3 the radius [m] that defines the thermally affected zone of the soil assumed to be equal to 0.5 m, i.e. half the distance between the axis of the buried pipes (Figure IV.4b,). k_{pipe} and k_{ground} are the thermal conductivities [$\text{W}/(\text{m} \cdot ^\circ\text{C})$] of the wall material of the pipe and of the ground/soil, respectively.

The internal convection heat transfer coefficient [$\text{W}/(\text{m}^2 \cdot ^\circ\text{C})$] is given by (after the Gnielinski correlation (Equation (33)):

$$h_i = \frac{\left(\frac{f}{8} \right) (Re - 1000) Pr \frac{k_{\text{fluid}}}{d_i}}{1.07 + 12.7 \left(\frac{f}{8} \right)^{0.5} \left(\frac{2}{Pr^3} - 1 \right)} \quad (57)$$

where k_{fluid} is the air thermal conductivity [$\text{W}/(\text{m} \cdot ^\circ\text{C})$]. The mean efficiency of the earth-to-air heat exchanger for a period t is calculated using Equation (51) (Chapter IV).

The pressure drop in the heat exchanger and the energy consumed by the fan are essential to calculate the COP of the system. The pressure drops in the system [Pa] given by:

$$\Delta p = \left(f \frac{L}{d_i} + \sum K_i \right) \rho \frac{v^2}{2} \quad (58)$$

where L is the pipe length [m], ρ is the air density [kg/m^3], v is the air velocity [m/s] and K_i the coefficients of local pressure drop.

The fan electrical efficiency is obtained by:

$$\eta_{fan} = \frac{\Delta p \dot{V}}{\dot{W}} \quad (59)$$

The fan efficiency was computed using measured values of electric power consumed by the heat recovery unit (\dot{W}) taking in account that the heat recovery unit has two fans working at the same speed (supply and extraction) and air flow rate. The measured average annual electric efficiency is 3.6 % with an average annual electric consumption of 351 Wh. With analytical procedures and using the measured electric efficiency, the annual average electric consumption obtained was 355 Wh.

Also, the fan electricity efficiency is within a range of 0.7 up to 4.7 % according with the airflow rate between 250 and above 350 m^3/h . The total rate of heat transfer [W] between the airflow and the soil can be obtained after the airflow temperature variation between inlet and outlet of the EAHE by Equations (49) and Equation (50). Assuming a uniform soil temperature T_s [$^{\circ}\text{C}$] along the tubes and taking the (measured or predicted) inlet air temperature $T_{a,in}$ [$^{\circ}\text{C}$] as an input at every step, the outlet air temperature in the EAHE is calculated by Equation (46), which is here recalled:

$$T_{a,out} = T_s - (T_s - T_{a,in}) \cdot e^{-\text{NTU}}$$

V.3.2. Model validation

This analytical model is here validated by comparison against *in situ* measurements. The following additional assumptions were applied in this model: (1) the undisturbed temperature of the ground is constant in the axial direction and equal to the value measured by Sensor A (Figure V.4a); (2) the physical and thermal

properties of the soil, air and pipes are constant and their values are given in Table V.3. The EAHE geometric features used in the model are given in Table V.4.

Table V.3 – Thermophysical properties used in model validation (Çengel, 2009).

Material	Thermal Conductivity [W/m/°C]	Thermal Capacity [J/kg/°C]	Density [kg/m ³]
PVC	0.17	-	-
Air [298 K]	0.025	1007	1.204
Soil	1.50	-	-

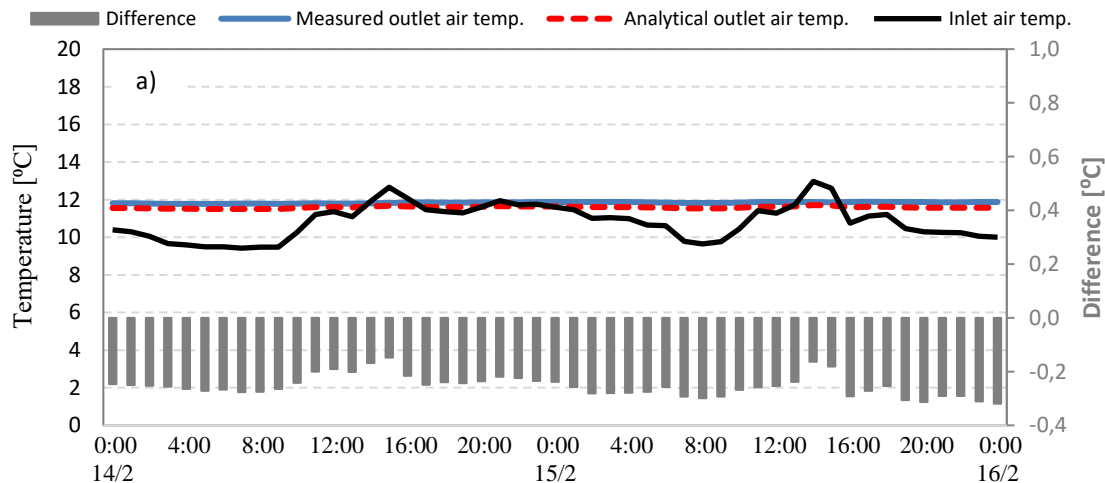
Table V.4 – EAHE geometric features used in model validation.

Feature	ø250 ⁽¹⁾	ø110 ⁽²⁾	Units
Pipe length	33.9	168.0	[m]
Pipe thickness	6.2	2.7	[mm]

⁽¹⁾ Connecting pipes diameter; ⁽²⁾ Longitudinal pipes diameter.

V.3.2.1. Heating season

The outlet air temperature predicted by the model and the one measured in the installation during a cloudy winter period of operation (see Figure V.8a) are represented in Figure V.12a. The accuracy of the model was measured in terms of the Mean Square Error (MSE), which was equal to 0.07 °C and an average temperature difference of - 0.25 °C. A similar comparison is presented in Figure V.12b for two winter sunny days (see Figure V.8b). The average temperature difference between measured and analytical outlet temperature was equal to -0.19 °C (MSE of 0.08 °C).



CHAPTER V

Modelling and performance analysis of an earth-to-air heat exchanger pilot installation in Csb climate

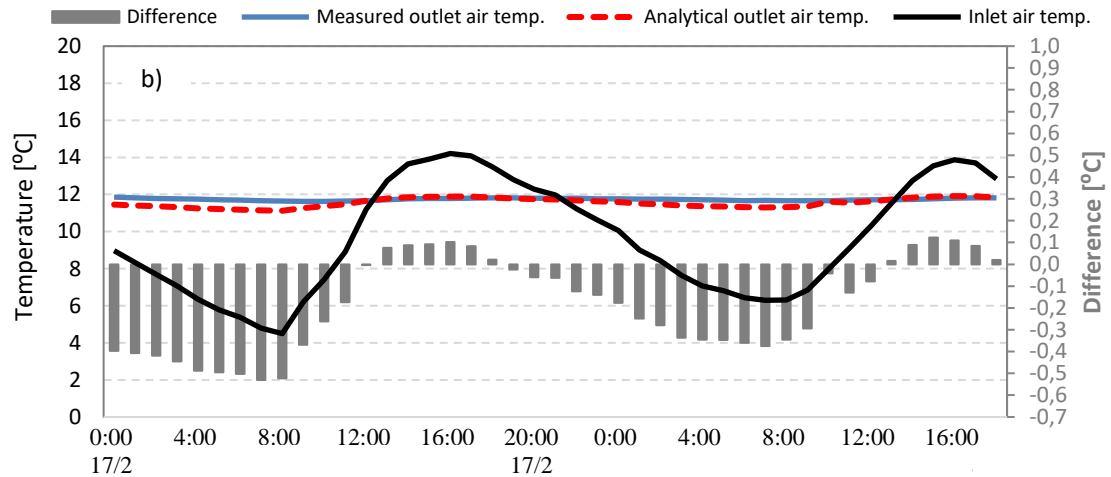


Figure V.12 – Measured and predicted outlet air temperatures in heating season for cloudy (a) and sunny (b) days.

V.3.2.2. Cooling season

A similar procedure was considered for the cooling season, as shown in Figure V.13. The average difference between analytical and measured values occurred for this cooling season period was -1.34°C (MSE of 1.80°C).

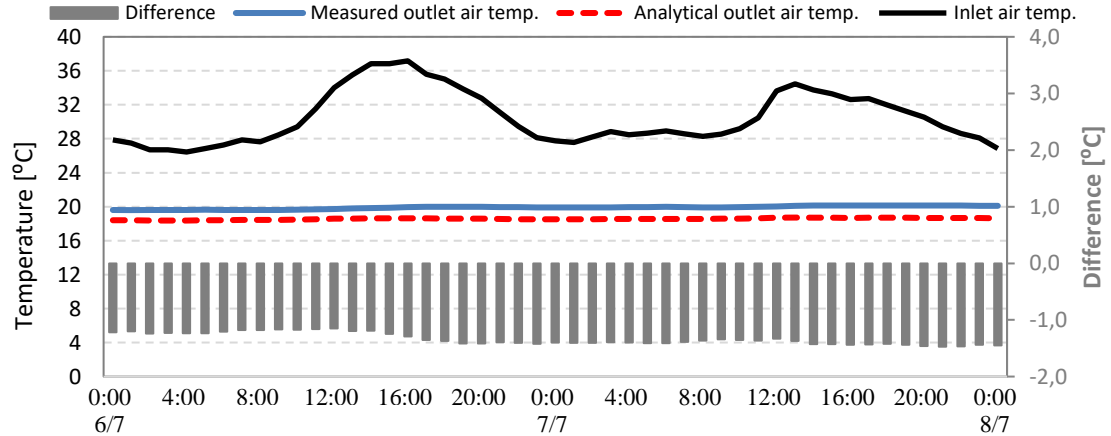
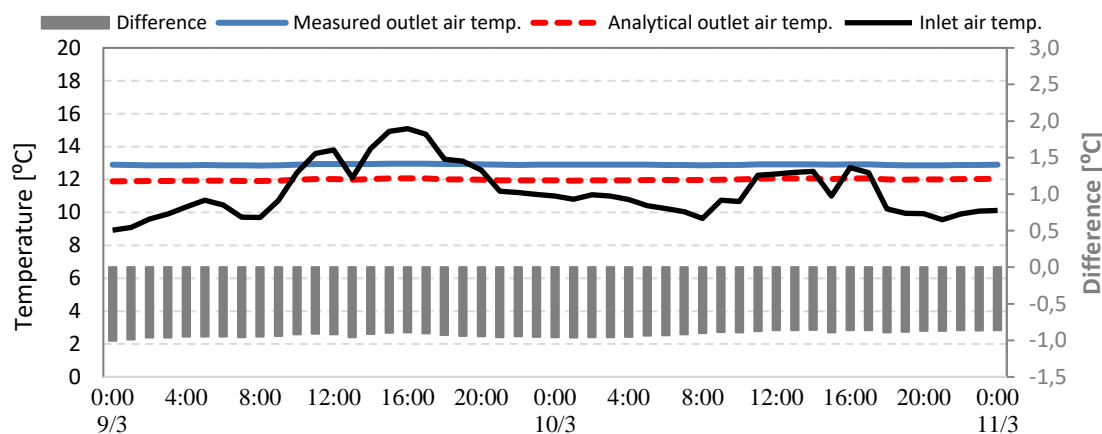


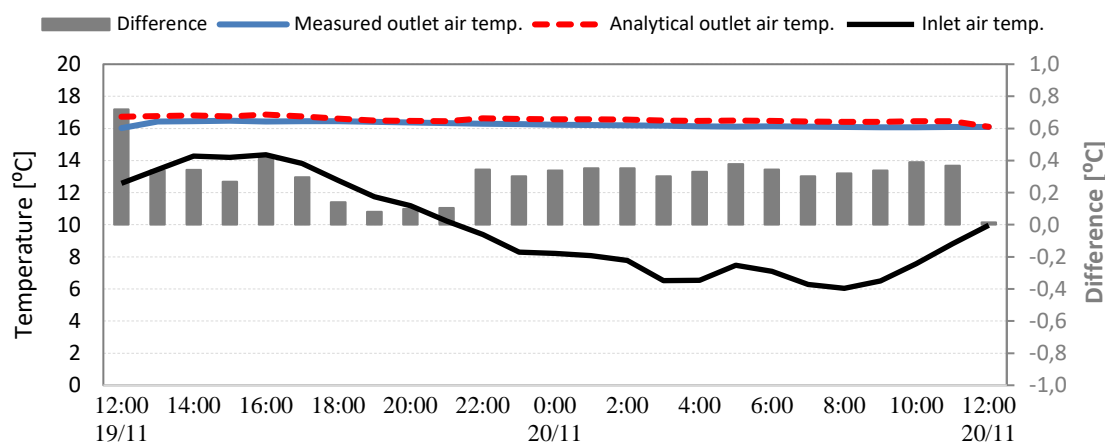
Figure V.13 – Measured and predicted outlet air temperature for cooling season

V.3.2.3. Mid seasons

Figure V.14a shows the validation results for spring season when the average difference is -0.92°C (MSE is 0.84°C). For autumn season Figure V.14b allows to verify the accuracy of the analytical model with an average difference and a MSE of 0.29°C and 0.09°C , respectively. Note that the values of the air temperature at the EAHE outlet predicted by the analytical model are generally lower than the measured ones for the analysed periods in any season of the year.



a) Spring season



b) Autumn season

Figure V.14 – Measured and predicted outlet air temperature for mid seasons.

Table V.5 presents the average outlet temperature difference between measured values and analytical model predictions and the Mean-Square Error (MSE). The analytical model is in good agreement with the *in situ* measurements with a MSE changing from 0.07 °C to 1.80 °C.

It is noticed that the maximum analytical error was obtained during the spring and summer seasons, where the difference between inlet air temperature and ground temperature is higher. Moreover, the outlet collecting pipe that is installed at lower depth where the outdoor conditions (i.e. thermal radiation) may have a significant contribution in the air outlet temperature.

Table V.5 - Analytical model accuracy overview.

Season	Average diff. [°C]	MSE [°C]
Winter (cloudy day)	- 0.25	0.07
Winter (sunny day)	- 0.19	0.08
Autumn	0.29	0.09
Spring	- 0.92	0.84
Summer	- 1.34	1.80

V.4. Parametric study

The sensitivity of the EAHE performance to the variation of certain parameters for heating and cooling seasons was evaluated based in the analytical model validated in the previous section. To analyse the potential of the EAHE system a parametric study was conducted for a 24 hours period during cooling (July 6) and heating (February 17) seasons. The analysed variables are: pipe length, diameter and thickness; air velocity; and soil typology (Table V.6). The influence of each parameter on the system's performance was evaluated based on its thermal efficiency calculated using Equation(51) and coefficient of performance (COP).

Table V.6 – Scheme of the parametric study for different pipe length and diameter, air velocity, pipe material and soil typology topology.

Influence of:											
Pipe Length [m]	10	20	24	30	40	50	60	70	80	90	100
Pipe diameter [mm]	104.6		152.0		190.2		237.6		299.6		380.4
Pipe thickness [mm]	2.7		4.0		4.9		6.2		7.7		9.8
Air velocity [m/s]	1	2	2.77	3	4	5	6	7	8	9	10
Pipe material	PVC				HDPE				Steel		
Thermal conductivity [W/(m.°C)]	0.17				0.5				60.5		
Soil typology	Dry sand			Sandy and clayey			Sandstone		Metaquartzite		
Thermal conductivity [W/(m.°C)]	0.5			1.5			2.3		5.8		

V.4.1. Pipe length

The study of the influence of the total pipes' length was conducted focusing on the seven $\phi 110$ -mm parallel pipes, which in the pilot installation were 24 m long each. For the parametric study, length values between 5 and 100 m were considered for the seven parallel pipes. Figure V.15 shows the results for the outlet temperature over the 24 hours of a day in heating and cooling modes, taking as inputs the environment air and ground temperatures measured on Feb 17 and July 6,

respectively. As expected it is observed that the outlet air temperature becomes closer to the ground temperature as the total pipe length increases. In heating mode (Figure V.15a), the increase of the pipes length from 5 to 50 m originates an increase of 2.4 °C in the outlet air temperature at $t = 8$ h, when the inlet temperature is minimal (4.5 °C). At the highest inlet air temperature (14.2 °C), $t = 16$ hours, the outlet temperature decreases 0.83 °C. In the case of cooling mode (Figure V.15b), when the ground is colder than the environment air at all time, the increase of the pipes' length from 5 to 50 m leads to a decrease of 3.4 °C in the outlet air temperature at the moment of maximum inlet temperature (37.2 °C), when the ground temperature is 18.3 °C. For the minimum air inlet temperature of 26.4 °C this variation is of 1.6 °C. Notice that an increase of the pipes' length causes an increase in the heat transfer surface area and, therefore, of the rate of heat transfer between the ground and the airflow, for the same remaining conditions and parameters. This leads to an enhanced cooling effect by the EAHE whenever the temperature difference between environment air and ground rises. It is also observed that there is no gain in doubling the pipes' length from 50 to 100 m (NTU from 5.7 to 11.4 in cooling and from 3.8 to 7.7 in heating), for the variation of the outlet air temperature (*e.g.*, 0.02 °C at $t = 16$ h). At this point, it is observed that the outlet air temperature practically converges to the ground temperature.

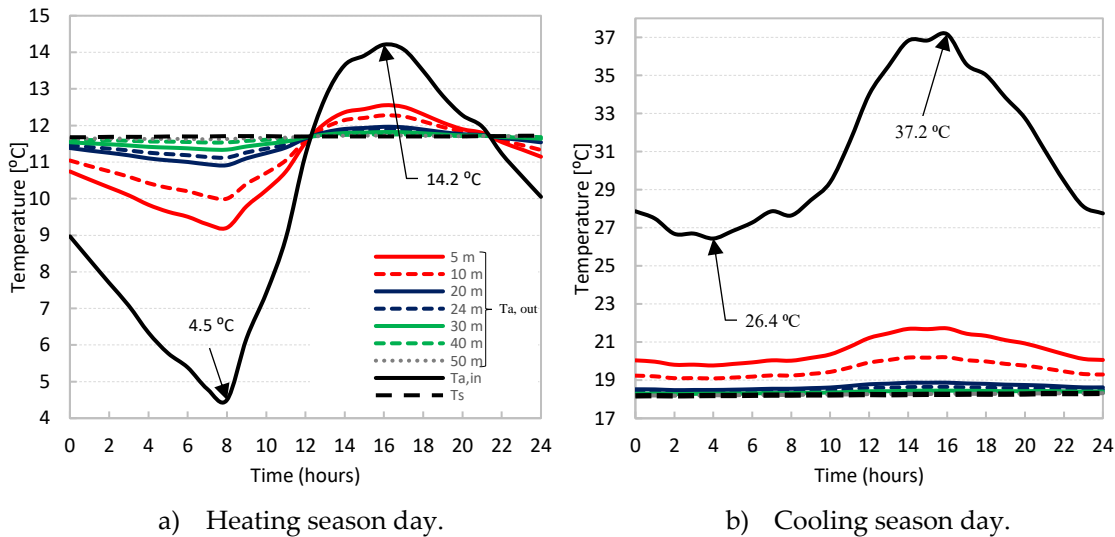
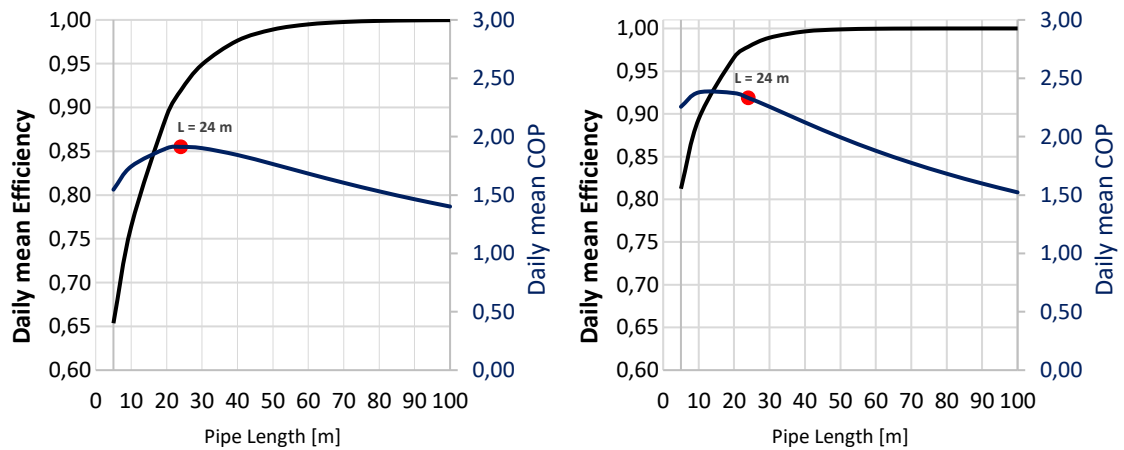


Figure V.15 – Outlet air temperature variation for different pipe lengths ($\dot{V} = 213$ m³/h in cooling and $\dot{V} = 455$ m³/h in heating)..

Figure V.16a and Figure V.16b show the variations with increasing pipes' length of the daily mean efficiency and coefficient of performance for the same heating and cooling mode cases of Figure V.15, respectively. The results for heating mode case

(Figure V.16a) indicates that the EAHE mean efficiency increases with the increasing pipes' length, showing a trend similar to that of the effectiveness-NTU relation of conventional heat exchangers. This is explained by the fact NTU (*cf.* Eq. (38)) varies proportionally with the pipes' length (via A_i), since the airflow rate and pipes' cross-section are keep constant. However, due to the length-proportional increase of the pressure drop and of the electric power consumed by the fan, there is a COP reduction for pipe lengths above 24 m. This feature allows to conclude that the EAHE system described in Section 2 was well designed, *i.e.* the optimum pipe length is around 24 m. It is noted that the daily average the heating COP has an improvement of 0.4, when the pipes' length is increased from 5 up to 24 m, and it drops from 1.9 to 1.4, the length rises from 24 up to 100 m. This illustrates again the importance of an adequate control of the EAHE operation. As for the daily mean efficiency for heating, it increases from 65 % to 92 % when the pipes' length is increased from 5 up to 24 m (NTU from 0.6 to 2.7 in cooling and from 0.4 to 1.9), and practically reaches 100% for pipe length of 50 m (NTU from 3.8 to 5.7).

In the cooling season (Figure V.16b), the EAHE exhibits much higher values of both daily mean efficiency and COP for smaller pipes' lengths mainly due to the higher difference between inlet and outlet air temperature. Figure V.16b also shows that the maximum cooling COP is obtained for pipe lengths between 10 and 20 m.



a) Heating season day.

b) Cooling season day.

Figure V.16 – Variation of the mean efficiency and COP with the pipes' length.

V.4.2. Pipe diameter

The influence of the parallel pipes' diameter was studied considering different commercial pipes ranging from DN110 to DN400, as displayed in Table V.7, keeping constant all the remaining parameters of the pilot installation. In this case, for a fixed

airflow rate, increasing the pipes' diameter will induce two contradictory effects on NTU and the heat rate: A_i increases, while U_i decreases (cf. Eq. (38)).

Table V.7 – Pipe diameters used in the sensitivity analysis ⁽¹⁾.

DN	110	160	200	250	315	400
Thickness [mm]	2.7	4.0	4.9	6.2	7.7	9.8
d_i [mm]	104.6	152.0	190.2	237.6	299.6	380.4

⁽¹⁾ Reference values in bold.

Considering a continuous 24-hour operation during a heating season day, Figure V.17 shows that, with the increasing of the pipe diameter, the difference between air inlet temperature and air outlet temperature decreases, thus evidencing an overall decrease of the heat rate. The same is observed for a cooling season day (Figure V.17b).

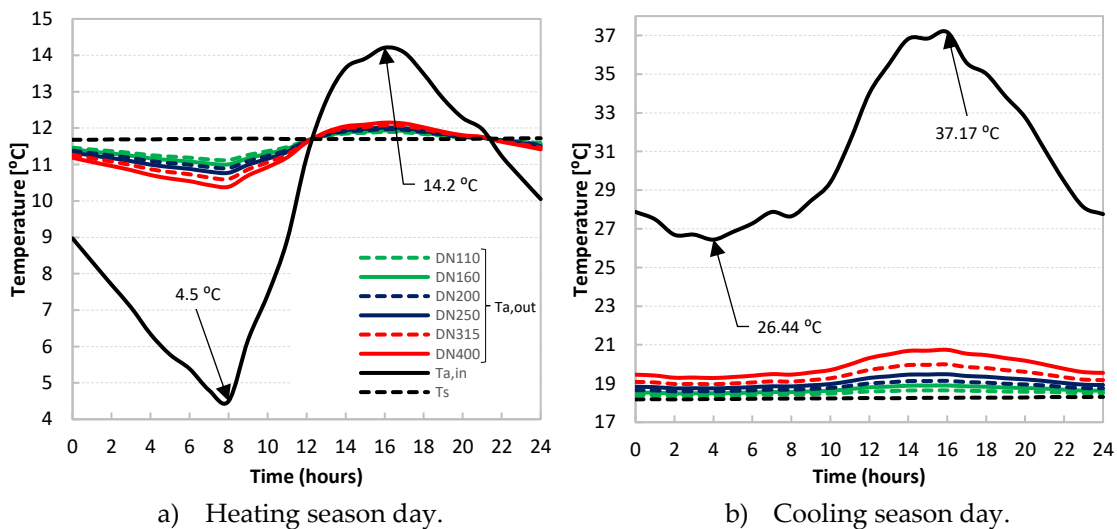


Figure V.17 – Outlet air temperature evolution for different commercial pipe diameters.

Figure V.18a and Figure V.18b display the influence of pipes' diameter on the daily mean efficiency and the coefficient of performance. It is seen that increasing the pipes' diameter has a strong detrimental effect on the thermal performance of the EAHE in both heating and cooling modes. However, regarding the COP, it comes out that higher pipe diameters (200 – 250 mm) would be desirable to achieve its maximum values, which is explained by the significant reduction of the pressure loss with increasing diameter, for the same airflow rate. In view of this, one could conclude that commercial pipes of DN160 might have been a better option than DN110 for the parallel pipes of the pilot EAHE installation. Nevertheless, this

statement should be given a relative importance, because the results obtained in the previous section would also be different for a different pipes' diameter.

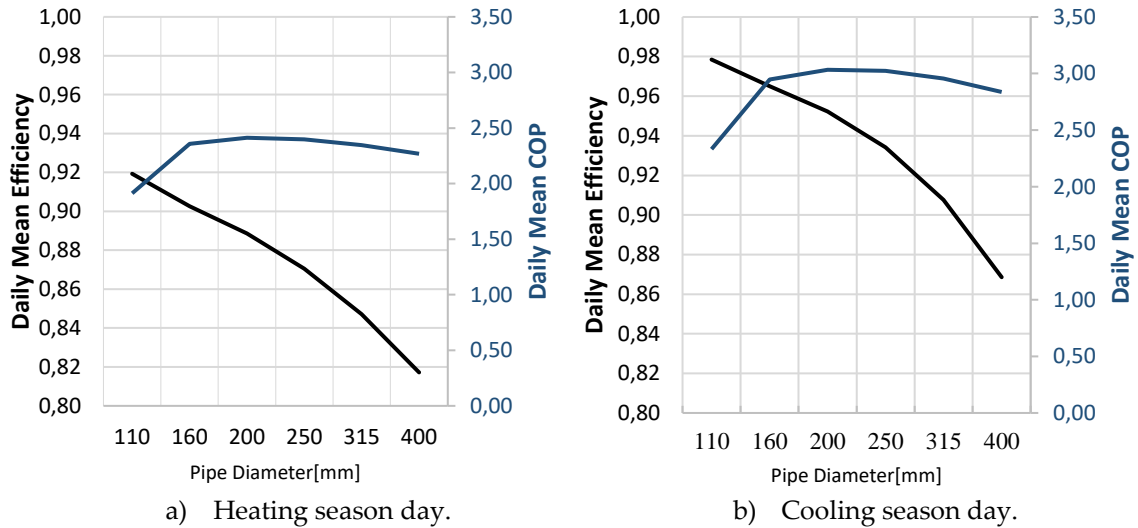


Figure V.18 – Evolution of mean efficiency and COP according with the pipe diameter.

V.4.3. Air velocity

In the pilot EAHE installation, the nominal ventilation airflow rate of 600 m³/h corresponds to an average velocity of 2.77 m/s ($Re_d \approx 19120$) of the air flowing inside the seven DN110 parallel pipes. Figure V.19 illustrates how the daily evolution of air outlet temperature changes as the air velocity inside the parallel pipes is made to vary from 1 m/s up to 5 m/s (total airflow rates from 217 to 1083 m³/h and (Re_d from ≈ 6900 to ≈ 34500), for both heating and cooling season days. As expected, the outlet air temperature is closer to the ground temperature for lower airflow rates. Looking at Equation (38), it is seen that increasing the air velocity increases both terms of the NTU defining ratio, however at a much lower for the upper one: the convection coefficient varies approximately with $v^{0.8}$ in turbulent flows inside ducts (*cf.* Eq. (35)) and convection is not the only component for the thermal resistances defining U_i . Meanwhile, the pressure loss in the pipes' circuit increases with v^2 , allowing to predict a strong detrimental effect of the increasing air velocity on the EAHE COP. The results presented in Figure V.20 illustrate these detrimental effects of increasing the airflow velocity, much more pronounced on the COP than on the thermal efficiency of the EAHE. Therefore, one can conclude that the pilot EAHE installation operation at the nominal (maximum) airflow rate is suitable, and that an improvement of its overall performance is expected if it operates at lower ventilation airflow rates.

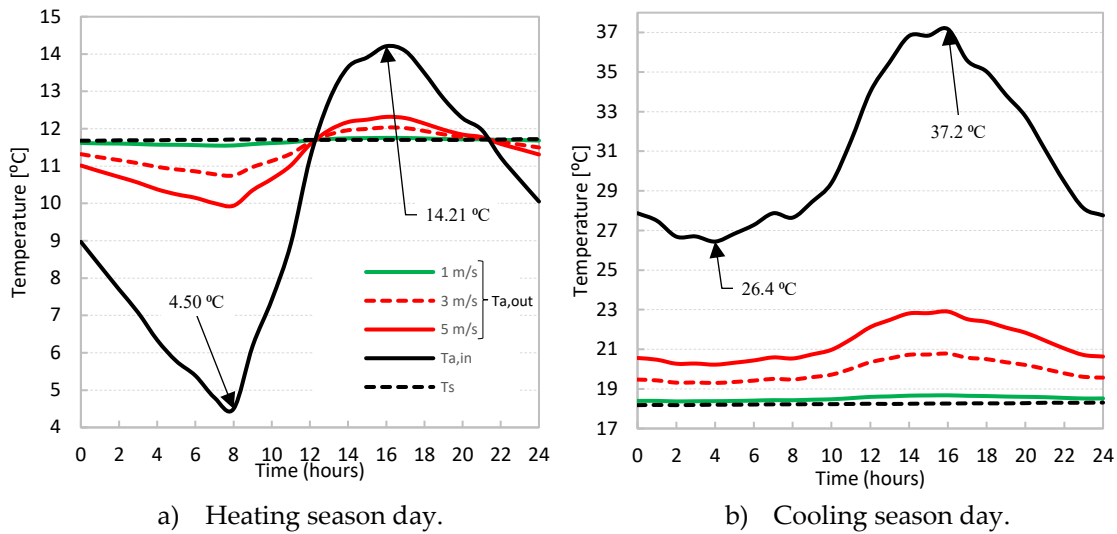


Figure V.19 – Outlet air temperatures evolution for different air velocities.

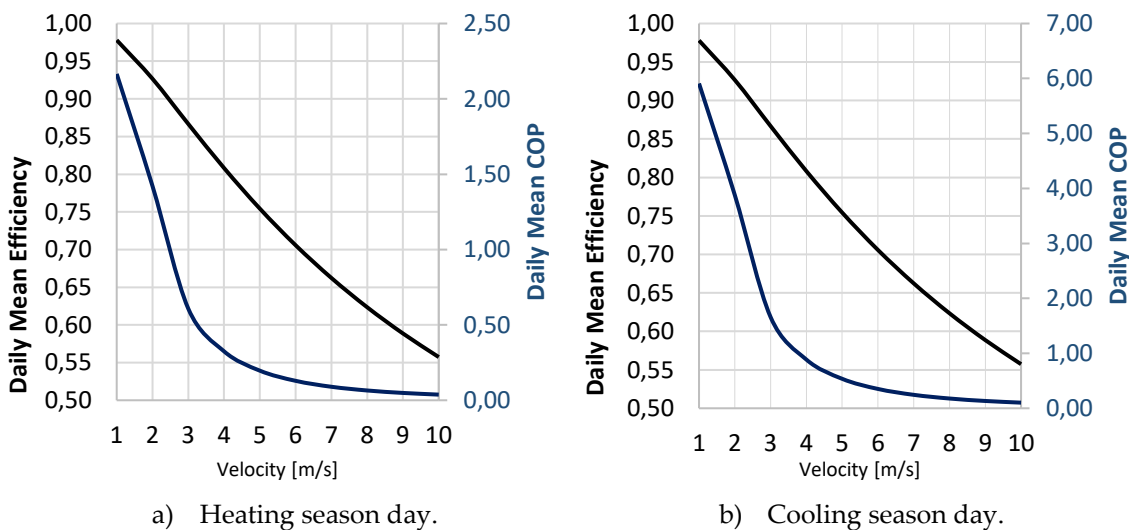


Figure V.20 – Variation of the mean efficiency and COP with the airflow velocity.

V.4.4. Pipe material

The pipe material influences its mechanical resistance, durability and thermal conductance. The present analytical model was used with the configuration and the nominal operating conditions of the pilot installation to compare the influence of the pipes' material on the thermal performance of the EAHE, considering three distinct materials: (i) PVC ($k_{pipe} = 0.17 \text{ W/m} \cdot ^\circ\text{C}$), (ii) HDPE ($0.5 \text{ W/m} \cdot ^\circ\text{C}$) and (iii) steel ($60.5 \text{ W/m} \cdot ^\circ\text{C}$). The calculations were done for the DN110 pipe route with 2.7 mm thickness. The results shown in Figure V.21 indicate a slightly better performance for higher thermal conductivity of the pipes' wall, for the outlet air temperature is closer to the ground temperature. However, it can be concluded that, compared with the other parameters, the pipes' material has a marginal, negligible influence on the

CHAPTER V

Modelling and performance analysis of an earth-to-air heat exchanger pilot installation in Csb climate

EAHE thermal performance; *e.g.*, for the cooling season day, the COP increases only from 2.33 to 2.34 when the pipe thermal conductivity rises from 0.17 to 60.5 W/(m. °C)), *cf.* Table V.8. This is explained by the fact that the pipe's thermal resistance is the lowest of all involved, mainly due to its small thickness: it represents only 10.8 %, against 36.7 % and 52.5 % of those of the soil and the airflow, respectively, for the nominal conditions. Therefore, improving the thermal conductivity of the pipes' wall produces a minor effect on the value of the overall heat transfer coefficient, U_i .

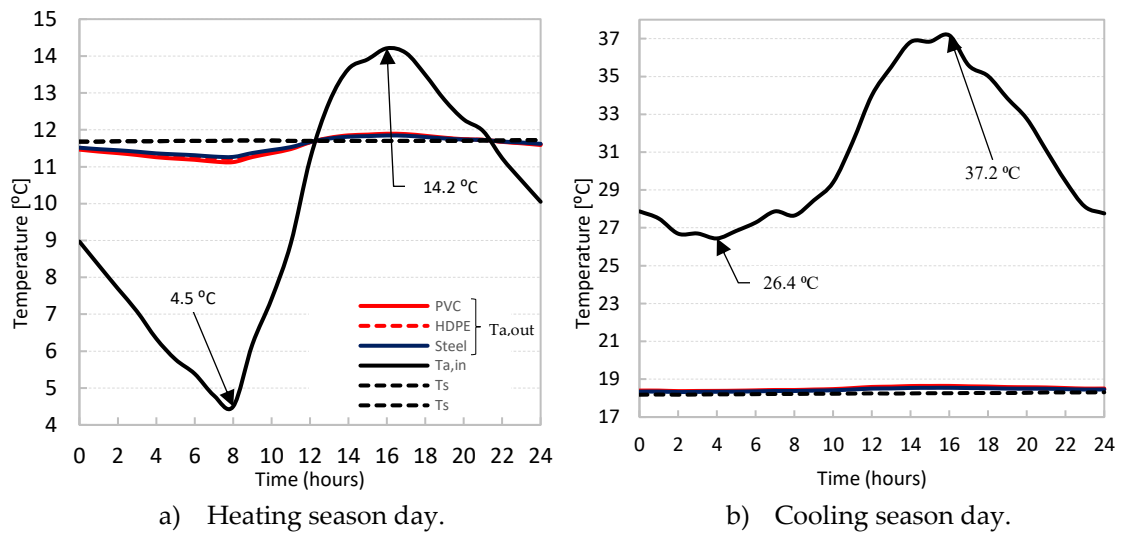


Figure V.21 – Outlet air temperatures for different pipe materials.

Table V.8 – Mean efficiency and COP according with the pipe material and season.

Material	Heating		Cooling	
	η_{mean}	COP	η_{mean}	COP
PVC ⁽¹⁾	0.92	1.91	0.98	2.33
HDPE	0.93	1.94	0.98	2.34
STEEL	0.94	1.95	0.98	2.34

⁽¹⁾Reference values in bold.

In conclusion, PVC can be identified as a good option in terms of cost-benefit ratio, since it combines advantages like low cost, good mechanical resistance and satisfactory thermal performance.

V.4.5. Soil typology

Figure V.22a and Figure V.22b illustrates the outlet air temperature time evolutions for different soil typologies with different thermal conductivities (VDI 4640, 2001) in the ranges 0.4 to 5.8 W/ (m.°C) as listed in Table V.9.

Table V.9 – Soil typologies and thermal conductivities used in the sensitivity analysis.

Soil Typology	k_{soil} [W/ (m.°C)]
Dry sand	0.4
Sandy and clayey⁽¹⁾	1.5
Sandstone	2.3
Metaquartzite	5.8

⁽¹⁾ Reference value in bold.

As expected, it is seen that the outlet air temperature is as closer to the ground temperature as the soil thermal conductivity is higher. However, the difference is much more notorious when changing from a dry-sand to a sandy-and-clayey soil than from the latter to a metaquartzite one, in spite of corresponding to similar increase ratios of the soil thermal conductivity (3.75 and 3.87). In fact, if it were of dry sand, the soil thermal resistance would be the predominant one (68.5%), and most limitative for the U_i value; for values of k_{soil} greater than 1.5 ~ 2 W/(m.°C), the convective resistance (of the internal airflow) tends to be the weighty one, and the soil's constitution becomes a matter of lesser concern (*e.g.*, for a metaquartzite soil, $R_3 \sim 13\%$ and $R_2 \sim 15\%$).

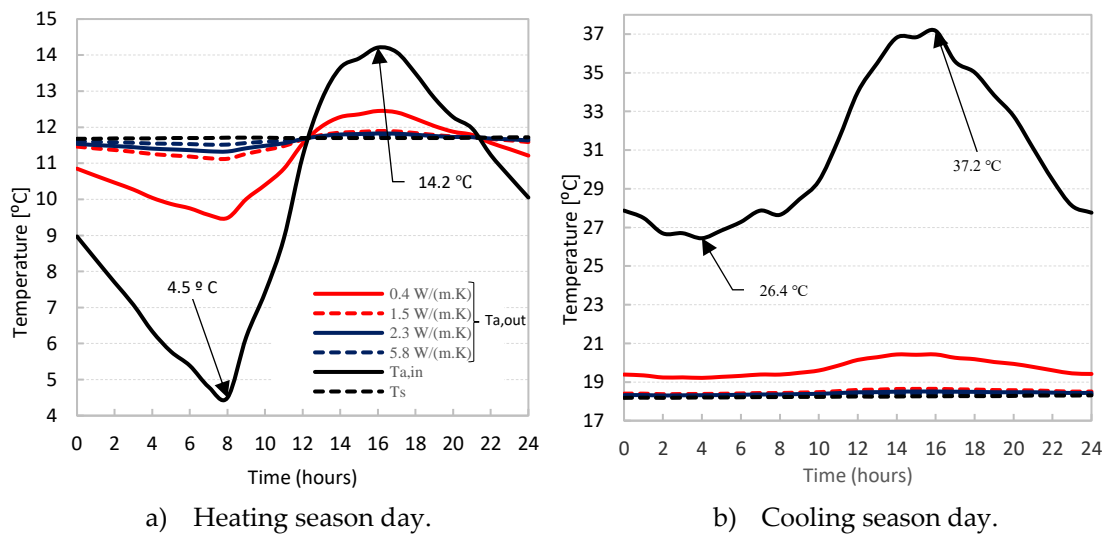


Figure V.22 – Outlet air temperatures for different soil thermal conductivities.

The above statement about the influence of the soil typology can be better inferred by the analysis of the values of the daily mean efficiency and COP presented in Table V.10. In conclusion, it can be stated that, for a suitable thermal performance of the EAHE, the soil constitution must be such to ensure a k_{soil} greater than 1.5 ~ 2 W/(m.°C).

Table V.10 – Mean efficiency and COP according with the soil thermal conductivity.

Soil	k_{soil} [W/(m.°C)]	Heating		Cooling	
		η_{mean}	COP	η_{mean}	COP
Dry sand	0.40	0.70	1.44	0.88	2.10
Sandy clayey⁽¹⁾	1.50	0.92	1.91	0.98	2.30
Sandstone	2.30	0.95	1.97	0.98	2.35
Metaquartzite	5.80	0.97	2.03	0.99	2.36

(1) Reference soil.

V.5. Conclusions

A parametric study was made of the heating and cooling energy performance of a earth-to-air heat exchanger was performed, taking as a reference the configuration and the nominal operation conditions of the pilot installation of a EAHE located in Coimbra (Portugal). This evaluation was conducted using the analytical model presented in the previous chapter: a simple steady-state one-dimensional model that was beforehand validated against the *in-situ* data recorded for the four seasons of the year.

The analysis allowed to conclude that the EAHE controlling system must be optimized mainly in the heating season, when the occupancy profile (that of an office building) is not suitable to take advantage of most of the EAHE potential (during night-time) and, additionally, avoid spurious energy consumption in periods when the ground temperature is lower than ambient temperature. Normally, the EAHE system is more thermally efficient during the cooling season, when the difference between ambient and the soil temperature rises significantly.

The parametric study was addressed to assess the influences of pipe length and diameter, air velocity, pipe material and soil topology on the thermal performance of the EAHE, while realizing whether and/or how the pilot EAHE, installed a few years before this thesis work started, could have be better installation could have a better achievement. The main conclusions were the following:

- The pipe length of 24 m has the better overall thermal performance. The difference between inlet and outlet air temperatures grows with the pipe length. In cooling, this difference increases when the inlet air temperature increases, heating when air temperature fall down. In the studied case, the maximum efficiency is achieved with pipe length of 100 m. However, from

the optimal length of 24 m the COP decreases due to the increase of pressure drop;

- For a suitable thermal performance of the EAHE, pipes diameter should be lower or equal to D200. For higher pipe diameters the efficiency of the heat exchanger and the COP drops;
- With the increase of air velocity on the DN110 pipes, the daily mean efficiency and the COP decrease due the rise of pressure losses;
- PVC is a good option in terms of costs, mechanical resistance and thermal performance. Pipes thermal conductivity has low influence on the overall system thermal performance as the thermal resistance for the thickness direction is almost null;
- For a suitable thermal performance, the soil thermal conductivity should be greater than $1.5 \sim 2 \text{ W/(m.}^\circ\text{C)}$. The coefficient of performance and the daily mean efficiency rises with the increase of soil thermal conductivity.

It should be remarked that a segregated parametric study is not an optimization one. In fact, when searching for the values of one of the considered parameters, it is not granted that the “optimal” values (already) found for the remaining ones keep the same. Therefore, the conclusions just listed should not be understood in their strict, absolute sense, but above all as indicative guidelines for a suitable design, and operation control, of an efficient EAHE

CHAPTER VI

Computational fluid dynamic modelling of an earth-to-air heat exchanger

VI.1. Introduction

Earth-to-air heat exchangers (EAHE's) are exclusively used for building ventilation when the outdoor temperature fluctuations are high when compared with ground temperature reducing the energy requirements for air conditioning in buildings. In this thesis work, transient three-dimensional models based on computational fluid dynamics (CFD) were developed in Ansys CFX 18.0 to predict the airflow and soil temperature distributions either in cooling or heating operation modes. The standard $k-\varepsilon$ model is used to simulate the turbulent characteristics of the airflow inside the EAHE pipes. CFD simulation is validated against experimental data obtained from the continuous monitoring of a pilot installation, which were presented in Chapter V. CFD results are also compared with results obtained with the ε -NTU formulation presented in Chapter V.

Based on the validated numerical configurations, a second CFD model is developed. This model is used to investigate in further detail one of the tubes of the EAHE pilot installation. This geometry consists in one single pipe with diameter of DN110, 24 meters of length buried at a 1.9 m depth. By simplifying the geometry, it is possible to study more accurately the transient effect of different parameters such as pipe diameter, air velocity and space between pipes. The main objective is to propose criteria which can be used during the design phase of an EAHE. The parametric study is performed by combining the three parameters and by analysing the effect of each on the air outlet temperature and on the heat transfer rate.

VI.2. CFD models

For better understanding of the transient behaviour of an earth-to-air heat exchanger, two 3D CFD models were developed to simulate the coupled heat

transfer and turbulent flow, using the Ansys CFX 18.0 commercial software. The first model reproduces the pilot installation (located in Coimbra, Portugal) presented in Chapter V (a full-scale 3D model) that is used to simulate two days of heating operation mode with higher environment temperature fluctuations. The second one is focussed on a single pipe of the EAHE pilot installation and is aimed at investigating the transient behaviour in both heating and cooling operation modes. CFD based analysis has been first employed to determine the temperature field around the buried pipe of EAHE. A grid sensitivity analysis was performed to determine a suitable grid refinement in the near-wall region of the airflow domain, in order to ensure an accurate representation of the boundary layer. Consequently, the first grid cell height is set small enough to accurately model the flow in regions of low turbulence level or complex/separated flow (the limit of $y^+ < 1$ for the highest dimensionless distance to the wall is a usual criterion for low-Reynolds turbulence models).

Since ground temperature gradients in the soil are sharper around the pipe, the numerical grid is denser in that zone, while it is sparser farther way from the pipe wall. An adaptive time-step is set for transient simulations. The pressure-velocity coupling in CFX is implemented using Rhie-Chow algorithm by default. The second-order backward Euler scheme is adopted for the discretization of the governing equations. The convergence criteria for all variables were set to 10^{-4} according with the minimum convergence criterion of Ansys CFX. Domain imbalance is also set to be lower than 1%. Due to the high complex geometry of the pilot installation, which would require a great computation capacity and time, the first CFD model was used only to validate the configurations implemented in CFX.

The CFD results are compared with experimental and analytical values presented in Chapter V. This model also allows the validation of ground temperature which is very difficult to calculate due to the ground thermal properties which usually are not well known. Based on the calibrated configurations, the second CFD model is used in detail and a parametric study is present. In this present study the following assumptions are used: (1) the air is assumed as an incompressible fluid; (2) the soil is homogeneous with constant thermophysical properties. The values of the ground thermal properties are presented in Table V.1, and were calibrated using Kusuda equation presented in Chapter IV.

Table VI.1 – Thermo-physical properties of materials used in simulation.

Material	Thermal Conductivity [W/m/°C]	Thermal Capacity [J/kg/°C]	Density [kg/m³]
Air (Ideal Gas)	0.026	1.004	1.250
PVC	0.17	900	1380
Soil	1.50	1408	2700

VI.2.1. Mathematical model

The heat flux through the Earth crust associated with the natural geothermal temperature gradient is essentially one-dimensional and dependent on the transient environmental conditions on its surface. Therefore, the temperature distribution in the ground is governed by the one-dimensional, unsteady heat conduction equation:

$$\frac{\partial^2 T}{\partial z^2} = \frac{1}{\alpha_s} \frac{\partial T}{\partial t} \quad (60)$$

where z is the vertical coordinate (ground depth) and α_s is the thermal diffusivity of the soil. On the other hand, when analyzing an EAHE, one must consider simultaneously the convective heat transfer between the pipes' internal wall surfaces and the airflow, coupled with heat conduction through the pipes' walls and the soil. The numerical modeling of these phenomena requires the solution of the mass, momentum and energy conservation equations [Eqs. (61), (62)-(64) and (65), respectively], which in Cartesian coordinates can be written as (Navier-Stokes Eqs.):

Continuity equation:

$$\frac{\partial \rho}{\partial t} + \frac{\partial(\rho u)}{\partial x} + \frac{\partial(\rho v)}{\partial y} + \frac{\partial(\rho w)}{\partial z} = 0 \quad (61)$$

x – Moment equation:

$$\frac{\partial(\rho u)}{\partial t} + \frac{\partial(\rho u^2)}{\partial x} + \frac{\partial(\rho uv)}{\partial y} + \frac{\partial(\rho uw)}{\partial z} = -\frac{\partial p}{\partial x} + \frac{1}{\text{Re}_d} \left[\frac{\partial \tau_{xx}}{\partial x} + \frac{\partial \tau_{xy}}{\partial y} + \frac{\partial \tau_{xz}}{\partial z} \right] \quad (62)$$

y – Moment equation:

$$\frac{\partial(\rho v)}{\partial t} + \frac{\partial(\rho uv)}{\partial x} + \frac{\partial(\rho v^2)}{\partial y} + \frac{\partial(\rho vw)}{\partial z} = -\frac{\partial p}{\partial y} + \frac{1}{\text{Re}_d} \left[\frac{\partial \tau_{xy}}{\partial x} + \frac{\partial \tau_{yy}}{\partial y} + \frac{\partial \tau_{yz}}{\partial z} \right] \quad (63)$$

z – Moment equation:

$$\frac{\partial(\rho w)}{\partial t} + \frac{\partial(\rho u w)}{\partial x} + \frac{\partial(\rho v w)}{\partial y} + \frac{\partial(\rho w^2)}{\partial z} = -\frac{\partial p}{\partial y} + \frac{1}{\text{Re}_d} \left[\frac{\partial \tau_{xz}}{\partial x} + \frac{\partial \tau_{yz}}{\partial y} + \frac{\partial \tau_{zz}}{\partial z} \right] \quad (64)$$

Energy equation:

$$\begin{aligned} \frac{\partial(E_t)}{\partial t} + \frac{\partial(uE_t)}{\partial x} + \frac{\partial(vE_t)}{\partial y} + \frac{\partial(wE_t)}{\partial z} = & -\frac{\partial(up)}{\partial x} - \frac{\partial(vp)}{\partial y} - \frac{\partial(wp)}{\partial z} - \frac{1}{\text{Re}_d \text{Pr}} \left[\frac{\partial q_x}{\partial x} + \frac{\partial q_y}{\partial y} + \frac{\partial q_z}{\partial z} \right] \\ & + \frac{1}{\text{Re}_d} \left[\frac{\partial}{\partial x} (u\tau_{xx} + v\tau_{xy} + w\tau_{xz}) + \frac{\partial}{\partial y} (u\tau_{xy} + v\tau_{yy} + w\tau_{yz}) + \frac{\partial}{\partial z} (u\tau_{xz} + v\tau_{yz} + w\tau_{zz}) \right] \end{aligned} \quad (65)$$

where u , v and w are the velocity components in x , y and z directions, and p is the pressure of the air flow. q , τ and E_t are the heat flux, the stress tensor and total energy.

To account for the effects of turbulence in CFD, there is a great variety of turbulence models. The k - ε turbulence model has been widely used in applied engineering problems and is suited to confined and mostly attached fully turbulent flows; it requires the solution of two additional equations (formally similar to the above conservation equations), namely for the:

Turbulence kinetic energy (k) and turbulence dissipation (ε_d):

$$\frac{\partial(\rho k)}{\partial t} + \frac{\partial(\rho k u_j)}{\partial x_j} = \frac{\partial}{\partial x_j} \left[\left(\mu + \frac{\mu_t}{\sigma_k} \right) \frac{\partial k}{\partial x_j} \right] + P_k - \rho \varepsilon_d + P_{kb} \quad (66)$$

$$\frac{\partial(\rho \varepsilon_d)}{\partial t} + \frac{\partial(\rho \varepsilon_d u_j)}{\partial x_j} = \frac{\partial}{\partial x_j} \left[\left(\mu + \frac{\mu_t}{\sigma_\varepsilon} \right) \frac{\partial \varepsilon_d}{\partial x_j} \right] + \frac{\varepsilon_d}{k} (C_{1\varepsilon} P_k - C_{2\varepsilon} \rho \varepsilon_d + C_{1\varepsilon} P_{\varepsilon b}) \quad (67)$$

where, u_j represents velocity component in each direction, P_{kb} and $P_{\varepsilon b}$ represent the influence of the buoyancy forces and P_k is the turbulence production due to viscous forces. μ_t represent the turbulent viscosity given by:

$$\mu_t = \rho C_\mu \frac{k^2}{\varepsilon_d} \quad (68)$$

The model constants are (Costa, Oliveira and Blay, 1999):

$$C_\mu = 0.09 \quad \sigma_k = 1.00 \quad \sigma_\varepsilon = 1.30 \quad C_{1\varepsilon} = 1.44 \quad C_{2\varepsilon} = 1.92 \quad (69)$$

VI.2.2. Initial and boundary conditions

To simulate the EAHE system in transient conditions, initial conditions must be defined. Regarding the ground temperature, a distribution is assigned, with values corresponding to the on *in-situ* measured data. As for the fluid domain, it is assumed as stagnant and at the measured ground temperature $t = 0$ h.

The calculation domain represents the ground as a parallelepiped homogeneous solid around the heat exchangers. The main initial and boundary conditions of the transient model are:

- (a) Soil boundary conditions: a time-varying vertical profile of the soil temperature based on the measured values is specified. Figure VI.1 presents the average ground temperature measured at different depths, used for the initial conditions ($t = 0$) and for the two consecutive days of transient simulation. To simplify, approached linear profiles are used for the vertical temperature distribution. Adiabatic conditions are set to the all lateral surfaces of the ground domain;

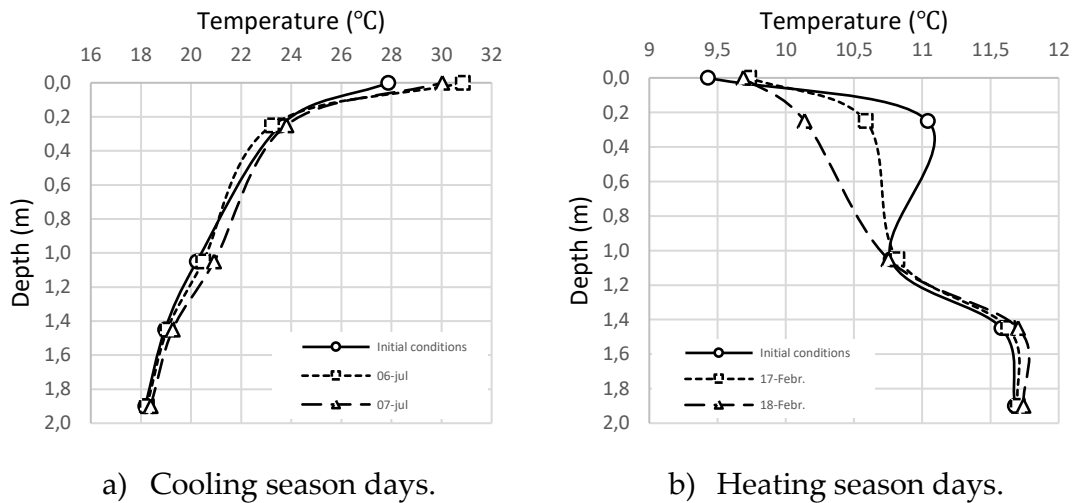


Figure VI.1 – Mean ground temperature profiles in cooling and heating operation modes (measured values).

- (b) Inlet boundary: at the air inlet section of the EAHE, a CFX Expression Language (CEL) function is used to specify a time-varying inlet temperature (*in-situ* measurements). Constant pressure (0 Pa) and turbulence intensity (5%) are assigned;
- (c) Outlet boundary: a CEL function that ensures overall mass conservation is used as input for time-varying mass flowrate (*in-situ* measurements) normal to the flow direction;

(d) A conservative interface flux condition between fluid and pipe was considered for heat transfer;

(e) The variations of the soil surface temperature due to solar radiation and heat convection are not considered in these models (they are implicit in the assigned time-varying vertical profiles).

VI.2.3. Validation of CFD models

VI.2.3.1. Geometry of the EAHE pilot installation (Model 01)

The first three-dimensional model reproduces the real EAHE pilot installation geometry investigated in Chapter V. This model aims to validate the CFX simulation setup. Further on, these configurations are used for a more detailed investigation with a single pipe (Model 02). The validation is carried out in heating operation mode. The CFD model simulates a 43-hour period of heating condition based on measured values of the environment air and ground temperatures on 17th and 18th of February. The average air flow rate of the system is 452 m³/h, as measured at the heat exchanger outlet. Figure VI.2a indicates a very good agreement between CFD simulation and experimental results, with a mean square error of 0.03 °C and an average temperature difference of 0.18 °C.

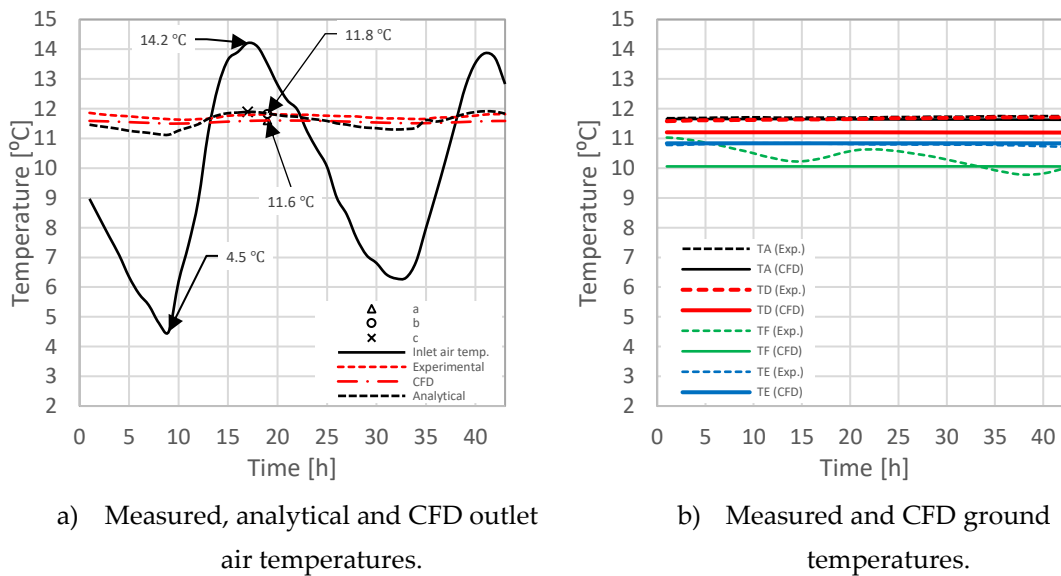


Figure VI.2 – CFD validation against measured values.

Figure VI.2a also presents the air outlet temperature values achieved by using the one-dimensional analytical model. This model was validated in Chapter V with a mean square error of 0.08 °C and average difference of 0.23 °C. The curves indicate that the CFD simulation fits better the experimental results than the analytical model. However, some assumptions considered in the analytical model, such as one-

dimensional and steady-state conditions during each 1-hour time-step, have influence on the heat transferred. The influence of the ground thermal inertia on the outlet air temperature is observed in both CFD and experimental results. Points a (CFD) and b (experimental) indicate the time when the maximum outlet air temperatures are achieved ($t = 19\text{h}$).

In the CFD results, it can be observed a delay of two hours between inlet and outlet air temperature. The analytical model cannot consider the ground inertia and the maximum outlet air temperature is observed at the same time as the inlet air temperature. For the minimum inlet air temperature ($4.5\text{ }^{\circ}\text{C}$ after 9h of simulation), the difference between CFD and measured values of the outlet temperature is $0.15\text{ }^{\circ}\text{C}$. Figure VI.3 shows a temperature distribution of the air along the pipes. It is observed an almost constant air temperature on the last distribution/collecting pipe. This means that the main amount of heat transfer is established, and almost uniformly, in the seven parallel pipes.

Figure VI.2b presents the ground temperature distribution with CFD and *in-situ* values. The ground temperature gradient was specified based on two points (sensors), sensor A (1.9) and E (1.05) (Figure VI.4). It was found a good agreement between CFD model and measured data with MSE of $0.075\text{ }^{\circ}\text{C}$ and $0.04\text{ }^{\circ}\text{C}$ for sensor A and E, respectively. Due to the (time-varying) linear profile set for the ground temperature, sensors D and F have higher mean square error of $0.46\text{ }^{\circ}\text{C}$ and $0.39\text{ }^{\circ}\text{C}$, respectively. From these results, it can be concluded that the numerical model provides an acceptable accuracy to perform further analyses with different EAHE configurations.

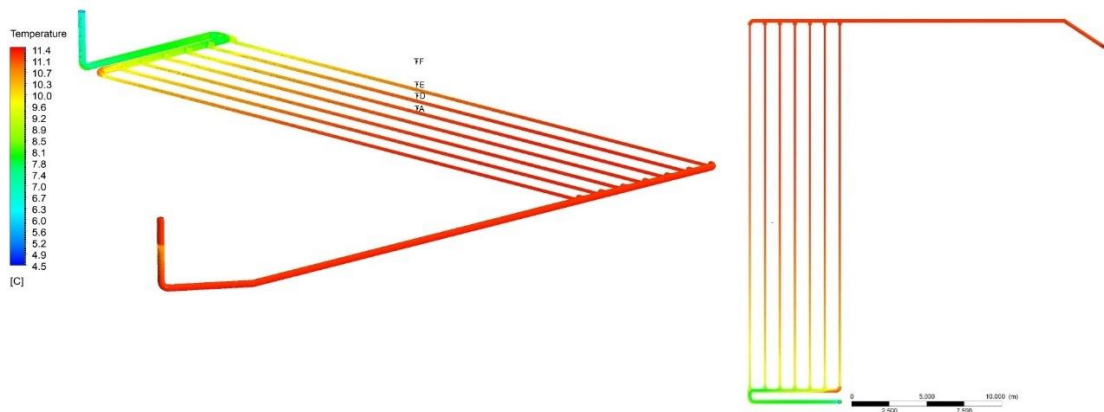


Figure VI.3 – Air temperature distribution along the EAHE at $t = 9$ hours ($T_{a, in} = 4.5^{\circ}\text{C}$) of simulation.

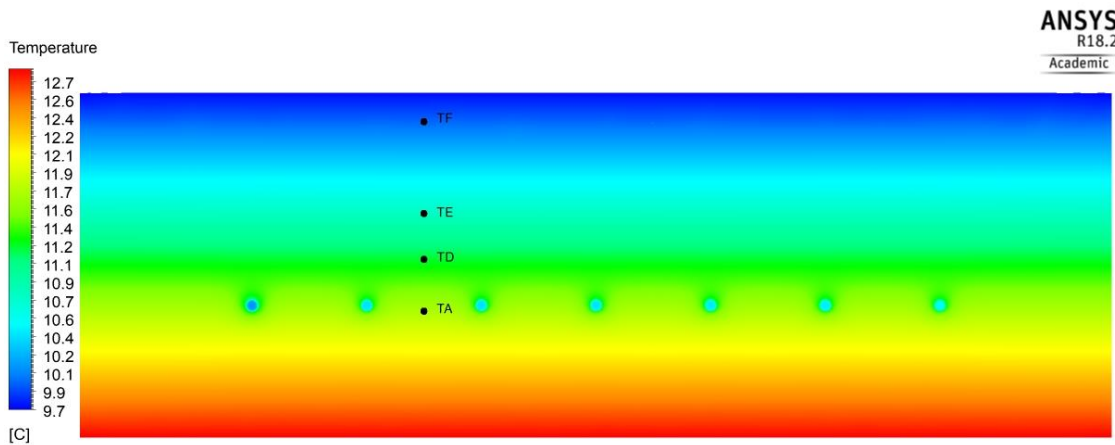


Figure VI.4 – Temperature contour for $t = 9$ hours at a 12 m length (sensors location).

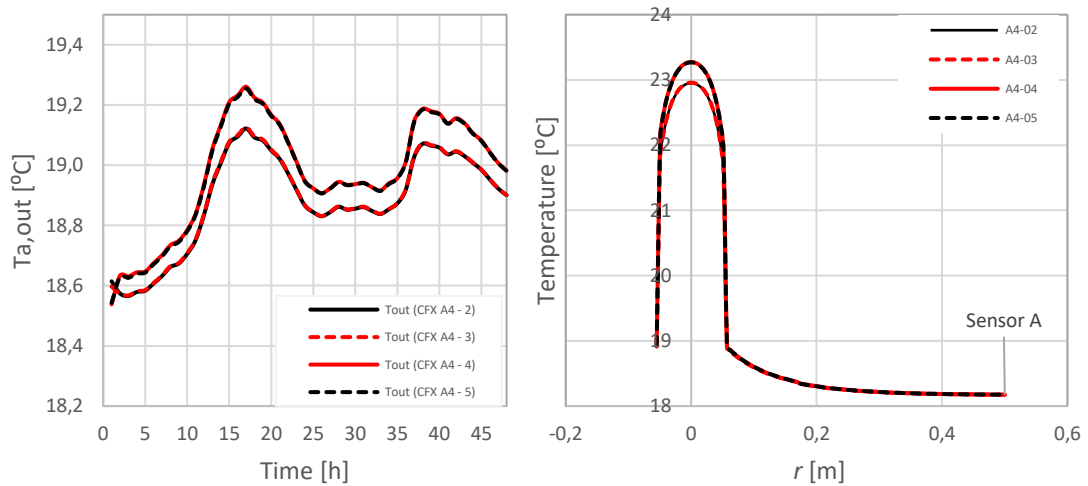
VI.2.3.2. Single pipe (Model 02)

The pilot installation modelled in the previous section has a rather complex geometry mainly due to the distribution pipes (perpendicular to the parallel pipes). This means that the CFD modelling of the complete geometry of a EAHE will take too much computational time in view of further parametric investigations. It took almost two weeks of simulation to achieve the results presented in the previous section. The computer used has a i7-6700 [CPU@3.40](#) GHz and 32 GB of internal memory. From the temperature contours (*cf.* Fig. VI.3), it is found that the seven parallel pipes of the pilot installation are the core of the EAHE, representing a major part of the heat exchange area. However, the distribution pipes still have a non-negligible effect on the outlet air temperature, mainly the one that brings the ventilation air into the building (it is longer). Some gradients of air temperature are also observed in Figure VI.3 in the vertical, terminal pipe branches which are associated with the soil temperature gradient near the surface.

In Chapter V, it was also found that the last distribution pipe influences the outlet air temperature mainly when the system is operating in cooling mode. However, the distribution pipes depend on the place where the EAHE will be buried, the distance from the building and the airflow rate. Knowing this, a second CFD model is developed. This model simulates one single pipe of the pilot installation ignoring the effects of the distribution pipes. This allows the characterization of thermal performance of one pipe which can be used during the design steps. Furthermore, due to the simplicity of the second model geometry, increased rates of accurate convergence are achieved. The model geometry consists in one single pipe with 24 m of length, 110 mm of diameter and buried at 1.9 depth. The ground domain is

considered a parallelepiped solid around the pipe with 24 m of length, 1 m height and 1 m width. The model is used to simulated 43 hours of heating and 48 hours of cooling operation modes. The mass airflow rates are considered equal to the measured values divided by seven. The mean air velocity is 0.96 and 2.1 m/s in cooling and heating simulations, respectively.

A grid-dependence study was carefully performed by monitoring the ground (sensor A) and outlet air temperatures. The complete study is presented as Annex of this thesis. Figure VI.5 illustrates the results of the grid dependence tests, by refining successively the air domain (from grids n. 2 to 5) considering low values of Reynolds ($y^+ < 1.0$) and low air velocities which are usually harder to converge. The graphs in Figure VI.5a) and b) plot, respectively, the air outlet temperature and domain temperature radial profiles in a cross section (at 12 meters length) for $t = 17$ h, when the maximum inlet temperature is registered. It is observed a convergence towards the grid independence. The highest difference between air outlet temperature predicted with the different grid is 0.15 °C, observed at 17 h (tolerance 0.5 °C). The cross-section temperature profiles in Figure VI.5b) also show the thermally affected zone of the ground; although the radial temperature gradient tends to zero for $r > 0.4$ m, it can be inferred that the distance between parallel pipes should preferably not be less than 1 m.



a) Air outlet temperature.

b) Cross-section temperature distribution.

Figure VI.5 – Numerical results for grid refining in air domain.

Figure VI.6 allows to compare the time evolutions of the outlet air temperatures predicted by CFD and by the analytical model, in cooling and heating conditions. It is observed a good agreement between both models in cooling with mean square error of 0.28 °C and a mean difference between wall heat transfer coefficient of 0.03

$\text{W/m}^2\cdot^\circ\text{C}$. In heating conditions this difference is higher. The MSE is $0.33\text{ }^\circ\text{C}$ and the mean difference between wall heat transfer coefficient is now $6.28\text{ W/m}^2\cdot^\circ\text{C}$. It can be also noticed a delay of one hour in the outlet air temperature obtained with CFD simulation due to the ground thermal inertia. This delay is now lower compared with the full geometry of the EAHE installation.

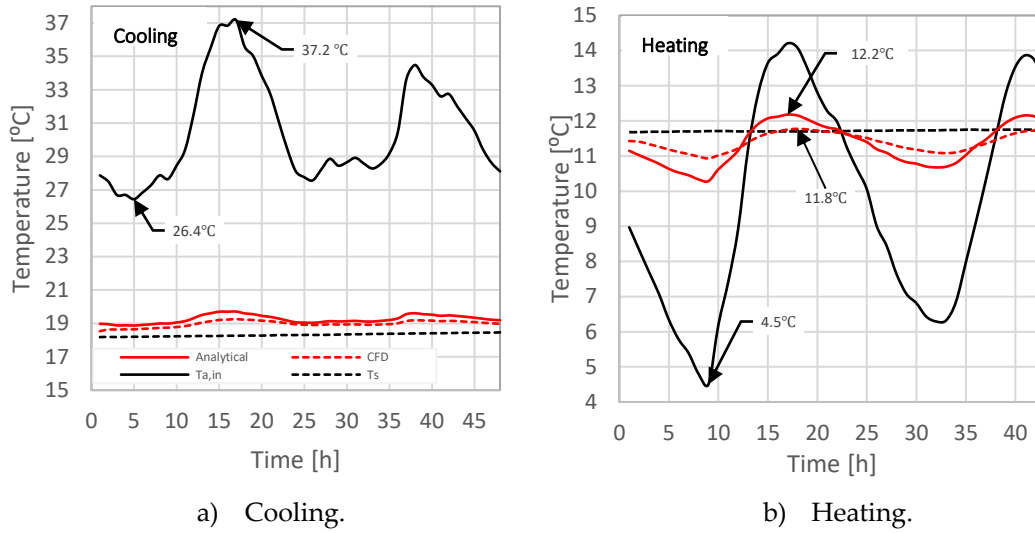


Figure VI.6 – CFD and analytical air outlet temperature for cooling and heating ($\dot{V} = 210\text{ m}^3/\text{h}$ in cooling and $\dot{V} = 433\text{ m}^3/\text{h}$ in heating).

VI.3. Parametric Study

The second CFD model is used to assess the effect of design and operating parameters on the transient outlet air temperature and heat transfer rate. Design parameters such as pipe diameter and distance between parallel pipes are studied for different air velocities (operation parameter). The parametric study is conducted for heating and cooling operation modes. Investigation is divided into two parts: (1) combined effects of air velocity and pipe diameters with one single pipe; and (2) influence of the pipes' distance testing values of 0.25, 0.5 and 1.0 m. The values of the air velocity considered are presented in Table VI.2, as well as the ones corresponding to the experimental airflow rates. The study is performed only for pipe diameters of DN110, D160 and DN200, since it was concluded in Chapter V that the COP and heat exchange efficiency decrease for higher diameters.

Table VI.2 – Parametric study with a single pipe EAHE for different air velocities and diameters.

DN	Mode	Experimental Air Velocity	1 m/s	2 m/s	3 m/s	4 m/s	5 m/s
110	Cooling	✓ (1 m/s)	✓	✓	✓	✓	✓
160		✓ (0.46 m/s)	✓	✓	✓		
200		✓ (0.29 m/s)	✓	✓	✓		
110	Heating	✓ (2 m/s)	✓	✓	✓	✓	✓
160		✓ (1 m/s)	✓	✓	✓		
200		✓ (0.63 m/s)	✓	✓	✓		

VI.3.1. Effect of pipe diameter operating with different air velocities

The effect of the pipe diameter operating with different air velocities is here presented. The section of air velocities is performed based on the airflow Reynolds number, of which some values are indicated below in Figure VI.7, for reference. The investigation is performed for air velocities between 1 m/s to 5 m/s in DN110 and between 1 m/s to 3 m/s in DN160 and DN200.

In most practical situations of fluid flows inside ducts, the flow regime is laminar for Reynolds number values below 2300, fully turbulent for $Re > 10000$, and transitional between these values. However, in many cases, depending on the existence of turbulence promoting factors (*e.g.*, surface roughness, flowrate fluctuations, duct vibrations, etc.), the flow becomes fully turbulent for $Re > 4000$ (Çengel, 2009). If enhancing the convection heat rate is a main goal, a fully turbulent flow regime is desirable. Therefore, in the case of the present EAHE pilot installation, with stationary, smooth-surface PVC pipes and operation at constant flow rate regimes, a reference value of $Re > 10^4$ should be envisaged for the sake of enhancing the EAHE thermal performance.

Since the Reynolds number varies inversely with the pipe diameter, for a given flow rate, it is easy to understand that combining the values of airflow rate recorded in the experiments with higher pipe diameters can result in laminar flow regimes, which is disadvantageous for the EAHE thermal efficiency. Note that, even for the DN110 pipe of the pilot installation, $Re \sim 2000$ for the lowest experimental value of the air velocity in Table VI.2 (0.29 m/s).

Figure III.7 shows the temperature distribution in a vertical cross section of the soil and flowing air domain at mid-length of the pipe, for $t = 17$ h of the EAHE simulation

in cooling operation. It is seen that by increasing the air velocity the temperature of the soil adjacent to the pipes increases (Figure III.7a *vs.* b) as consequence of the enhanced heat flux (increased U_i by way of rising the internal convection coefficient, h_i). That influence on the soil temperature gradient is much more pronounced when the pipe diameter is increased considering the same air velocity (Figure III.7b and c); in this case, there is a threefold effect on the pipe heat rate (see Eq. 36.a): both U_i and A_i increase, and ΔT_{mi} as well. The comparison between Figure III.7a and b illustrates the difference of having a transitional or a fully turbulent airflow regime (although ΔT_{mi} also increases from a) to b)). Figure III.7c shows a much higher temperature of the air flow in the same pipe section, in spite of the evident increase of the convective heat flux to the soil. This is explained by the fact that the airflow rate increases with d^2 , leading in the overall to a significant reduction of NTU, and thus of the temperature variation of the circulating air along the pipe.

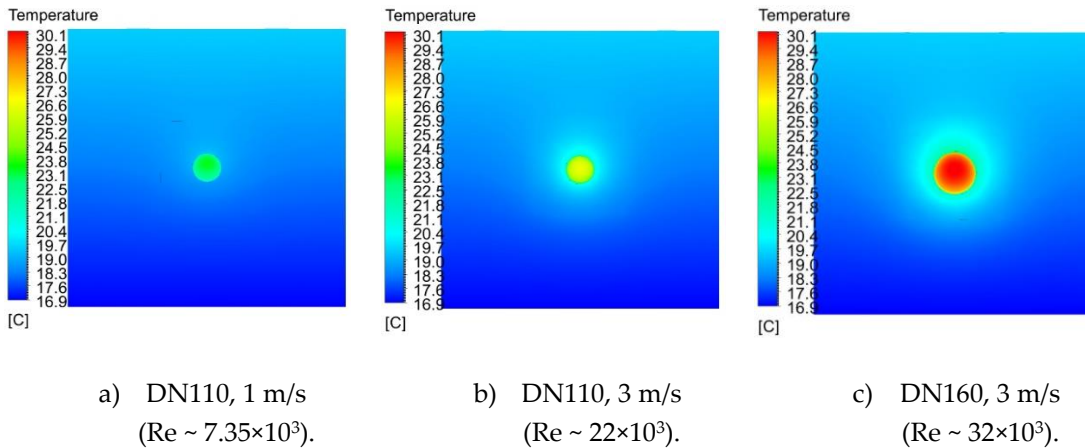


Figure VI.7 – Temperature distribution of the soil and flowing air domain in a vertical plane at the pipe mid-length for $t = 17$ h in cooling operation.

Figure VI.8 presents the outlet air temperatures for different air velocities and pipe diameters in cooling and heating operation modes. These results corroborate the above interpretation. In Chapter V it was found that, for the experimental airflow rates, pipe diameters with DN160 and DN200 led to better overall COP values, due to lower pressure losses. However, the daily mean efficiency of the EAHE becomes penalized. This is due to a lower thermal performance associated with transitional flow regimes (not fully turbulent), which happen for pipe diameters of DN160 and DN200 with mean air velocities of 0.46 m/s ($Re = 4762$) and 0.29 m/s ($Re = 3986$), respectively. Cooling mode simulations show that, with an increase of the pipe diameter from DN110 to DN160, the mean air outlet temperature increases 1.47 °C and 2.38 °C for air velocities of 1 m/s and 3 m/s, respectively, revealing a decrease in

CHAPTER VI

Computational fluid dynamic modelling of an earth-to-air heat exchanger

the desired cooling effect. This difference increases to 2.53 °C and 3.57 °C when the pipe diameter increases from DN110 to DN200. With DN200 pipe operating at 3 m/s, it is observed an air outlet temperature of 26.4 °C when the maximum environment, inlet air temperature is achieved. This air outlet temperature is higher than indoor comfort temperature (25 °C).

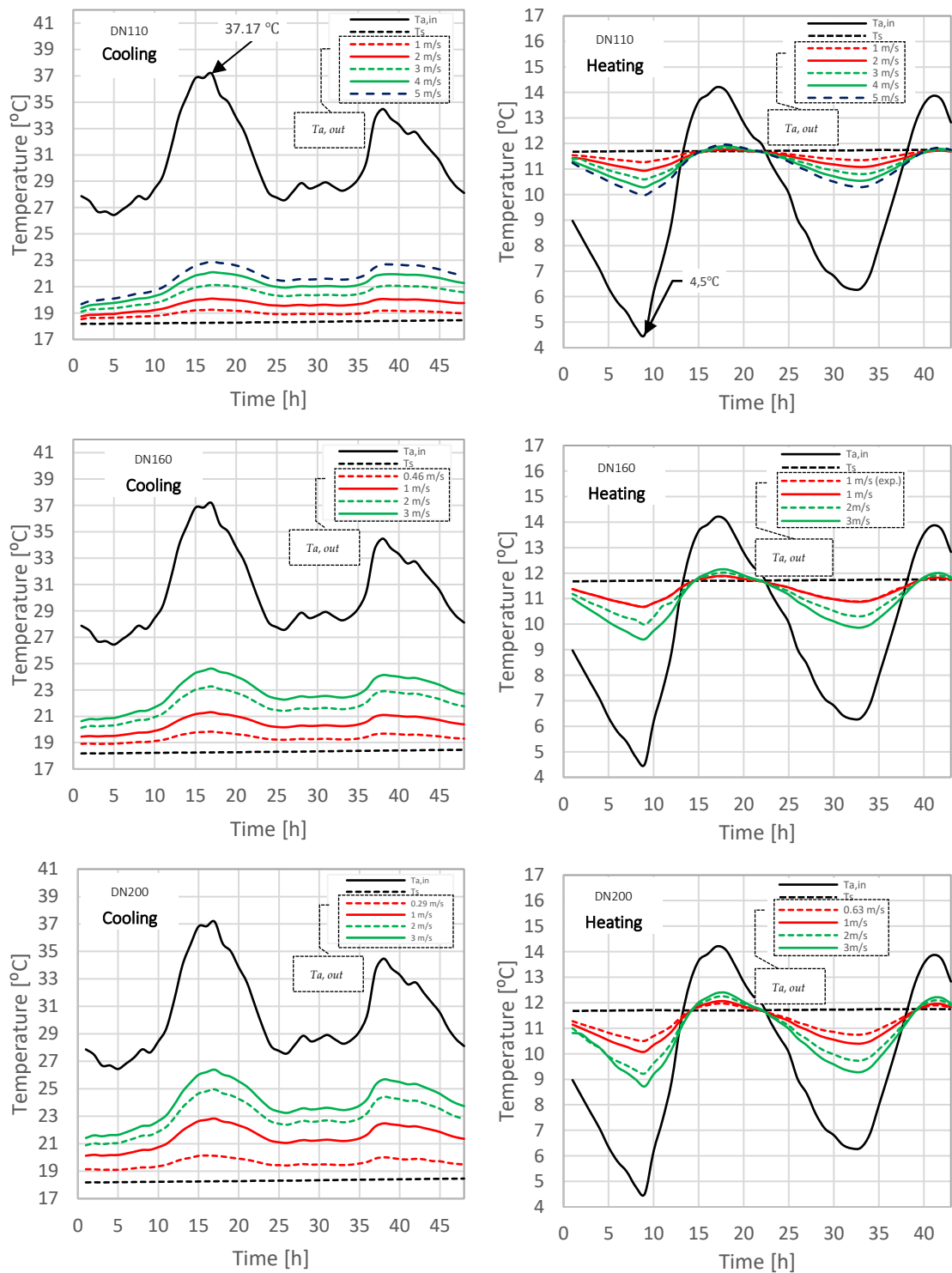


Figure VI.8 – Results from one-pipe simulation.

In heating mode, results are analysed only the time when the system is effectively gaining energy. With the increase of pipe diameter from DN110 to DN160 it is observed a decrease of the mean outlet air temperature of $-0.32\text{ }^{\circ}\text{C}$ and $-0.64\text{ }^{\circ}\text{C}$ for air velocities of 1 m/s and 3 m/s , respectively. This difference still increases when the pipe diameter is increased to DN200. These simulation results for the heating mode show that the EAHE cannot by itself render a sufficiently warm indoor environment.

The mean heat rate for different pipe diameters and air velocities is presented in Figure VI.9. The diameter (d_i) of DN160 and DN200 with respect to DN110 is 2.1 and 3.3 higher, respectively. Based on the mean heat transfer rate and considering the pilot installation conditions (*i.e.* air velocity), the number of parallel pipes can be reduced near to a half or one third using pipe diameters of DN160 and DN200, respectively.

The COP of DN160 and DN200 is higher regardless of the air outlet temperature as it was shown in Chapter V. DN200 with air velocity of 3 m/s will not fit the indoor temperature requirements. DN160 is a good option in terms of thermal performance and number of pipes.

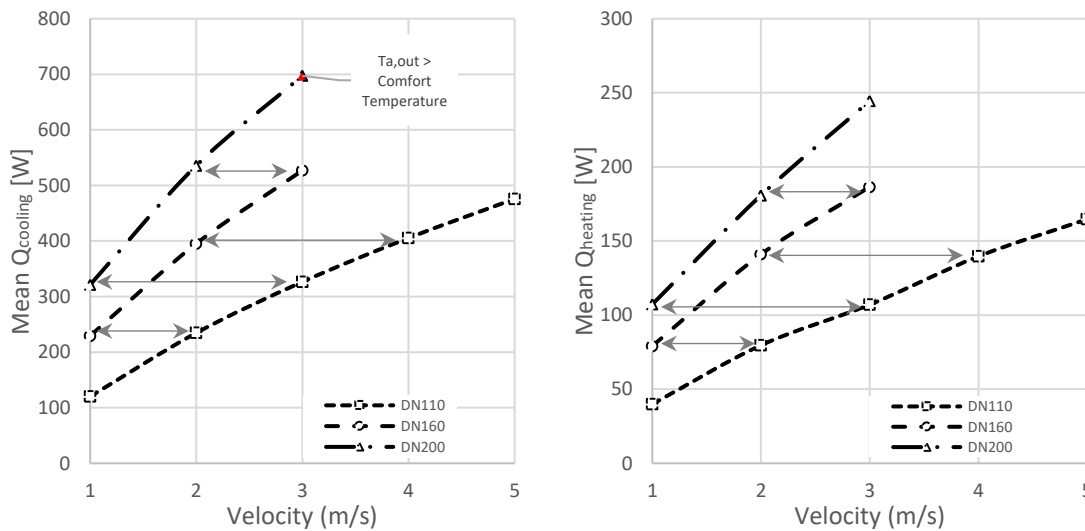


Figure VI.9 – Mean heat rate for different pipe diameter and air velocities.

VI.3.2. Space between adjacent pipes

To investigate the effect of the spacing between adjacent pipes, a second parametric study is performed. Table VI.3 summarises the parametric investigation. The CFD models are developed considering three pipe diameters and different air velocities. The distance between pipes (d_p) is considered equal to 1.0 , 0.5 and 0.25 m . Higher Pipe spacings higher than that in the pilot installation (1.0 m) were not considered in this study because it was found before that the thermally affected zone of the soil

was lower than $r = 0.5$ m (*e.g.* Fig.VI.5. b and Fig.VI.7b). For DN200 the pipe spacing of 0.25 m was not considered in this study because it makes no sense: the parallel pipes would be too close to one another (just 5 cm between outer surfaces).

Table VI.3 – Parametric study for different pipe diameters, air velocities and pipe spacing.

DN	d_p (m)	Operation mode	Experimental Air Velocity	1 m/s	3 m/s	5 m/s
110	1, 0.5, 0.25	Cooling	✓ (1 m/s)		✓	✓
160			✓ (0.46 m/s)	✓	✓	
200			✓ (0.29 m/s)	✓	✓	
110	1, 0.5, 0.25	Heating	✓ (2 m/s)		✓	✓
160			✓ (1 m/s)	✓	✓	
200			✓ (0.63 m/s)	✓	✓	

Figure VI.10 presents the outlet air temperature for different pipe spacings and diameters, and air velocities. These simulations were carried out for heating and cooling modes. The detrimental effect on the outlet air temperature of reducing the pipes' spacing is more pronounced during cooling and much more evident for smaller distances between pipes. In heating operation mode this effect is not well noticed. This happens due to the fluctuations of the inlet air temperature, which happens frequently to have values above the soil temperature, during the day, and below, during the night. These temperature fluctuations in time override the effect of the soil inertia.

Figure VI.11 plots the difference in the heat transfer rate with the decrease of pipe spacing, relatively to the nominal value $d_p = 1.0$ m. Results are plotted for cooling and heating. This loss in the thermal performance increases due to the variation of the soil temperature along the simulation period, meaning that the thermally affected region of the soil is not wide enough for longer operation times. However, this type of system usually operates only over relatively short periods of time (*e.g.* residential and offices). This means that the temperature of the soil adjacent to the pipes would not vary continuously. Note also (especially in the graph for DN110) that, for the first time steps of simulation when the soil temperature has not changed yet significantly, the heat rate is higher for higher air velocities. This is due to the increased values of both U_i and ΔT_{ml} . On the other hand, as the soil temperature gets affected, the decay of becomes ΔT_{ml} predominant.

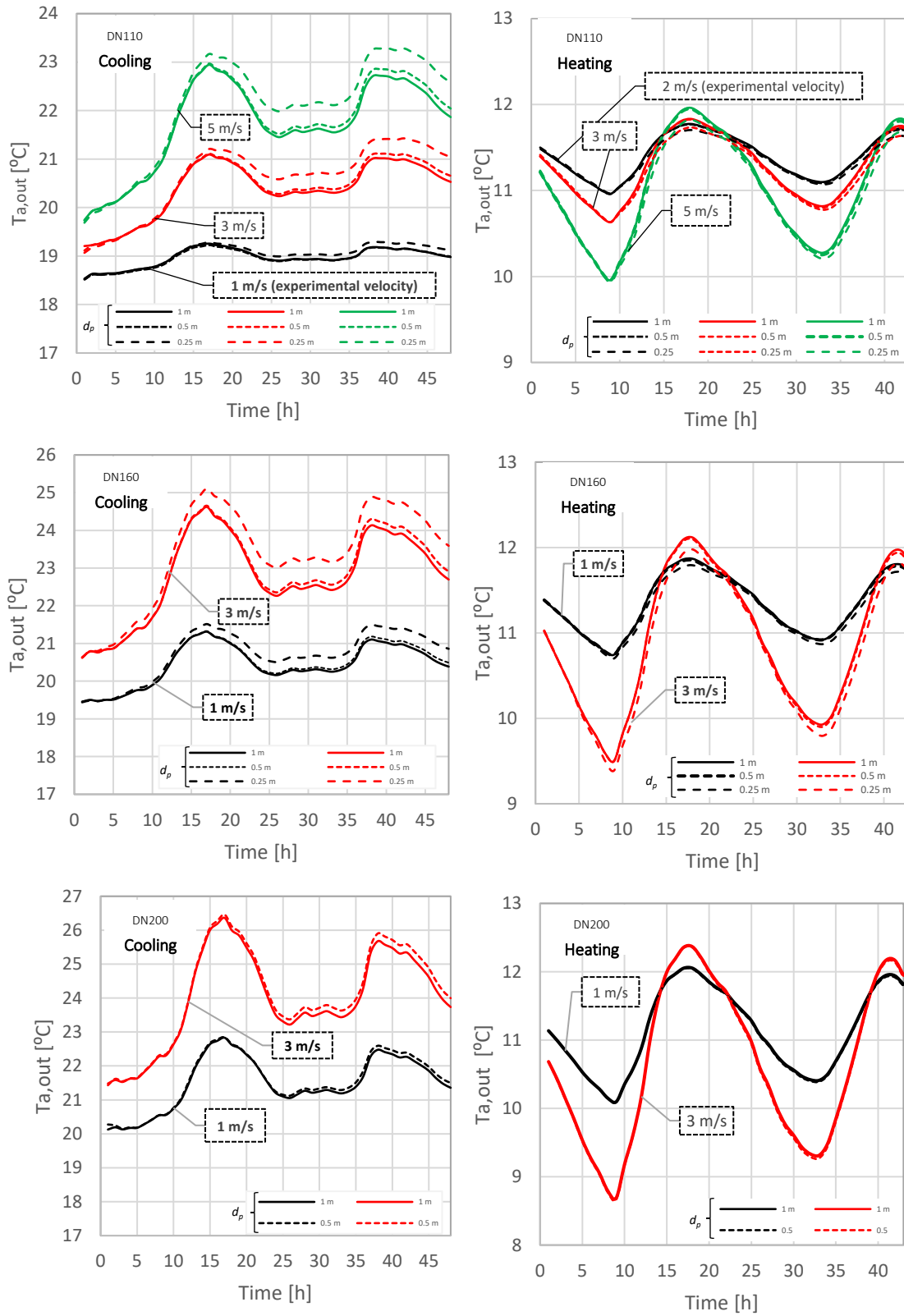


Figure VI.10 – Results for different pipe spacing and diameter, and air velocity.

CHAPTER VI

Computational fluid dynamic modelling of an earth-to-air heat exchanger

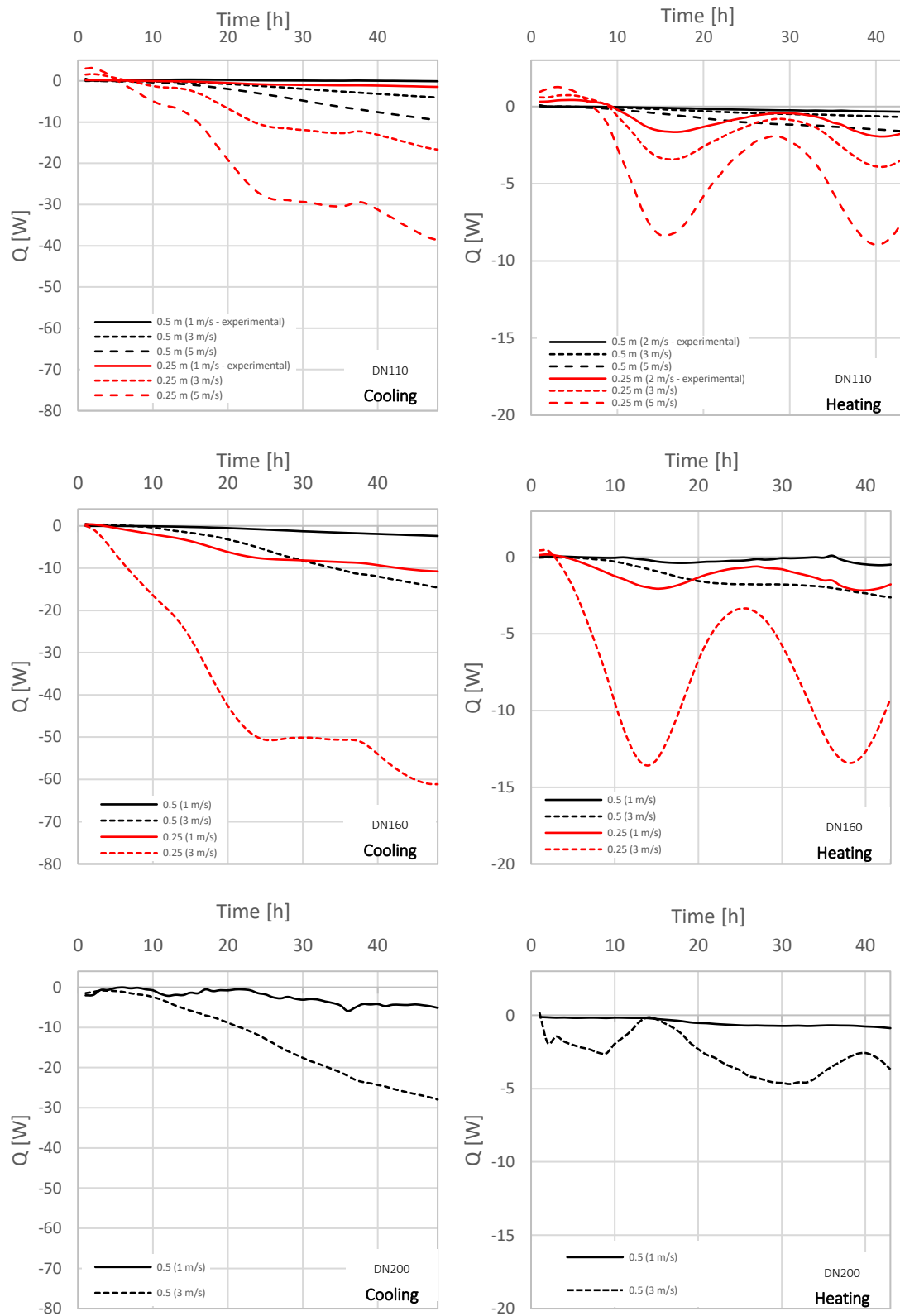


Figure VI.11 – Variation of the heat transfer rate per pipe with decreasing pipe spacing, relatively to $d_p = 1.0$ m.

Table VI.4 presents the maximum difference in outlet air temperature with the decrease of pipe spacing, relatively to the nominal $d_p = 1.0$ m. The maximum values were achieved at $t = 48$ h (final time-step). Results show that the effect of reducing the pipe spacing from 1.0 to 0.5 can be practically neglected for such a period of continuous operation. For instance, with DN160 pipes operating at 3 m/s, it is observed an increment of 0.21 °C on outlet air temperature, relatively to a nominal $d_p = 1.0$ m spacing. An increase of 0.89 °C is found when the spacing between pipes decreases from 1.0 to 0.25 m, for an air velocity of 3 m/s.

In heating (Table VI.5), it is apparent from the results that there is only a minor change in the air outlet temperature. The maximum decrease of 0.19 °C is achieved for pipe spacings of 0.25 m and with DN160 pipes operating at 3 m/s, relatively to a nominal $d_p = 1.0$ m.

Table VI.4 – Maximum difference in outlet air temperature with the decrease of pipe space, relatively to $d_p = 1.0$ m in cooling mode.

	$d_p = 0.5$ m $v = 1$ m/s	$d_p = 0.25$ $v = 1$ m/s	$d_p = 0.5$ m $v = 3$ m/s	$d_p = 0.25$ $v = 3$ m/s	$d_p = 0.5$ m $v = 5$ m/s	$d_p = 0.25$ m $v = 5$ m/s
DN110	0.01 °C	0.14 °C	0.12 °C	0.52 °C	0.18 °C	0.72 °C
DN160	0.10 °C	0.47 °C	0.21 °C	0.89 °C	-	-
DN200	0.17 °C	-	0.26 °C	-	-	-

Table VI.5 – Maximum difference in outlet air temperature with the decrease of pipe space, relatively to $d_p = 1.0$ m in heating mode.

	$d_p = 0.5$ m $v = 1$ m/s	$d_p = 0.25$ m $v = 1$ m/s	$d_p = 0.5$ m $v = 2$ m/s	$d_p = 0.25$ $v = 2$ m/s	$d_p = 0.5$ m $v = 3$ m/s	$d_p = 0.25$ $v = 3$ m/s	$d_p = 0.5$ m $v = 5$ m/s	$d_p = 0.25$ m $v = 5$ m/s
DN110			-0.02 °C	-0.09 °C	-0.02 °C	-0.12 °C	-0.03 °C	-0.17 °C
DN160	-0.02 °C	-0.10 °C			-0.04 °C	-0.19 °C		
DN200	-0.02 °C				-0.04 °C			

Table VI.6 and VI.7 present the loss of heat transfer rate per pipe relatively to the nominal $d_p = 1.0$ m. The maximum loss of heat transfer rate (-16.52 % in cooling and -12.61% in heating) is achieved in DN160 pipes spaced of 0.25 m and air velocity equal to 3 m/s. A lower effect is found for low air velocities and pipe spacing of 0.5 m.

Table VI.6 – Maximum difference in heat loss rate per pipe with the decrease of pipe spacing, relatively to $d_p = 1.0$ m in cooling.

	$d_p = 0.5$ m $v = 1$ m/s	$d_p = 0.25$ $v = 1$ m/s	$d_p = 0.5$ m $v = 3$ m/s	$d_p = 0.25$ $v = 3$ m/s	$d_p = 0.5$ m $v = 5$ m/s	$d_p = 0.25$ m $v = 5$ m/s
DN110	-0.11 %	-1.56 %	-1.64 %	-6.80 %	-2.83 %	-11.46 %
DN160	-1.36 %	-6.12%	-8.30 %	-16.52 %		
DN200	-2.12 %	-	-6.00%			

Table VI.7 – Maximum difference in heat loss rate per pipe with the decrease of pipe spacing, relatively to $d_p = 1.0$ m in heating.

	$d_p = 0.5$ m $v = 1$ m/s	$d_p = 0.25$ m $v = 1$ m/s	$d_p = 0.5$ m $v = 2$ m/s	$d_p = 0.25$ $v = 2$ m/s	$d_p = 0.5$ m $v = 3$ m/s	$d_p = 0.25$ $v = 3$ m/s	$d_p = 0.5$ m $v = 5$ m/s	$d_p = 0.25$ m $v = 5$ m/s
DN110		-	-0.93 %	-3.82 %	-1.38 %	-5.25 %	-2.33 %	-7.52 %
DN160	-1.46 %	-3.72 %			-3.60%	-12.61%		
DN200	-2.48%				-3.91%			

Considering the overall results of air outlet temperature and loss of heat transfer rate per pipe, it can be concluded that DN160 pipes operating with an air velocity range of 1 to 3 m/s and $d_p = 0.5$ would be a perfect fit for the presented conditions. This will allow reducing the number of pipes and terrain area.

VI.4. Conclusions

In this chapter, the temperature distribution and heat rate of flowing air through Earth-to-Air Heat Exchanger (EAHE) were studied using computation fluid dynamics (CFD) modelling with the commercial software Ansys CFX. The CFD models were used to predict the transient distributions of the air and ground temperature in heating and cooling operation modes, using the standard $k-\epsilon$ turbulence model. Two models were developed. The first model reproduces the pilot installation geometry (Chapter V). The second model simulates only one of the (main) parallel pipes of the installation to assess the influence of several geometrical and operating parameters on the EAHE thermal performance, neglecting the effect of the distribution pipes. The first CFD model was validated against experimental data with a mean square error of 0.03 °C and an average difference of 0.18 °C. CFD results were also compared with the ones achieved using the simple one-dimensional analytical model presented in Chapter IV. CFD modelling fits better the experimental results than the analytical model does. The CFD results illustrate the influence of ground thermal inertia. Further on, the second CFD model was used to investigate the effect of both design and operating parameters. The effect of pipe

diameter, pipe spacing, and air velocity were investigated. The following conclusions were drawn:

- The increase of air velocity leads to an increase of temperature of the soil adjacent to the pipes as a consequence of the enhanced heat flux. This is much more pronounced when the pipe diameter is increased considering the same air velocity;
- DN200 with air velocity of 3 m/s will not fit the indoor temperature requirements. An increase of the pipe length or a decrease in air velocity is recommended;
- These simulation results for the heating mode show that the EAHE cannot by itself render a sufficiently warm indoor environment.
- DN160 is a good option in terms of thermal performance, number of pipes and terrain area;
- The smaller space between pipes the higher the loss of heat transfer rate. This is more pronounced when the pipe diameter and air velocity increases;
- The spacing between pipes can be reduce to 0.5 m. A spacing of 0.25 m is only recommended for the DN110 pipes and air velocities lower than 3 m/s;
- In heating mode, the loss of heat transfer rate between pipes decreases due the environment air temperature fluctuations which annuls the effect of ground inertia;

The loss of heat transfer rate when the spacing between pipes decreases may be more pronounced for longer periods of continuous operation and for higher soil thermal conductivities. However, usually this type of systems only operates during short periods of time and the soil thermal properties (sandy and clayey soil) are suitable for a good thermal performance.

PART D

TROMBE WALL TECHNOLOGY

CHAPTER VII

Trombe walls review and design methods

VII.1. Introduction

Walls usually represents the largest envelope area of building that is exposed to outdoor conditions including solar radiation. Over the last years several passive wall/façade technologies are being used such as green walls, double skin walls, PCMs and solar walls. These technologies have been designed and proposed for better thermal insulation, shading the solar radiation, improved thermal comfort (ventilation and/or with thermal storage systems) and visual quality/comfort. Nowadays *intelligent façades* and *Kinetic façades* are being studied for different weather conditions and to be able to adapt to individual preferences. These façades can include solar shading devices (e.g. south-façade), and also with the ability to adapt their shapes considering the solar radiation, daylighting control, ventilation control and energy generation (Omran et al. 2016). When the temperature rises, especially in cities with warm weather, cost-effective and green solutions are necessary to increase buildings energy efficiency. Green walls are one of the main suggestions for this problem. They are composed with climbing plants that grow either directly against or on support structures integrated to exterior building walls (Cuce, 2016). The main advantage of these walls is the reduction of internal building temperatures mitigating building energy consumption. They can provide shading and thermal insulation reducing the external wall temperatures during warmer days and act as an additional exterior insulation material during colder days.

Double skin façades (DSFs) which are a “*special type of envelope where a second skin, usually a transparent glazing, is placed in front of a regular building façade*” (Safer et al. 2005). The air space between the two layers of DSFs performs as an insulating block and can integrate a controllable shading device (Shameri et al. 2011). DSFs wall can also be used to promote natural ventilation, and thermal comfort without any electric energy consumption. However, this system has higher costs (design, construction and maintaining), they increase the weight of buildings and there is a risk of overheating during sunny days (Omran et al. 2016). Usually the traditional TES

used in buildings can only store sensible heat by changing the temperature of a storage material that releases thermal energy. However, comparing with latent heat storages, by changing the phase of storage material, a much larger volume of material is necessary to store the same amount of energy (Soares *et al.* 2013). The application of Phase Changer Materials (PCMs) in walls is a well-known technology that can reduce the energy consumption in buildings. PCMs change phase from solid to liquid when the temperature rises, absorbing the heat. When the temperature drops, the PCMs change phase from liquid to solid realising thermal energy (Soares *et al.* 2013). Soares *et al.* presented a review of passive PCMs where can be found the main advantages and disadvantages of different kind of PCMs (Organic, Inorganic and Eutectic) based on literature. They concluded that PCMs systems can contribute to: (a) improve the thermal comfort; (b) improve the building envelope performance and to increase systems efficiency such as insulation; (c) reduce the energy loads and energy consumption; (d) use of solar energy and (e) the reduction of CO₂ emissions. The application of PCMs in LSF construction can be a solution to improve building thermal inertia. Another well-known technology is the passive solar walls or Trombe walls. The main function of passive solar walls is to enable solar energy collection in order to reduce the energy consumed for space heating. In the next section, it is presented a Trombe wall review based on literature. In this chapter a literature review of Trombe Wall technologies and the heat transfer fundamentals for design and energy performance evaluation is presented. This review is important to understand the design principles based on previous investigations and heat transfer fundamentals.

VII.2. Trombe wall technologies

Passive solar technologies are known as a way to use solar energy as a heating source for buildings space heating. The Trombe wall concept was presented by Edward S. Morse in 1881, and later developed by Felix Trombe and Jacques Michel gained popularization during the 60's (Omran *et al.* 2016). Trombe walls can reduce up to 30% of the energy consumed by the building for the HVAC systems (Zamora and Kaiser, 2009). Trombe wall can be used for space heating, cooling and ventilation by promoting buildings thermal comfort in several climatic zones (Figure VII.1). The main function of this type of wall is to convert the solar radiation into thermal energy that can be conserved and used when the occupants of the building desire (Llovera *et al.* 2011). The wall is composed by a glass layer, an air box or ventilated air layer and an inner storage wall composed of various materials that absorb and store thermal energy (Figure VII.1a). In the ventilated air layer, the air flow could be originated by natural convection in thermosiphon or by forced convection requiring

a fan. After absorbing thermal energy from the direct and diffuse radiation, the air flows to the interior of the building. The heat capacity of the wall is one of the greatest advantages of this kind of systems. This allows to storage the solar thermal gains obtained during the day-time and release it into the building overnight period (Abbassi *et al.* 2014). Between the air box and the compartment there are square-shaped holes or vents located in the lower and upper part of the wall which allows airflow through thermosiphon to the building interior. During the heating season, heat is absorbed by the storage layer (normally painted black) and released to the building interior during night periods. The vents must be open to increase the heat exchange between the air layer and building interior (Figure VII.1b). Appropriate use of the vents can increase the air changes between the air box layer and the building interior, as the stack effect is higher by incoming solar radiation through the glass. The stack effect can be defined as the movement of air into and out of building resulting from air buoyancy. In winter, warm air inside the building rises. The pressure in the bottom of the building is lower and the hot air is pushed to the top of the building (Lim *et al.* 2011). However, during the night periods, when the energy storage is not enough to provide thermal comfort, the vents can be closed to preserve the internal thermal energy of the building and to reduce the thermal losses to outside. During cooling season, the interior bottom vents should be opened, and the upper vents closed. Vents placed on the outside layer or glass layer, allows the hot air flows from inside to outside of the building (Figure VII.1 c).

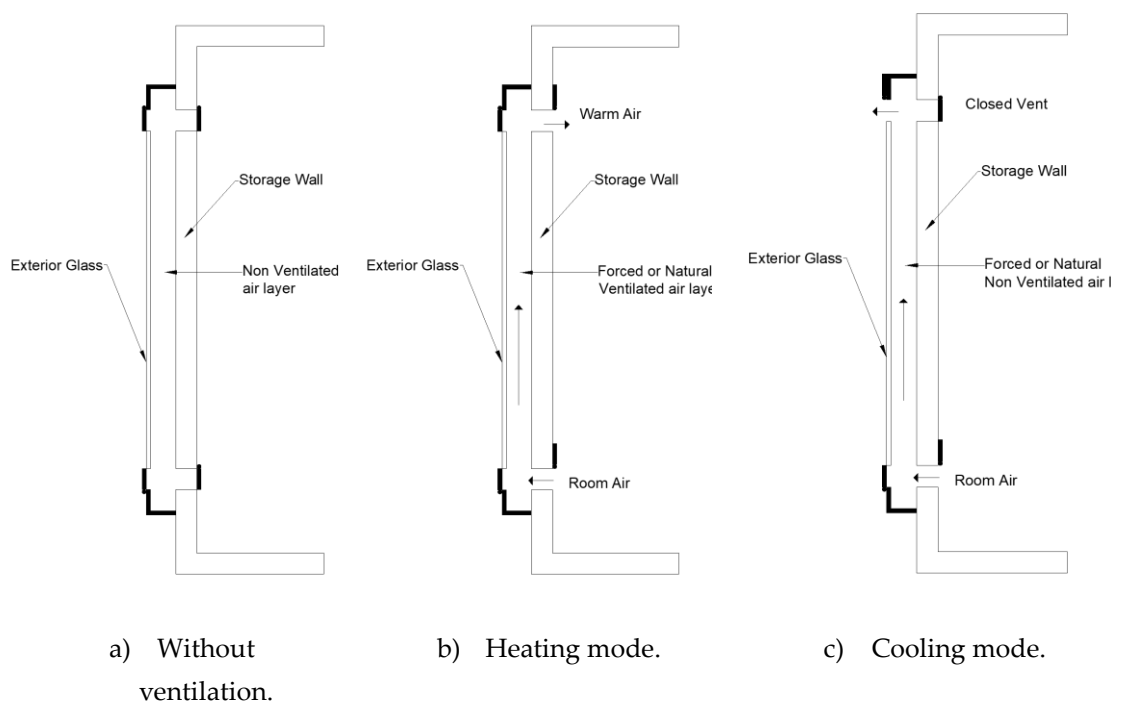


Figure VII.1 – Trombe wall operation modes.

VII.2.1. Trombe wall typologies

Saadatian *et al.* (2013) presented a review about Trombe walls where they can be found with several configurations adapted to climates, purposes and seasons. There are nine different kinds of Trombe walls: (1) Standard Trombe Wall; (2) Composite Trombe Wall; (3) Water Trombe Wall; (4) Zigzag Trombe Wall, (5) TransWall; (7) Trombe Wall PCM; (8) Fluidised Trombe Wall; and (9) Photovoltaic Trombe Wall. A standard Trombe wall design is based on using material with high thermal storage capacity such as concrete, stone and bricks. Normally the external surface of the storage wall is painted in black to increase the absorption of solar radiation. The exterior layer of the standard Trombe wall is glazed with an air-gap between the glass and the storage wall.

One of the disadvantages of Trombe wall systems is the low thermal resistance during night periods or cloudy days where the heat is transferred from the inside to the outside of the building (Shen *et al.* 2007). To increase the thermal resistance of a standard Trombe walls, the *Composite Trombe Wall* (Figure VII.2a) was developed, also known as Trombe-Michel wall (Shen *et al.* 2007). The Composite Trombe Wall works exactly in the same way as the Standard Trombe Wall (Figure VII.1). The main difference between the Composite Trombe Wall and the standard version is the massive composite storage layer. The composite layer absorbs solar energy and heats up by greenhouse effect. The thermal energy can be transferred by convection while using the thermosiphon phenomena and at the same time reducing the heat transfer by conduction through the storage wall. The storage wall, now can work as a TES and provide thermal insulation, avoiding the heat losses during night-periods. Also, the user can control the rate of heating always by adjusting the air circulation.

Another disadvantage of Trombe walls is the inverse thermosiphon phenomena that happens during night periods when the storage wall is colder than the ventilated layer. Comparing with massive building materials (concrete, brick, adobe, etc.) there are other possibilities for a thermal storage wall that can reduce the inverse thermosiphon phenomena during night periods. Water has higher specific heat and volumetric heat capacity and has been used extensively as a heat storage medium, showing to be superior to mass walls (Wilson, 1979). Because it is a fluid, convection currents distribute heat very quickly. Combining with the high volumetric heat capacity, water storage walls have a greater solar heating fraction (Wilson, 1979). Due to the high specific heat, the water's surface temperature does not rise as high as that of the masonry. Taking into account the properties of this fluid, the Water

Trombe Wall ((Figure VII.2b) was studied by Adams *et al.* (2010) and Wang *et al.* (2013a).

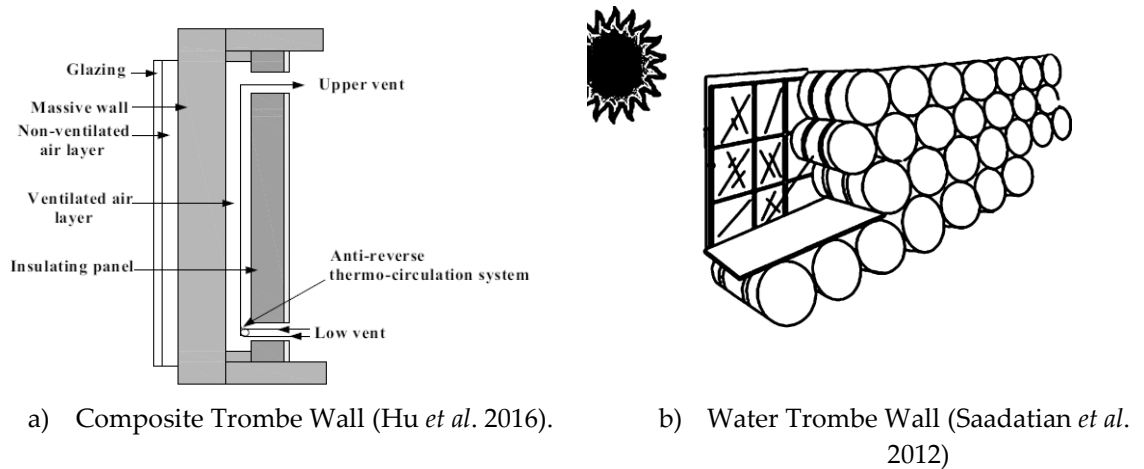


Figure VII.2 – Composite and water Trombe Wall.

Another Trombe wall configuration is known as the zigzag Trombe wall (Figure VII.3a). This configuration was designed to reduce the excessive heat gains during sunny days and redistribute heat during cold nights. The first section is oriented to south while the other two are angled inward forming a V-shaped wall (Hu *et al.* 2016). The section oriented to southeast has a window that provides heat and light during morning. The other two sections that form a V-shape work as a typical Trombe wall system that stores heat during day-time and redistributes during night-time. Transwall or *Transparent wall* ((Figure VII.3b) is another configuration of Trombe wall that provides heating and illumination and plays an aesthetic role by providing visual access to building's exterior. These walls are comprised of water container between two parallel glass panes supported by metal frames. A semi-transparent plate absorbs and transmits solar energy. Incident radiation is absorbed by the water and semi-transparent glass plate and the rest of the transmitted radiation is used for heating the space. Therefore, TransWall uses direct and indirect gain systems and is suitable for climates where the daytime temperature is high (Al-Karaghoul and Kazmerski, 2010).

The use of PCMs in walls and their function was discussed earlier. The use of PCMs in Trombe walls can reduce energy consumption in building (Onishi *et al.* 2001). In previously studies it was concluded that an 8 cm thick hydrated salt storage (encapsulated in copper capsules) wall is more efficient than 20 cm thick concrete, increasing thermal inertia (Khalifa and Abbas, 2009). Other study demonstrates that a Trombe wall with hydrated salt storage (PCM) can release solar heat gains with a time lag of two hours and 40 minutes (Zalewski *et al.* 2012). Another configuration

of Trombe wall with PCMs is the ventilated active façades with PCMs. Here, the glass of a typical Trombe wall is substituted by a PCM in its outer layer. Diarce *et al.* (2013) presented an experimental and numerical study of ventilated active façades. The results showed that the PCM can reduce the overheating of the façade and improve the buildings thermal inertia.

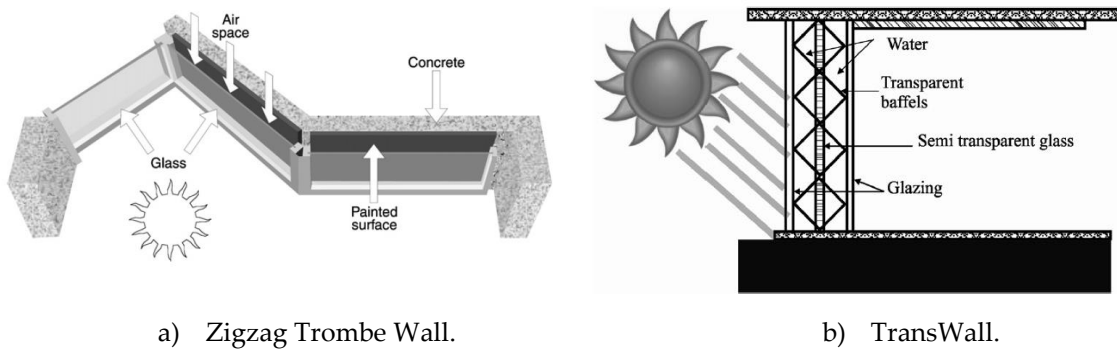


Figure VII.3 – Zigzag Trombe wall and TransWall (Saadatian *et al.* 2012).

Another Trombe wall type is entitled Fluidized Trombe wall system (Figure VII.4b). The operation mode is like a standard Trombe wall. However, the glass is filled with highly absorbing, low-density particles that absorb solar energy and release it to the indoor through fan-circulated air (Omran *et al.* 2016). The wall has two filters, located at the top and bottom vents to prevent the fluidised particles from entering in the room (Tunç and Uysal, 1991). Finally, the last Trombe wall type is known as photovoltaic (PV) Trombe Wall (Figure VII.4a). A PV Trombe Wall joins solar cells to generate electricity with a standard Trombe wall to provide heat. The solar cell covers the glass giving a good aesthetic to the building. However, PV Trombe Wall has lower thermal performance comparing with other typologies due to PV panel that reduces the penetration of solar rays into the air layer between the walls and glazing (Dehra, 2009).

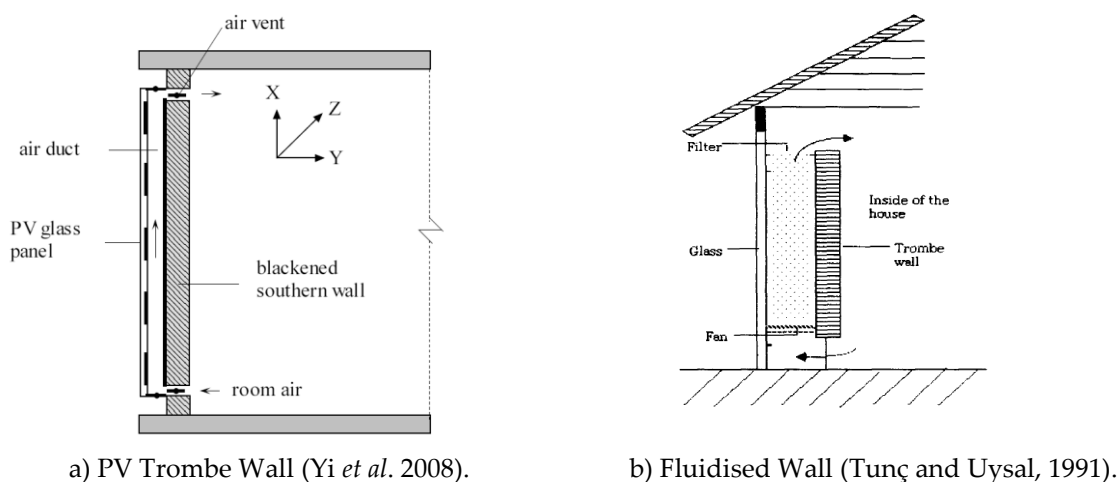


Figure VII.4 – PV and Fluidised Trombe walls.

VII.3. Overview of previous scientific researches

VII.3.1. Experimental analysis

During the past years a few experimental studies were presented in papers. This section presents some experimental tests with Trombe wall systems in different climates, and with different geometric and physical characteristics. Chen *et al.* (2006) conducted experimental tests to evaluate the thermal performance of a Trombe wall with shading devices in the air gap during winter nights. The experimental setup comprises two rooms (reference room and Trombe wall room with two systems, one with shading devices and other without shading devices) with 3.9 m length, 3.9 m wide and 2.7 m high. The storage wall is constructed of 300 mm thick concrete and a shading device with low emissivity is introduced in the air gap to avoid overheating in summer and improve insulation in winter. Figure V.5 presents a photo of the experimental layout.

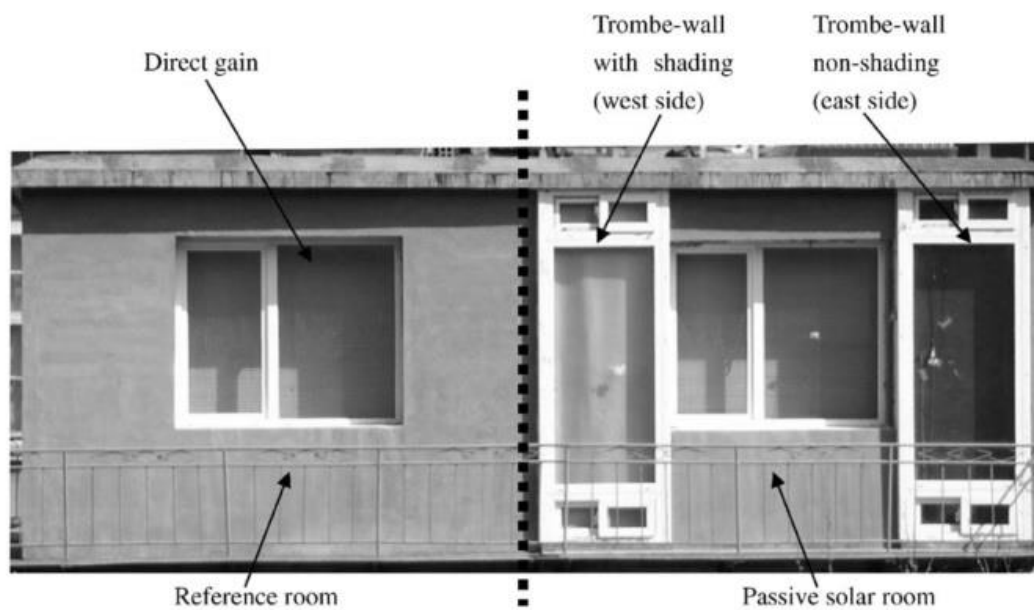


Figure VII.5 – Chen *et al.* (2006) experimental layout.

The thermal performance was evaluated measuring temperatures and heat gains. They concluded that using shading devices can decrease convective heat loss of the air gap and prevent radiative heat transfer from Trombe wall to outside. The results showed that the insulation can reduce between 20 up to 40 % of heat losses in the air gap on a winter night and increase the external surface temperature of the Trombe wall. An optimized location of the shading device in the air layer can reduce 20% of the total convective heat loss.

Burek and Habeb (2007) made an experimental investigation with solar chimneys and Trombe walls. The test involved a vertical open-ended channel with closed sides, like a solar collector or solar chimney with 1 m², measuring the temperatures and air velocity. The channel depth was studied for depths between 20 and 110 mm and it was used an electrical heating system. The results shown that the mass flow rate through the channel was a function of both heat input and channel depth. Also, it was concluded that the thermal efficiency of the system, as a solar collector, was a function of the heat input and not dependent on the channel depth.

Stazi *et al.* (2012) present an experimental study of an Trombe wall system in summer season under Mediterranean climate conditions through changing of shading, ventilation and operational conditions. Two Trombe walls were monitored, one as reference and other where the conditions were changed. They also performed several dynamical simulations according with experimental measurements. Results showed that shading, ventilation and occupancy conditions significantly affect the thermal performance of Trombe wall during summer. Roller shutters could decrease internal surface temperature of the wall around 1.4 °C and decreases 0.5 MJ/m² of heat gains. The use of roller shutters, overhangs and cross-ventilation can assure good thermal comfort in summer and a reduction of cooling energy needs.

Liu *et al.* (2013) presented an experimental and numerical study of a Trombe wall system to achieve the optimum opening and closing modes of air vents analysing the performance parameters of an experimental Trombe wall. The parameters considered are: air vent velocity, air vent temperature, temperature distribution of air layer and indoor air temperature. The experimental layout is located in QingHai, China, and it was constructed a house compartment with 3.3 m width, 3.9 m length and 2.9 m height. All the facades were constructed with 240 mm thick brick walls, except the south wall, where the Trombe wall systems was installed. The Trombe wall has a 4-mm simple glass (1500 × 1800 mm), 100 mm air layer, 10 mm red corrugated iron, 240 mm brick wall and a 50-mm polystyrene cystosepim.

The wall has two air vents (200 × 200 mm) on the top and three on the bottom of the wall. They concluded that the optimum opening duration of the vent is 2 – 3 hours after sunrise and for closing air vent 1 hour before sunset. They also concluded that the difference between opening and closing mode of the air vent under the condition of the air vent closed is poorer than with the air vent open. Also, the closing the vents has little effect on the heat storage and release. The maximum heat storage capacity was achieved at 16:00 and the minimum at 7:30.



a) Live-action of test object.

b) Interior view of the test room.

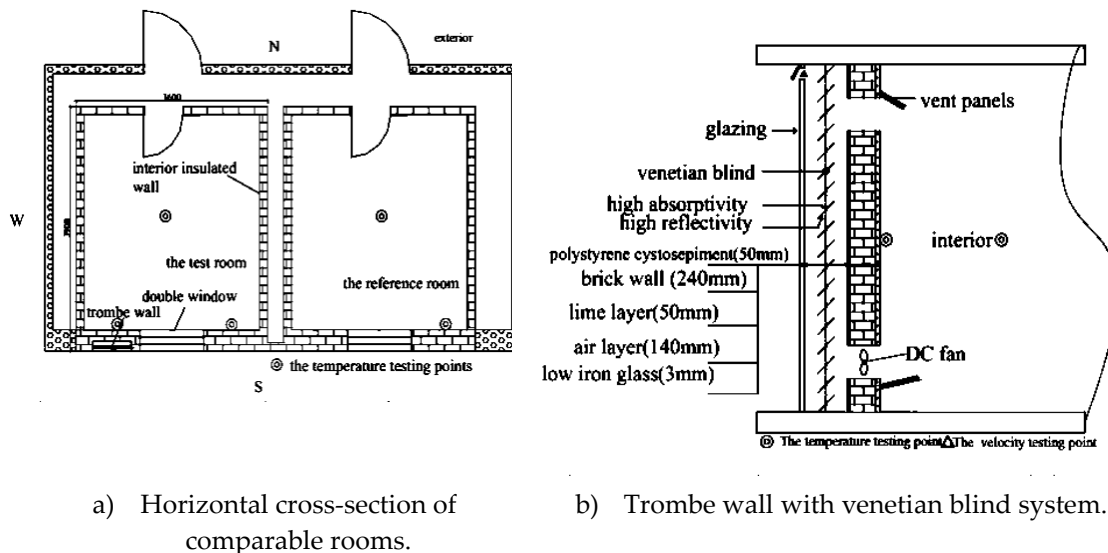
Figure VII.6 – Liu *et al.* (2013) experimental Trombe wall system.

Krüger *et al.* (2013) build two test cells with 5.25 m^3 (2.6 m^2 of floor area) for testing an Trombe wall system under subtropical conditions (Curitiba, Brazil) during cold periods in 2011 and for 2012 summer. One of the test cell is used as reference and the other with the Trombe wall. The distance between the two test cells was 1.5 m to avoid overshadowing. The walls of the cells were made from 9 cm thick hollow concrete blocks with no exterior insulation layer. Attached to the north-facing (south hemisphere) of the Trombe wall there is a $1.5 \times 2.0 \text{ m}^2$ aluminium window frame in light colour. The researchers used a double glazing for the external surface, horizontal air vents with opening area of $1.4 \times 0.15 \text{ m}^2$. The lower air vent is at 20 cm and the upper vent at 1.85 m above the floor and near to the ceiling. As dampers two extruded polystyrene foam blocks were used to fit the air vents of the storage wall. Results showed that a higher performance is achieved within the test cell where the Trombe wall was installed.

Abbassi *et al.* (2014) developed an experimental prototype of Trombe wall in Tunisia. The prototype was used to validate a numerical model developed in TRNSYS. The experimental setup is a test room with $1.86 \times 1.52 \times 1.52 \text{ m}^3$ made of wood with 0.02 m of thickness and insulated by a panel of 0.04 m thick polystyrene. The south façade has a Trombe wall system with a 0.1 m thick storage wall made up of solid concrete brick with black paint. To reduce the lateral heat losses of the storage wall it was used insulating panels. The thickness of air layer is 0.12 m and the air vents have 0.25 m (top) and 0.15 m (bottom). The numerical model was validated against

experimental data, and it was concluded that a Trombe wall with 8 m² can give 77% of the total heating demand of a 16 m² non-insulated building.

Hu *et al.* (2015) presented an experimental study on the thermal performance of a Trombe wall system with a DC fan and a venetian blind structure during summer and winter in Hefei, China. In winter, the experimental tests were conducted varying the slat angles between 0°, 45° and 90°. It was found that the temperature value rises when the slat angle is 45°. During summer, to minimize the overheating problem and enhance air vent velocity, the blind slab angle was set to 90° and the fan turned on. It was concluded that the maximum value of reduced heat gains from the south wall, was 3660 kJ. The overall results shown that the integration of venetian blind structures improves the thermal performance of Trombe walls systems.



a) Horizontal cross-section of comparable rooms.

b) Trombe wall with venetian blind system.

Figure VII.7 – Hu *et al.* (2015) schematic of experimental layout.

Rabani *et al.* (2015) published a paper with an experimental study where a Trombe wall system was combined with a solar chimney and a water spraying system. The experimental setup, a room with dimensions of 3 x 2 x 3 m, was installed in Iran (dry climate). The Trombe wall area is 50% of the south wall. Results showed that the use of the water spraying system helps to decrease indoor temperatures and increase the relative humidity by 8 °C and 17%, respectively. The system can also enhance thermal efficiency by approximately 30%. The results also showed that the storage energy of the Trombe wall has an important contribute in the air ventilation during non-sunny periods.



Figure VII.8 – Rabani *et al.* (2015) experimental layout.

VII.3.2. Analytical and numerical modelling

Modelling a Trombe wall can be very tricky because involves knowledge's in heat transfer by conduction, convection and radiation. The models can be divided in analytical and numerical, in steady-state or in transient conditions. Analytical methodologies are simple to developed and use. Some analytical methods are available in standards or books such as ISO 13790 – 2008, ASHRAE Handbook and even in Heat and Mass Transfer from Çengel, (2009). These 1D methodologies are also incorporated in some dynamic building simulation software's such as Design Builder, Energy Plus and TRNSYS. However, if a detailed study is necessary it is more convenient the use of 2D or 3D numerical solutions. The use of tree-dimensional numerical CFD analysis in Trombe walls is normally used to study the temperature fields in these systems and also in the adjacent room for a long specific period of time (transient conditions). Trombe walls have a very unpredictable behaviour during the year when the climatic conditions changes. Therefore, many research also conducted several studies of this system integrated in building using dynamic building simulation tools. In this section, a few analytical and numerical models were selected considering the final results in terms of improving Trombe walls' thermal performance.

VII.3.2.1. Analytical modelling

During the past years many scientific researchers worked on the development of analytical solutions based on heat transfer phenomena involved in Trombe wall systems. In 1978, Balcomb and Mcfarland presented an interesting study where they developed a simple procedure to predict the thermal performance of solar heat structures using monthly values of solar radiation, environment temperature, the

heat losses and solar gains of buildings. They presented two analytical methods for estimating the annual solar heating performance of a building using a passive thermal storage wall of the Trombe Wall or Water Wall type with night insulation and with or without a reflector. The methodology is accurate to around 3% comparing with computer simulations. Bilgen (1987) made a parametric study with analytical procedures to evaluate the thermal performance of a composite Trombe wall, which consists on a glazing, a massive wall and an insulation wall. However, the air layer with the vents is not placed between glass and storage, is located between the storage and a thermal insulation. The idea is the reduction of thermal loss due to the low thermal resistance of Trombe walls. The theoretical analysis was carried out determining the net heat exchange by radiation, convection and conduction, assuming the following assumptions: (1) one-dimensional model; (2) the heat transfer through the glazing and insulating wall is at steady state; (3) material properties are constant; (4) all surfaces are considered as *gray bodies*; (5) air is considered as a nonparticipating medium in radiation heat exchange; (6) the dwelling air temperature is thermostatically; (7) no lateral heat losses. The results showed that the storage wall thickness should be between 0.5 and 0.15 m, and the insulation wall 0.10 m of thickness. The composite wall system is suitable to LSF construction.

Dragicevic and Lambic (2011) presents a steady-state one-dimensional mathematical model for simplified analysis of thermal performance of Trombe wall in heating mode, by varying the construction and operating parameters of the system. The model has the following assumptions: (1) steady-state; (2) heat transfer through the system is one-dimensional; (3) uniform temperature for different layers of wall; (4) constant thermal physical properties of air and all materials; (5) the thermal resistance of glass is neglected; (6) air is considered as nonparticipating medium in radiation heat exchange; (7) the system is considered to be well insulated without lateral heat losses (two adiabatic boundaries); (8) capacity of the massive wall was not considered. The results showed that the efficiency of the heating mode is increased with the increase of air velocity in the inlet vet, solar radiation, ambient temperature, and decrease of wall height and inlet air temperature in the inlet vent.

In ISO 13790:2008 standard is presented an analytical method for the evaluation and design of Trombe walls systems. Based on this standard, Ruiz-Pardo *et al.* (2010) revised the methodology in order to check if it could be implemented within Mediterranean climates. They concluded that the proposed methodology contains some error in the equations for steady-state conditions. The authors, proposed new

modified equations and new correlations for Mediterranean climates. In 2014, Briga-Sá *et al.* presented a study that aims the adaptation of ISO 13790:2008 to the Portuguese climatic conditions. They concluded that the adaptation of this standard allows the calculation of thermal behaviour of the Trombe wall system in Portugal. It was also concluded that the methodology application allows to analyse the influence of different heat transfer phenomena in the global heat gains of the Trombe wall. The authors also mentioned that the presence of a ventilation system in the massive storage wall has an important contribution in the thermal performance of the Trombe wall which increases with the increase of storage wall thickness. Trombe wall systems can reduce around 16.36 % of the heating energy demands.

Olenets *et al.* (2015) describes in their paper the heat transfer and air movement that occur in the ventilated air layer of Trombe wall under summer and winter conditions. The physical and mathematical models were present for a Trombe wall with and without venetian blind arranged in the air gap. The analytical model allows to determinate the heat and air stream distribution and surface temperature of all elements. The model separates the heat transfer by radiation and convection allowing to estimate the influence of construction materials and covering properties on the heat flow distribution. They concluded that in the cold season, for the Trombe wall with the venetian blind the total heat gain into to room increases by 14 % when the solar radiation was 320 W/m^2 and by 3.5 times when the intensity of the solar radiation is 160 W/m^2 comparing to a standard Trombe wall. They also concluded that using a coating (covered on the glazing) which has a high reflectivity for long-wave radiation, and a high transmittance for short-wave radiation, can increase the heat gains by 1.8 to 13 times, for solar radiations of 320 W/m^2 and 160 W/m^2 , respectively.

Duan *et al.* (2016) presented one study where two different Trombe walls with double glass were compared, one with the absorber plate placed on the thermal storage wall (type 1) and another with the absorber plate placed between the glass cover and the thermal storage wall (type 2). The thermal performance of this system was evaluated for different air channel depths, solar radiation intensities and for different glasses emissivities. To evaluate the energy performance of this system the researches developed an analytical solution based on the energy balance equations assuming the following assumptions: (1) Steady-state conditions; (2) the air temperature in the channel changes only in the direction of the flow; (3) 1D heat transfer model; (4) the lateral heat losses were neglected. These researchers also presented an exergy methodology based on exergy balance equation for a Trombe

wall system. They concluded that the airflow rate and air temperature rise in the air channel/layer in the Trombe wall with the absorber plate placed between the glass cover and the storage wall. They also concluded that the energy and exergy efficiency in both Trombe walls increases until a certain radiation intensity point. The maximum energy performance is obtained for a solar radiation intensity of 600 W/m² and 900 W/m² for type 1 and 2, respectively. The researchers also concluded that decreasing the glazing emissivity which reduces the radiation heat losses of Trombe wall, the energy and exergy efficiencies increases.

VII.3.2.2. Numerical modelling

Sebald (1985) presented a mathematical study using thermal network models to simulate a Trombe wall system. It was concluded that thermal network models solved by forward differencing are accurate, and the results are easy analysed and extracted. Gan (1998) studied a Trombe wall system for summer cooling of buildings using CFD analysis. The CFD model was validated against experimental data from literature with very good agreement between measure and numerical values. A parametric study was conducted to evaluate the effect of the distance between wall and glazing, wall height, glazing type and wall insulation. It was found that during summer cooling, the ventilation rate induced by the buoyancy effect increases with the wall temperature, solar gain, wall height and thickness. The ventilation rate increases with the increase of distance between glass and storage and with the increase of inlet and outlet air vents. The use of double glazing is a better option comparing with single glass, because the heat losses decreases and enhances passive cooling in summer. They also concluded that the storage wall must be insulated to prevent overheating due to convection and radiation heat transfer from the wall. Buzzoni *et al.* (1998) presented the development of a numerical solution to a natural convection problem in a Trombe wall system. The numerical solution was based on energy and mass conservation equations achieved using finite difference method. The numerical model was validated against experimental data showing a very satisfactory agreement.

Shen *et al.* (2007) presented their numerical evaluation of a composite Trombe wall using a finite difference method. The simulation model was developed and validated to be integrated into library of elements of TRNSYS software. The model developed in TRNSYS and the one obtained with finite difference method was compared with Type 36, a model presented on TRNSYS library used for modelling standard Trombe walls.

Jaber and Ajib (2011) studied the thermal, environment and economic impact of a Trombe wall system for residential building in Mediterranean region. The optimum size of this system was defined by using Life Cycle Cost (LCC) criterion. The researchers conducted energy computer simulations with TRNSYS to analyse the thermal performance of the system. Finally, taking into account the economic and numeric results they concluded that the optimum Trombe wall area ratio is 37 %. Liu *et al.* (2013) developed a numerical method to analyse the air vent management and heat storage characteristics of a Trombe wall. The physical model, is a room with 3.3 m width, 3.9 m length and 2.9 m height, has a glass window and five air vents (200 x 200 mm). The model considers the heat storage and the release law of the Trombe wall, the heat convection of indoor air and air layer of Trombe wall and heat transfer process in thermal storage. They assumed that: (1) the air in the air layer is a single-phase incompressible fluid; (2) the buoyancy caused by temperature difference is take into consideration, disturbance to air current distribution caused by air infiltration from the door and windows and personnel activity are ignored; (3) no other heat sources in room.

Kundakci Koyunbaba and Yilmaz (2012) presented a CFD model (Ansys CFX) of a Trombe wall that was validated against experimental data. The CFD code could predict the radiation, conduction and natural convection in Trombe wall systems with PV panels, single glass and double glass. The researchers used k-epsilon turbulence model and the heat transfer was modelled using Monte Carlo model. They concluded that the double glass has higher insulation character during night time and the evening. However, the single glass provides higher solar radiation gain for the thermal wall during day time. They, recommended the use of a single glass with a shutter for night time to provide more thermal gain for winter heating.

Fiorito (2012) presented his research results of the thermal performance of a Trombe wall system integrated in LSF constructions, where the heavy thermal storage walls were replaced by PCMs. Dynamic building simulations were conducted using Energy Plus software. The results of the study showed that: (1) in mild-cold and temperature climates, the integration of PCMs on the outside surface of the intermediate partition of a Trombe wall increases building thermal inertia; (2) in mid-hot and subtropical climates the integration of PCMs in the inside surface of the intermediate partition of a Trombe wall reduces the superficial temperature variability; (3) in hot and dry climates the PCMs placed on inside or on outside surface of intermediate partition reduces surface temperature variations; (4) the adoption of highest PCMs thickness shows better benefits; (5) in all climate regions,

the use of PCMs in Trombe wall systems, increases thermal inertia of LSF construction.

Soussi *et al.* (2013) studied the impact of passive heating technique for an office building located in Tunisia. Their study was conducted using dynamic building simulation tools (TRNSYS). It was found that Trombe walls have contributed in decreasing the total heating requirements by 21%, improving the comfort level in winter. However, it was also found an overheating effect during summer. This effect can be partially avoided by the integration of a 1.5 m solar overhang. These researchers considered in their simulations movable overhang applied during summer and removed during winter. The results of the simulations shown a reduction in annual required cooling energy. Ferreira and Pinheiro (2011) conducted dynamic simulations using Energy Plus for three different climatic regions of Portugal. It was concluded that this passive measure has a very positive contribution in winter but is very undesirable in summer. They also mentioned that a rigorous design of these devices is needed.

In 2015, Bajc *et al.* presented a 3D numerical CFD (Ansys Fluent) analysis of the temperature fields in a Trombe wall and in the adjacent room for several days in a moderate continental climate. The numerical model has a few assumptions: (1) Air was considered as incompressible ideal gas; (2) The solver was pressure based with coupled pressure-velocity coupling scheme; (3) All spatial discretization were of second order; (4) Steady-state and transient models; (5) $k-\varepsilon$ model was used for closing the set of governing equations; (6) The discrete ordinates (OD) radiation model was used to solve radiative heat transfer. Simulation have shown a big impact of the Trombe wall indoor temperature of a model house in Belgrade. The contribution of PV strips in electricity production for cooling devices operation is significant. Bellos *et al.* (2016) analysed the thermal performance of an innovative Trombe wall with an extra window in the massive/storage wall. The thermal performance of this wall was compared with the conventional Trombe wall system and the usual insulated wall. The study was conducted using the Finite Element Method of SolidWorks Flow Simulation. The results showed that the new Trombe wall concept is most appropriate creating warmer indoor profile comparing with the other cases, especially the hours between noon and afternoon.

VII.3.3. Guidance overview

Considering the results presented by the select researchers of the literature review. Table VII.1 displays a list of design considerations in Trombe wall systems. This

CHAPTER VII

Trombe walls review and design methods

section pretends to show an overview of the importance of physical and geometrical parameters in Trombe wall design. The selected parameters are: Vents; Channel/Air layer depth; Shading devices; Glazing; Storage wall; Air velocity in the air layer; Area; Fan (forced convection); Solar radiation intensity.

Table VII.1 – Summary of researcher's achievements in experimental, analytical and numerical analysis of Trombe walls, according with the main design parameter focused (1st column).

Trombe Wall Parameter	Authors	Methodology	Description	Major Achievement
Vents Effect	(Liu <i>et al.</i> 2013)	Numerical/ Experimental	Optimum opening and closing modes in the management of air vents	Open the air vent 1 – 3 h after sunrise and close it 1 h before sunset
	(Ferreira and Pinheiro, 2011)	Numerical (Dynamical)	Dynamical simulation of a Building with passive solutions	Positive contribution in winter but undesirable in summer
Channel Depth	(Burek and Habeb, 2007)	Experimental	Tests were conducted in a vertical channel with closed sides	The depth of the channel does not affect the thermal efficiency of the heat output. However, the mass flow rate is increased
Shading Devices	(Chen <i>et al.</i> 2006)	Experimental	Shading effects on winter thermal performance of the Trombe wall air gap	The use of shading can decrease convective heat loss of air gap and prevent radiative heat transfer from T.W to the outside.
	(Stazi <i>et al.</i> 2012)	Experimental/ Numerical	Trombe wall management in Mediterranean summer conditions	The use of roller shutters, overhangs and cross ventilation can assure good thermal comfort and a reduction of the cooling energy needs.
	(Hu <i>et al.</i> 2015)	Experimental	Thermal performance of Trombe walls with venetian blind structure in summer and winter	The venetian blind structure is an effective active way to improve thermal performance preventing over-heating and increase the heat accumulation
	(Olenets <i>et al.</i> 2015)	Analytical	Heat transfer and air movement in the ventilated air gap with regulation of heat supply	The venetian blind arrange in the air gap allows an increase of heat entry into the room in the winter and prevents the entry of cooled air into the room
	(Soussi <i>et al.</i> 2013)	Numerical (Dynamical)	Energy performance analysis of a solar-cooled building	Overhangs shading decrease the total energy needs for cooling

Trombe Wall Parameter	Authors	Methodology	Description	Major Achievement
Glazing	(Gan, 1998)	Numerical	Parametric study conducted using CFD program	The use of double glazing reduces the heat losses in winter and enhances passive cooling in summer
	(Kundakci Koyunbaba and Yilmaz, 2012)	Numerical (CFD)	Comparison of Trombe wall systems with single glass, double glass and PV panel The effect of emissivity of the glass cover in the energy and exergy performance of Trombe walls	The use of sing glass with shutter for the night time will provide more thermal gain for winter heating
	(Bellos <i>et al.</i> 2016)	Analytical		With a decrease in glassing emissivity the energy and exergy efficiency increases
Storage Wall	(Gan, 1998)	Numerical	-	Storage wall should be properly insulated to prevent overheating by convection and radiation.
	(Shen <i>et al.</i> (2007)	Numerical	Numerical study of standard and composite solar walls	Composite wall has better thermal performance at heating in cold climates.
	(Bilgen, 1987)	Analytical	Theoretical study of a composite Trombe wall	Storage wall should have thickness between 0.5 up to 0.15 m depending on climatic conditions and insulating. The composite wall with insulating has better thermal behaviour.
	(Fiorito, 2012)	Numerical	Trombe walls with PCMs for LSF construction in temperature and hot climates	The integration of PCMs on the outside or on the inside partition of a Trombe wall improve thermal performance
Air velocity	(Dragicevic and Lambic, 2011)	Analytical	Trombe wall efficiency with one-dimensional mathematic model	Efficiency of the heating system increases with the increase of air velocity
Area	(Jaber and Ajib, 2011)	Numerical (Dynamical)	Thermal, environment and economic analysis of a Trombe wall for a residential building in Mediterranean region	The optimum Trombe wall area ratio is 37 %
Fan	(Sebald, 1985)	Numerical	Efficient simulation of large controlled passive solar systems using thermal network models	The use of a fan can improve the performance of Trombe walls by up to 8 %

CHAPTER VII

Trombe walls review and design methods

Trombe Wall Parameter	Authors	Methodology	Description	Major Achievement
Solar Radiation	(Bellos <i>et al.</i> 2016)	Analytical	The effect of solar radiation intensity in Trombe walls	The energy and exergy efficiency of Trombe walls increase until a maximum value of solar radiation intensity (600 to 900 W/ m ²). After that the efficiency decreases

VII.4. Heat transfer fundamentals for a double glass Trombe Wall system

The heat transfer in a Trombe wall involves heat exchanges by conduction, convection and radiation (Ruiz-Pardo *et al.* 2010). The thermal performance of a Trombe wall (total heat supply) with double glass, air channel and storage wall can be evaluated considering the following assumptions given by Duan *et al.* (2016):

- Steady state conditions;
- Air temperature changes only in the vertical flow;
- Heat transfer through the elements can be considered as unidimensional;
- The heat losses on the lateral boundaries are neglected.

Figure VII.9 illustrates the main variables of the energy balance in a Trombe wall with double glazing.

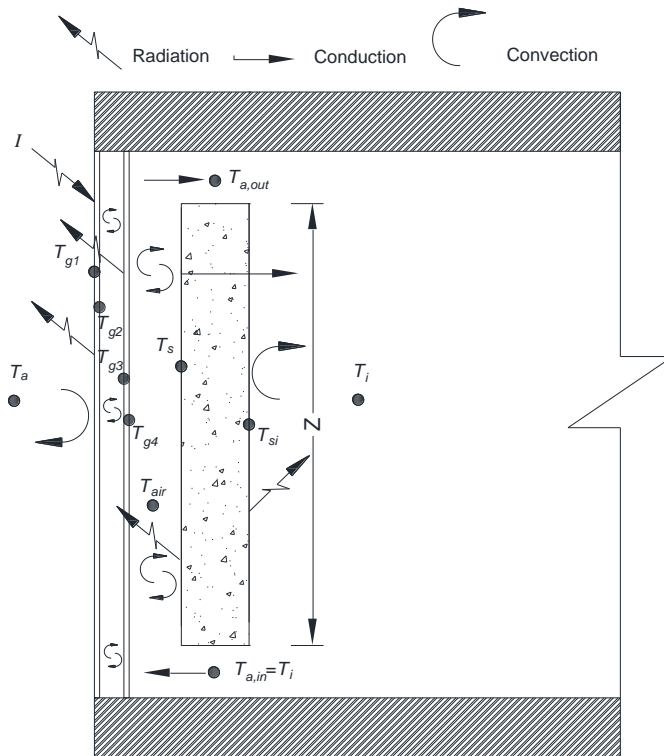


Figure VII.9 – Energy balance in a double glass Trombe wall system.

A double glass type has four surfaces and one air/gas layer (Figure VII.9). The energy balance equations for the first and second surfaces of the glass are:

$$h_{e,g} A_g (T_{g1} - T_a) + h_{r,g1} A_g (T_{g1} - T_a) + \frac{k_g}{e_g} A_g (T_{g1} - T_{g2}) = \alpha_g A_g I \quad (70)$$

$$(h_{r,g2} + \frac{k_{fluid}}{e_{fluid}} A_g (T_{g2} - T_{g3}) + \frac{k_g}{\delta_g} A_g (T_{g2} - T_{g1}) = 0 \quad (71)$$

where T_{g1} , T_{g2} and T_{g3} are the temperatures [°C] of the first glass surface, second and third, respectively. T_a is the ambient temperature [°C]; A_g the area of the double glass [m²]; I is the solar radiation intensity [W/m²]; α_g is the absorptivity of the glass; k_g and k_{fluid} are the thermal conductivities of the glass and the fluid between the two glasses [W/(m.°C)]; e_g and e_{fluid} are the thicknesses of glass and fluid layer [m]. The convection heat transfer coefficient due to wind $h_{e,g}$ on the glass surface can be achieved using the formulation proposed by W.H. Mcadams (Duan *et al.* 2016):

$$h_{e,g} = 5.7 + 3.8u_w \quad (72)$$

where u_w is the wind speed [m/s]. The radiation heat transfer coefficient $h_{r,g1}$ from the for the outdoor conditions is obtained by:

$$h_{r,g1} = \frac{\sigma \epsilon_{g1} (T_{g1}^4 - T_s^4)}{T_{g1} - T_a} \quad (73)$$

where σ is the Stefan-Boltzmann constant [5.67×10^{-8} W/(m².K⁴)] and ϵ_{g1} is the emissivity of the first surface of the glass cover. The sky temperature (T_{sky}) parameter can be considered the outdoor temperature minus 11 °C (ISO 13790, 2008). However, sky temperature can be calculated using a methodology presented in ASHRAE handbook of fundamentals, which is given by:

$$T_{sky} = \left(\frac{Hor_IR}{\sigma} \right) - 273 \quad (74)$$

Hor_IR represents the infrared radiation emitted by sky [W/m²] recorded in a horizontal plane calculated in the following way:

$$Hor_IR = Sky_{emissivity} 9T_e^4 \quad (75)$$

The emissivity of the sky is estimated using the equation:

$$Sky_{emissivity} = \left(0.787 + 0.764 \ln \left(\frac{T_0}{273} \right) \right) + 0.0224N - 0.0035N^2 + 0.00028N^3 \quad (76)$$

where N is the opaque sky cover [tenths] and T_0 is the dew point temperature [K].

The radiation heat transfer coefficient [W/(m².°C)] from the third surface to the second surface of the double glass $h_{r,g2}$ can be obtained by:

$$h_{r,g2} = \frac{\sigma(T_{g3}^2 + T_{g2}^2)(T_{g3} + T_{g2})}{\frac{1}{\epsilon_{g,3}} + \frac{1}{\epsilon_{g,2}} - 1} \quad (77)$$

where ϵ_{g2} , ϵ_{g3} are respectively the emissivity's of the second and third surfaces of the double glazing. The energy balance equation for the third and fourth surfaces of the double glazing are:

$$(h_{r,g2} + \frac{k_{air}}{e_{air}})A_g(T_{g3} - T_{g2}) + \frac{k_g}{e_g}A_g(T_{g3} - T_{g4}) = \alpha_g A_g \tau_g I \quad (78)$$

$$(h_{air} + \frac{k_{air}}{e_{air}})A_{st}(T_{g4} - T_{st}) + \frac{k_g}{e_g}A_g(T_{g4} - T_{g3}) + h_{r,s}A_g(T_{g4} - T_{air}) = 0 \quad (79)$$

with T_{g4} being the temperature of the fourth surface of the double glass [°C]; T_{st} and T_{air} are the surface temperatures of the storage wall and air in air cavity [°C], respectively; A_{st} is the area of storage wall [m²]; τ_g is the transmissivity of the double glazing; k_{air} is the thermal conductivity of the air [W/(m.°C)]; and e_{air} is the thickness of the air cavity [m]. $h_{r,g3}$ is the radiation heat transfer coefficient [W/(m².°C)] from the storage wall to the fourth surface of the glass:

$$h_{r,g3} = \frac{\sigma(T_s^2 + T_{g4}^2)(T_s + T_{g4})}{\frac{1}{\epsilon_s} + \frac{1}{\epsilon_{g,4}} - 1} \quad (80)$$

where ϵ_s , ϵ_{g4} are respectively the emissivity's of the storage wall and fourth surfaces of the system. In Equation (79) h_{air} represent the heat convection coefficient between the fourth layer and the storage wall, obtained by:

$$h_{air} = \frac{Nu \times k_{fluid}}{e_{air}} \quad (81)$$

where Nu represents the *Nusselt* number. The *Nusselt* number for laminar ($6000 < Ra < 2 \times 10^5$) and turbulent ($2 \times 10^5 < Ra < 1.1 \times 10^7$) natural convection flow is calculated by:

$$Nu = 0.197 R_a^{1/4} (e_{air} / Z)^{1/9} \quad (82)$$

$$Nu = 0.073 R_a^{1/4} (e_{air} / Z)^{1/9} \quad (83)$$

where $R_a = G \cdot Pr \cdot Gr = g \cdot \beta \cdot e^3 \Delta T / \nu^2$. β is the coefficient of thermal expansion [K^{-1}], ΔT is the temperature difference of surfaces [$^{\circ}C$]. The density, thermal conductivity and kinematic viscosity coefficient of the air should be calculated considering the air temperature. The energy balance for the air in the air cavity/channel can be achieved by:

$$h_{air} A_g (T_{g4} - T_{air}) = \dot{m} c_p (T_{a,out} - T_{a,in}) \quad (84)$$

The mean temperature in the air cavity can be estimated by (Hirunlabh *et al.* 1999):

$$T_{air} = \gamma T_{a,out} + (1 - \gamma) T_i \quad (\gamma = 0.74) \quad (85)$$

The mass flow rate [kg/s] can be calculated by:

$$\dot{m} = A c_d \sqrt{2 g Z \frac{|T_{a,out} - T_i|}{T_i}} \quad (86)$$

where c_d is the discharge coefficient ($c_d = 0.57$) (Akbarzadeh *et al.* 1982). A is the effective area of the opening [m^2]:

$$A = \sqrt{2} A_{bottom} A_{top} / \sqrt{A_{bottom}^2 + A_{top}^2} \quad (87)$$

A_{bottom} and A_{top} are the areas of the bottom and top vent, respectively [m^2] and Z the vertical distance between them [m]. The total heat supply from Trombe walls is given by:

$$\dot{Q} = \dot{m} c_p (T_{a,out} - T_i) + U A_s (T_s - T_i) \quad (88)$$

VII.4.1. Energy performance analysis

The standard document ISO 13790:2008 presents an analytical quasi-steady-state methodology to calculate the heat transfer and the solar heat gains in Trombe wall systems. This method has been used due to cause-effect relationship between the excitation of temperature and heat loss and the excitation of solar radiation and heat gain (Ruiz-Pardo *et al.* 2010). The heat transfer coefficient of the Trombe wall is given by:

$$H = H_0 + \Delta H \quad (89)$$

where H_0 is the heat transfer coefficient of non-ventilated wall [W/°C] and ΔH is an additional heat transfer coefficient [W/°C] only used in heating mode, when the air vents are opened. This additional heat transfer coefficient is given by:

$$\Delta H = \rho_{air} C_{p,a} \dot{V} \left[\frac{U_{ext}}{U_{int}} \right] g_a k_{sw} \quad (90)$$

where ρ_{air} represents the air density [kg/m³], U_{ext} and U_{int} are the external and internal thermal transmittances [W/(m².°C)]. g_a is the ratio of the accumulated internal-external temperature difference when the ventilation is on, to its value over the whole calculation and it is calculated by:

$$g_a = 0.3\gamma_{al} + 0.03\rho_{air} (0.0003\gamma_{al} - 1) \quad (91)$$

γ_{al} is the ratio of the solar heat gains ($Q_{gn,sw}$) to the heat loss of the air cavity ($Q_{ht,al}$). k_{sw} represent an adimensional parameter function of the air flow rate through the ventilated layer. k_{sw} is calculated further (Equation 100). The thermal transmittances can be obtained using the following expressions:

$$U_e = \frac{1}{R_e + \left(\frac{R_{air}}{2} \right)} \quad (92)$$

$$U_i = \frac{1}{R_i + \left(\frac{R_{air}}{2} \right)} \quad (93)$$

where R_e and R_i represents the thermal resistances of the exterior and interior materials [(m².°C)/W] plus the surface thermal resistances due to heat convection,

respectively. These thermal resistances can be calculated using the following equations:

$$R_e = \frac{1}{h_e} + R_{ext} \quad (94)$$

$$R_i = \frac{1}{h_i} + R_{int} \quad (95)$$

h_e and h_i represents the heat convection coefficient of external and internal surfaces [W/(m².°C)], respectively. Figure VII.10 illustrates the thermal resistances diagrams (triangle and equivalent) of the Trombe wall.

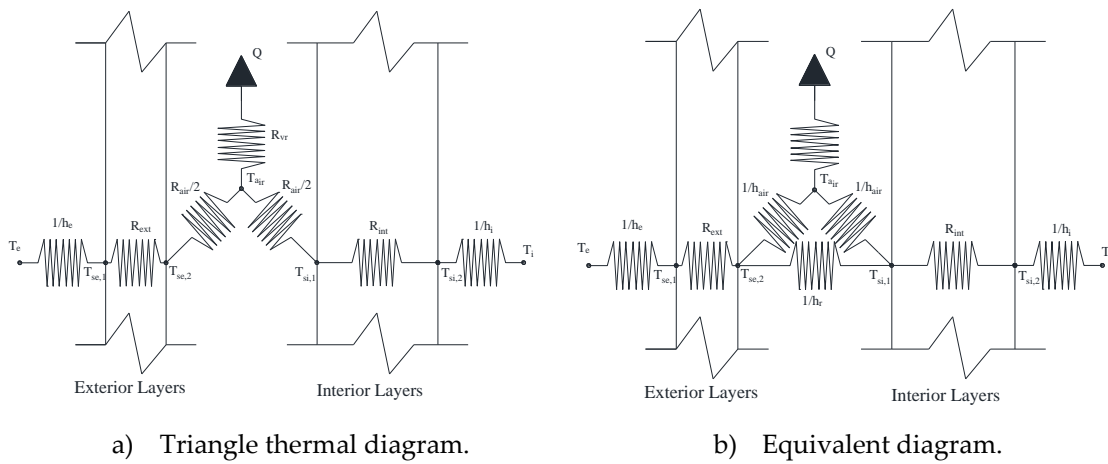


Figure VII.10 – Thermal resistance of the Trombe wall system.

The thermal resistance of the air is achieved according with the thermal resistances diagrams by the following equations:

$$R_{air} = \frac{1}{h_r + \left(\frac{h_{air}}{2} \right)} \quad (96)$$

$$R_{VR} = \frac{1}{h_c + (2h_r + h_{air})} \quad (97)$$

where h_r is radiative surface heat transfer coefficient in the air layer [W/(m².°C)] and h_{air} the convective surface heat transfers in the air layer [W/(m².°C)]. R_{VR} and R_{air} represents the equivalent thermal resistance of the air layer for equivalent diagram [(m².°C)/W] and the thermal resistance of the air layer [(m².°C)/W], respectively. For a first approximation, h_r can be considered equal to 5ϵ , depending on the emissivity of the glazing surface (Briga-Sá *et al.* 2014).

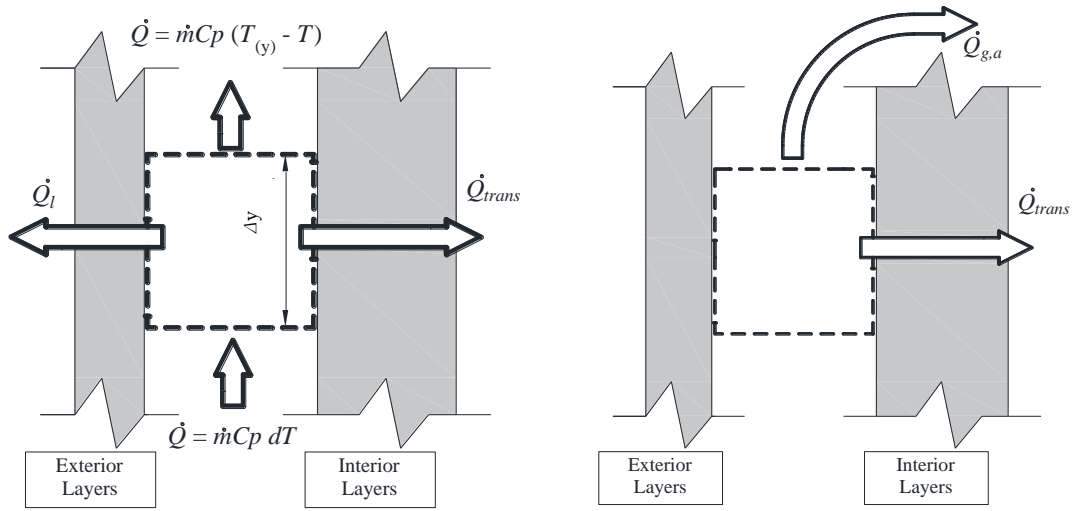
The total thermal transmittance of the Trombe wall can be obtained by:

$$\frac{1}{U_0} = \frac{1}{U_i} + \frac{1}{U_e} \quad (98)$$

The evaluation of heat losses and heat gains strongly depends on the difference between the inlet air and outlet air temperature in the Trombe wall. The Trombe wall air channel can be considered a heat exchanger system where c is equal to zero, when the average surface temperatures ($T_{se,2}$ and $T_{si,1}$) in time, are the same. However, the air that flows in the vertical upward direction gradually increases temperature. For an infinite channel length, the outlet air temperature is going to converge to the surfaces temperatures.

$$T_{(y)} = T(y = \infty) = \frac{T_{se,2} + T_{si,1}}{2} \quad (99)$$

Figure VII.11 illustrates the heat balance in the Trombe wall system.



a) Energy balance in the control volume.

b) Global heat gains.

Figure VII.11 – Heat balance in the Trombe wall system.

The temperature evolution can be obtained applying the energy balance (Figure VII.11a) in the air channel (Ruiz-Pardo *et al.* 2010):

$$T_{(y)} = T_{a,in} + (T_{(y=\infty)} - T_{a,in})k_{sw} \rightarrow k_{sw} = \left[1 - \exp\left(\frac{-ZA_{st}}{\dot{m}Cp_{air}}\right) \right] \quad (100)$$

where A_{st} represents the total surface area of the wall and Z is given by (ISO 13790):

$$\frac{1}{Z} = R_{vr} + \frac{1}{U_i + U_e} \quad (101)$$

As it can be seen, the presented model follows the relation of ε -NTU, where the effectiveness of the air layer (ε) can be achieved by:

$$\frac{T_{a,out} - T_{a,in}}{T_{(y=\infty)} - T_{a,in}} = \varepsilon \Leftrightarrow \varepsilon = 1 - \exp(-NTU) \text{ when } C = 0 \quad (102)$$

where NTU is given by:

$$NTU = \left(\frac{-ZAs}{\dot{m}_a C_{p,a}} \right) \quad (103)$$

in ISO 13790:2008, ε is known as k_{sh} .

The outlet air temperature can also be achieved considering the inlet air temperature and the surfaces temperatures of the air channel. The surface temperatures ($T_{Surface}$) are considered as uniform in the flowing direction Δy . In heating mode, the outlet air temperature can be achieved analysing the energy balance applied to a differential control volume (Figure VII.11a):

$$\begin{aligned} \int_{T_{a,in}}^{T_{a,out}} \frac{1}{T_{Surface} - T} dT &= \frac{Zw}{-\dot{m}_a C_{p,a}} \int_0^h dy \Leftrightarrow \\ \Leftrightarrow \left[\ln(T_{Surface} - T) \right]_{T_{a,in}}^{T_{a,out}} &= -\frac{Zw}{\dot{m}_a C_{p,a}} [y]_0^h \\ \Leftrightarrow \ln \left(\frac{T_{Surface} - T_{a,out}}{T_{Surface} - T_{a,in}} \right) &= -NTU \end{aligned} \quad (104)$$

The outlet air temperature for heating can be achieved with the following expression:

$$T_{a,out} = T_{Surface} + (T_{Surface} - T_{a,in}) e^{-NTU} \quad (105)$$

It can be seen that Equation (105) is similar to Equation (46) used to calculate the outlet air temperature in Earth-to-Air Heat Exchangers. The thermal performance of a Trombe wall system can be evaluated considering the heat losses and heat gains by conduction, convection and radiation.

The heat losses through the exterior layer (glass) can be calculated using the equation of heat conduction between the air layer/channel and the outdoors. The following equation represents only the heat losses [W] through the glass:

$$\dot{Q}_l = U_e A_{st} (T_{air} - T_e) \quad (106)$$

Ruiz-Pardo *et al.* (2010). presented in their paper the development of an expression where it is considered all the interior–exterior elements:

$$\dot{Q}_l = \left[U_0 A_{st} + \rho_{air} C_{p,a} \dot{V} \frac{U_0^2}{U_i^2} k_{sw} \right] (T_i - T_e) \quad (107)$$

The global heat gains in a Trombe wall system [MJ] are based on solar heat gains \dot{Q}_{sol} , and heat transfer by conduction through interior layers \dot{Q}_{trans} , (Figure VII.11b):

$$\dot{Q}_g = \dot{Q}_{sol} + \dot{Q}_{trans} \quad (108)$$

The following equations to calculate the energy performance of the ventilated Trombe wall, are presented in ISO 13790:2008. Briga-Sá *et al.* (2014) adapted them to the Portuguese climate conditions during heating and cooling seasons. The solar gains [MJ] during heating season, can be calculated using the following expression:

$$\dot{Q}_{sol} = \left(\sum_k \phi_{sol,mm,k} \right) t + \left(\sum_l (1 - b_{tr,l}) \phi_{sol,mm,u,l} \right) t \quad (109)$$

where, $b_{tr,l}$ is the reduction factor for adjacent unconditioned space with internal heat source l . $\Phi_{sol,mm,k}$ represents the time-average heat flow rate from solar heat source k . The time-average heat flow rate [W] is obtained by:

$$\phi_{sol,mm,u,l} = F_{sh,oh,k} A_{sol,k} I_{sol,k} - F_{r,k} \phi_{r,k} \quad (110)$$

Briga-Sá *et al.* in their study considered that the space with the Trombe wall is surrounded by spaces with equal indoor temperature, except where the Trombe wall is installed. Also, no heat gains or losses were considered from surrounding spaces. Considering these assumptions, Equation (109) can be expressed in the following form:

$$\dot{Q}_{sol} = (F_{sh,oh,k} A_{sol,k} I_{sol,k} - F_{r,k} \phi_{r,k}) t \quad (111)$$

where $F_{r,k}$ and $\Phi_{r,k}$ represents the form factor between the Trombe wall and the sky and the extra heat flow due to thermal radiation to the sky from the Trombe wall

[W], respectively. $F_{sh,ob,k}$ represents the shading reduction factor for external obstacles. These values can be achieved using the Portuguese standard (DL n.118/2013) *Regulamento de Desempenho Energético dos Edifícios de Habitação* (REH):

$$F_{sh,ob,k} = F_h F_0 F_f \quad (112)$$

where F_h is the reduction factor for obstacles from other building exterior elements, F_0 is the shading reduction factor for obstacles from the horizontal elements overlapping the glazing and F_f represents the shading reduction for obstacles from the vertical side fins of the glazing. $I_{sol,k}$ is the mean energy of solar irradiation in the heating season [W/m²] obtained by:

$$I_{sol,k \text{ (heating)}} = \frac{M \cdot G_{sul}}{t_{d,1}} \times 10^3 \quad (113)$$

where M is the heating season duration [days], G_{sul} the monthly average solar energy incident on South vertical surface [kWh/m² month] and $t_{d,1}$ the heating season duration in hours. In cooling season, these values are calculated by:

$$I_{sol,k \text{ (cooling)}} = \frac{I_r}{t_{d,2}} \times 10^3 \quad (114)$$

where I_r represents the solar irradiance [kWh/m²] and $t_{d,2}$ the cooling season duration in hours. $A_{sol,k}$ is the effective collecting area of the Trombe wall [m²] during heating and cooling is calculated according with ISO 13790:2008 and adapted for the Portuguese climate conditions by Briga-Sá *et al.* (2014). Equation (115) and Equation (116) present the $A_{sol,k}$ expressions for heating and cooling, respectively. In cooling season Equation (116) considers that the air vents are closed, so there is no flowrate.

$$A_{sol,k \text{ (heating)}} = A_{ssw} \alpha_{st} F_F g_{\perp} \left[U_0 R_e + \frac{U_0^2}{U_i U_e} \rho_{air} C_{p,a} \frac{\dot{V}}{A_{sw}} k_{sw} \omega \right] \quad (115)$$

$$A_{sol,k \text{ (cooling)}} = A_{ssw} \alpha_{st} F_F g_{\perp} [U_0 R_e] \quad (116)$$

where F_F represents the glazed fraction, α_{st} the solar absorption coefficient of the storage wall exterior surface and g_{\perp} the glazing factor (REH). ω is a dimensionless parameter that represents the total solar radiation ratio incident on the element when the air layer is open to the solar radiation during the whole calculation step. This parameter can be achieved using the following expression:

$$w = 1 - \exp(-2.2\gamma_{al}) \quad (117)$$

where γ_{al} represents the ratio between the solar gains, see Equation (118), and heat loss of the air layer given by Equations (106) and (107). The solar heat gains in the air cavity

$$\dot{Q}_{gn,sw} = I_w A_s \quad (118)$$

where I_w is the solar irradiance, the mean energy of solar irradiation in heat season [(W Mseg)/m²] given by:

$$I_w = 3.6 M.G_{sul} \quad (119)$$

Finally, the value of the extra heat flow rate due to thermal radiation to the sky from the Trombe wall, $\Phi_{r,k}$ [W], is achieved using Equation (120).

$$\Phi_{r,k} = R_{se} U_0 A_s h_r \Delta\theta \quad (120)$$

where $\Delta\theta$ is the average difference between the external air temperature and the sky temperature [°C].

VII.5. Final remarks

A literature review of Trombe Wall technologies and the heat transfer fundamentals for design and energy evaluation was presented in this chapter. For later calculations (Chapter VIII), the heat transfer equations are used. Based on the main conclusions of the published research a guidance overview was presented. Trombe Walls have a very complex behaviour and their physical and geometrical parameters strongly depend on climate. Saadatian *et al.* (2012) listed the advantages and disadvantages of Trombe walls systems considering the state-of-the-art made by previous researchers. The following list shows a few advantages found in the literature:

- Trombe walls produce large temperature variation in building's materials. However, this system causes insignificant temperature variation in heated spaces;
- Trombe wall not only can provide thermal comfort in the spaces connected to the system but also can provide thermal comfort in adjacent spaces (Boukhris *et al.* 2009);
- Trombe wall can improve buildings thermal comfort and reduce the energy consumption by 30% and decrease the moisture and humidity of interior spaces in humid regions;

- Trombe wall use solar energy to heat, ventilate and increase thermal comfort in buildings in various climatic regions (Zamora and Kaiser, 2009).

However, Trombe walls systems have also a few drawbacks:

- Trombe walls have a complex behaviour because involves different heat transfer phenomena's and strongly depends on weather conditions;
- During night periods or cloudy days, Trombe walls lose heat from inside to outside of a building due to their low thermal resistance;
- Also, during nigh periods or cloudy days, an inverse thermos-siphon phenomenon occurs when the storage wall has lower temperature than room temperature;
- The global heat transfer is uncertainly; it depends mainly on the solar heat gains;
- A Trombe wall system performance should be controlled considering the weather conditions.

In the next chapter, is presented the development of a new Trombe Wall (Water Trombe Wall) for LSF modular construction.

CHAPTER VIII

Development of a Water Trombe Wall system for LSF modular construction

VIII.1. Introduction

Nowadays passive solar technologies are a very attractive solution to reduce energy consumption in residential and commercial buildings. However, one of these technologies known as *Water Walls*, was not widely study by scientific community. The first water wall in the world was built at MIT (*Massachusetts Institute of Technology*) in 1947 by Hottel and his students (Bainbridge, 2005). In 1972, Steve Baer designed a water wall combined with a glass and an air layer (Water Trombe Wall). Water walls offers an excellent solution which increases buildings thermal inertia and thermal comfort while reducing energy consumption. A water wall system is normally composed by a thermal energy storage filled with water. Water has been used extensively as a heat storage medium, and in many applications is superior to mass walls made by concrete, bricks or wood which have lower heat and volumetric heat capacities (Wilson, 1979).

Thermal energy storage systems are divided in short-term TES (daily) and long term-TES (seasonal). In water walls, the storage wall is considered a sensible heat TES system, where the heat is stored during the day and released with the temperature change of the storage (during the night). However, comparing with other typical short-term TES made with traditional material, the water wall is cheaper due to its abundance, and the heat stored in water may be redistributed by convection and water also provides faster heat exchanges comparing with other materials (Wu and Lei, 2016). Water walls can be divided in: (1) Water wall with opaque building envelope; (2) Water wall with a semi-transparent building envelope; (3) Water wall with PCMs; (4) Water wall combined with other passive technologies (Water Trombe Walls). Water walls are very similar in terms of design, except the materials that they are made and their integration in buildings.

Only a few studies of Water Trombe Walls were present by scientific community. This kind of system has not yet been well studied by researchers and more attention should be given.

In this Chapter, the development of a new Water Trombe Wall (WTW) system is presented. This system was developed to be assembled in a LSF construction. The thermal performance of the thermal storage system is analysed with experimental, numerical and analytical approaches. Later preliminary results on the full-scale Water Trombe Wall system are discussed.

VIII.2. Brief review of Water Trombe Walls

Water walls can store huge amounts of sensible heat due to the high specific heat of water. The Water Trombe Wall system which is a passive solution to increase the thermal performance of a typical Trombe wall reducing the inverse thermos-siphon phenomenon that occurs during night periods, and also increasing the thermal resistance and temperature distribution of the storage wall. The water Trombe wall design is the same as a typical Trombe wall, with a difference in the storage wall that is filled by water. The first experimental analyses of water a Trombe wall system was carried by Hoyt Hottel. Their water wall used a full height array of one and five-gallon cans with black paint and double pane glass. These water Trombe wall system could provide 38 up to 48 % of the heating demand. However, this value could increase with proper design, including curtains between water wall and window glass, proper insulation and a proper separation between the storage tanks and the room.

In 1972 in New Mexico, Steve Baer Corrales used stacked 55 – gallon drums full of water to provide thermal mass. The south walls have single glasses and were properly insulated. He concluded that the system worked well during winter for space heating. After Hottel and Steve Baer work, a few variety of water walls were presented and their integration in residential and commercial buildings investigated. Adams *et al.* (2010) presented a study of the optimal water wall thickness of water Trombe walls. To evaluate the temperature fluctuation, a controlled environment was assembled. The environment consisted of three parts: an “exterior” volume containing a heat source, an “interior” volume, and a water wall. The variable explored was the thickness of the water wall, where three different thicknesses were used: 7.6 cm, 15.2 cm and 22.9 cm. A heat source is turned on for 5 hours and then turn off for 19 hours to evaluate the temperature evolution difference between the three prototypes. Both interior and exterior spaces are 1 ft³ (1' x 1' x 1')

volumes, constructed using OSB panels. The “outdoor” wall was constructed using OSB panels and an outer glass. The “indoor” box tried to simulate a room space where the water wall is placed. Finally, the water wall was constructed of glass pieces held together. Results showed that higher thickness was better, maintaining the water temperature for longer periods of time.

Wang *et al.* (2012) presented a numerical simulation method and an experimental campaign to study the performance of a Trombe wall equipped with a thermal storage tanks. The experimental house is in Tianjin (China). This passive house has 700 m² of floor area and in south side there is a sun space corridor. This corridor has 1.4 m width, left of which is hollow glass while right of which is the so-called water tank thermal storage wall. The tanks are used as internal wall to store and release heat. This tank has 0.4 m width and with a total water usage of 41 tons. Hollow glass and polycarbonate sheet are used to reduce the thermal losses from the envelope. They concluded that using a water Trombe wall during summer season, other cooling measures are not required. The thermal storage effect of the water tanks could decrease the maximum indoor temperature by 4 °C and increase the minimum by 3 °C. In winter season, the water tanks can make regulation of the heating system simple and feasible. In 2013, Wang *et al.* made another investigation to understand the influence of water storage wall on the indoor thermal environment. The simulation was carried using TRNSYS to simulate the variation of indoor air temperature. Results shown that a Trombe wall with water storage system can reduce yearly energy consumption by 8.6 % and improve thermal comfort evaluation index by 12.9 %.

VIII.3. Development of the Thermal Energy Storage system for the Water Trombe Wall

A building efficiency strongly depends on the consumption of energy resources and water. In Europe more than 5 m³ of water per capita is consumed (European Commission, 2012) where 70 % corresponds to domestic consumption of which 24% are used in flushing systems and 46% for personal hygiene (Sapiano, 2013). Rainwater harvesting systems uses the building roof (Farreny *et al.* 2011), a filtration system and pipes that allow the water to flow into a reservoir. Since water has a high specific heat element, 4180 J/(kg.°C), and also has a high thermal conductivity, it can be used to store thermal energy (Saadatian *et al.* 2012). Solar thermal energy is normally used for water heating or pre-heating, and can be stored in long term (seasonally) or in short time periods, usually daily (Dincer, 2002). Seasonal storage systems require large volumes of water, making them less attractive economically

(Fisch *et al.* 1998) and considerably more complex than short-term systems (Ochs *et al.* 2009). In contrast, thermal energy storage systems for short periods of time are even more attractive because they have higher operating temperatures (Novo *et al.* 2010). As part of the *EcoSteelPanel* scientific research project, experimental prototypes of a Lightweight Steel Framing (LSF) fully water-filled panel were developed. The prototypes were exposed to outdoor condition for different orientations (South, East and West). Analytical methods combined with FEM were developed to predict transient thermal behaviour of the panel.

VIII.3.1. Thermal storage system design

EcoSteelPanel aims the development of an innovative façade (opaque water wall) solution able to store thermal energy and rainwater. This water wall geometry was developed to be integrated into LSF modular construction only with screw connections. The first panel version (Figure VIII.1a) has 0.59 m width, 0.104 m thick and 2.7 m height with a volume capacity of 156.7 liters. The second version of the water wall has a different geometry to simplify their assemblage and construction, mainly the steel plates welding. The second version (Figure VIII.1b) has the same width and height of the first generation, however the water thick was reduced to 0.05 m decreasing the total weight of the wall.

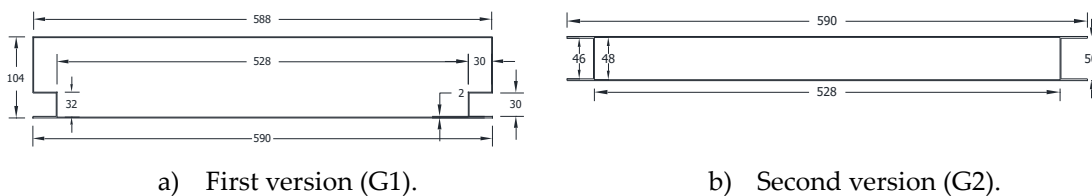


Figure VIII.1 – Water wall horizontal cross-section (*EcoSteelPanel*).

The assemblage of this water wall to the LSF structure is done with screw connections and a steel plate. The following figure illustrates a scheme screw connection of the panel.

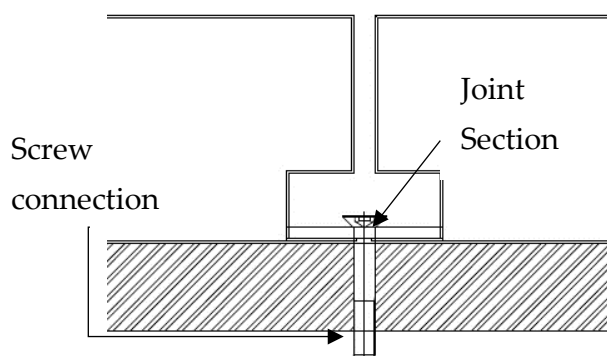


Figure VIII.2 – Screw connection of the *EcoSteelPanel* water wall.

The joint section is critical in terms of thermal insulation. The influence of the joint section between two adjacent panels was verified. The thermal analysis was performed with THERM software for both panel versions (G1 and G2). Four models were created and analysed the influence of the joint section and lateral section of the panels, with opened and closed boundaries when exposed to outdoor conditions. The following table presents the boundary conditions of the models. T_i represents and T_a represents the interior and exterior temperatures [°C], respectively. h_i and h_e are the heat convection coefficients for the interior and exterior boundaries, respectively. These values are reference values from the software and the temperatures boundaries are not important to analyse the thermal transmittance of the panels configurations.

Table VIII.1 – Boundary conditions of the 2D models for both panel generation.

Model	Interior		Exterior		Joint section		Lateral section	
	T_i [°C]	h_i [W/m ² .°C]	T_a [°C]	h_e [W/m ² .°C]	Opened	Closed	Adiabatic	Non-Adiabatic
01	21	2,44	-18	26	X		X	
02	21	2,44	-18	26		X	X	
03	21	2,44	-18	26	X			X
04	21	2,44	-18	26		X	X	

Figure VIII.3 shows the obtained isothermal lines of the bi-dimensional models.

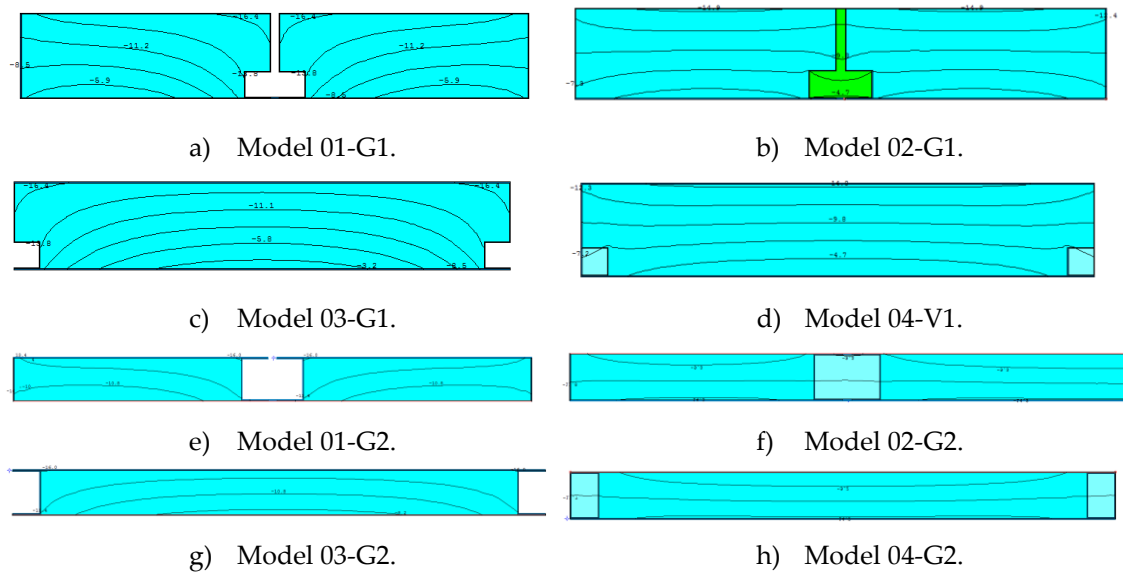


Figure VIII.3 – 2D isothermal lines of the *EcoSteelPanel* water wall joint connection.

The U -values analysis allows the comparison between G1 and G2 panels considering the joint section between adjacent panels. Figure VIII.4 presents the numerical results

for both panel versions. It is observed that when the joint section was considered opened, the G2 has improvements in terms of U-value. However, considering a closed joint section G1 is better due to higher thickness of the panel and due to the smaller air layer thickness in the joint section. The difference between the two panel versions with opened joint section was $0.150 \text{ W}/(\text{m}^2 \cdot ^\circ\text{C})$ (model 01 G1 and G2) and $0.091 \text{ W}/(\text{m}^2 \cdot ^\circ\text{C})$ between model 02 G1 and G2. The most significant difference was achieved in the models with closed joint section. The difference obtained between model 04 G1 and G2 was $0.396 \text{ W}/(\text{m}^2 \cdot ^\circ\text{C})$.

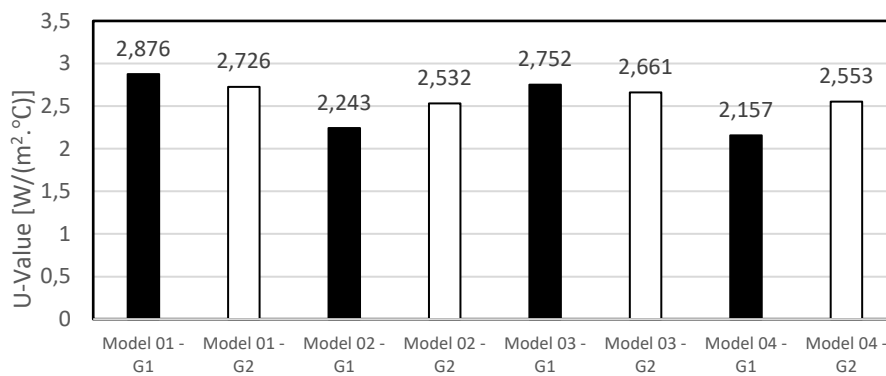


Figure VIII.4 – Thermal transmittance results for the *EcoSteelPanel* water walls.

VIII.3.2. Experimental small-scale prototype

With the purpose of studying the thermal performance of the panel, one experimental prototype was built and tested over the four seasons of the year. The experimental prototype illustrated in Figure VIII.5 (model) and Figure VIII.6 is made of DX51d + Z cold-formed steel with 1.0 mm thick, 600 mm high, 590 mm wide and 100 mm of water thickness.

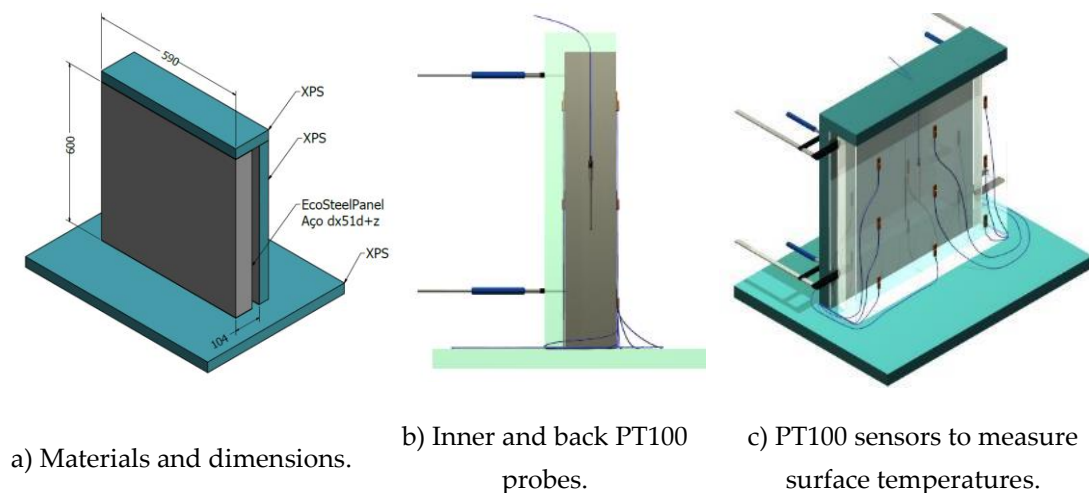
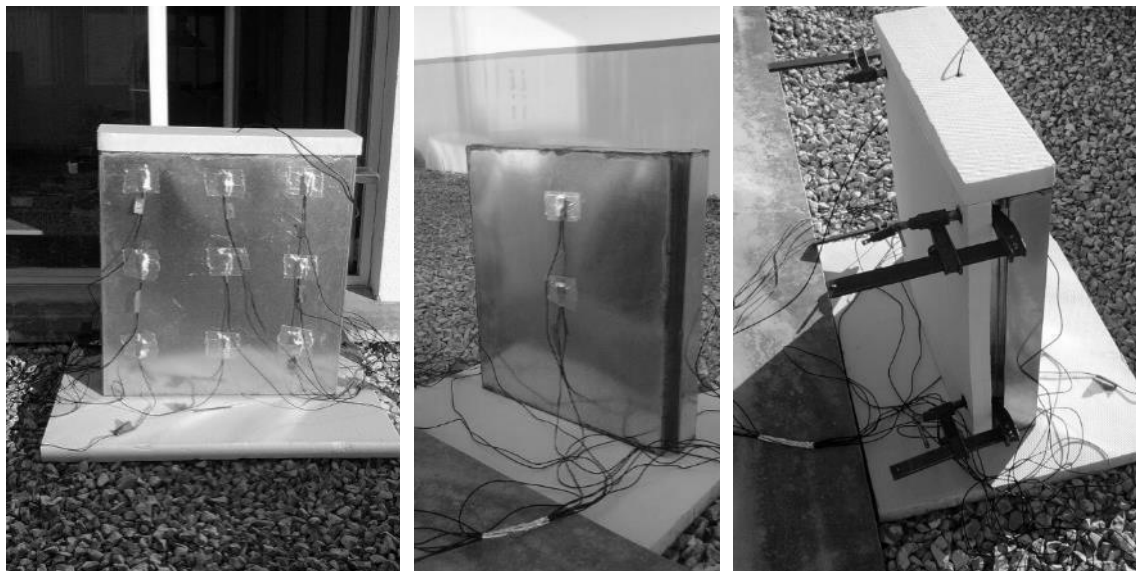


Figure VIII.5 – 3D model of the water TES small-scale prototype.

The geometry has been developed so that the panel can be integrated into any wall using only bolted connections. The top and back surfaces were properly insulated with extruded polystyrene (XPS) (40 mm thick). Below the prototype, a XPS base with 800 mm width, 600 mm length and 40 mm thick was assembled to minimize the heat exchanges between ground and to minimize the heat gains by reflected radiation.

The outer surface temperature which is exposed to the solar radiation was obtained using nine temperature sensors, type PT100 (precision of $\pm 0.4^\circ\text{C}$), placed in a matrix form with a spacing between them of 200 mm. For the back surface, two PT100 sensors allow to verify the influence of the prototype thermal inertia. The water temperature was measured with a PT100 probe placed at 300 mm below the highest water level (Figure VIII.5b). For data acquisition, a *Campbell Scientific* CR1000 data logger was used.



a) Outer/Front PT100 probes.

b) Back PT100 probes.

c) Insulated prototype.

Figure VIII.6 – Experimental tests of the water TES small-scale prototype.

VIII.3.3. Analytical approach

The temperature and the heat flux on the prototype exposed surface are obtained by imposing a thermal equilibrium between the front surface and the back surface. Climatic data such as wind, precipitation and solar radiation reflected by surrounding areas make the analytical approach more complex, and these variables are neglected in the model.

Figure VIII.7 shows the variables under study.

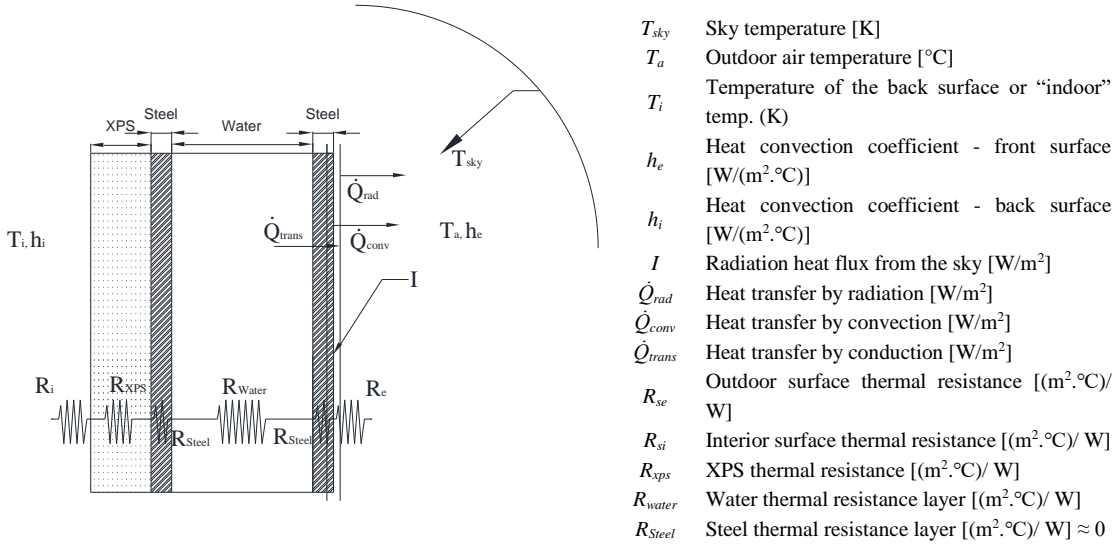


Figure VIII.7 – Illustration of the studied variables applied in the thermal balance of the prototype.

The temperature of the panel front surface is obtained applying a thermal equilibrium between the front and back surfaces, considering the energy stored by the water and the enveloping steel. The one-dimensional thermal equilibrium equation in the panel is given by:

$$I - \dot{Q}_{trans} - \dot{Q}_{conv} + \dot{Q}_{rad} = \dot{m} c_p \Delta T / \Delta t^{(Water+Steel)} \quad (121)$$

Equation (121) with the respective variables is transformed into the following equation:

$$A \dot{q} \alpha - U A_{st} (T_s - T_i) - h_e A_{st} (T_{surf} - T_a) + A_{st} \epsilon \sigma (T_{surf}^4 - T_{sky}^4) = \rho_s v_s c_{p,s} \frac{dT_s}{dt} + \rho_w v_w c_{p,w} \frac{dT_w}{dt} \quad (122)$$

where A_{st} represent the surface area of the prototype [m²], \dot{q} the (diffuse and direct) radiation from the sky to an azimuth [W/m²] of 90 °, α the absorption coefficient of the steel DX51d + Z, U the heat transfer coefficient [W/ (m².°C)], h_e the convective heat transfer coefficient on the prototype surface [W/(m².°C)], ϵ the emissivity of the panel surface and σ the Stefan-Boltzmann constant [5.67 × 10⁻⁸ W/(m².K⁴)]. The variables ρ_s , v_s , $c_{p,s}$ and ρ_w , v_w , $c_{p,w}$ represents the density [kg/ m³], the volume [m³] and specific heat [J/(kg. °C)] of steel and water, respectively.

The water and steel temperature are analysed for a time range Δt of 3600 seconds. To obtain the outer surface temperature it is important to calculate the heat flux. Equation (123) was solved by programming Visual Basic in a MS Excel spreadsheet,

$$\int_{T(t=0)}^{T_{surf}} \frac{1}{T(t)-T} = \frac{T_{surf} (h_e A_{st} - UA_{st}) + A_{st} \varepsilon \sigma T_{surf}^4 - A_{st} \dot{q} \alpha - h_e A_{st} T_a - A_{st} \varepsilon \sigma T_{sky}^4 - UA_{st} T_i}{(\rho_s v_s c_{p,s} - \rho_w v_w c_{p,w})} \int_{t=0}^t dt \quad (123)$$

where $T_{(t=0)}$ represents the surface temperature at $t = 0$. Due to the high thermal conductivity of the steel, 60.5 W/(m.°C) (Ansys value) and considering that water can distribute heat, it can be assumed that steel temperature is going to be equal to water temperature, during heating. During cooling this temperature can be obtained using, Equation (124) and performing a thermal balance for a control volume, where only heat losses by conduction are considered.

$$\int_{T(t=0)}^{T_{surf}} \frac{1}{T(t)-T} = \frac{UA_{st}}{(\rho_s v_s c_{p,s} - \rho_w v_w c_{p,w})} \int_{t=0}^t dt \quad (124)$$

The following table shows the information regarding the calculation conditions, considered fixed in time. The U -value was obtained numerically through a Finite Elements software (Ansys CFX), in a transient regime, as will be described in the next section.

Table VIII.2 – Input parameters.

ρ_s	ρ_w	$c_{p,s}$	$c_{p,w}$	v_s	v_w	U
[kg/m ³]	[kg/m ³]	[J/(kg.°C)]	[J/(kg.°C)]	[m ³]	[m ³]	[W/(m ² .°C)]
7854.0	999.8	434.0	4180.0	0.001	0.035	1.185

VIII.3.4. Numerical approach

The numerical value of the global heat transfer coefficient was obtained considering the solar radiation (direct and diffuse), external temperature and the effect of the heat convection on the surfaces. The total time used in this model for numerical convergence in transient conditions is 3600 seconds, with a time-step of 120 seconds. The considered initial conditions were obtained by experimental data for $t = 0$. Figure VIII.8 a) and b) show the numerical results for temperature and heat flux distribution, respectively.

The external convection coefficient was equal to 25 W/(m².°C), where the surface thermal resistance is 0.04 (m².°C)/W, according with ISO 6946. The outdoor temperature considered was 26 °C (measured value). The isotropic radiation flux with direct horizontal values of 978.3 W/m², direct radiation on the vertical plane of 444.34 W/m² and diffuse radiation of 141.01 W/m² on all surfaces. These values were measured using a weather station located in Coimbra. The water was modelled as a

fluid element with initial condition of 27.71 °C (measured value). For radiation effects, the Monte Carlo algorithm was considered and implemented in the numerical model.

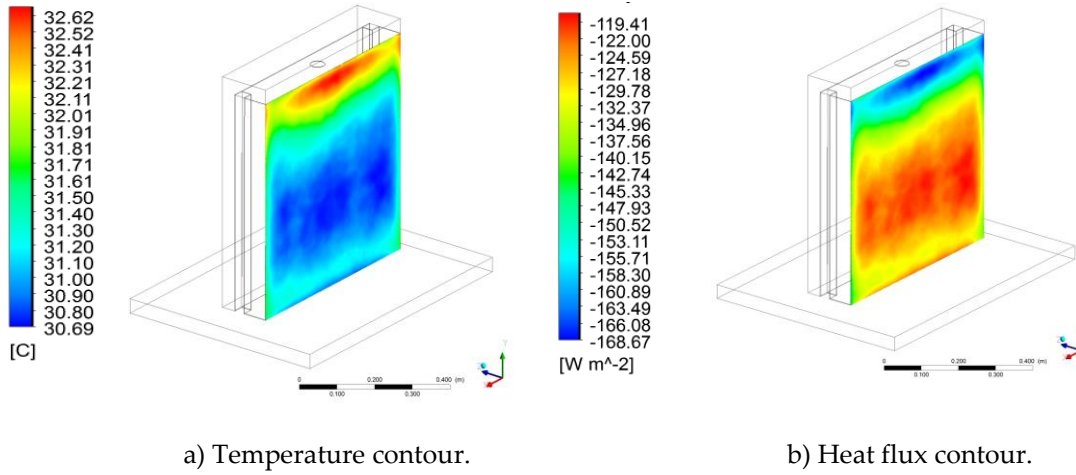


Figure VIII.8 – Numerical results for the exterior surface of the small-scale prototype.

The following table presents the numerical results and experimental measurements for water (T_w) and front surface average (T_s) temperatures. The U -value was achieved numerically taking into consideration the transient heat flux. It was observed a good agreement between the measured temperature and the one obtained numerically.

Table VIII.3 – Numerical results and experimental measurements.

Approach	T_w [°C]	T_{surf} [°C]	U [W/ (m². °C)]
Experimental	33.29	30.10	-
Numerical	31.24	30.24	1.185

VIII.3.5. Analytical model validation

The analytical model used to calculate the prototype surface and water temperatures, was validated against experimental data. The experimental data used was registered during a summer day (27/07/2014) where the outdoor temperature change between 17.73 °C and 27.55 °C. Total solar radiation (direct and diffuse) reached maximum values of 847.72 W/m² for an azimuth of 180° and a zenith of 90°. Figure VIII.9 plots the analytical and experimental surface and water temperatures evolution.

CHAPTER VIII

Development of a Water Trombe Wall system for LSF modular construction

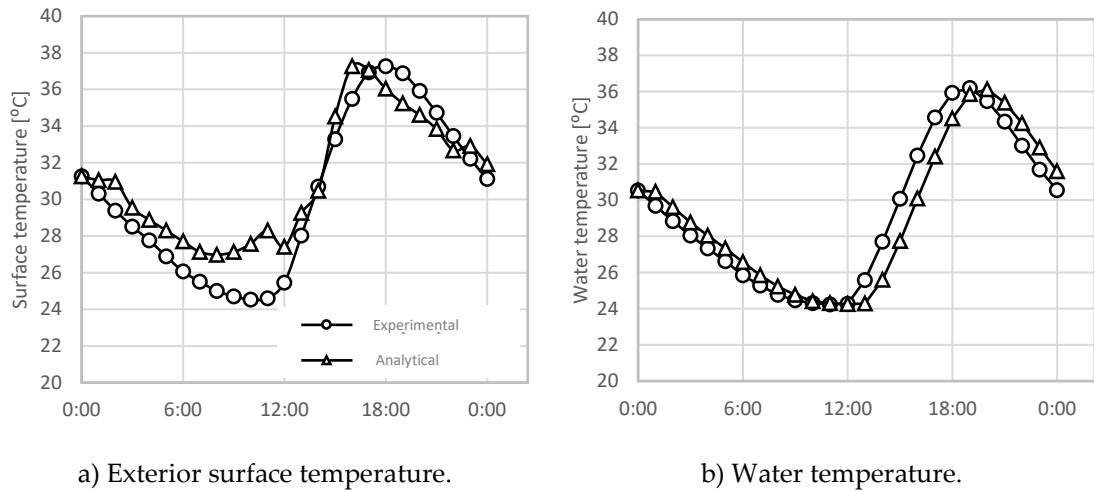


Figure VIII.9 – Experimental and analytical results comparison.

The absorption and emissivity coefficients were calibrated according with the curves approximation between experimental and analytical, with values of 0.35 and 0.8, respectively. The analysis of these results allowed to conclude that the analytical model has a good agreement against experimental data, with an average difference, in module of 1.6 °C for the external surface temperature and 0.23 °C for water temperature.

VIII.3.6. Thermal behaviour of TES Wall

The *EcoSteelPanel* system is designed to be assembled to buildings façades. After the validation of the analytical model the thermal behaviour of the TES panel assembled in a façade is going to be studied. Table VIII.4 presents the façade layers including material thickness and thermal properties according with ISO 6946, except the steel thermal conductivity which is considered equal to the value given by Ansys Database. The theoretical study was done for three consecutive days of clear sky and three days of cloudy sky. The *U-value* of the façade is presented in Table VIII.4, with a value of 0.46 W/(m².°C).

Table VIII.4 – Wall materials thermal properties and thickness.

	e_i [m]	$\sum e_i$ [m]	k_i [W/(m °C)]	R [(m ² .°C)/W]
Plasterboard	0.013	0.013	0.025	0.520
XPS	0.040	0.053	0.037	1.080
Air cavity	0.100	0.153	0.0210	0.180
Steel (1)	0.002	0.155	60.50	≈0
Non –ventilated air cavity	0.030	0.185	-	0.180
Steel (2)	0.001	0.186	60.50	≈0
Water	0.070	0.256	0.600	0.120
Steel (3)	0.001	0.257	60.50	≈0

The weather conditions were measured with a weather station located in Coimbra. The cloudiness is measured using the rate of U/V (weather station parameter), in range between 0 to -100 W/m², where 0 W/m² represents a cloudy sky and 100 W/m² a clear sky. Figure VIII.10 shows the solar radiation evolution for both conditions, as well the dry-bulb temperature, the wet-bulb temperature and the sky temperature calculated considering the infrared radiation. Figure VIII.10 shows that during clear sky, sky temperature has negative values, below -10 °C. For this climatic region, ISO 13790 gives an average sky temperature value of -11 °C. For cloudy conditions, the sky temperature is like dry bulb temperature.

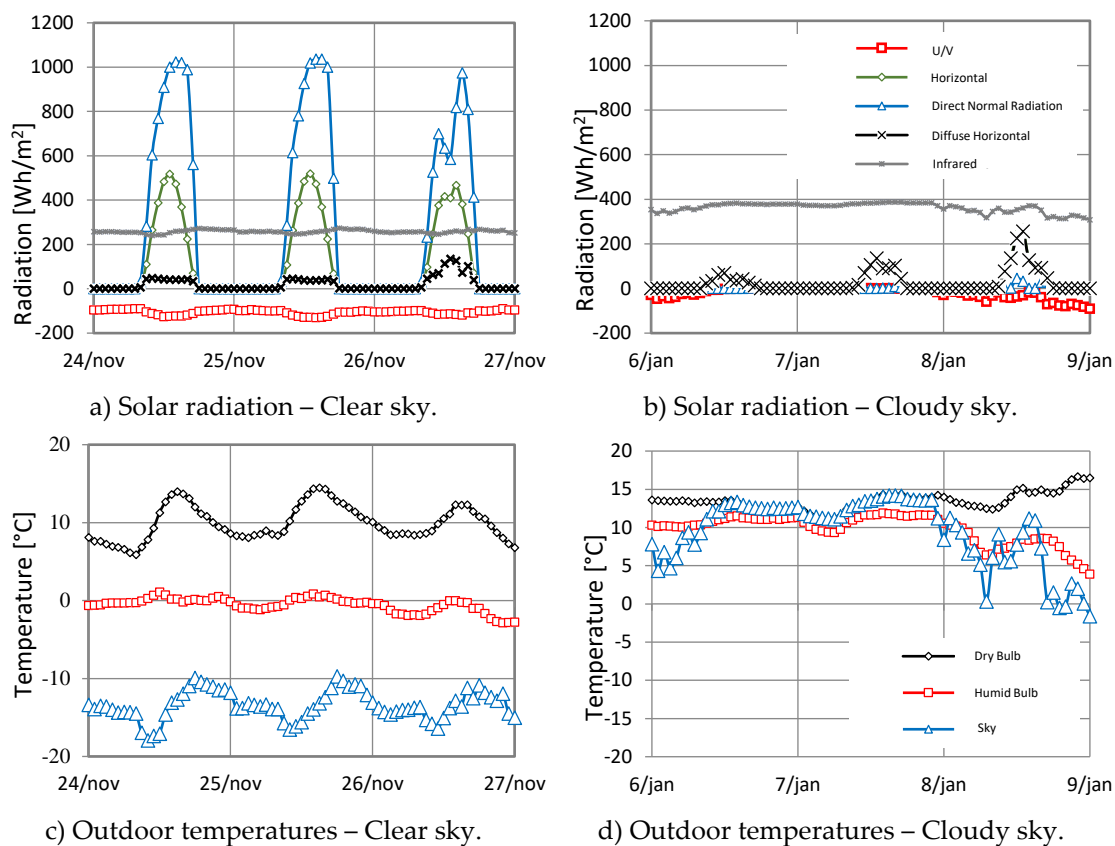


Figure VIII.10 – Weather conditions for three days of clear and cloudy sky.

VIII.3.6.1. Clear sky conditions

The evaluation of the thermal behaviour of the TES *Ecosteelpanel*, integrated in a façade wall, is made considering the calculation conditions previously exposed, where surface temperatures were necessary to evaluate the heat flux. Figure VIII.11 plots measured values of the environment air dry-bulb temperature, the water wall/panel surface temperature and the solar radiation for different orientations: South, North, East and West. This figure shows that the highest temperature value is obtained on the south façade panel, where the maximum temperature achieved was 25.98 °C, for an environment temperature of 14.46 °C.

The panel surface temperature oriented to North is near the ambient temperature due to the absence of direct solar radiation and consequently lower thermal storage. The surface temperature fluctuation for East panels achieved the maximum value during the morning, as expected. However, given the lack of direct solar radiation, after the morning time the panel temperature drops, losing the thermal energy accumulated by water. When the panel is orientated for West, the maximum temperature was achieved at the end of the day, however, there isn't enough time to accumulate sufficient heat for space heating.

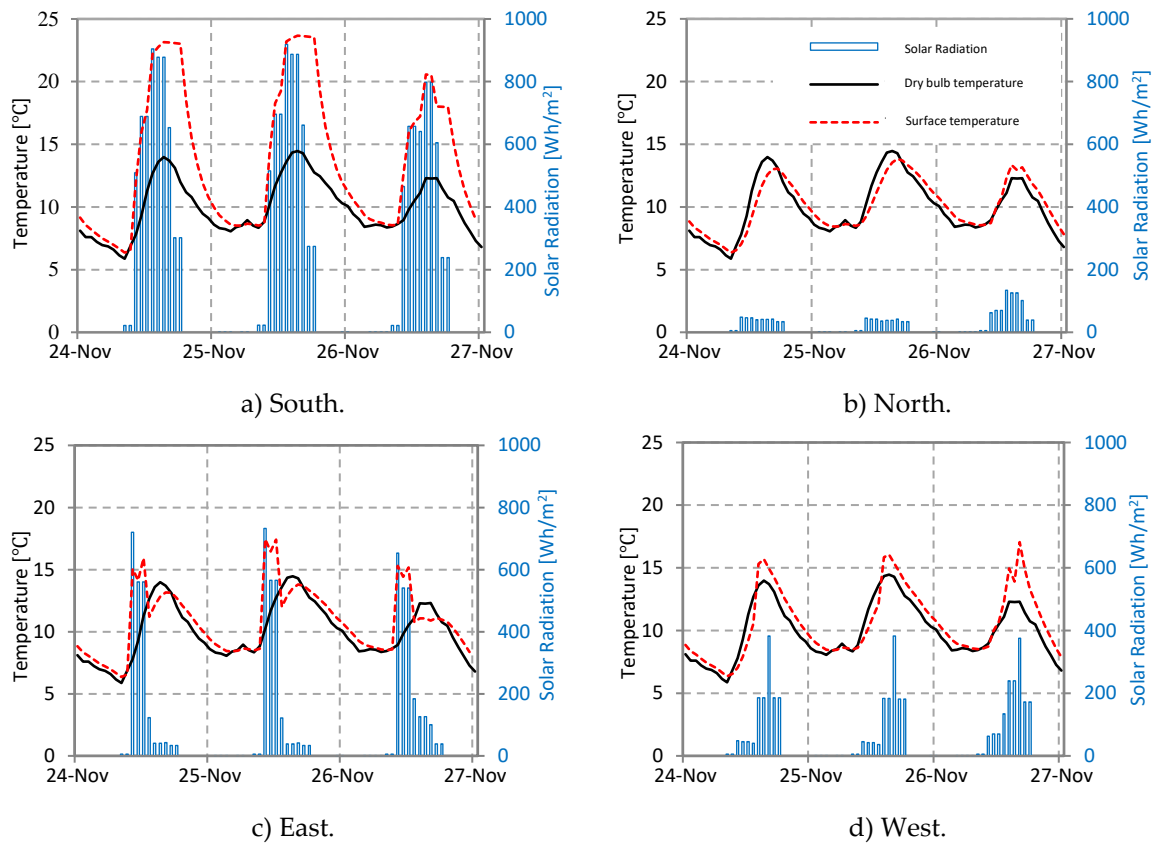


Figure VIII.11 – Analytical prediction of the external surface temperature for different orientations during a clear sky day.

The heat transfer is analysed for a set-point of 20 °C (panel temperature) in heating, according to the building comfort temperature. Figure VIII.12 shows the heat transfer during clear sky conditions. The heat transferred is obtained considering only heat gains/losses by conduction (\dot{Q}_{trans}). It was concluded that with a clear sky, the South oriented panel system has higher heat gains during the day due to the high panel surface temperature and heat storage by water. For other orientations, it was observed that there are no favourable conditions for significant heat gains, and the heat losses from the interior of the building to the exterior are always present. The maximum heat transfer value through the panel is 17 Wh/m², obtained when the

surface temperature reaches the maximum value. When the panel temperature is below the building comfort temperature ($20\text{ }^{\circ}\text{C}$), heat losses near to 5 Wh/m^2 occur.

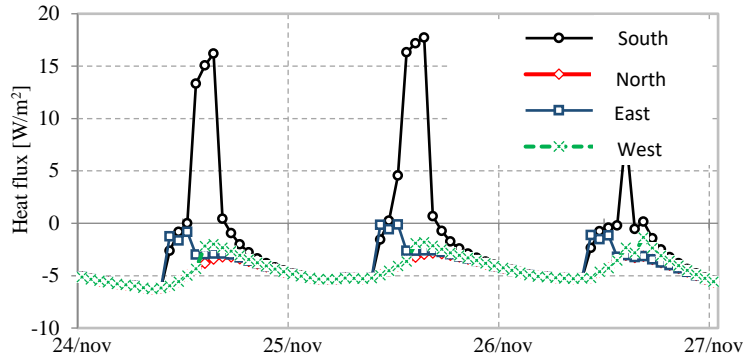


Figure VIII.12 – Analytical prediction of the heat flux for different orientations during clear sky.

VIII.3.6.2. Cloudy conditions

Figure VIII.13 shows the surface temperature fluctuation for different orientations. Under cloudy conditions, direct solar radiation has lower influence on the panel surface temperature.

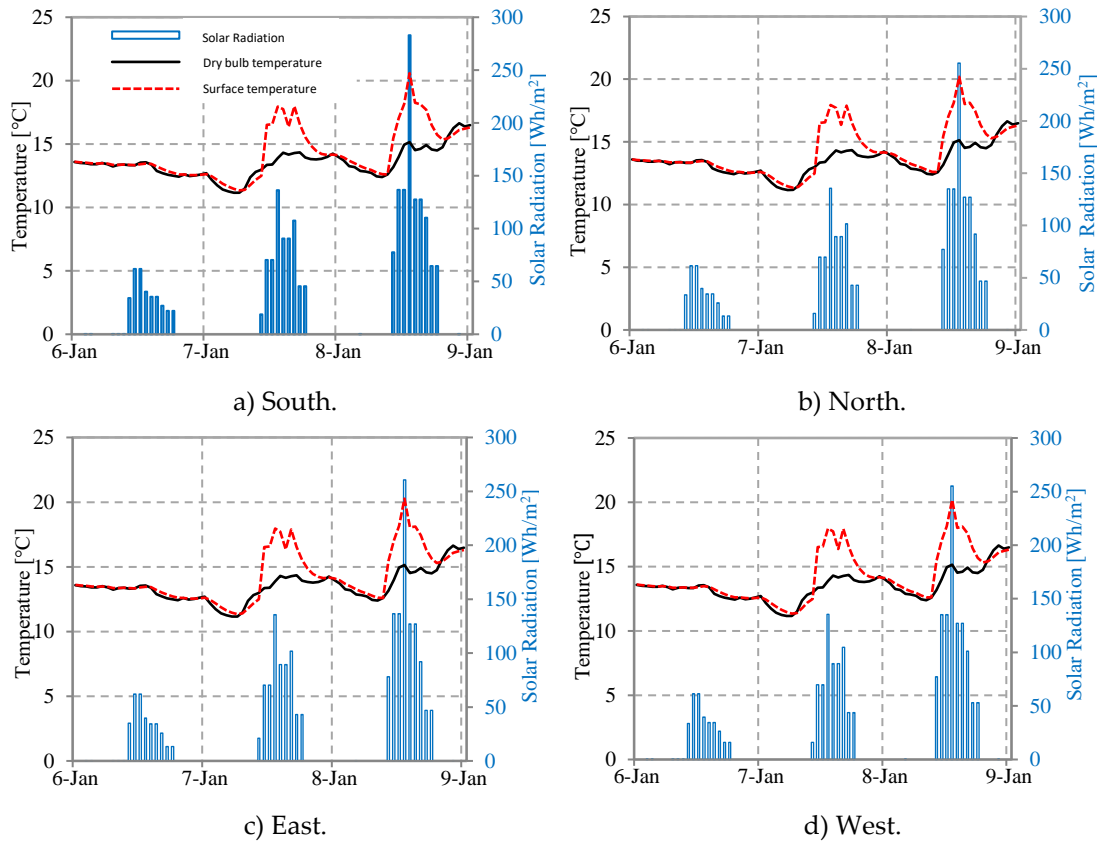


Figure VIII.13 – Analytical prediction of the external surface temperature for different orientations during a cloudy day.

It was concluded that the panel surface temperature is similar for all orientations, and it is closest to the dry-bulb temperature. In this case study, the solar radiation peak was 70 Wh/m^2 on a horizontal plane. For a zenith angle of 90° the sum of both direct and diffuse radiation is 61.41 Wh/m^2 .

During the cloudy sky period (Figure VIII.14), the weather conditions are not favourable for heat storage, and the panel temperature is almost the same as the environment dry-bulb temperature (Figure VIII.13). The average heat losses during the period is 2.66 Wh/m^2 .

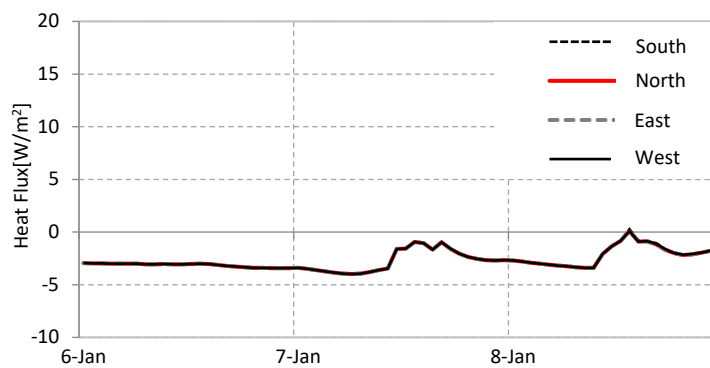


Figure VIII.14 – Analytical prediction of the heat flux for different orientations during cloudy sky.

VIII.3.7. Parametric study

The wall/panel heat storage capacity strongly depends on meteorological effects, azimuth and the materials thermal properties. Figure VIII.15 shows the daily average prototype temperatures measured between 27/11/2013 to 07/02/2014 for different orientations always with the same prototype.

Based on the temperature measurements it is possible to verify that heat storage capacity is higher when the prototype is South oriented. The temperature fluctuations permit to verify the influence of using water on the prototype thermal inertia, where it was measured on the back surface a mean temperature of 1.68°C above the surface temperature exposed to direct solar radiation (south surface).

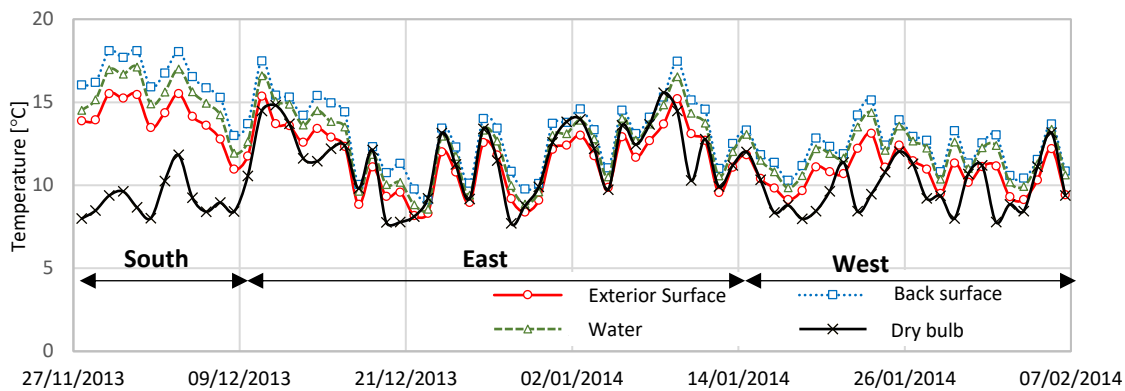


Figure VIII.15 – Measured daily average temperatures of the prototype for different orientations.

In order to analyse the influence of the water thickness (50 mm instead of 100 mm) and also surface colour (black colour instead of natural grey steel colour) increasing the absorption (≈ 1) and the emissivity (≈ 1) coefficients, two more prototypes were tested (Figure VIII.16). Prototype 1 is the same prototype previously studied (with 100 mm of water thickness). Prototype 2 has the same geometric characteristics of prototype 3 (50 mm of thickness), except the exterior colour. Prototype 3 has a black vinyl film. The three prototypes were tested simultaneously (same climatic conditions) with their frontal surface exposed to South (Figure VIII.16). Figure VIII.17 plots the temperatures measured on the frontal surface (a), water temperature (b) and the prototype back surface (c). Water thickness has influence on the thermal storage capacity.

During night periods, the thicker panel (Prototype 1) can maintain the water temperature for longest periods, with an average temperature between 2 to 6 °C above the values obtained with prototype 2 and 3 (Figure VIII.17b). However, thinner panels can achieve higher operation temperatures during day-time. The third prototype, with the black vinyl, could increase the average water temperature by of 6 °C to 9 °C, compared to prototype 2 and 1, respectively. Despite of this temperature increase during day-time, due to its highest emissivity of black colour, prototype 3 has higher heat losses during the night, where a 2 °C mean temperature decrease occurred. During cooling season, the water could have reached peaks of 50 °C, showing a great potential to work with a heat exchanger system for domestic hot water (DHW) production.

CHAPTER VIII

Development of a Water Trombe Wall system for LSF modular construction

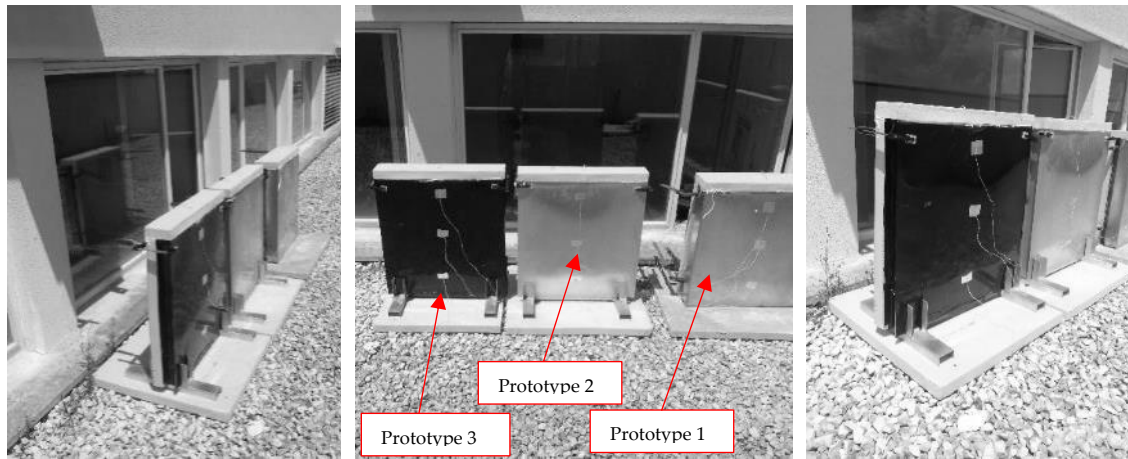
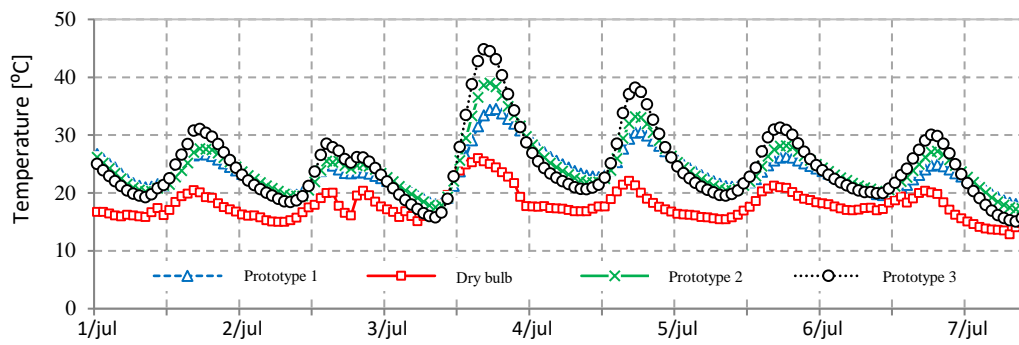
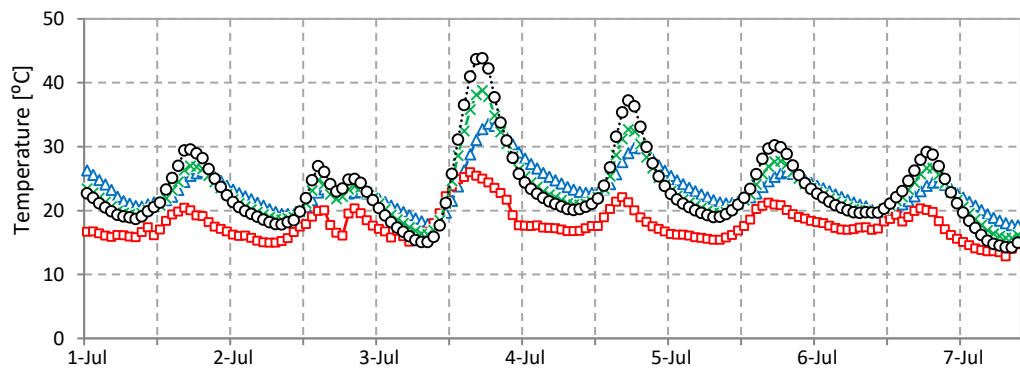


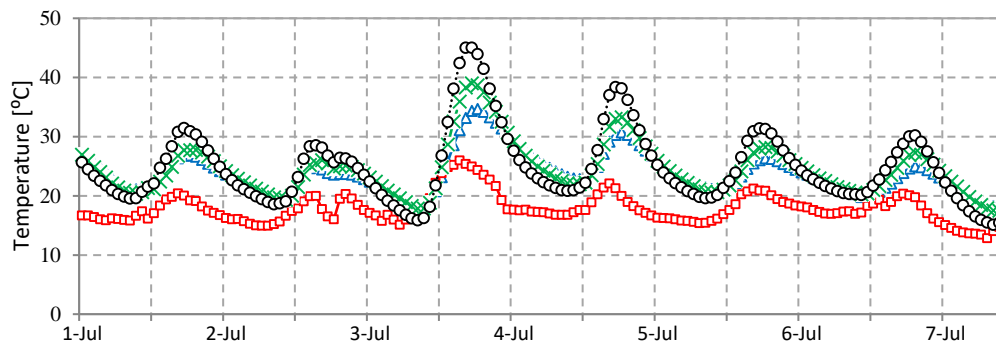
Figure VIII.16 – Experimental prototypes for the parametric study.



a) Frontal surface temperature.



b) Water temperature.



c) Back surface temperature

Figure VIII.17 – Temperatures measured on the water-filled prototypes.

VIII.3.8. Computational fluid dynamics modelling of a dynamic water wall

It was already verified that the opaque water wall previously studied only is more efficient as a thermal energy storage when it is assembled on the south façade. However, the increase or decrease of water temperature can lead to undesirable heat gains or losses during cooling and heating periods, respectively. To verify the influence of using the façades as a heat exchanger, where water could flow through the façades, a 3D CFD model was developed. The numerical results of this dynamic water wall allow to know the temperature gradient [$^{\circ}\text{C}$] and the heat flux [W/m^2] when water flows between different façades. The calculation is performed considering water natural and forced convection, allowing to analyse the flow velocity inside the panels and pipes [mm/s]. It was assumed in the numerical model a cubic compartment with $3 \times 3 \times 3$ meters. Five panels with 50 mm water thick were considered for each façade. All the panels were filled with water and exposed to external heat convection and a surface temperature was considered. To simplify the model, the steel structure of LSF construction was not considered. The module was composed by a layer of XPS (50 mm thick), an air cavity (50 mm thick) and the real scale steel panel with 3.0 meters high and filled with water. Figure VIII.18 presents a schematic representation of the model's geometry.

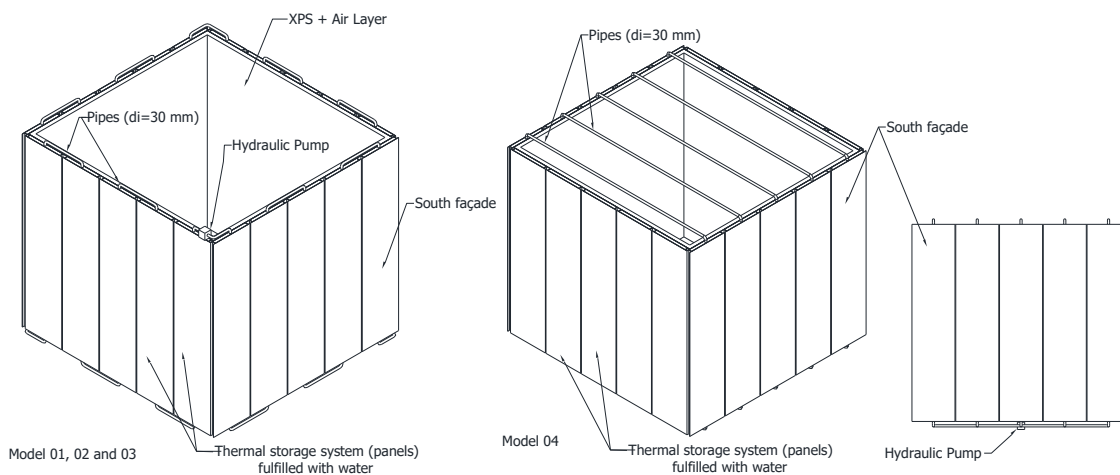


Figure VIII.18 – Schematic representation of the CFD models.

The CFD model 01 was performed to verify if there was no error in the three-dimensional drawing. It was imposed the same temperature and heat convection at all surfaces. Figure VIII.19a) shows the temperature distribution obtained in this model, where can be seen a uniform temperature distribution. The value of the heat flux is the same in all façades (21.70 W), showing that there were no numerical and/or geometric errors of the model. Model 02 contains a hydraulic pump system that was

CHAPTER VIII

Development of a Water Trombe Wall system for LSF modular construction

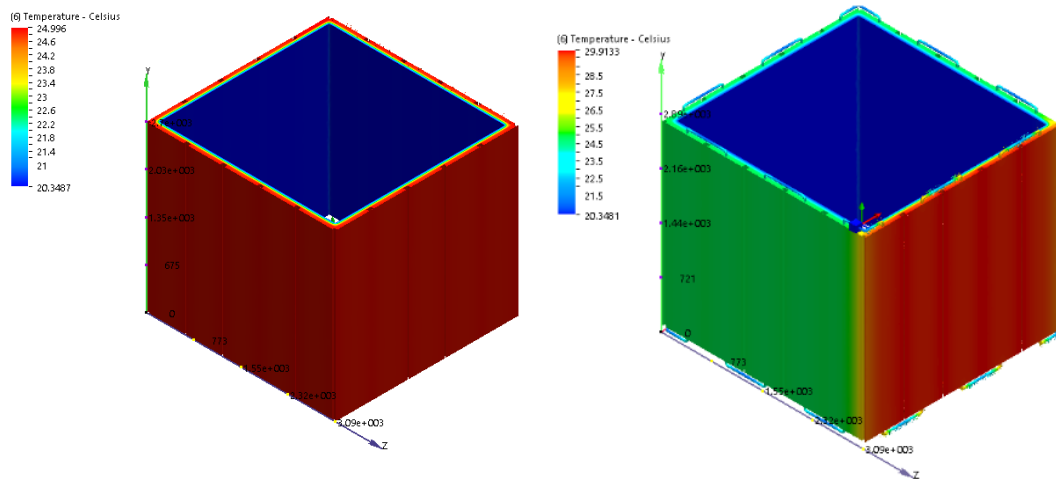
implemented with 30 mm (diameter) network pipes. The outer pipe surface was considered adiabatic, without heat losses when the water flows between panels. This second model aims to verify the water flow in natural convection, with the hydraulic pump off.

Table VIII.5 presents the CFD boundary conditions in the four models. The considered boundary conditions are: (1) Indoor temperature (T_i); (2) Outdoor temperature (T_a); (3) Surface temperature (T_s); (4) Heat convection (h) and (5) Water flow rate. The surface temperature is based on measured values, except in model 01.

Table VIII.5 – CFD boundary conditions.

Model	T_i [°C]	T_a [°C]	T_{surf} (South) [°C]	h_i [W/m ² .°C]	h_e [W/m ² .°C]	g [m/s ²]	Heat convection	Water flow [m ³ /h]
01	20	25	25	7.69	25	9.81	Natural	0
02	20	25	30	7.69	25	9.81	Natural	0
03	20	25	30	7.69	25	9.81	Forced	5
04	20	25	35	7.69	25	9.81	Forced	5

Figure VIII.19b) shows the obtained temperature distribution on the compartment model. In the three-dimensional space x and z axes represents East and South orientations.



a) Model 01 (uniform temperatures).

b) Model 02 (south façade with radiation).

Figure VIII.19 – CFD module for permanent conditions and transient south temperature.

Figure VIII.20 shows the water velocity/temperature in natural convection. As expected, water velocity (flow) in natural convection is not enough to promote for

heat exchange between adjacent water panels. The water velocities are between 6.0×10^{-7} mm/s and 3.67×10^{-7} mm/s.

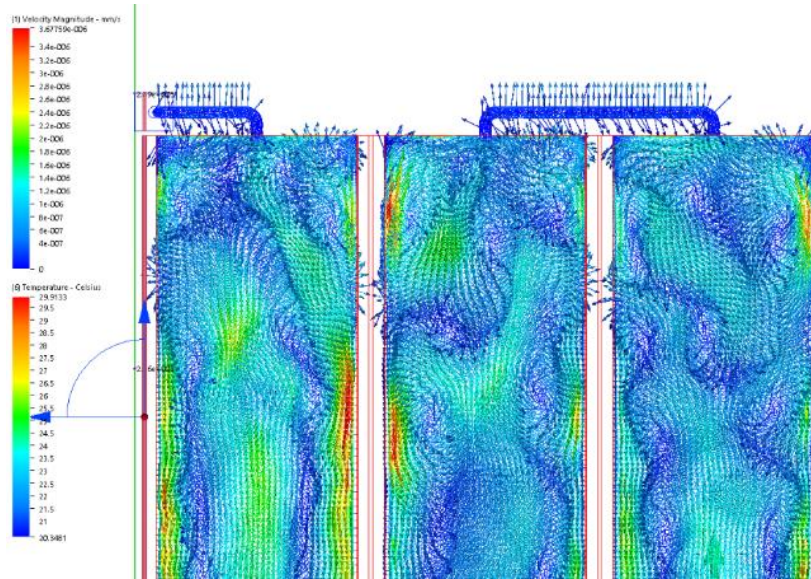


Figure VIII.20 – Temperature and velocity vectors of water flow between south panels (natural convection).

After the verification that this system can't work as a passive heat exchanger, the effects of forced water flow between panels was numerically studied, turning on a hydraulic pump with a constant flow rate of $5 \text{ m}^3/\text{h}$. For model 03, the water circulation is performed as a closed loop circuit between all the façades.

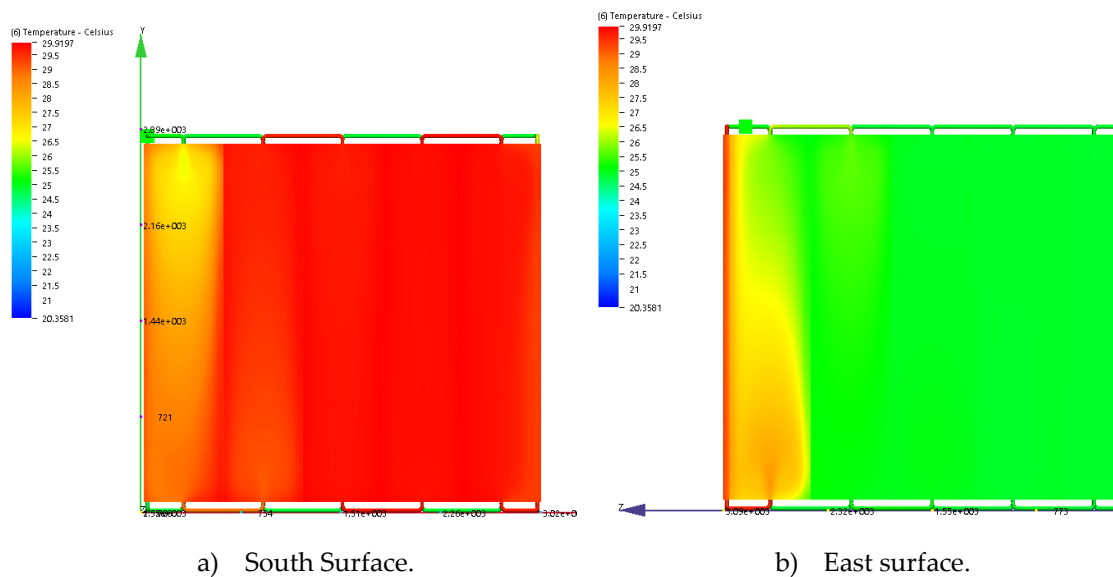


Figure VIII.21 – Temperature distribution for model 03.

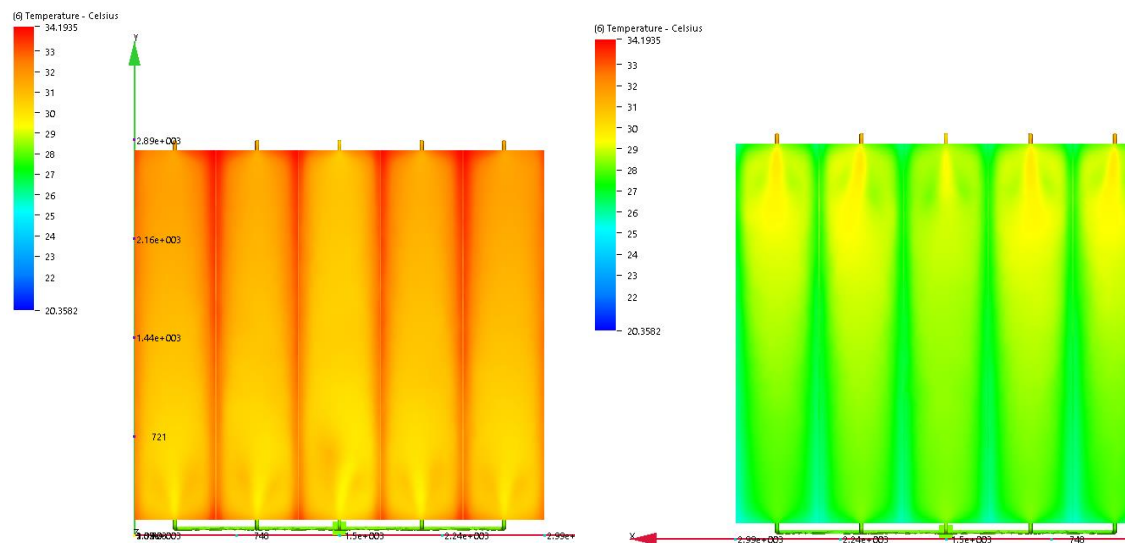
The south façade surface temperature is higher due to direct solar radiation (Figure VIII.21a). Results allowed to verify that it was not possible to totally cool down the south surface (Figure VIII.21). It was also observed that only the first panel could be

CHAPTER VIII

Development of a Water Trombe Wall system for LSF modular construction

cooled down around 3°C. This is a small temperature decrease where the heat flux decreases by 2.06%. In model 04 the closed circuit is performed between North façade (usually the one with the lowest temperature) and South façade (higher temperature due to solar radiation). The pipes have 30 mm of diameter and the hydraulic pump delivers 5 m³/h, but now the water circuit is done between north and south panels. The following figures show the North and South facades with the system working in a steady-state conditions in a closed loop.

The numerical results from model 04 (Figure VIII.22) show that in a steady-state conditions the heat flux on south surface decreases 25.29% and increases 41.95% on North façade. The study presented in this section allowed to verify that moving water between wall panels in different orientations, can contribute for a reduction or increase of the heat gains/losses. However, it is obvious that this system may have some drawbacks: (1) big installation and operation costs; (2) cavitation problems; (3) corrosion; (4) water volume; (5) hydraulic pressures; (6) control automation systems.



a) South Surface.

b) North façade.

Figure VIII.22 – Temperature distribution for model 04.

VIII.4.Design and thermal performance analysis of a Water Trombe Wall prototype

Passive solar systems can reduce 25% of a building's energy consumption (Liu and Feng, 2011). As already seen, Trombe walls can reduce the total building consumption (HVAC) by 30% (Zamora and Kaiser, 2009), (Saadatian *et al.* 2012). Despite of having a complex thermal behaviour, these systems can easily operate in different climate regions. In this section, a pre-design of a Water Trombe Wall (WTW) is presented. The heat storage system used in this WTW has the same

configurations presented in Section VIII.3. During the development of this system the assemblage of the heat storage system in the LSF structure was analysed. The first layer of the system was developed to be assembled directly on the façades. The heat exchanges would be performed between the LSF structure and the TES panel. However, usually LSF structures have horizontal profiles (nogging) in the air cavity. Based on results presented in previous section a new configuration for the WTW with a double glass is suggested. Later, the assessment of the thermal performance of a WTW prototype is conducted experimentally. At this stage, results are only preliminary. To evaluate the WTW performance two identical experimental modules like cubicles located in Coimbra (Portugal) were designed, constructed and monitored during a Mid-season in the Csb climate. In one of them the WTW prototype is assemblage in the south wall. The main functions of this system: (1) absorbing heat gains from solar irradiation during the day and transfer the stored heat indoors by both radiation and convection during the night; (2) increase thermal inertia in LSF buildings; (3) the system will work as a TES; (4) neutralise the inverse thermosiphon during the night.

VIII.4.1.Pre-design

The first WTW design considered heat exchanges between TES panels and an OSB board. However, the presence of nogging's can reduce the heat exchange efficiency due the interference on the air flow interfering the heat gains by convection. The heat gains of this wall are calculated based on the outlet air temperature. The outlet air temperature is calculated using Equation (105), considering that all the elements are in steady state conditions; *e.g.* the same temperature. The steel frame used in this study can be seen in Figure VIII.23.

Nogging area may have a high influence on the heat transfer. Because it restricts heat exchanges area. For this calculation it is assumed that the vertical profiles will not obstruct the air flow. However, two proposals are considered for the convective heat transfer areas. The first proposal (A1) that air flow is obstructed only by the nogging area (Figure VIII.23a). For the second proposal (A2) it is assumed that the obstructed area is three times greater than noggins area (Figure VIII.23b). The total heat transfer area without noggins presence is 1.66 m². The obstructed areas are 0.192 m² and 0.538 m² for A1 and A2, respectively. These obstructed areas decrease the heat transfer by 11.59% and 32.37% in A1 and A2, respectively. It is also considered an inlet temperature of 20 °C (indoor comfort temperature) and an exterior temperature of 30 °C (considering the average measured values of maximum panel surface temperature) for a typical sunny day. The air velocity inside the air cavity is 0.05 m/s

CHAPTER VIII

Development of a Water Trombe Wall system for LSF modular construction

(0.004 kg/s) and 0.2 m/s (0.015 kg/s), considering natural or force convection, respectively.

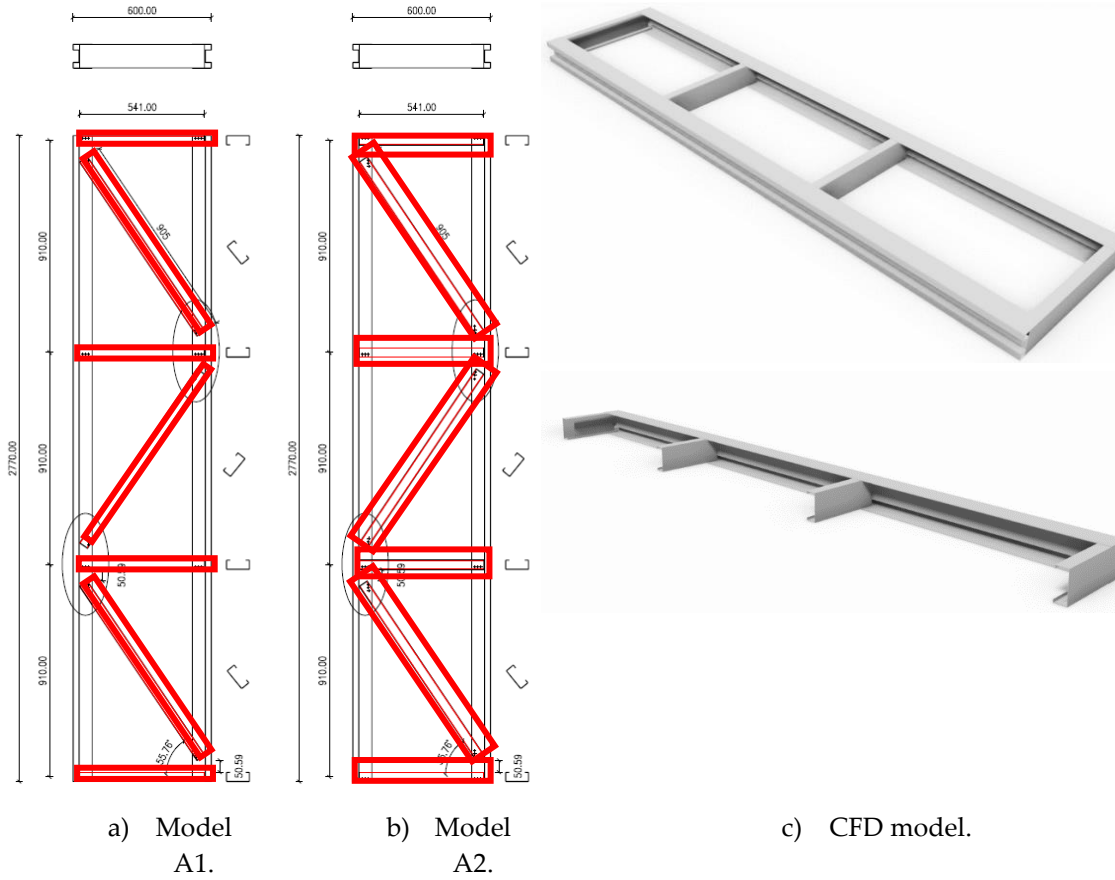


Figure VIII.23 – Steel frames used in analytical and numerical study.

Three approaches are used in this study. The first approach considers a perfect contact between the air cavity and building interior and thermal resistance of the inner layers can be neglected. In this case and according with DL No 118/2013 all inner wall layers have null thermal resistances. Natural convection in a confined vertical space is considered in the second approach. The heat convection is achieved by:

$$h = \frac{Nu k_{air}}{e} \quad (125)$$

Where k_{air} is the air thermal conductivity [0.021 W/(m.°C)] and Nu represents the Nusselt number for natural convection and e the air thickness (0.1 m). The Nusselt number is obtained using the Grashof number:

$$G_{R,L} = \frac{\rho^2 g \beta \Delta T Z^3}{\mu^2} \quad (126)$$

where g represents the gravity acceleration (9.81 m/s^2), β the volumetric expansion coefficient, μ the air viscosity ($2.0 \times 10^{-5} \text{ N.s/m}^2$), Z the heat transfer length (distance between vents) and ΔT the temperature difference between inlet and outlet. The Nusselt number can be calculated using the following expression:

$$Nu_{air} = 0.18 G_{R,L}^{1/4} \left(\frac{L}{g} \right)^{1/9}, \quad 10^8 < G_{R,L} < 10^9 \quad (127)$$

Finally, the third approach considers that the system was working with forced convection, where the Nusselt number can be calculated with the following expression:

$$Nu = 1.86 \left(R_{ed} P_r \frac{d_i}{g} \right)^{1/3} \left(\frac{\mu}{\mu_p} \right) \quad (128)$$

The heat transfer decrease is estimated using the relation between total heat transfer without steel profiles and with profiles. Figure VIII.24 present the result of heat transfer losses. Results based on DL No 118/2013 are more reliable in terms of air outlet temperature. However, the second approach shows better approximation to what is expected in terms of heat transfer decrease. Heat transfer decreases of 13 up to 40%, are observed in the results achieved with the second approach. These values are lower using the first approach. It is found a heat transfer decrease of 6 up to 20% without forced convection and between 10 to 30% considering forced convection. To verify more accurately the influence of steel profiles, a simple CFD model was developed (Figure VIII.25). An air flow rate of $0.03 \text{ m}^3/\text{s}$ is considered. It is found by CFD results that the influence area is 1.07 m^2 which is higher than A1 (0.192 m^2) and A2 (0.538 m^2). This leads to heat transfer decrease between 51 to 77%.

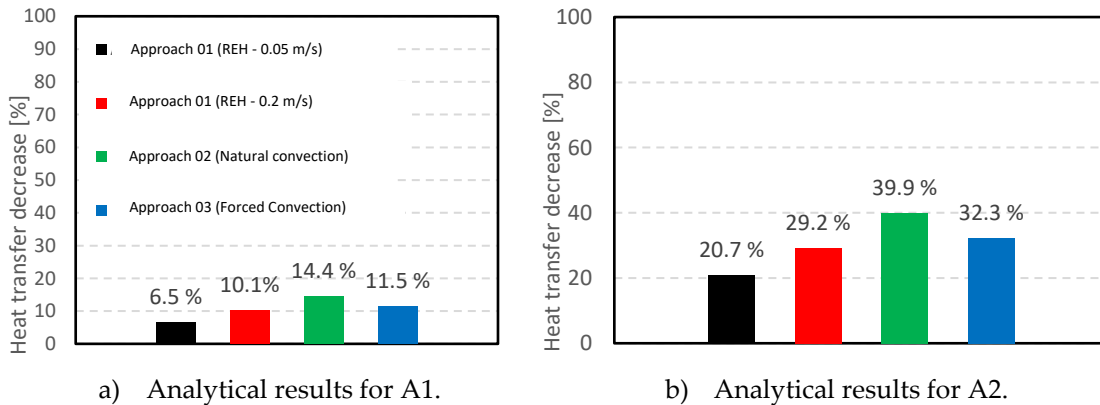


Figure VIII.24 – Heat transfer decrease results for the WTW with noggings.

CHAPTER VIII

Development of a Water Trombe Wall system for LSF modular construction

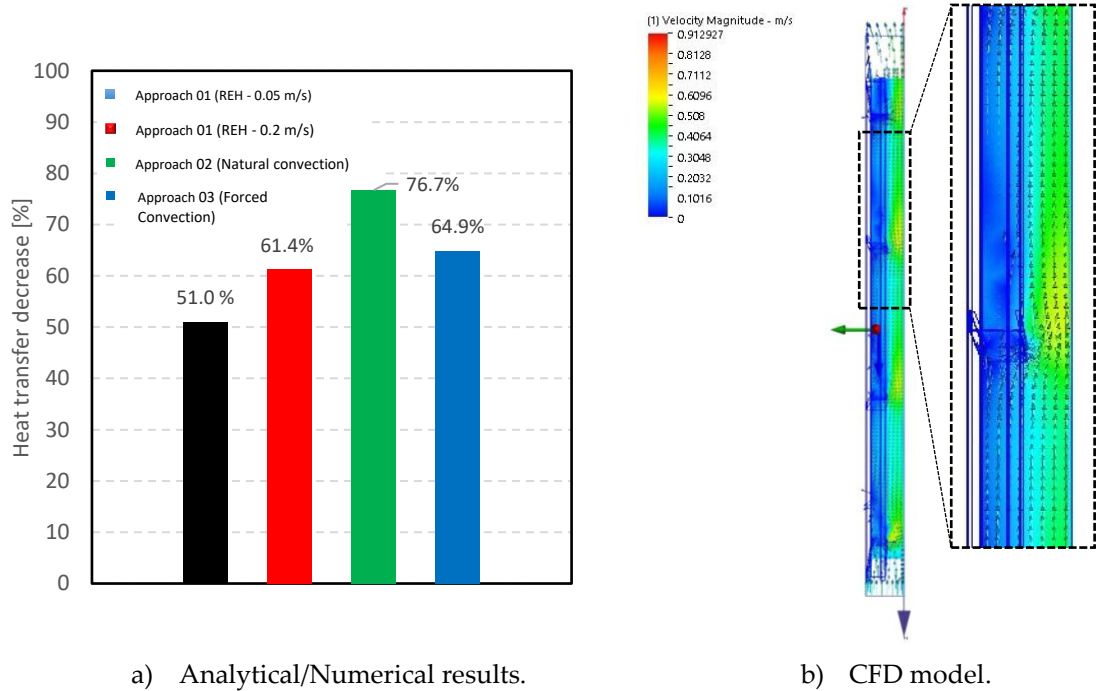


Figure VIII.25 – Analytical and CFD results.

Results showed that using the LSF structure to promote heat exchanges by convection between the TES panel and indoors, is not the best approach. The best way to promote heat exchanges between the TES panel and building interior is by combining a standard Trombe Wall with the TES panel. Figure VIII.26 illustrates the first design of the Water Trombe Wall (WTW). Layer 01 is the steel structure of the LSF wall.

- (1) Transparent double glass (with vents);
- (2) Upper vent with grills (150 x 200 mm). Here a fan should be installed for forced ventilation;
- (3) Plasterboard with 12.5 mm thick;
- (4) Bottom vent with lower thickness (50 x 300 mm) to increase air speed in the air cavity of the Trombe wall and for better esthetical aspect;
- (5) Ripped wood (30 x 30 mm) and XPS (30 mm);
- (6) Vacuum insulated panel which is evacuated, encased and sealed in a thin, gas-tight envelope with lower thermal conductivity (0.007 W/(m.°C));
- (7) OSB with 12 mm thick;
- (8) Thermal Storage Wall (*EcoSteelPanel*) with 50 mm thick.

Figure VIII.27 presents a 3D rendering of this WTW installed in a LSF modular construction house. This residential house is produced by Cool Haven company. This building integrates the steel structure studied in Chapter III. EAHE system studied in Chapter V and VI is also installed in this building. In the next section a first

prototype is presented and monitored to assess the thermal performance of the WTW.

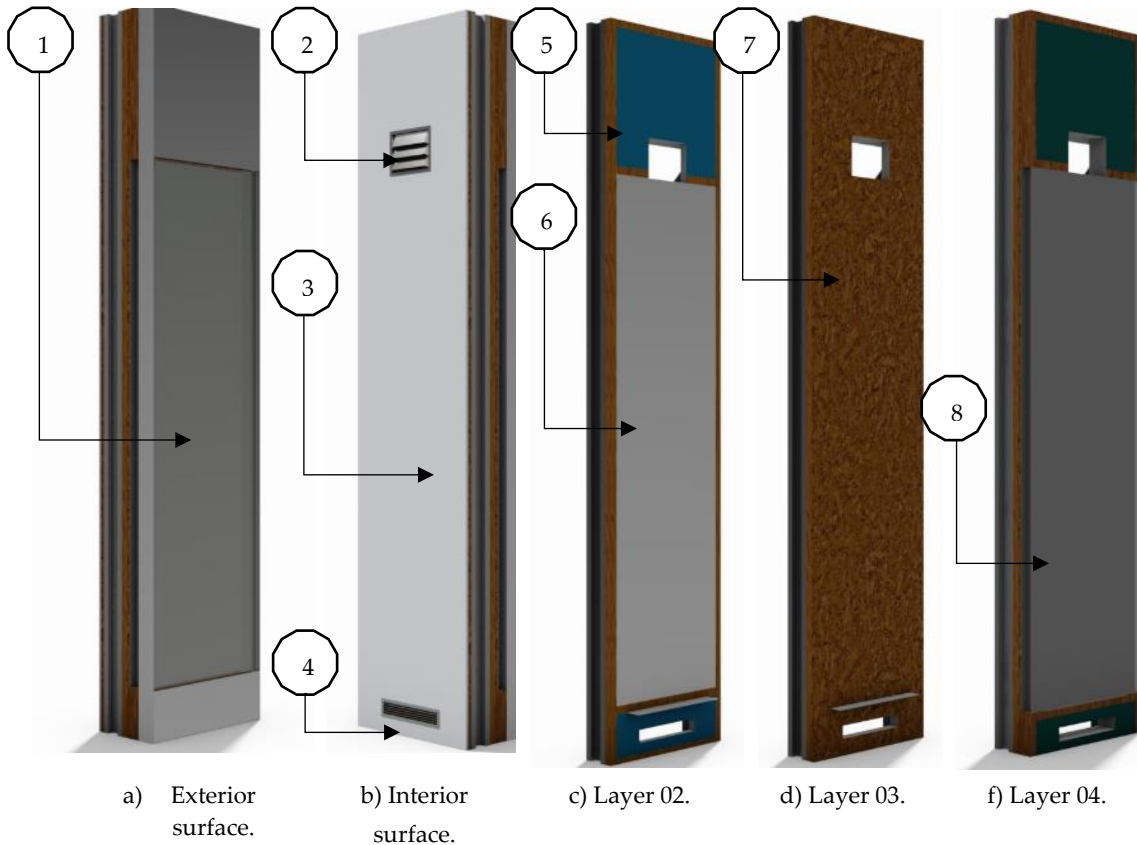


Figure VIII.26 – Tri-dimensional WTW module design.



Figure VIII.27 – Tri-dimensional rendering of the water Trombe wall with six modules in a LSF construction (Cool Haven).

VIII.4.2. Experimental set-up and instrumentation

To test the improvement of thermal performance of a compartment due to the use of a Trombe Wall with TES panel (Water Trombe Wall), two identical experimental modules in LSF (cubic houses) with the same inner dimensions (2.75m x 2.75m x 2.8 m) were designed, constructed and monitored. The experimental modules are

CHAPTER VIII

Development of a Water Trombe Wall system for LSF modular construction

located in Coimbra (Portugal) in a Csb climate region (Kottek *et al.* 2006). One of the modules is used as “reference” while the other has the WTW system in the south façade (Figure VIII.28). The construction details of the modules are illustrated in Figure VIII.29.

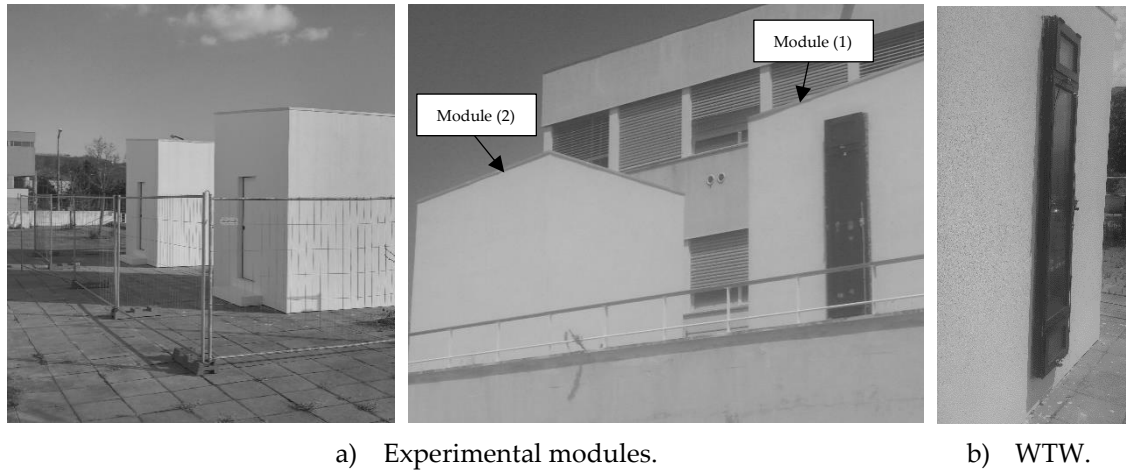


Figure VIII.28 – Experimental set-up: WTW module (1) and reference module (2).

The steel structure of the modules is composed by C100x45 mm steel profiles. The walls steel profiles are filled with stone wool (100 mm of thick). The steel profiles are closed with OSB3 with 12 mm thick in both sides. Expanded polystyrene with 50 mm thick is used as external insulation (ETICS). The roof is composed with the same steel profiles (C100x45) and is closed with OSB boards with 12/18 mm of thickness. The external insulation of the roof is extruded polystyrene with 60 mm thick. The floor is also composed with 60 mm thick of extruded polystyrene and OSB with 18 mm thick.

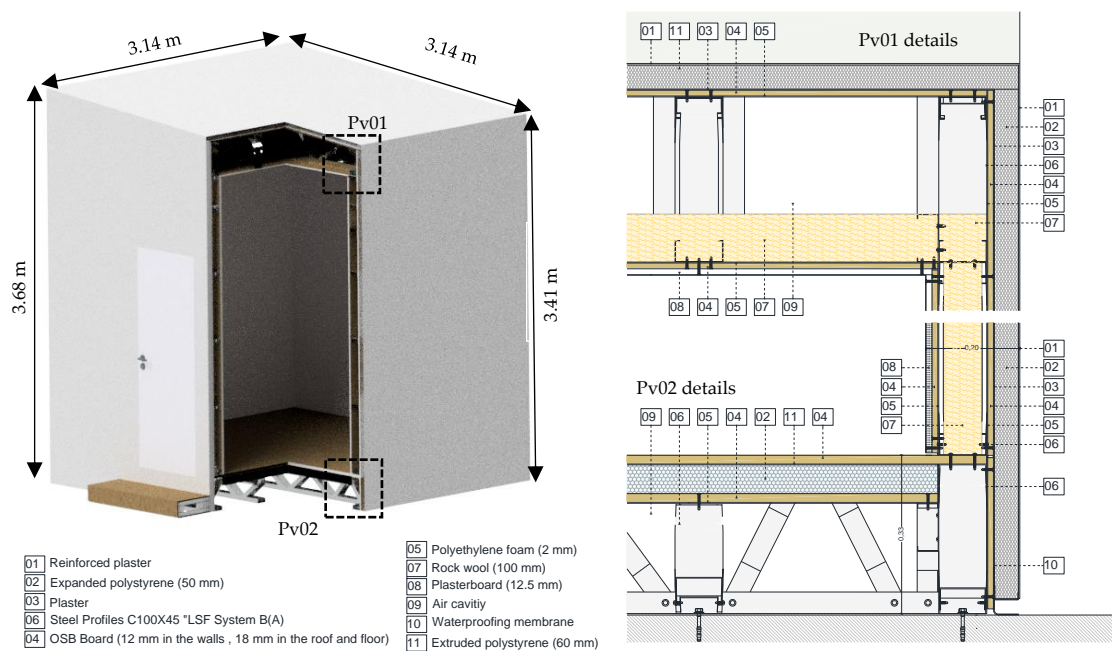


Figure VIII.29 – Construction details of the experimental modules.

The experimental Water Trombe wall consists on the assembly of two components: (1) a thermal storage system (TES) filled with water and (2) a double glass aluminium frame. The WTW frame (Figure VIII.30) has two exterior openings (at top and bottom) for cooling proposes (Figure VII.1c). The outer glazing is a double glass with 4 mm + 16 mm of argon + planistar 6 mm. The effective solar absorption area is 1.1 m². The thermal storage system is an *EcoSteelPanel* (Figure VIII.1b) with inner reinforcements to resist the water pressures without having significantly deformations. The panel dimensions are 50 mm thick, 590 mm width and 2800 mm height (Figure III.31). The air cavity has 2800x550x70 mm of dimensions.

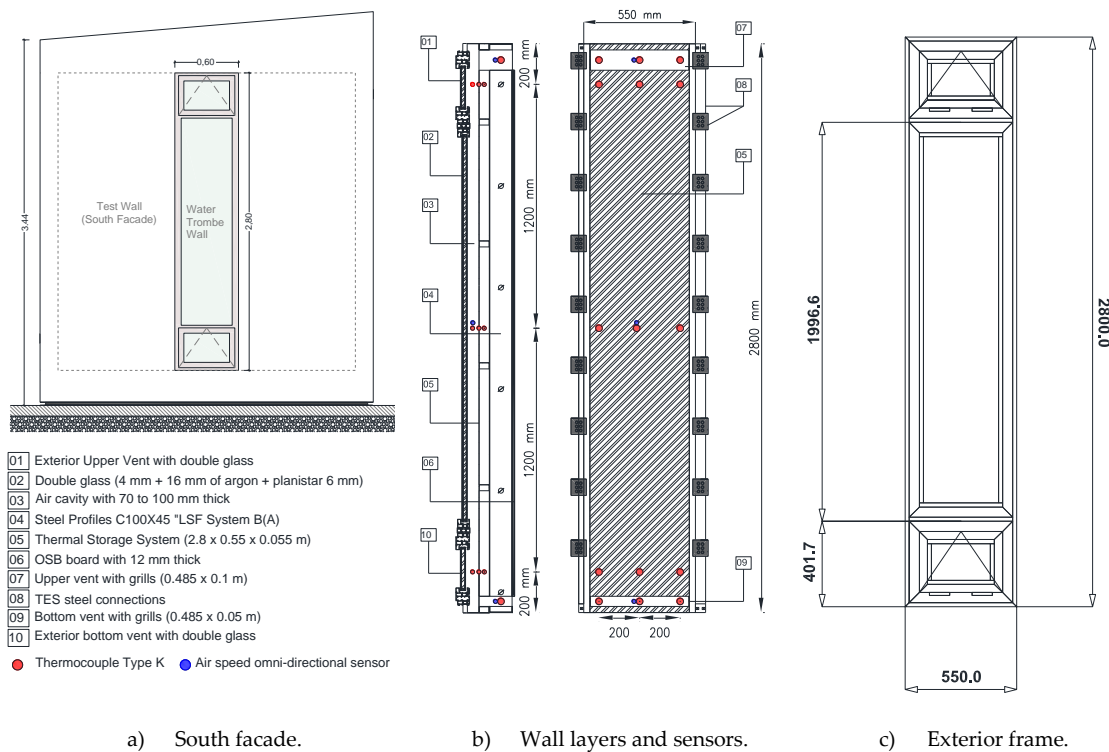


Figure VIII.30 – Water Trombe Wall prototype assemblage and sensors location.

Both experimental modules were fully instrumented, and data was registered at 5 minutes intervals to evaluate the thermal performance. Internal walls (east, west, north, south, roof and slab) temperature are measured with thermocouples type K (Figure VIII.31). The thermocouples were calibrated in groups connect to a datalogger CR1000 with a multiplexer AB16/32B, using a calibration bath *Heto Lab Equipment* DBTKB21 (accuracy of ± 0.1 °C) equipped with the *HetoTherm* DBT 200 thermostat and a PT100 probe, for a temperature range of 10- 50 °C. The DBT K2I bath is filled with 7 liters of distilled water. The calibration procedure is: (1) water temperature was initially stabilized to 5 °C; (2) thermocouples were immersed into the water at the same depth. Temperature reading and the data was recorded by data acquisition system; (3) repeat the procedure by increasing the temperature reads

CHAPTER VIII

Development of a Water Trombe Wall system for LSF modular construction

from 5 °C to 45 °C. The data acquisition was programmed for time-steps of 10 seconds and a total time of 5 minutes for each temperature. After measurements the average temperature was calculated and linear least-squares curve-fitting method was used to fit a line to recorded data for each thermocouple.

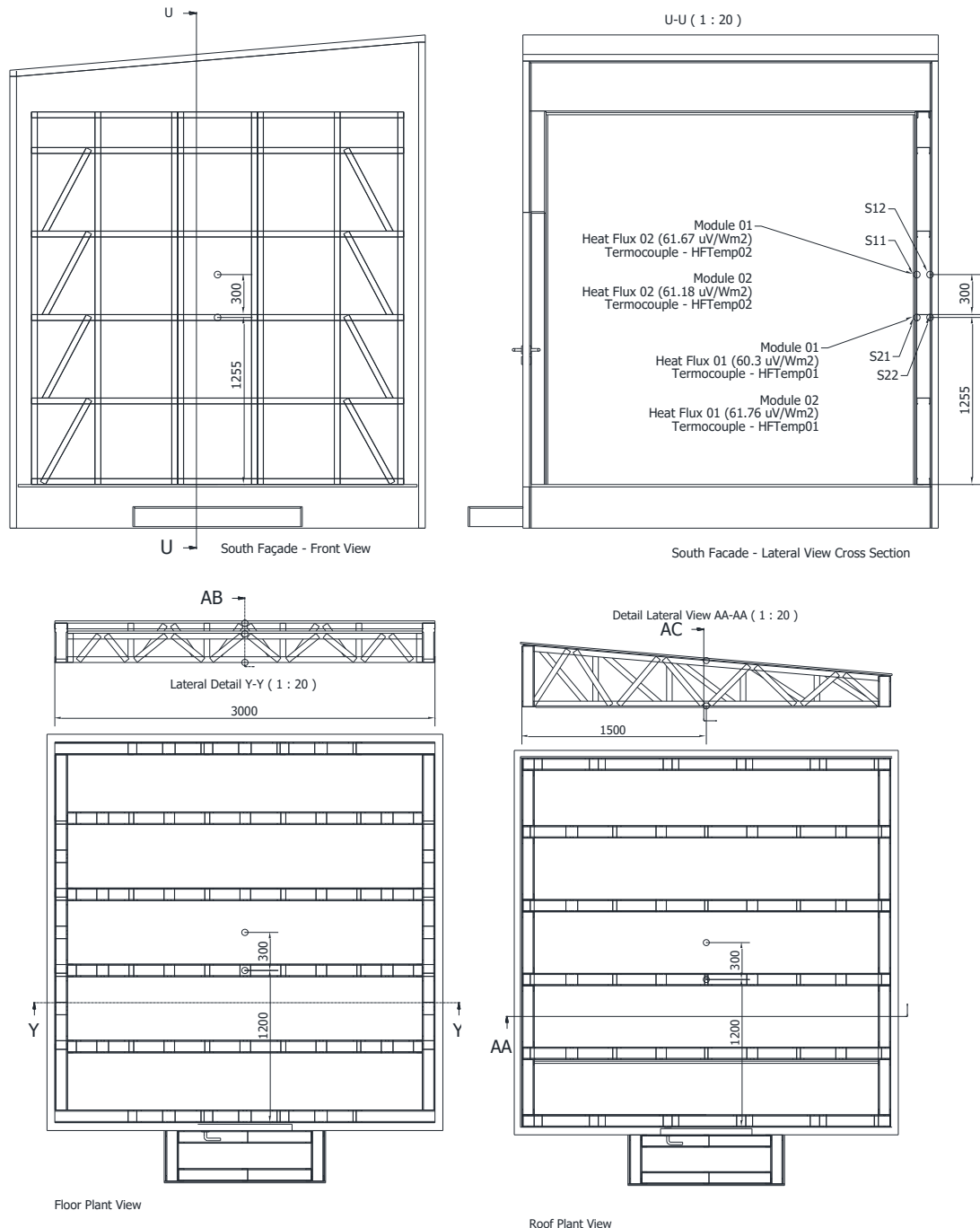


Figure VIII.31 – Example of sensors map for south wall, roof and slab.

Indoor air temperature and humidity was measured using *TinyTag Ultra 4500* (at a height of 1.5 m). The sensor has a RH precision of $\pm 3.0\%$ and a temperature precision of ± 0.4 °C to ± 0.5 °C for 25 °C and 0 °C, respectively. The sensors readings were

verified by comparing both sensors at the same time for air temperatures between 8.5 °C and 23 °C. The maximum difference between sensors was 0.07°C and 0.12 °C for air temperatures of 23 °C and 8.5 °C, respectively. The heat flux transferred to indoor was measured using two HUKSEFLUX HFP01. The sensors were installed on south façades in two distinct zones (1) at noggings zone at a height of 1.25 m; and (2) zone without noggings at a height of 1.5 m. The correct calibration parameters were programmed and implemented in dataloggers (Campbell Scientific CR1000 with three multiplexers AM16/32B with 32 channels) and in Excel software.

Moreover, to analyse the behaviour of the Water Trombe Wall system, the following data was also measured (Figure VIII.30b):

1. external surface temperature of the TES panel was measured with 9 thermocouples placed at different heights and locations;
2. water temperature inside the TES was measured by 3 thermocouples placed at different heights and in the middle of panels thick;
3. air temperature inside the air cavity of the WTW was measured with 9 thermocouples at the same locations of the external surface sensors;
4. back surface of the TES panels was measured at 1.5 m of height to have the same temperature points as module 02;
5. inlet and outlet air temperatures were measured with 6 thermocouples;
6. air velocity at the inlet, outlet and in the middle of the air cavity of the WTW was measured with three active air speed omni-directional sensors for speed ranges from 0.08 to 5 m/s.

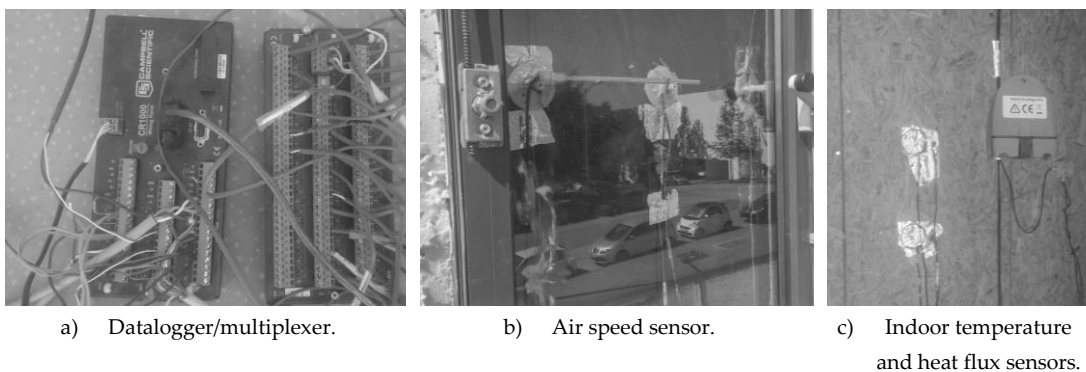


Figure VIII.32 – Example of some experimental instrumentation.

The outdoor conditions were measured by a wireless vantage Pro2 Plus. An excel sheet was developed and programmed with Visual Basic to update and plot automatically all the measured values.

VIII.4.3. Experimental Modules Verification

To verify the thermal and air permeability of the modules a few tests were performed. The air permeability validation was performed using the tracer-gas technique. This technique was applied to measure the air changes per hour (ACH) of the experimental modules. The tracer gas method used is the concentration decay method. The method consists by injecting a dose of tracer gas and measure the tracer gas concentration during a period. The tracer gas used for these tests was the CO₂. The tests were performed initially with the modules with the same conditions and without the WTW system. Later the modules were compared but now with the WTW system installed on south surface of module (1). Figure VIII.33a and b show the experimental results without the WTW. It can be seen a good agreement between the ACH with an average difference of 0.0016 ACH. Figure VIII.33 shows the results with the WTW installed. It is found an average difference of 0.0019 ACH between module 01 and 02. Results have shown that both modules are very similar in terms of air permeability.

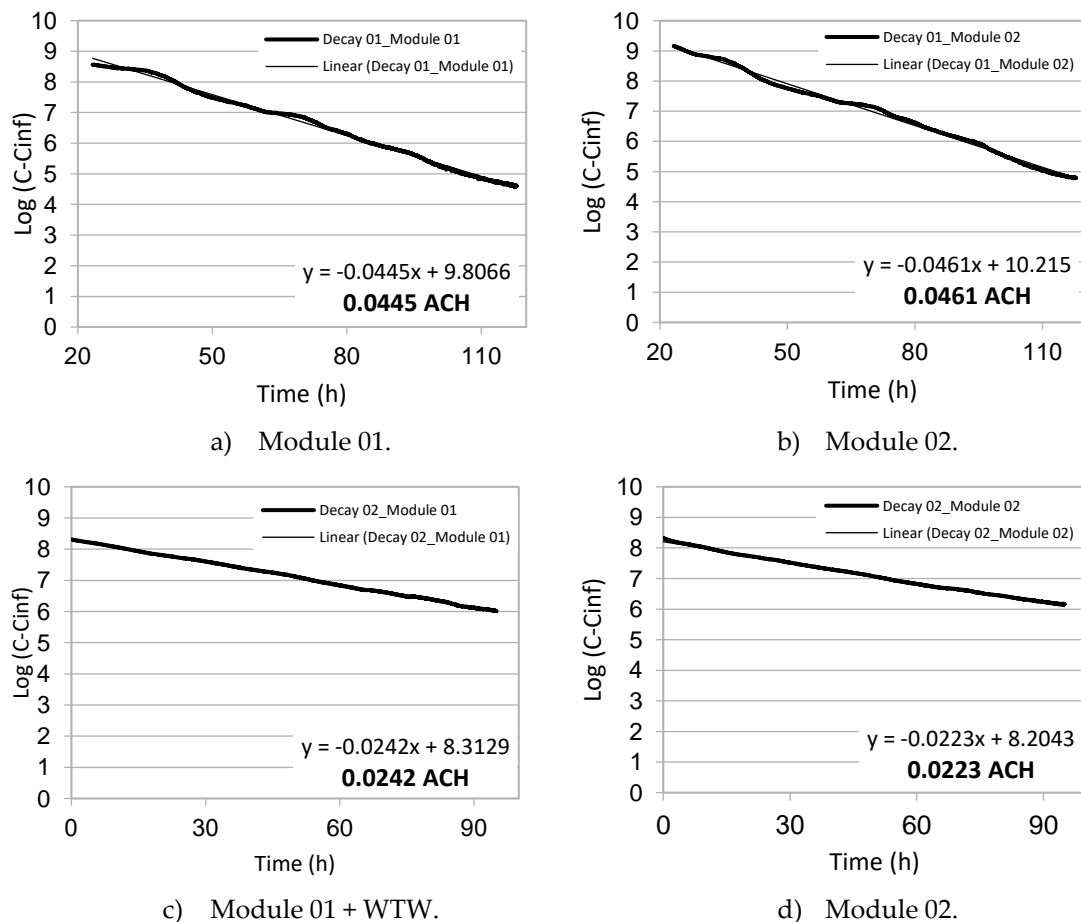


Figure VIII.33 – Experimental results with CO₂ concentration decay method.

Infrared thermographic inspections were done in two stages: (1) inspection performed inside the modules during a sunny day; (2) inspection performed outside the modules during night-time. In this last stage the modules were heated using two air heaters fans (2000 W). This allowed and higher temperature gradient between indoor and outdoor when the outdoor temperature decreased. Wind conditions were always taken in account during the experimental periods. However, it is very difficult to predict the air flows around the modules due their proximity to a building. Figure VIII.34 shows infrared photos of the bottom zone of the doors. This area of the modules was the most affected. However, the bottom doors were sealed.

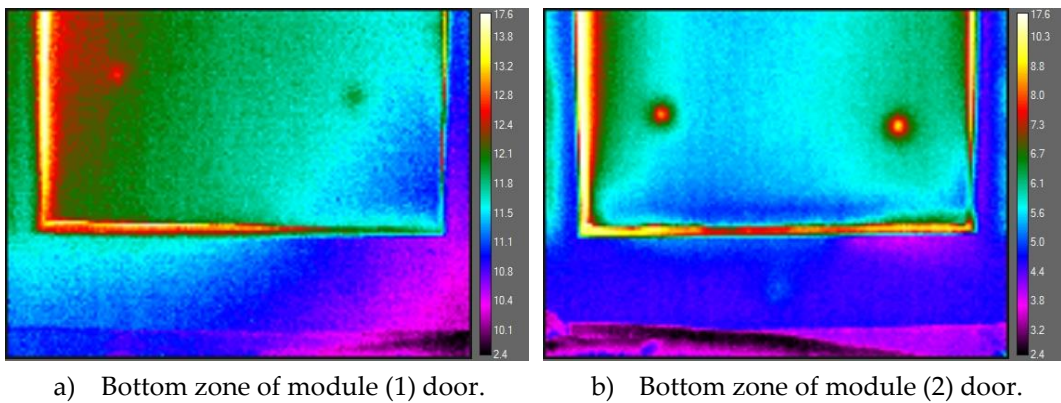


Figure VIII.34 – Infrared thermographic inspections (*e.g.* doors).

The temperature and air humidity fluctuations were also compared. It is very important to have similar initial conditions before assembling the WTW. Figure VIII.35a and b) shows the indoor temperature and air humidity of the experimental modules.

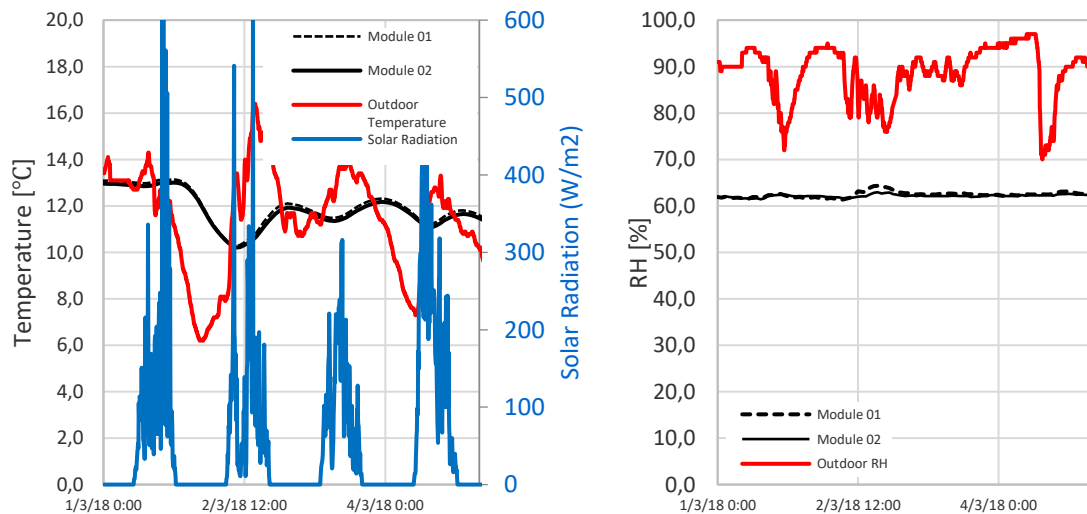


Figure VIII.35 – Temperature and relative humidity verification between experimental modules.

The plots only show results between 01/03/2018 until 05/03/2018. However, the same behaviour was observed for longer periods. Results show a very good approximation between the experimental modules behaviour. It was found an average difference of 0.13 °C and 0.42% for indoor air temperature and air humidity, respectively. After these tests it was concluded that the experimental modules have a very similar behaviour which means that they can be used for later tests with the WTW prototype.

VIII.4.4. Methodology

In this section, the thermal performance of the Water Trombe Wall prototype is experimentally tested during different weather conditions in Csb climate. At this stage the system was tested only in heating operation mode illustrated (Figure VII.1b). These preliminary results are important to understand the prototype operating temperatures and drawbacks. These characteristic values are the main set-points to control the air vents and fans in future experiments. The tests were performed from 6th of May to 11th of June of 2018. Figure VIII.36 shows the weather conditions for this period.

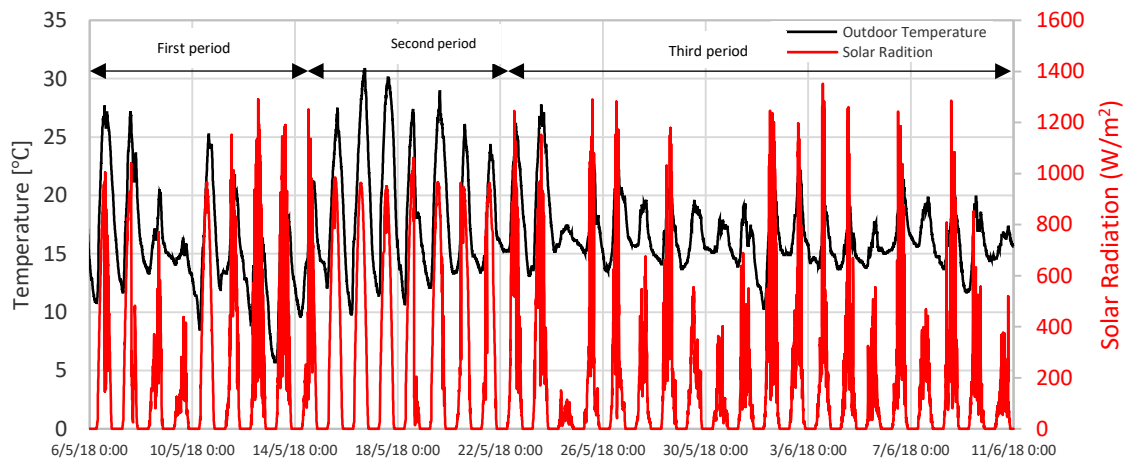


Figure VIII.36 – Outdoor air temperature and solar radiation.

The experimental tests were divided into three periods: (1) from 6th of May to 14th of May – WTW naturally ventilated under clear sunny days and with high outdoor temperature fluctuations. The maximum outdoor temperature is 28 °C (global solar radiation of 946 W/m²) and the minimum is 5.7 °C; (2) from 15th of May to 22th of May – WTW mechanically ventilated with a small fan (15 W) under clear sunny conditions and for high outdoor temperatures (peak of 31 °C); (3) from 23th of May to 11th of June: WTW naturally ventilated under sunny and cloudy conditions with lower outdoor air temperatures. In this final period global solar radiation reaches the

maximum peak of 1352 W/m^2 and the minimum temperature is 10.3°C . The main objectives of these first three experimental stages/tests are: (1) to analyse the air temperature inside the airgap and compare it with the water temperature; (2) to compared the WTW thermal inertia against indoor temperature; (3) to analyse the operation set-points of temperature and time under the present conditions; (4) to investigate if the TES system can prevent the reverse thermosyphon effect of typical Trombe walls; (5) to verify the effect of forced convection in heat demand (Equation 90); and finally (6) to compare indoor temperatures between module 01 and 02.

VIII.4.5.Preliminary results

The first period of experiments, the WTW system operate under natural convection and mainly during sunny conditions. However, between 8th and 10th of May cloudy conditions are observed. Figure VIII.37 shows the indoor and outdoor temperature and relatively humidity. The maximum temperature difference between modules is 3.97°C observed at 15:00 (maximum solar radiation of 1039 W/m^2) of 7th of May (sunny day). Overheating ($>25^\circ\text{C}$) is found between 19h:00 to 00h00 of 7th of May. Based on measured values (temperature and solar radiation) inner vents should be closed at 15h:00 for warmer days when the solar radiation reaches the maximum values. When the sky is cloudy the maximum difference is 1.53°C (9th of May). The minimum difference of 0.58°C is found for 10th of May at 8h00. Module 01 is warmer than module 02, even during the night. For instance, for the minimum outdoor temperature of 5.7°C at 6h:00 of 13th of May, the difference between modules is $\approx 1.5^\circ\text{C}$. The mean temperature difference between modules is 2.1°C . Module 01 is always warmer than module 02 (indoor, façades, roof and floor), however, it is found a faster decrease of indoor temperature at night. It was found that the WTW system can reduce the mean relative humidity (RH) by 7%.

It was observed an average air velocity of 0.3 m/s during day-time due to stack effect. However, between 21h00 and 9h00 the air velocity it is near to zero mainly. In the second period of experiments the air velocity was slightly increase to 0.8 m/s (constant value). Figure VIII.38 plots the measured values. In this second period the outdoor temperature is high and overheating is observed (module 01). According with previous results, inner vents should be closed at 15h00 (maximum solar radiation) for these conditions. At this period cooling operation mode illustrated in Figure VII.1c should be activated. However, in this preliminary study only heating mode was considered. The mean RH is similar to previous results. With the forced convection (0.8 m/s), it was observed a faster decrease of indoor temperature at night. According with measured values, it is recommended to turn off the fan at 21h00

when overheating is not observed. It is also found a delay of one hour between heat losses between modules. This effect was not observed with the system operating under natural convection. However, both modules have similar inertia. The mass of the WTW prototype has no significantly effect on module thermal inertia. Would be recommended the assemble of more prototypes. To avoid overheating effect due to the increase of prototypes number, air vents must be controlled based (e.g. KNX protocol) on indoor temperature.

The third period of experimental tests was performed between 22th of May to 11 of June 2018. Figure VIII.39 presents measured values of indoor air temperature and relatively humidity. The outdoor conditions are also present in Figure VIII.39. Outdoor temperature is typically lower than 20 °C. The minimum outdoor air temperature is 10.3 °C. The sky conditions exchange from sunny to cloudy/rainy between 28th and 31th of May. The maximum global solar radiation (1352 W/m²) is verified at 15h:00 of third day of June. From the results it can be concluded that under outdoor temperatures below 25 °C the inner vents should be closed at 21h00 for cloudy days and between 22h00 and 00h00 in sunny days. Heat losses were observed after these set-points. These set-points are important and may prevent some of the heat losses mainly by conduction through the glass. Later the heat gains and losses are analysed. It is also observed that the temperature inside the module only starts increasing after 10h:00, when direct solar radiation on south façade starts increasing. The maximum temperature difference between modules was 2.41 °C (3rd of June at 19h:00). The minimum temperature difference (0.72 °C) is observed after in first day of June (at 10h00) after three consecutive cloudy days. However, module 01 is always warmer even under cloudy/rainy conditions.

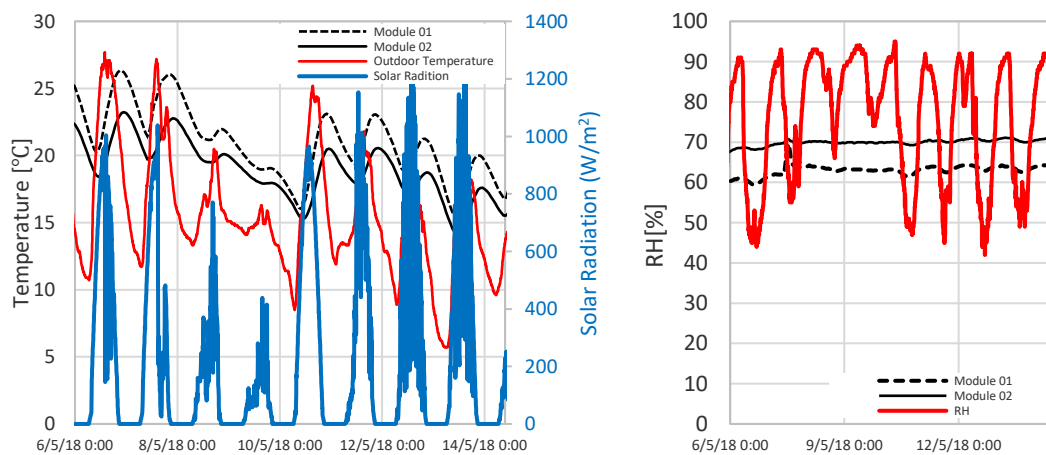


Figure VIII.37 – Indoor and outdoor conditions from 6th of May to 14th of May of 2018 (first period).

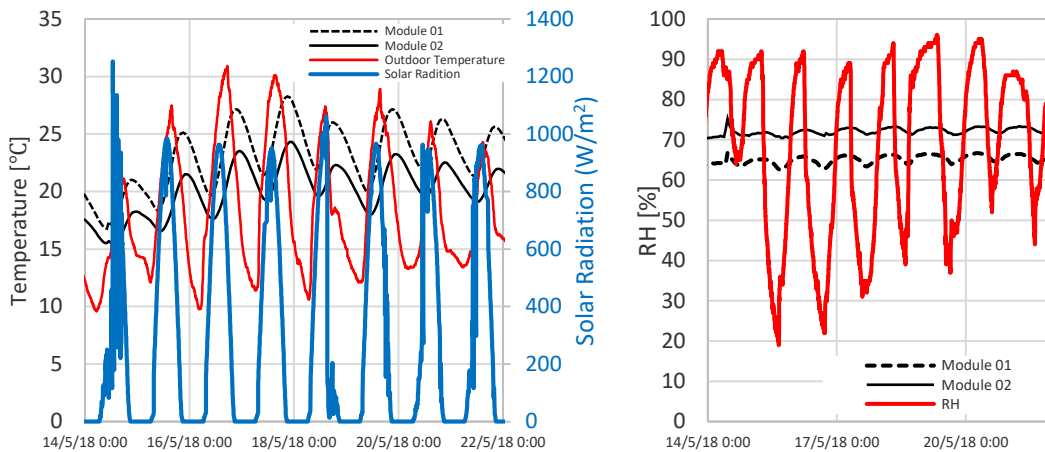


Figure VIII.38 – Indoor and outdoor conditions from 14th of May to 22th of May of 2018 (second period).

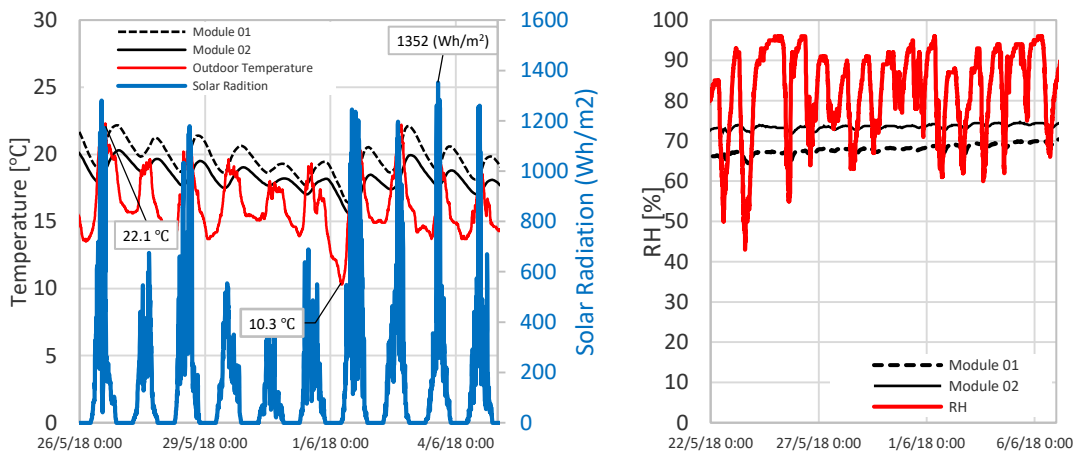


Figure VIII.39 – Indoor and outdoor conditions from 26th of May to 05th of June (third period).

To have a better understanding of the WTW thermal behaviour Figure VIII.40 presents values for the main parameters. The parameters under study are: (1) water temperature measured at different heights; (2) inlet and outlet air temperature; (3) indoor and outdoor temperature over four days of sunny and cloudy/rainy conditions. In heating period, the outlet air temperature shows a similar behaviour to water temperature. However, the maximum outlet air temperature is observed for the maximum peak of solar radiation. After the maximum solar radiation values, outlet air temperature drops above water temperature. Water temperature remains higher for longer periods of time. The WTW prototype is losing some heat through the glass and even through the lateral frame. A window shutter may prevent some of the heat losses. After 21h00 the outlet air temperature has similar values to the inlet temperature which indicates that there is not heat gains from the prototype.

The maximum measured water temperature is 34 °C at 19h00 of 17th of May (Figure VIII.40a). At this instant the outdoor air temperature is 18.4 °C. Water heat gains could be used to pre-heat domestic hot water operating like a solar panel. Even at night water temperature is always higher than 20 °C. For an outdoor temperature of 10.6 °C (at 7h:00) module 01 is warmer by 2.4 °C than module 02 (Figure VIII.40a). Figure VIII.40b present results for cloudy and rainy conditions. In the third day the minimum difference between modules is 0.7 °C at 6h:00. At this instant water temperature is 1.8°C higher than module 01 indoor temperature. Figure VIII.40c and d presents the heat gains of the WTW system during the same period.

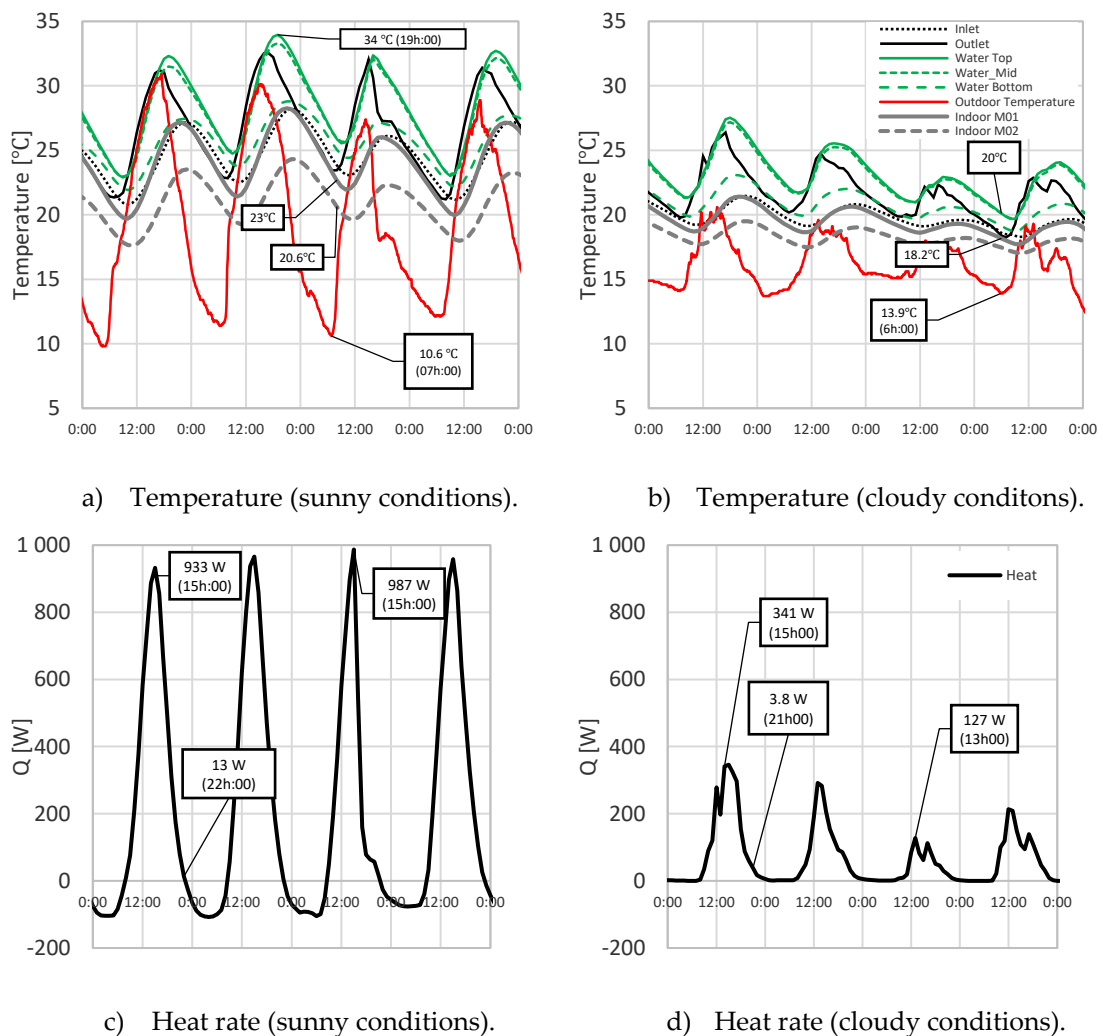


Figure VIII.40 – WTW and experimental modules temperatures and heat rate.

When the system is operating under natural convection there are only significant heat gains between 10h00 until 15h00 when the maximum solar radiation is achieved. After 15h00 the heat delivered by the wall starts decreasing. The system injects lower values of heat until 22h00. After 21h00 the heat injected inside the module is not enough to maintain indoor temperature more “stable”. With forced

convection (Figure VIII.40c) the heat gains are near 1000 W due to the increase of airflow rate. At night the heat losses increase. It is recommended to turn off the fan after 21h:00. The traditional inverse thermosyphon of Trombe Walls is analysed. Under natural convection (Figure VIII.40d) it was found a slight reverse of the flow, however, the heat losses are lower than 1W. This may happen due to the panel temperature which is always higher than air temperatures (indoor and outdoor) preventing the reverse stack effect on the Trombe wall air cavity.

VIII.5. Conclusions and future developments

One of the drawbacks of LSF construction is the presence of thermal bridges and low thermal inertia. Considering that the façades are the most exposed area of the buildings to outdoor conditions, a Water Trombe Wall (WTW) prototype is suggested and studied. This WTW system is an evolution from *EcoSteelPanel* project that aimed to develop an opaque water wall for LSF construction. In this chapter, a study of this Thermal Energy Storage system (TES) was conducted with experimental, analytical and numerical methods. It was concluded that this TES system could storage between 69.43 up to 145.75 liters of water which represents a total of 8009 to 14415 Joules of thermal energy capacity (for panel). It was also presented the thermal behaviour of TES wall assembled in a building façade. For this study an analytical model was developed and validated against experimental data acquired from a small-scale prototype. It was concluded that this TES is only able to storage thermal energy when exposed to south, where the maximum water temperature achieved was 50 °C, during a sunny summer day. The water volume shows to have a positive influence on the water and energy storage capacity and increasing thermal inertia. However, it is found that the operation temperatures are lower. The application of a black colour on the exterior surface allowed an increase of the maximum temperatures by 6 °C to 9 °C, however, at night the TES panel loses heat by radiation.

To verify the influence of using all building façades to promote water heat exchanges between them, CFD models were developed. It was concluded that moving the water between façades was not the best overall solution to promote heat exchanges between the water wall and indoor spaces. Thus, a Water Trombe Wall system may be the best solution, promoting the exchanges by convection, conduction and by radiation. The developed TES panel is used as the “massive wall” of this system, where the water can store thermal energy during the day and release it during night periods, preventing the inverse-thermosiphon effect in Trombe walls.

To study the thermal performance of the Water Trombe Wall, two identical experimental modules with the same inner dimensions were designed, constructed and monitored. The experimental modules were constructed with LSF technology and are located Coimbra (Portugal). Results presented in this chapter are only preliminary but important has first “impression” of the WTW thermal behaviour. From the preliminary results it can be concluded:

- Module 01 with the WTW system remains always warmer than module 02. It is found a maximum difference of 4.59 °C at 18h:00 of 19th of May. The minimum difference of 0.58 °C was observed at 08h:00 of 10th of May;
- For higher outdoor air temperatures (>25°C) overheating was observed. There are four solutions that may avoid this effect: (1) close inner vents after the maximum solar radiation peak (at 15h:00); (2) exchange the operation mode to cooling by closing the bottom inner vent and open the top outer vent; (3) close inner vents after the maximum solar radiation and open the outer vents to cooldown the TES panel; (4) close inner vents only in periods where the solar radiation is higher (12h00 until 15h00);
- For outdoor temperatures below 25 °C the inner vents should be closed at 21h:00 in cloudy days and between 22h00 and 00h00 during sunny days. It is observed that for these periods the outlet air temperature has similar values to inlet air temperature. A window shutter is recommended after this period to avoid heat losses mainly by conduction during the night. It is also recommended to insulate the lateral frame of the WTW;
- When the WTW is operating under forced convection with low air velocity, the fan must be turned off after 21h:00. This is because after this time the heat losses will increase during the night and the temperature inside the module drops quickly. During the day is observed an increase of heat gains when the WTW is operating under forced convection;
- WTW prototype do not show significantly effect on module thermal inertia. It would be recommended the assembly of more panels and increase the mass of the south façade;
- The reverse air flow (or reverse of the stack effect) is not well noticed with this WTW.

It was already mentioned a few suggestions to improve the WTW behaviour such as: (1) to insulate the lateral frame of the WTW; (2) to implement a window shutter for night periods; (3) to assemble more prototypes on south façade to analyse the real effect of the WTW thermal inertia. However, for future work it is also recommend

the following: (1) a control system for air vents based on these results and future results during winter season; (2) assembly a fix fan with air velocity control unit and a thermostat; (3) to analyse the thermal and energy performance of the WTW, air conditioners units should be installed to analyse the amount of energy delivered by the WTW system and energy savings.

CHAPTER IX

Conclusions and future developments

IX.1. Overview

This thesis was carried out in the framework of Steel and Composite Construction doctoral program. In this work, the structural and thermal performance of different technologies for LSF modular construction were analysed. In a global way, the main objectives of this thesis were: (1) to give better understanding of the behaviour of LSF wall panels subjected to a lateral loading using screw connection; and (2) to analyse the thermal performance of two different technologies that can improve buildings energy performance using renewable energy sources such as geothermal energy and solar energy. This work was done by carrying out experimental campaigns and by developing numerical and analytical models.

The research was divided into four parts: Part A presents a brief overview of LSF modular construction and an experimental campaign which allowed the characterization (mechanical/thermal) of the main materials. In Part B, the structural performance of LSF panels subject to a lateral loading using screw connections was investigated. Part C and D present the thermal performance of an EAHE and a WTW system in a Csb climate region.

The main objectives were achieved by means of: (i) experimental and numerical evaluation of steel-steel connections, (ii) experimental and analytical evaluation of steel-OSB connections; (iii) experimental, numerical and analytical evaluation of LSF wall panels when subject to a lateral load; (iv) development of a methodology for design and prediction of the thermal performance of an EAHE systems; (v) experimental campaign over one year with an EAHE pilot installation and optimization of KNX control; (vi) analytical and numerical study to predict the effect of geometrical, physical and dynamic parameters of an EAHE; (vii) development and construction of a WTW prototype design specifically for a LSF construction; (viii) evaluation of preliminary results of the WTW prototype in a Csb climate.

IX.2. Conclusions and contributes of this thesis

The panelised modular construction is increasingly being used as a modular construction method. These method is based on the assemblage and production of LSF panels that are transported to the construction site. Usually, the most common way to connect the structural and non-structural elements is by using screw connections. These screw connections were detailed studied. One drawback of LSF buildings is the usual low thermal inertia due to the lightness of the elements. Buildings thermal inertia can be improved by using passive/active technologies such as PCMs, Trombe Walls and EAHEs. Two systems. systems were investigated: the Trombe Wall and an EAHE.

In the context of LSF modular construction, two conference papers “*Edifícios com estrutura leve em aço enformado a frio (LSF): vantagens e desvantagens*” and “*Desempenho térmico de paredes com estrutura leve em aço enformado a frio*” were presented at Congresso de Construção Metálica e Mista XI and X, respectively.

The mechanical and thermal properties of the main materials used in LSF building were investigated. The main objective was the characterization of the mechanical properties of OSB according with the test methods of EN 789 (1996). The values were compared with reference values given by EN 12369-1 (2001) and EN 300 (2006). It was verified a non-uniform behaviour of OSB under tensile and compression forces due to the non-uniform microstructure of the OSB panels.

The behaviour of steel-to-steel, steel-to-OSB screw connections and the global behaviour of LSF panels subject to a lateral load using screw connections was presented. Experimental campaigns, numerical and analytical investigations were carried out. This study was already published “*Structural performance of light steel framing panels using screw connections subjected to lateral loading*” in Thin-Walled Structures journal (Henriques, J. and Rosa, N., 2017) and a paper “*Resistência mecânica de painéis com estrutura em aço leve sujeitos a cargas laterais*” was presented at XI Congresso de Construção Metálica e Mista (Rosa, N. *et al.* 2017).

The main conclusions of Part B of the thesis are:

- In steel-to-steel screw connections results, it was found that the analytical approach given by AISI offers more accurate results than the EN 1993-1-3 (2006) comparing against experimental results;
 - Numerical results of steel-to-steel connection showed that the deformation only due to the connection is negligible in comparison to the deformation that may
-

arise in other parts or due to eccentricities. It is found that these connections can be consider rigid for reasonable results;

- From OSB-steel screwed connections results, it was observed some variability on the post-elastic resistance since the failure is governed by the OSB part of the connection due to the highly non-uniform microstructure of the OSB;
- The EN 1995-1-1 (2004) approach shows to be more conservative when compared with experimental results. This can be justified by the high variability on the material properties of the OSB boards;
- Experimental results show that the contribution of OSB board is significant and should be considered as a solution for the lateral loading stability of LSF structures. This was also observed when the results when the experimental results were compared with the numerical results using a flat steel strips bracing system;
- The EN 1993-1-3 (2006) neglects the contribution of OSB boards in LSF structure stability, however, is not the case of the AISI that addresses the use of these elements;
- Experimental results show that the screw connections have significate effect on the lateral capacity and lateral stiffness of the panels.
- From results present in Part B of this thesis, a revision of the EN 1993-1-3 (2006) to address the contribution of timber derived boards on lateral stiffness of LSF is therefore recommended.

An overview of EAHEs, scientific achievements and heat transfer fundamentals was presented. The heating and cooling energy performance of an EAHE located in Coimbra (Portugal) was evaluated using experimental data, analytical and numerical (CFD) models. A simplified steady-state one dimensional analytical model based on ϵ -NTU method was proposed and validated against measured data. Both analytical (steady-state) and CFD models (transient) were used for a parametric investigation. This study was already published “Modelling and performance of an earth-to-air heat exchanger in a pilot installation” in Journal of Building and Physics by Rosa, N. *et al.* 2018 and a paper was presented at XI Congresso de Construção Metálica e Mista (Rosa, N. *et al.* (2018). The CFD results “*Computational fluid dynamic modelling of an earth-to-air heat exchanger*” will be also submitted for publication.

The main conclusions were:

- From experimental results it was concluded that the EAHE controlling system (KNX) must be optimized for heating season to avoid unnecessary energy consumptions;
-

- The EAHE show better thermal performance when the system is operating in cooling mode;
 - The difference between inlet and outlet air temperatures grows with the pipe length. In cooling, this difference increases when the inlet air temperature increases, heating when air temperature falls down. In the studied case, the maximum efficiency is achieved with the pipe length of 100 m. However, from a specific optimal length of 24 meters the COP decreases due to the increase of pressure drop in the system;
 - For a suitable thermal performance of the EAHE, pipe diameters should be lower or equal to DN200. For higher pipe diameters the efficiency of the EAHE and the COP drops;
 - Increasing the air velocity leads to a decrease of heat gains from soil to fluid due to the short time in thermal energy exchanges. On the DN110 pipes, the daily mean efficiency and COP decreases mainly due to the increase of pressure losses;
 - For a suitable thermal performance, the soil thermal conductivity should be greater or equal than $1.5 \sim 2 \text{ W/(m} \cdot ^\circ\text{C)}$. The COP and the daily mean efficiency rises with the increase of soil thermal conductivity;
 - PVC is a good option in terms of costs, mechanical resistance and thermal performance. The effect of pipe thermal conductivity has low influence on the EAHE thermal performance due to the low thermal resistance for the thickness direction;
 - DN200 with air velocity of 3 m/s will not fit the indoor temperature requirements. An increase of the pipe length or decrease of air velocity is recommended;
 - Heating simulations show that the EAHE cannot itself warm the indoor. An additional HVAC system is recommended;
 - Considering the pilot installation conditions (*i.e.* air velocity), the number of parallel pipes can be reduced near to half or one third using pipe diameters of DN160 and DN200, respectively;
 - DN160 is a good option in terms of thermal performance, number of pipes and terrain area;
 - The space between pipes the higher the loss of heat transfer rate. This is more pronounced for larger pipe diameters and with the increase of air velocity;
 - The spacing between pipes can be reduced to 0.5 m. A spacing of 0.25 m is only recommended for the DN110 pipes and air velocities lower than 3 m/s;
 - The loss of heat transfer rate when the spacing between pipes decreases may be more pronounced for longer periods of continuous operation and for higher soil thermal conductivities. However, usually this type of systems only operates during
-

short periods of time and the soil thermal properties (sandy and clayey) are suitable for a good thermal performance.

In the final part of this thesis an overview of Trombe wall technologies and previous scientific achievements was presented. The heat transfer fundamentals and energy performance evaluation were also presented for later and future works. In this part the thermal performance of a Water Trombe Wall prototype was investigated using experimental, analytical and numerical results. This work was divided into two sections: (i) to investigate the thermal performance of the Thermal Energy Storage system using experimental, analytical and numerical methods; and (ii) to give preliminary results of the thermal performance of a WTW prototype.

A paper “*Desenvolvimento de uma parede em aço enformado a frio para armazenamento de energia térmica*” was presented at Congresso de Construção Metálica e Mista X (Rosa, N. *et al.* 2015).

The main conclusions are:

- The TES system can storage between 69.43 up to 145.75 liters of water, which represents a total of 8009 to 14415 Joules of thermal energy capacity;
- The TES is only able to storage thermal energy when exposed to south (Csb climate), achieving operation temperature of 50 °C during a sunny summer day;
- Water volume shows to have a positive influence on the water and energy capacity and increases thermal inertia, however, for bigger water volumes it was found a decrease of operation temperatures;
- After applying a black colour on the exterior surface it was found an increase of maximum operation temperature of 6 °C to 9 °C. However, due to the high emissivity of black colour the TES panels more losses heat during night-periods;

CFD simulations show that the influence of using all building façades to performed water heat exchanges between them by means of pipes (30 mm of internal diameter). For a water flow of 5 m³/h, it was observed a reduction of the heat flux of 2.06% when the water moves in a closed circuit between the four façades. A reduction of the heat flux by 25% (south surface) and 42% (north surface) was found when water flows from the north façade to the south façade. However, this solution has too many drawbacks and a Trombe Wall combined with the TES (Water Trombe Wall) may be the best solution to promote heat exchanges between the prototype and building interior;

To understand the thermal behaviour/performance of the WTW, two identical experimental modules constructed in LSF and with the same inner dimensions were designed, constructed and monitored. One module was used as “reference” and the other one with the WTW prototype assemble on the south façade. It was concluded that:

- The module with the WTW prototype is warmer every time-step. It was found a maximum and minimum difference between modules of 4.59 °C and 0.58 °C, respectively;
- During higher outdoor temperatures, overheating was observed (indoor temperature > 25 °C). However, this can be prevented by: (i) closing inner vents after 15h00 (maximum solar load); (ii) set the cooling operation mode; (iii) closing the inner vents and open the outer vents to cool down the TES panel; (iv) closing the inner vents between 12h00 until 15h00;
- With this prototype, the inner vents must be closed at 21h00 in cloudy days and between 22h00 and 00h00 during sunny days. A window shutter is recommended to mitigate the heat losses by conduction during night periods;
- There was an increase of heat gains when the system was operating under forced convection. However, at night the heat losses also increase. Forced ventilation should be turned off after 21h00;
- It was not found an increase of the experimental module thermal inertia. However, this may happen due to the reduced mass of the WTW when compared to the module. South surface should be filled with WTW prototypes to improve inertia;
- The typical inverse thermosyphon of Trombe walls was not observed using this prototype.

The last part of this thesis is still very preliminary; however, these were the first steps of this project. Next section presents some forthcoming work and future researches.

IX.3. Forthcoming work and future research

During the first part of this thesis, OSB specimens were tested in tensile and compression. Due to the non-uniform microstructure of OSB, these experiments should be performed in a larger sample. This will allow a higher convergence of the results which can be used for future numerical models. In the second part of this thesis, LSF wall panels subjected to a lateral loading using screw connections were tested. For future research, a revision of the EN 1993-1-3 (2006) should be performed to consider the contribution of timber derived boards on lateral stiffness of LSF constructions. Numerical models of LSF walls using a flat steel strips bracing system

were developed. It is recommended in future researches an experimental campaign with a larger sample of LSF wall specimens including the LSF wall using a flat steel strip bracing system. In Part C an EAHE system was studied using experimental, analytical and numerical methods. For future research dynamic building simulations (*e.g.* with TRNSYS) are very important to predict the energy performance of the building with the EAHE in different climatic zones and considering the different geometric, physic and dynamic parameters.

The development of a Water Trombe Wall was presented in Part D. Based on preliminary results some recommendations which may allow the improvement of the WTW thermal performance were presented in Chapter VIII. The WTW system will be tested over one year in heating and cooling operation modes. A 3D CFD model (ANSYS CFX/FLUENT) must be developed to analyse the transient thermal efficiency of this system. This stage alongside with the analytical methods presented in Chapter VII allows the optimization of WTW parameters such as air cavity thickness, air velocity, vents control to avoid thermal losses. Based on recorded data and CFD/analytical results, algorithms will be created and implemented in a dynamic building simulation tool. The dynamic building software (TRNSYS) is used to predict the thermal performance of the system installed into a typical residential building in different climate zones.

Finally, this WTW prototype can be also used as a hybrid system by combining the TES panels with a reversible heat pump system. Since water has a high specific heat coefficient the TES panel can accumulate thermal energy from solar radiation or can be used to dissipate heat from the building. Inside of TES panels a closed loop heat exchanger (copper or aluminium pipes) with a working fluid (glycol) will perform heat exchanges with a reversible heat pump. Previous results showed that the water temperature inside the panels could reach temperatures higher than 40 °C losing gradually the temperature during night-periods. However, by combining the panels with a heat pump the panels could be used for pre-heat domestic hot water. During winter water has always a higher temperature and thermal inertia when compared to outdoor temperature. The development of this final stage of the prototype requires studies of new materials that could be used on the TES panels to avoid heat losses during night-periods, increasing the heat pump efficiency. The use of new insulation materials (*e.g.* Aerogel or vacuum panels), the use of tubular PCMs to cover the heat exchanger surface of the pipes would and the development of a more efficient energy collector surfaces may increase the WTW efficiency.

REFERENCES

- Abbassi, F., Dimassi, N. and Dehmani, L. (2014) 'Energetic study of a Trombe wall system under different Tunisian building configurations', *Energy and Buildings*. Elsevier B.V., 80, pp. 302–308. doi: 10.1016/j.enbuild.2014.05.036.
- Abbaspour-fard, M. H., Gholami, A. and Khojastehpour, M. (2011.) 'Evaluation of an Earth-to-Air Heat Exchanger for the North-East of Iran with Semi-Arid Climate', *International Journal of Green energy* (May 2011), pp. 37–41. doi: 10.1080/15435075.2011.576289.
- Adams, S., Becker, M., Krauss, D. and Gilman, C. (2010) 'Not a dry subject: optimizing water Trombe wall', *SOLAR 2010 conference*.
- AISI (1999). AISI Statistical Highlights of the North American Steel Industry, American Iron and Steel Institute.
- AISI S100 (2007). North American specification for the design of cold-formed steel structural members. AISI-S100, Washington, DC.
- AISI S213-07 w/ S1-09 (2012). North American Standard for Cold-Formed Steel Framing – Lateral Design, 2007 Edition with Supplement 1 (Reaffirmed 2012), American Iron and Steel Institute, Washington, D.C.
- AISI, AISI S400-15 (2015) North American Standard for Seismic Design of Cold-Formed Steel Structural Systems, American Iron and Steel Institute, Washington, D.C.
- ASHRAE (2003), Geothermal energy, in: *ASHRAE Handbook HVAC Applications*, American Society of Heating, Refrigerating and Air-Conditioning Engineers, Inc., Atlanta, 2003, pp. 11e28.
- ASHRAE (2005), *Handbook of fundamentals*. American Society of Heating, Refrigerating and Air-Conditioning Engineers, Inc., Atlanta, 2005, chapter 31.
- Akbarzadeh, A., Charters, W. W. S. and Lesslie, D. A. (1982) 'Thermocirculation characteristics of a Trombe wall passive test cell', *Solar Energy*, 28(6), pp. 461–468. doi: 10.1016/0038-092X(82)90317-6.
- Al-Ajmi, F., Loveday, D. L. and Hanby, V. I. (2006) 'The cooling potential of earth-air heat exchangers for domestic buildings in a desert climate', *Building and Environment*, 41(3), pp. 235–244. doi: 10.1016/j.buildenv.2005.01.027.
- Al-Karaghoul, A. and Kazmerski, L. L. (2010) 'Optimization and life-cycle cost of health clinic PV system for a rural area in southern Iraq using HOMER software', *Solar Energy*. Elsevier Ltd, 84(4), pp. 710–714. doi: 10.1016/j.solener.2010.01.024.
- Ascione, F., Bellia, L. and Minichiello, F. (2011) 'Earth-to-air heat exchangers for
-

-
- Italian climates', *Renewable Energy*, 36(8), pp. 2177–2188. doi: 10.1016/j.renene.2011.01.013.
- ASTM E564 – 06 (2012). Standard Practice for Static Load Test for Shear Resistance of Framed Walls for Buildings, ASTM International, West Conshohocken, PA.
- ASTM E72-15, (2015). Standard Test Methods of Conducting Strength Tests of Panels for Building Construction, ASTM International, West Conshohocken, PA.
- Badescu, V. (2007) 'Simple and accurate model for the ground heat exchanger of a passive house', *Renewable Energy*, 32(5), pp. 845–855. doi: 10.1016/j.renene.2006.03.004.
- Bainbridge, D. A. (2005) 'A Water Wall Solar Design Manual: For environmentally responsive buildings that increase comfort, save money, and protect the environment', pp. 1–29.
- Bajc, T., Todorović, M. N. and Svorcan, J. (2015) 'CFD analyses for passive house with Trombe wall and impact to energy demand', *Energy and Buildings*, 98, pp. 39–44. doi: 10.1016/j.enbuild.2014.11.018.
- Balcomb, J. D. and Mcfarland, R. D. (1978) 'A simple empirical method for estimating the performance of a passive solar heated building of the thermal storage wall type', *2nd National Passive Solar*.
- Bansal, V., Misra, R., Agrawal, G. Das and Mathur, J. (2009) 'Performance analysis of earth-pipe-air heat exchanger for winter heating', *Energy and Buildings*, 41(11), pp. 1151–1154. doi: 10.1016/j.enbuild.2009.05.010.
- Bansal, V., Misra, R., Agrawal, G. Das and Mathur, J. (2010) 'Performance analysis of earth-pipe-air heat exchanger for summer cooling', *Energy and Buildings*, 42(5), pp. 645–648. doi: 10.1016/j.enbuild.2009.11.001.
- Bansal, V., Misra, R., Agrawal, G. Das and Mathur, J. (2012) 'Performance analysis of integrated earth-air-tunnel-evaporative cooling system in hot and dry climate', *Energy and Buildings*. Elsevier B.V., 47, pp. 525–532. doi: 10.1016/j.enbuild.2011.12.024.
- Bansal, V., Misra, R., Agrawal, G. Das and Mathur, J. (2012) 'Performance evaluation and economic analysis of integrated earth-air-tunnel heat exchanger-evaporative cooling system', *Energy and Buildings*. Elsevier B.V., 55, pp. 102–108. doi: 10.1016/j.enbuild.2012.08.047.
- Baxter, D. (1994). "Energy Exchange and Related Temperature of an Earth-tube Heat Exchanger in Heating Mode". Trans ASAE, Vol.35, Issue 1, pp. 275-85.
- Baran, E. and Alica, C. (2012) 'Behavior of cold-formed steel wall panels under monotonic horizontal loading', *Journal of Constructional Steel Research*. Elsevier Ltd, 79, pp. 1–8. doi: 10.1016/j.jcsr.2012.07.020.
- Belatrache, D., Bentouba, S. and Bourouis, M. (2016) 'Numerical analysis of earth air
-

REFERENCES

- heat exchangers at operating conditions in arid climates', *International Journal of Hydrogen Energy*, pp. 1–7. doi: 10.1016/j.ijhydene.2016.08.221.
- Bellos, E., Tzivanidis, C., Zisopoulou, E., Mitsopoulos, G. and Antonopoulos, K. A. (2016) 'An innovative Trombe wall as a passive heating system for a building in Athens???A comparison with the conventional Trombe wall and the insulated wall', *Energy and Buildings*. Elsevier B.V., 133, pp. 754–769. doi: 10.1016/j.enbuild.2016.10.035.
- Benhammou, M. and Draoui, B. (2015) 'Parametric study on thermal performance of earth-to-air heat exchanger used for cooling of buildings', *Renewable and Sustainable Energy Reviews*. Elsevier, 44, pp. 348–355. doi: 10.1016/j.rser.2014.12.030.
- Bharadwaj, S. S. and Bansal, N. K. (1981) 'Temperature distribution inside ground for various surface conditions', *Building and Environment*, 16(3), pp. 183–192. doi: 10.1016/0360-1323(81)90012-3.
- Bilgen, Z. (1987) 'Theoretical Study of a Composite Trombe Michel Wall Solar Collector System', *Solar Energy*, 39(5), pp. 409–419.
- Bisoniya, T. S., Kumar, A. and Baredar, P. (2015) 'Heating potential evaluation of earth-air heat exchanger system for winter season', *Journal of Building Physics*, 39(3), pp. 242–260. doi: 10.1177/1744259114542403.
- Bojic, M., Trifunovic, N., Papadakis, G. and Kyritsis, S. (1997) 'Numerical simulation, technical and economic evaluation of air-to-earth heat exchanger coupled to a building', *Energy*, 22(12), pp. 1151–1158. doi: 10.1016/S0360-5442(97)00055-8.
- Bojić, M., Papadakis, G. and Kyritsis, S. (1999) 'Energy from a two-pipe, earth-to-air heat exchanger', *Energy*, 24(6), pp. 519–523. doi: 10.1016/S0360-5442(99)00012-2.
- Boukhris, Y., Gharbi, L. and Ghrab-Morcos, N. (2009) 'Modeling coupled heat transfer and air flow in a partitioned building with a zonal model: Application to the winter thermal comfort', *Building Simulation*, 2(1), pp. 67–74. doi: 10.1007/S12273-009-9405-8.
- Branston, A. E., Boudreault, F. A., Chen, C. Y. and Rogers, C. A. (2006) 'Testing of light-gauge steel-frame - wood structural panel shear walls', *Canadian Journal of Civil Engineering*, 33(5), pp. 573–587. doi: Doi 10.1139/L06-015.
- Briga-Sá, A., Martins, A., Boaventura-Cunha, J., Lanzinha, J. C. and Paiva, A. (2014) 'Energy performance of Trombe walls: Adaptation of ISO 13790:2008(E) to the Portuguese reality', *Energy and Buildings*. Elsevier B.V., 74, pp. 111–119. doi: 10.1016/j.enbuild.2014.01.040.
- BS EN 789, 1996. Test methods. Determination of mechanical properties of wood-based panels.
- EN12369-1, 2001. Wood based panels – Characteristic values for structural design –

-
- Part 1: OSB, particleboards and fibreboards. Brussels: European Committee for Standardization: CEN.
- Buonopane, S. G. *et al.* (2015) 'Computationally efficient fastener-based models of cold-formed steel shear walls with wood sheathing', *Journal of Constructional Steel Research*. Elsevier Ltd, 110, pp. 137–148. doi: 10.1016/j.jcsr.2015.03.008.
- Burek, S. A. M. and Habeb, A. (2007) 'Air flow and thermal efficiency characteristics in solar chimneys and Trombe Walls', *Energy and Buildings*, 39(2), pp. 128–135. doi: 10.1016/j.enbuild.2006.04.015.
- Buzzoni, L., Olio, D. and Spigab, M. (1998) 'Energy analysis of a passive solar system', pp. 411–416.
- Casafont, M., Arnedo, A., Roure, F. and Rodríguez-Ferran, A. (2007) 'Experimental testing of joints for seismic design of lightweight structures. Part 3: Gussets, corner joints, x-braced frames', *Thin-Walled Structures*, 45(7–8), pp. 637–659. doi: 10.1016/j.tws.2007.05.008.
- Çengel, Y.A., 2009a. Heat Exchangers. In Çengel. pp. 609–662.
- Çengel, Y.A., 2009b. Transferência de Calor e Massa. In Transferência de Calor e Massa. pp. 451–502.
- Chel, A. and Tiwari, G. N. (2010) 'Stand-alone photovoltaic (PV) integrated with earth to air heat exchanger (EAHE) for space heating/cooling of adobe house in New Delhi (India)', *Energy Conversion and Management*. Elsevier Ltd, 51(3), pp. 393–409. doi: 10.1016/j.enconman.2009.10.001.
- Chen, B., Chen, X., Ding, Y. H. and Jia, X. (2006) 'Shading effects on the winter thermal performance of the Trombe wall air gap: An experimental study in Dalian', *Renewable Energy*, 31(12), pp. 1961–1971. doi: 10.1016/j.renene.2005.07.014.
- Corner, S. M. W. (2014) 'Screw-Fastened Cold-Formed Steel-to-Steel Shear Connection Behavior and Models'.
- Costa, J. J., Oliveira, L. A. and Blay, D. (1999) 'Test of several versions for the k-epsilon type turbulence modelling of internal mixed convection flows', *International Journal of Heat and Mass Transfer*, 42(23), pp. 4391–4409.
- Cuce, E. (2016) 'Thermal regulation impact of green walls: An experimental and numerical investigation', *Applied Energy*. Elsevier Ltd. doi: 10.1016/j.apenergy.2016.09.079.
- Cucumo, M., Cucumo, S., Montoro, L. and Vulcano, A. (2008) 'A one-dimensional transient analytical model for earth-to-air heat exchangers, taking into account condensation phenomena and thermal perturbation from the upper free surface as well as around the buried pipes', *International Journal of Heat and Mass Transfer*, 51(3–4), pp. 506–516. doi: 10.1016/j.ijheatmasstransfer.2007.05.006.
-

REFERENCES

-
- Davies, J.M. (1991). Connections for cold-formed steelwork, in: J. Rhodes (Ed.), *Design of Cold-Formed Steel Members*, Elsevier Applied Science, London and New York.
- Davies, J. M. (2006) 'Light gauge steel cassette wall construction - theory and practice', *Journal of Constructional Steel Research*, 62(11), pp. 1077–1086. doi: 10.1016/j.jcsr.2006.06.028.
- Dehra, H. (2009) 'A two dimensional thermal network model for a photovoltaic solar wall', *Solar Energy*, 83(11), pp. 1933–1942. doi: 10.1016/j.solener.2008.07.014.
- DL No 118/2013 (2013) 'Decreto-Lei n.º 118/2013, de 20 de Agosto', *Diário da República N.º 159, 1.ª série*, p. 4988–5005, Lisboa, Portugal (in Portuguese).
- Diarce, G., Urresti, A., García-Romero, A., Delgado, A., Erkoreka, A., Escudero, C. and Campos-Celador, álvaro (2013) 'Ventilated active fa??ades with PCM', *Applied Energy*. Elsevier Ltd, 109, pp. 530–537. doi: 10.1016/j.apenergy.2013.01.032.
- Dincer, I. (2002) 'On thermal energy storage systems and applications in buildings', *Energy and Buildings*, 34(4), pp. 377–388. doi: 10.1016/S0378-7788(01)00126-8.
- Dragicevic, S. and Lambic, M. (2011) 'Influence of constructive and operating parameters on a modified Trombe wall efficiency', *Archives of Civil and Mechanical Engineering*, 11(4), pp. 825–838. doi: 10.1016/S1644-9665(12)60080-6.
- Duan, S., Jing, C. and Zhao, Z. (2016) 'Energy and exergy analysis of different Trombe walls', *Energy and Buildings*. Elsevier B.V., 126, pp. 517–523. doi: 10.1016/j.enbuild.2016.04.052.
- EN 1990 (2002). Eurocode - Basis of structural design', CEN, Brussels, Belgium.
- EN 1993-1-1 (2005). Design of steel structures - Part 1-1: General rules and rules for buildings, European Committee for Standardization (CEN), Brussels, Belgium.
- EN 1993-1-3 (2006). 'Design of Steel Structures – Part 1-3: General Rules Supplementary Rules for Cold-formed Members and Sheetting', European Committee for Standardization (CEN), Brussels, Belgium.
- EN 1993-4 (2017): Eurocode 2 – Design of Concrete Structures – Part 4: Design of Fastenings for Use in Concrete, European Committee for Standardization, Brussels, Belgium.
- EN 1995-1-1 (2004) 'Design of Timber Structures - Part 1 - 1: General - Common Rules and Rules for Buildings', European Committee for Standardization (CEN), Brussels, Belgium.
- EN 1998-1 (2005): Eurocode 8 – Design of Structures for Earthquake Resistance – Part1: General Rules, Seismic Actions and Rules for Buildings, European Committee for Standardization, Brussels, Belgium.
-

-
- EN 300 (2006) 'Orientated Strand Boards (OSB) – Definitions, classification and specifications'. Brussels: European Committee for Standardization: CEN.
- EN 508-1 (2008) 'Roofing products from metal sheet – Specification for self-supporting products of steel, aluminium or stainless sheet – Part 1: Steel'.
- EN 779 (2012) 'Particulate air filters for general ventilation; requirements, testing and marking.
- EN 10002-1 (2001). Metallic materials Tensile Testing Part 1: method of test at ambient temperature. European Committee for Standardization (CEN).
- EN 10326 (2004). Continuously hot-dip coated strip and sheet of structural steels – Technical delivery conditions. Brussels: European Committee for Standardization: CEN.
- EN 13162:2012+A1 (2015). Thermal insulation products for buildings - Factory made mineral wool (MW) products - Specification. Brussels: European Committee for Standardization: CEN.
- EN 13499 (2003). Thermal insulation products for buildings – External thermal insulation composite systems (ETICS) based on expanded polystyrene – Specification. Brussels: European Committee for Standardization: CEN.
- EN-ISO 12944-2 (1998) 'Paints and varishes. Corrosion protection of structures by protective paint systems. Part 2: Classification of environments'.
- EPS Packaging Group (2012). Expanded Polystyrene (EPS) and the Environment, pp.1-11. Available at: http://www.eps.co.uk/pdfs/eps_and_the_environment.pdf.
- Erhorn-Kluttig, H. and Erhorn, H. (2009). 'Impact of thermal bridges on the energy performance of buildings', ASIEPI Information Paper, P.148, pp. 1–8.
- EU (2008). The Climate Action and Renewable Energy Package, Europe's Climate Change Opportunity Available at: http://ec.europa.eu/environment/climat/climate_action.htm.
- EU (2010). 'Directive 2010/31/EU of the European Parliament and of the Council of 19 May 2010 on the energy performance of buildings (recast)', Official Journal of the European Union, pp. 13–35. doi: 10.3000/17252555.L_2010.153.eng.
- EU (2016). Communication from the Commission to the European Parliament, the Council, the European Economic and Social Committee and the Committee of the Regions on an EU Strategy for Heating and Cooling, COMMISSION STAFF WORKING DOCUMENT. Brussels. doi: 10.1128/AAC.03728-14.
- EU (2018). 'Directive (EU) 2018/ of the European Parliament and of the Council of 30 May 2018 amending Directive 2010/31/EU on the energy performance of
-

REFERENCES

- buildings and Directive 2012/27/EU on energy efficiency', *Official Journal of the European Union*, 2018(May), pp. 75–91.
- European Commission (2012) Strategy for the sustainable competitiveness of the construction sector and its enterprises, Strategy for the sustainable competitiveness of the construction sector and its enterprises.
- FABORY, Self-Drilling Screw ST4.8x13 Technical Specification. <www.fabory.com>.
- Farreny, R., Morales-Pinzón, T., Guisasola, A., Tayà, C., Rieradevall, J. and Gabarrell, X. (2011) 'Roof selection for rainwater harvesting: Quantity and quality assessments in Spain', *Water Research*, 45(10), pp. 3245–3254. doi: 10.1016/j.watres.2011.03.036.
- Ferreira, J. and Pinheiro, M. (2011) 'In search of better energy performance in the Portuguese buildings-The case of the Portuguese regulation', *Energy Policy*. Elsevier, 39(12), pp. 7666–7683. doi: 10.1016/j.enpol.2011.08.062.
- Fiorino, L., Della Corte, G. and Landolfo, R. (2007) 'Experimental tests on typical screw connections for cold-formed steel housing', *Engineering Structures*, 29(8), pp. 1761–1773. doi: 10.1016/j.engstruct.2006.09.006.
- Fiorino, L., Iuorio, O. and Landolfo, R. (2009) 'Sheathed cold-formed steel housing: A seismic design procedure', *Thin-Walled Structures*, 47(8–9), pp. 919–930. doi: 10.1016/j.tws.2009.02.004.
- Fiorino, L., Terracciano, M. T. and Landolfo, R. (2016) 'Experimental investigation of seismic behaviour of low dissipative CFS strap-braced stud walls', *Journal of Constructional Steel Research*. Elsevier Ltd, 127, pp. 92–107. doi: 10.1016/j.jcsr.2016.07.027.
- Fiorito, F. (2012) 'Trombe walls for lightweight buildings in temperate and hot climates. Exploring the use of phase-change materials for performances improvement', *Energy Procedia*. The Authors, 30, pp. 1110–1119. doi: 10.1016/j.egypro.2012.11.124.
- Fisch, M. N., Guigas, M. and Dalenbäck, J.-O. (1998) 'A review of large-scale solar heating systems in Europe', *Solar Energy*, 63(6), pp. 355–366. doi: 10.1016/S0038-092X(98)00103-0.
- Fülöp, L. A. and Dubina, D. (2004). 'Performance of wall-stud cold-formed shear panels under monotonic and cyclic loading - Part I: Experimental research', *Thin-Walled Structures*, 42(2), pp. 321–338. doi: 10.1016/S0263-8231(03)00063-6.
- Gan, G. (1998) 'A parametric study of Trombe Walls for Passive Cooling of Buildings', *Energy and Buildings* 27 (1998) 37-43, 8.
- Gan, G. (2014) 'Dynamic interactions between the ground heat exchanger and environments in earth-air tunnel ventilation of buildings', *Energy and Buildings*. Elsevier B.V., 85, pp. 12–22. doi: 10.1016/j.enbuild.2014.09.030.

-
- Gauthier, C., Lacroix, M. and Bernier, H. (1997) 'Numerical simulation of soil heat exchanger-storage systems for greenhouses', *Solar Energy*, 60(6), pp. 333–346. doi: 10.1016/S0038-092X(97)00022-4.
- Ge, H. and Baba, F. (2015) 'Dynamic effect of thermal bridges on the energy performance of a low-rise residential building', *Energy and Buildings*, 105, pp. 106–118. doi: 10.1016/j.enbuild.2015.07.023.
- Ghosal, M. K., Tiwari, G. N. and Srivastava, N. S. L. (2004) 'Thermal modeling of a greenhouse with an integrated earth to air heat exchanger: An experimental validation', *Energy and Buildings*, 36(3), pp. 219–227. doi: 10.1016/j.enbuild.2003.10.006.
- Goswami, D. Y. and Ileslamlou, S. (1990) 'Performance Analysis of a Closed-Loop Climate Control System Using Underground Air Tunnel', *Journal of Solar Energy Engineering*, 112(2), p. 76. doi: 10.1115/1.2929650.
- Griffiths, N. and Nolte, I. (2011) *Principles For nearly Zero-energy Buildings, Buildings*. Available at: http://www.bpie.eu/nearly_zero.html.
- Henriques, J., Simões da Silva, L., Valente, I. (2013) Numerical modelling of composite beam to reinforced concrete wall joints: part I: Calibration of joint components, *Eng. Struct.* 52 (2013) 747–761.
- Henriques, J., Rosa, N., Gervasio, H., Santos, P., and da Silva, L. S. (2017). Structural performance of light steel framing panels using screw connections subjected to lateral loading. *Thin-Walled Structures*, 121 (January), 67–88. <https://doi.org/10.1016/j.tws.2017.09.024>.
- Hirunlabh, J., Kongduang, W., Namprakai, P. and Khedari, J. (1999) 'Study of natural ventilation of houses by a metallic solar wall under tropical climate', *Renewable Energy*, 18(1), pp. 109–119. doi: 10.1016/S0960-1481(98)00783-6.
- Hollmuller, P. and Lachal, B. (2001) 'Cooling and preheating with buried pipe systems: Monitoring, simulation and economic aspects', *Energy and Buildings*, 33(5), pp. 509–518. doi: 10.1016/S0378-7788(00)00105-5.
- Hu, Z., He, W., Ji, J. and Zhang, S. (2016) 'A review on the application of Trombe wall system in buildings', *Renewable and Sustainable Energy Reviews*. Elsevier, (February), pp. 0–1. doi: 10.1016/j.rser.2016.12.003.
- Hu, Z., Luo, B. and He, W. (2015) 'An Experimental Investigation of a Novel Trombe Wall with Venetian Blind Structure', *Energy Procedia*. Elsevier B.V., 70, pp. 691–698. doi: 10.1016/j.egypro.2015.02.177.
- ISO 10456 (2007). Building materials and products – Hydrothermal properties – Tabulated design values and procedures for determining declared and design thermal values.
- ISO 13790:2008 Energy Performance of Buildings – Calculation of Energy Use for
-

REFERENCES

- Space Heating and Cooling; ISO: Geneva, Switzerland, 2008.
- Iuorio, O., Macillo, V., Terracciano, M. T., Pali, T., Fiorino, L. and Landolfo, R. (2014) 'Seismic response of Cfs strap-braced stud walls: Experimental investigation', *Thin-Walled Structures*. Elsevier, 85, pp. 466–480. doi: 10.1016/j.tws.2014.09.008.
- Jaber, S. and Ajib, S. (2011) 'Optimum design of Trombe wall system in mediterranean region', *Solar Energy*. Elsevier Ltd, 85(9), pp. 1891–1898. doi: 10.1016/j.solener.2011.04.025.
- Jakhar, S., Misra, R., Bansal, V. and Soni, M. S. (2015) 'Thermal performance investigation of earth air tunnel heat exchanger coupled with a solar air heating duct for northwestern India', *Energy and Buildings*. Elsevier B.V., 87, pp. 360–369. doi: 10.1016/j.enbuild.2014.11.070.
- Jellen, A. C. and Memari, A. M. (2013) 'The state-of-the-art application of modular construction to multi-story', *1st Residential Building Design & Construction Conference*, pp. 284–293.
- Jos, D. *et al.* (2016) 'Elementos de apoio ao dimensionamento de secções compostas em light steel framing'.
- José Vinagre Díaz, J., Richard Wilby, M. and Belén Rodríguez González, A. (2013) 'Setting up GHG-based energy efficiency targets in buildings: The Ecolabel', *Energy Policy*, 59, pp. 633–642. doi: 10.1016/j.enpol.2013.04.021.
- Kabashnikov, V. P., Danilevskii, L. N., Nekrasov, V. P. and Vityaz, I. P. (2002) 'Analytical and numerical investigation of the characteristics of a soil heat exchanger for ventilation systems', *International Journal of Heat and Mass Transfer*, 45(11), pp. 2407–2418. doi: 10.1016/S0017-9310(01)00319-2.
- Khabbaz, M., Benhamou, B., Limam, K., Hollmuller, P., Hamdi, H. and Bennouna, A. (2016) 'Experimental and numerical study of an earth-to-air heat exchanger for air cooling in a residential building in hot semi-arid climate', *Energy and Buildings*, 125, pp. 109–121. doi: 10.1016/j.enbuild.2016.04.071.
- Khalifa, A. J. N. and Abbas, E. F. (2009) 'A comparative performance study of some thermal storage materials used for solar space heating', *Energy and Buildings*, 41(4), pp. 407–415. doi: 10.1016/j.enbuild.2008.11.005.
- Khatry, A. K., Sodha, M. S. and Malik, M. A. S. (1978) 'Periodic variation of ground temperature with depth', *Solar Energy*, 20(5), pp. 425–427. doi: 10.1016/0038-092X(78)90161-5.
- Kottek, M., Grieser, J., Beck, C., Rudolf, B. and Rubel, F. (2006) 'World map of the Köppen-Geiger climate classification updated', *Meteorologische Zeitschrift*, 15(3), pp. 259–263. doi: 10.1127/0941-2948/2006/0130.
- Krüger, E., Suzuki, E. and Matoski, A. (2013) 'Evaluation of a Trombe wall system in a subtropical location', *Energy and Buildings*. Elsevier B.V., 66, pp. 364–372. doi:

10.1016/j.enbuild.2013.07.035.

- Kumar, R., Ramesh, S. and Kaushik, S. C. (2003) 'Performance evaluation and energy conservation potential of earth – air – tunnel system coupled with non-air-conditioned building', *Building and Environment*, 38, pp. 807–813. doi: 10.1016/S0360-1323(03)00024-6.
- Kundakci Koyunbaba, B. and Yilmaz, Z. (2012) 'The comparison of Trombe wall systems with single glass, double glass and PV panels', *Renewable Energy*. Elsevier Ltd, 45, pp. 111–118. doi: 10.1016/j.renene.2012.02.026.
- Kusuda, T. and Achenbach, P. R. (1965) 'Earth Temperatures and Thermal Diffusivity at Selected Stations in the United States', pp. 1–230. Available at: <http://www.dtic.mil/dtic/tr/fulltext/u2/472916.pdf>.
- LaBoube, R. A. and Sokol, M. A. (2002) 'Behavior of Screw Connections in Residential Construction', *Journal of Structural Engineering*, 128(January), pp. 115–118. doi: 10.1061/(ASCE)0733-9445(2002)128:1(115).
- Landolfo, R., Fiorino L., Della Corte G (2007) Seismic response of light weight cold-formed steel low-rise residential buildings: modelling based on screw connection test results, in: F.M. Mazzolani (Ed.), *Innovative Steel Structures for Seismic Protection of Buildings: Design Criteria and Methodologies – PRIN 2003*, Polimetrica Publisher. Polimetrica Publisher, Italy, 2007, pp. 203–250.
- Lange, J. and Naujoks, B. (2007) 'Behaviour of cold-formed steel shear walls under horizontal and vertical loads', *Thin-Walled Structures*, 44(12), pp. 1214–1222. doi: 10.1016/j.tws.2007.01.007.
- Lee, Y. H., Tan, C. S., Mohammad, S., Md Tahir, M. and Shek, P. N. (2014) 'Review on cold-formed steel connections', *The Scientific World Journal*, 2014. doi: 10.1155/2014/951216.
- Lim, T., Cho, J. and Kim, B. S. (2011) 'Predictions and measurements of the stack effect on indoor airborne virus transmission in a high-rise hospital building', *Building and Environment*. Elsevier Ltd, 46(12), pp. 2413–2424. doi: 10.1016/j.buildenv.2011.04.015.
- Liu, Y. W. and Feng, W. (2011) 'Integrating Passive Cooling and Solar Techniques into the Existing Building in South China', *Advanced Materials Research*, 368–373, pp. 3717–3720. doi: 10.4028/www.scientific.net/AMR.368-373.3717.
- Liu, Y., Wang, D., Ma, C. and Liu, J. (2013) 'A numerical and experimental analysis of the air vent management and heat storage characteristics of a trombe wall', *Solar Energy*. Elsevier Ltd, 91, pp. 1–10. doi: 10.1016/j.solener.2013.01.016.
- Llovera, J., Potau, X., Medrano, M. and Cabeza, L. F. (2011) 'Design and performance of energy-efficient solar residential house in Andorra', *Applied Energy*. Elsevier Ltd, 88(4), pp. 1343–1353. doi: 10.1016/j.apenergy.2010.10.015.

REFERENCES

- LSK (2005). European Lightweight Steel-framed Construction, Isk – European Light Steel Construction Association, Brussels, Belgium.
- Macillo, V., Iuorio, O., Terracciano, M. T., Pali, T., Fiorino, L. and Landolfo, R. (2014) 'Seismic response of Cfs strap-braced stud walls: Experimental investigation', *Thin-Walled Structures*. Elsevier, 85, pp. 466–480. doi: 10.1016/j.tws.2014.09.008.
- Mahdavinejad, M., Hajian, M. and Doroodgar, A. (2011) 'Role of LSF technology in economic housing for urban sustainability, case of Iran', *Procedia Engineering*, 21, pp. 2–7. doi: 10.1016/j.proeng.2011.11.1980.
- Martins, C., Santos, P. and da Silva, L. S. (2015) 'Lightweight steel-framed thermal bridges mitigation strategies: A parametric study', *Journal of Building Physics*, 39(4), pp. 342–372. doi: 10.1177/1744259115572130.
- Martins, C., Rosa, N., Santos, P., and Simões, L. (2015). Desempenho Térmico de Paredes com Estrutura Leve em Aço Enformado a Frio. Paper presented at X Congresso de Construção Metálica e Mista, Coimbra.
- Martins, C., Rosa, N., Santos, P., and Simões, L. (2017). Edifícios Com Estrutura Leve Em Aço Enformado a Frio (LSF): Vantagens E Desvantagens Do Sistema. Paper presented at XI Congresso de Construção Metálica e Mista, Coimbra.
- Mathur, A., Srivastava, A., Agrawal, G. D., Mathur, S. and Mathur, J. (2015) 'CFD analysis of EATHE system under transient conditions for intermittent operation', *Energy and Buildings*. Elsevier B.V., 87, pp. 37–44. doi: 10.1016/j.enbuild.2014.11.022.
- Mavroyanopoulos, G. N. and Kyritsis, S. (1986) 'The performance of a greenhouse heated by an earth-air heat exchanger', *Agricultural and Forest Meteorology*, 36(3), pp. 263–268. doi: 10.1016/0168-1923(86)90040-7.
- Mihalakakou, G., Lewis, J. O. and Santamouris, M. (1996) 'The influence of different ground covers on the heating potential of earth-to-air heat exchangers', *Renewable Energy*, 7(1), pp. 33–46. doi: 10.1016/0960-1481(95)00114-X.
- Mihalakakou, G., Santamouris, M. and Assimakopoulos, D. N. (1994) 'Use of the ground for heat dissipation', *Energy*, 19(I), pp. 17–25.
- Mihalakakou, G., Santamouris, M., Asimakopoulos, D. and Tselepidaki, I. (1995) 'Parametric prediction of the buried pipes cooling potential for passive cooling applications', *Solar Energy*, 55(3), pp. 163–173. doi: 10.1016/0038-092X(95)00045-S.
- Mihalakakou, G., Santamouris, M., Lewis, J. O. and Asimakopoulos, D. N. (1997) (1997) 'On the application of the energy balance equation to predict ground temperature profiles', *Solar Energy*, 60(3–4), pp. 181–190. doi: 10.1016/S0038-092X(97)00012-1.
- Misra, R., Bansal, V., Agarwal, G. Das, Mathur, J. and Aseri, T. (2012) 'Thermal

- performance investigation of hybrid earth air tunnel heat exchanger', *Energy and Buildings*. Elsevier B.V., 49, pp. 531–535. doi: 10.1016/j.enbuild.2012.02.049.
- Misra, R., Bansal, V., Agrawal, G. Das, Mathur, J. and Aseri, T. K. (2013) 'CFD analysis based parametric study of derating factor for Earth Air Tunnel Heat Exchanger', *Applied Energy*. Elsevier Ltd, 103(March), pp. 266–277. doi: 10.1016/j.apenergy.2012.09.041.
- Mogharreb, M. M., Abbaspour-Fard, M. H., Goldani, M. and Emadi, B. (2014) 'The effect of greenhouse vegetation coverage and area on the performance of an earth-to-air heat exchanger for heating and cooling modes', *International Journal of Sustainable Engineering*, 7(3), pp. 245–252. doi: 10.1080/19397038.2013.811559.
- Niu, F., Yu, Y., Yu, D. and Li, H. (2015) 'Heat and mass transfer performance analysis and cooling capacity prediction of earth to air heat exchanger', *Applied Energy*. Elsevier Ltd, 137, pp. 211–221. doi: 10.1016/j.apenergy.2014.10.008.
- Novo, A. V., Bayon, J. R., Castro-Fresno, D. and Rodriguez-Hernandez, J. (2010) 'Review of seasonal heat storage in large basins: Water tanks and gravel-water pits', *Applied Energy*. Elsevier Ltd, 87(2), pp. 390–397. doi: 10.1016/j.apenergy.2009.06.033.
- Ochs, F., Heidemann, W. and Müller-Steinhagen, H. (2009) 'Performance of Large-Scale Seasonal Thermal Energy Stores', *Journal of Solar Energy Engineering*, 131(4), p. 41005. doi: 10.1115/1.3197842.
- Ochsner, K. (2007) *Geothermal Heat Pumps-A Guide for Planning and Installing*.
- Olenets, M., Piotrowski, J. Z. and Stroy, A. (2015) 'Heat transfer and air movement in the ventilated air gap of passive solar heating systems with regulation of the heat supply', *Energy and Buildings*. Elsevier B.V., 103, pp. 198–205. doi: 10.1016/j.enbuild.2015.05.051.
- Omojaro, P. and Breitkopf, C. (2013) 'Direct expansion solar assisted heat pumps: A review of applications and recent research', *Renewable and Sustainable Energy Reviews*. Elsevier, 22, pp. 33–45. doi: 10.1016/j.rser.2013.01.029.
- Omran, H., GhaffarianHoseini, A., GhaffarianHoseini, A., Raahemifar, K. and Tookey, J. (2016) 'Application of passive wall systems for improving the energy efficiency in buildings: A comprehensive review', *Renewable and Sustainable Energy Reviews*, 62, pp. 1252–1269. doi: 10.1016/j.rser.2016.04.010.
- Onishi, J., Soeda, H. and Mizuno, M. (2001) 'Numerical study on a low energy architecture based upon distributed heat storage system', *Renewable Energy*, 22(1–3), pp. 61–66. doi: 10.1016/S0960-1481(00)00049-5.
- De Paepe, M. and Janssens, A. (2003) 'Thermo-hydraulic design of earth-air heat exchangers', *Energy and Buildings*, 35(4), pp. 389–397. doi: 10.1016/S0378-7788(02)00113-5.

REFERENCES

- Pfafferott, J. (2003) 'Evaluation of earth-to-air heat exchangers with a standardised method to calculate energy efficiency', *Energy and Buildings*, 35(10), pp. 971–983. doi: 10.1016/S0378-7788(03)00055-0.
- Pintaldi, S., Perfumo, C., Sethuvenkatraman, S., White, S. and Rosengarten, G. (2015) 'A review of thermal energy storage technologies and control approaches for solar cooling', 41, pp. 975–995. doi: 10.1016/j.rser.2014.08.062.
- R.M. Richard, B. J. A. (1975) 'Versatile elastic–plastic stress–strain formula, J. Eng.', *ASCE 101* (4), pp. 511–515.
- Rabani, M., Kalantar, V., Dehghan, A. A. and Faghih, A. K. (2015) 'Empirical investigation of the cooling performance of a new designed Trombe wall in combination with solar chimney and water spraying system', *Energy and Buildings*. Elsevier B.V., 102, pp. 45–57. doi: <http://dx.doi.org/10.1016/j.enbuild.2015.05.010>.
- Rodrigues, M., da Silva Brum, R., Vaz, J., Oliveira Rocha, L. A., Domingues dos Santos, E. and Isoldi, L. A. (2015) 'Numerical investigation about the improvement of the thermal potential of an Earth-Air Heat Exchanger (EAHE) employing the Constructal Design method', *Renewable Energy*, 80, pp. 538–551. doi: 10.1016/j.renene.2015.02.041.
- Rodrigues, L. T. and Gillott, M. (2013) 'A novel low-carbon space conditioning system incorporating phase-change materials and earth-air heat exchangers', *International Journal of Low-Carbon Technologies*, 10(3), pp. 176–187. doi: 10.1093/ijlct/ctt023.
- Rosa, N., Martins, C., Santos, P., Gervásio, H., da Silva, L.S. (2015). Desenvolvimento de uma Parede em Aço Enformado a Frio para Armazenamento de Energia Térmica. Paper presented at X Congresso de Construção Metálica e Mista, Coimbra.
- Rosa, N., Martins, C., Henriques, J., Santos, P., Gervásio, H., da Silva, L.S. (2017). Resistência Mecânica De Painéis Com Estrutura Leve Em Aço (LSF) Sujeitos a Cargas Laterais. Paper presented at XI Congresso de Construção Metálica e Mista, Coimbra. ResearchGate.
- Rosa, N., Santos, P., Costa, J., Gervásio, H. (2018). Modeling and performance of an earth-to-air heat exchanger in a pilot installation. *Journal of Building Physics*. <https://doi.org/10.1177/1744259117754298>.
- Ruiz-Pardo, Á., Domínguez, S. Á. and Fernández, J. A. S. (2010) 'Revision of the Trombe wall calculation method proposed by UNE-EN ISO 13790', *Energy and Buildings*, pp. 763–773. doi: 10.1016/j.enbuild.2009.11.018.
- Saadatian, O., Lim, C. H., Sopian, K. and Salleh, E. (2013) 'A state of the art review of solar walls: Concepts and applications', *Journal of Building Physics*, 37, pp. 55–79. doi: 10.1177/1744259113479336.

-
- Saadatian, O., Sopian, K., Lim, C. H., Asim, N. and Sulaiman, M. Y. (2012) 'Trombe walls: A review of opportunities and challenges in research and development', *Renewable and Sustainable Energy Reviews*. Elsevier, 16(8), pp. 6340–6351. doi: 10.1016/j.rser.2012.06.032.
- Safer, N., Woloszyn, M. and Roux, J. J. (2005) 'Three-dimensional simulation with a CFD tool of the airflow phenomena in single floor double-skin facade equipped with a venetian blind', *Solar Energy*, 79(2), pp. 193–203. doi: 10.1016/j.solener.2004.09.016.
- Santos, P., Simões da Silva, L., Gervásio, H. and Gameiro Lopes, A. (2011) 'Parametric analysis of the thermal performance of light steel residential buildings in Csb climatic regions', *Journal of Building Physics*, 35(1), pp. 7–53. doi: 10.1177/1744259111403440.
- Santos P, Simões da Silva L, Ungureanu V. (2012). Energy Efficiency of Light-weight Steel-framed Buildings. 1st ed. European Convention for Constructional Steelwork (ECCS), 36 Technical Committee 14 - Sustainability & Eco-Efficiency of Steel Construction, ISBN 978-92-9147-105-8, N. 129.
- Santos, P. (2017) 'Energy Efficiency of Lightweight Steel -Framed Buildings', *World's largest Science, Technology & Medicine Open Access book publisher*, Energy efficient buildings, Chapter 3, INTECH. doi: 10.5772/66136
- Sapiano, M., (2013) 'Water consumption in domestic sector in Malta', Ministry for energy and the conservation of water.
- Serageldin, A. A., Abdelrahman, A. K. and Ookawara, S. (2016) 'Earth-Air Heat Exchanger thermal performance in Egyptian conditions: Experimental results, mathematical model, and Computational Fluid Dynamics simulation', *Energy Conversion and Management*, 122, pp. 25–38. doi: 10.1016/j.enconman.2016.05.053.
- Serrette, R. L., Encalada, J., Juadines, M. and Nguyen, H. (1997) 'Static Racking Behavior of Plywood, OSB, Gypsum, and FiberBond Walls with Metal Framing', *Journal of Structural Engineering*, 123(AUGUST), pp. 1079–1086. doi: 10.1061/(ASCE)0733-9445(1997)123:8(1079).
- Serrette, R. and Ogunfunmi, K. (1996) 'Shear Resistance of Gypsum-Sheathed Light-Gauge Steel Stud Walls', *Journal of Structural Engineering*, 122(April), pp. 383–389. doi: 10.1061/(ASCE)0733-9445(1996)122:4(383).
- SFS Intec, Self-Drilling Screw SL3-F4.2x15 Technical Specification www.sfsintec.com.
- Shameri, M. A., Alghoul, M. A., Sopian, K., Zain, M. F. M. and Elayeb, O. (2011) 'Perspectives of double skin fa??ade systems in buildings and energy saving', *Renewable and Sustainable Energy Reviews*. Elsevier Ltd, 15(3), pp. 1468–1475. doi: 10.1016/j.rser.2010.10.016.
- Sebald, A.V. (1985) 'Efficient Simulation of Large, Controlled Passive Solar Systems:
-

REFERENCES

- Forward Differencing in Thermal Networks', *Solar Energy*, 34(3), pp. 221–230.
- Shen, J., Lassue, S., Zalewski, L. and Huang, D. (2007) 'Numerical study of classical and composite solar walls by TRNSYS', *Journal of Thermal Science*, 16(1), pp. 46–55. doi: 10.1007/s11630-007-0046-x.
- Simões da Silva, L. (2008) 'Towards a consistent design approach for steel joints under generalized loading', *Journal of Constructional Steel Research*, 64(9), pp. 1059–1075. doi: 10.1016/j.jcsr.2008.02.017.
- Singh, T., Kumar, A. and Baredar, P. (2013) 'Experimental and analytical studies of earth – air heat exchanger (EAHE) systems in India : A review', *Renewable and Sustainable Energy Reviews*, 19, pp. 238–246. doi: 10.1016/j.rser.2012.11.023.
- Soares, N., Costa, J. J., Gaspar, A. R. and Santos, P. (2013) 'Review of passive PCM latent heat thermal energy storage systems towards buildings' energy efficiency', *Energy and Buildings*. Elsevier B.V., 59, pp. 82–103. doi: 10.1016/j.enbuild.2012.12.042.
- Soares, N., Santos, P., Gervásio, H., Costa, J. J. and Simões da Silva, L. (2017) 'Energy efficiency and thermal performance of lightweight steel-framed (LSF) construction: A review', *Renewable and Sustainable Energy Reviews*, 78(March 2016), pp. 194–209. doi: 10.1016/j.rser.2017.04.066.
- Sodha, M. S., Buddhi, D. and Sawhney, R. L. (1993) 'Optimization of pipe parameters of an underground air pipe cooling system', *Energy Conversion and Management*, 34(6), pp. 465–470. doi: 10.1016/0196-8904(93)90077-N.
- Soussi, M., Balghouthi, M. and Guizani, A. (2013) 'Energy performance analysis of a solar-cooled building in Tunisia: Passive strategies impact and improvement techniques', *Energy and Buildings*. Elsevier B.V., 67, pp. 374–386. doi: 10.1016/j.enbuild.2013.08.033.
- Stazi, F., Mastrucci, A. and di Perna, C. (2012) 'Trombe wall management in summer conditions: An experimental study', *Solar Energy*. Elsevier Ltd, 86(9), pp. 2839–2851. doi: 10.1016/j.solener.2012.06.025.
- Thiers, S. and Peuportier, B. (2008) 'Thermal and environmental assessment of a passive building equipped with an earth-to-air heat exchanger in France', *Solar Energy*, 82(9), pp. 820–831. doi: 10.1016/j.solener.2008.02.014.
- Tian, Y. S., Wang, J. and Lu, T. J. (2004) 'Racking strength and stiffness of cold-formed steel wall frames', *Journal of Constructional Steel Research*, 60(7), pp. 1069–1093. doi: 10.1016/j.jcsr.2003.10.002.
- Tittlein, P., Achard, G. and Wurtz, E. (2009) 'Modelling earth-to-air heat exchanger behaviour with the convolutive response factors method', *Applied Energy*. Elsevier Ltd, 86(9), pp. 1683–1691. doi: 10.1016/j.apenergy.2009.02.010.
- Tunç, M. and Uysal, M. (1991) 'Passive solar heating of buildings using a fluidized

-
- bed plus Trombe wall system', *Applied Energy*, 38(3), pp. 199–213. doi: 10.1016/0306-2619(91)90033-T.
- Vaz, J., Sattler, M. A., Dos Santos, E. D. and Isoldi, L. A. (2011) 'Experimental and numerical analysis of an earth-air heat exchanger', *Energy and Buildings*. Elsevier B.V., 43(9), pp. 2476–2482. doi: 10.1016/j.enbuild.2011.06.003.
- VDI 4640 (2001), 'Thermische Nutzung des Untergrundes – Richtlinie VDI 4640, Blatt 1 – Grundlagen, Genehmigungen', Umweltaspekte. Beuth Verlag, Berlin.
- Vieira, L. C. M. and Schafer, B. W. (2012) 'Lateral stiffness and strength of sheathing braced cold-formed steel stud walls', *Engineering Structures*. Elsevier Ltd, 37, pp. 205–213. doi: 10.1016/j.engstruct.2011.12.029.
- Vijayavenkataraman, S., Iniyan, S. and Goic, R. (2012) 'A review of climate change, mitigation and adaptation', *Renewable and Sustainable Energy Reviews*. Elsevier Ltd, 16(1), pp. 878–897. doi: 10.1016/j.rser.2011.09.009.
- Vilcekova, S., Selecka, I. and Burdova, E. K. (2016) 'Sustainability Assessment of Family House', *Energy Procedia*. The Author(s), 96(October), pp. 551–559. doi: 10.1016/j.egypro.2016.09.098.
- Wang, W. L., Tian, Z., Niu, X. L. and Xu, X. (2012) 'Investigation on a Passive Solar House Equipped with Water Thermal Storage Wall', *Applied Mechanics and Materials*, 178–181, pp. 193–196. doi: 10.4028/www.scientific.net/AMM.178-181.193.
- Wang, W., Tian, Z. and Ding, Y. (2013a) 'Investigation on the influencing factors of energy consumption and thermal comfort for a passive solar house with water thermal storage wall', *Energy and Buildings*, 64, pp. 218–223. doi: 10.1016/j.enbuild.2013.05.007.
- Wang, W., Tian, Z. and Ding, Y. (2013b) 'Investigation on the influencing factors of energy consumption and thermal comfort for a passive solar house with water thermal storage wall', *Energy and Buildings*. Elsevier B.V., 64, pp. 218–223. doi: 10.1016/j.enbuild.2013.05.007.
- Wilson, A. (1979) 'Thermal Storage Wall Design Manual', p. 40. Available at: <http://www.nmsea.org/lib/ThermalStorageWallDesignManual.pdf>.
- Woodson, T., Coulibaly, Y. and Traoré, E. S. (2012) 'Earth-Air Heat Exchangers for Passive Air Conditioning: Case study burkina faso', *Journal of Construction in Developing Countries*, 17(1), pp. 21–33.
- Wu, T. and Lei, C. (2016) 'A review of research and development on water wall for building applications', *Energy and Buildings*. Elsevier B.V., 112, pp. 198–208. doi: 10.1016/j.enbuild.2015.12.003.
- Xamán, J., Hernández-López, I., Alvarado-Juárez, R., Hernández-Pérez, I., Álvarez, G. and Chávez, Y. (2015) 'Pseudo transient numerical study of an earth-To-Air
-

REFERENCES

-
- heat exchanger for different climates of México', *Energy and Buildings*. Elsevier B.V., 99, pp. 273–283. doi: 10.1016/j.enbuild.2015.04.041.
- Yi, H., Jie, J., Hanfeng, H., Aiguo, J., Chongwei, H. and Chenglong, L. (2008) 'Optimized Simulation for PV-TW System Using DC Fan', *Proceedings of ISES World Congress 2007 (Vol. I – Vol. V)*, pp. 1617–1622. doi: 10.1007/978-3-540-75997-3_332.
- Zalewski, L., Joulin, A., Lassue, S., Dutil, Y. and Rousse, D. (2012) 'Experimental study of small-scale solar wall integrating phase change material', *Solar Energy*, 86(1), pp. 208–219. doi: 10.1016/j.solener.2011.09.026.
- Zamora, B. and Kaiser, A. S. (2009) 'Thermal and dynamic optimization of the convective flow in trombe wall shaped channels by numerical investigation', *Heat and Mass Transfer/Waerme- und Stoffuebertragung*, 45(11), pp. 1393–1407. doi: 10.1007/s00231-009-0509-6.
- Zhai, X. Q., Wang, X. L., Pei, H. T., Yang, Y. and Wang, R. Z. (2012) 'Experimental investigation and optimization of a ground source heat pump system under different indoor set temperatures', *Applied Thermal Engineering*. Elsevier Ltd, 48, pp. 105–116. doi: 10.1016/j.applthermaleng.2012.05.005.
- Zhang, J. and Haghighat, F. (2009) 'Convective heat transfer prediction in large rectangular cross-sectional area Earth-to-Air Heat Exchangers', *Building and Environment*. Elsevier Ltd, 44(9), pp. 1892/1898. doi:10.1016/j.buildenv.2009.01.011.
-

ANNEX A.

Grid analysis and numerical convergence of EAHE CFD models

A1.1 Grid and time-step convergence

In CFD modelling finer meshes are typically required for more accurate solutions. However, when the mesh is finer, the computation time increases and this can lead to overflow errors. Due to this, a mesh convergence study must be performed to achieve valid results. The numerical convergence for Steady-State (initial conditions) and Transient simulations must ensure that the solution satisfies the following three conditions: (1) convergence criteria's (RMS values) must be set to an acceptable value (10^{-4} or 10^{-5}); (2) convergence of the monitor points values such as *e.g.* ground and air temperature profiles; (3) domain imbalances must be lower than 1%. After checking if the numerical solution satisfies the convergence criteria's the mesh study should be performed by refining the mesh for each domain. The monitor points used for this study are: (1) the outlet air temperature; and (2) the temperature profile in a cross-section at 12-meter length. The main objective is to reach solution values that are independent of the mesh resolution. The values of interest must be within a specified tolerance, and in this case study, this tolerance was set to be 0.5 °C. The mesh study was performed initially with an unstructured mesh/grid and then with a hybrid mesh/grid. The study was divided into three parts: (1) sensitivity in the ground domain with an unstructured mesh/grid; (2) mesh sensitivity in the air domain with unstructured grid; and (3) mesh sensitivity in air domain with structured grid and ground domain with a hybrid grid. For the mesh sensitivity in air domain, it was important to define a proper value of y^+ in combination with a turbulence model. The numerical results were compared against the effectiveness-NTU method.

A1.1.1 First cell height calculation

The first cell height is calculated based on a desired y^+ value. For this case study, the near-wall modelling strategy is used to deal with the viscous sublayer. This strategy is required for full resolution of the boundary layers and is also required when the wall-bounded effects are a high priority (*e.g.* heat transfer). For this strategy, the wall adjacent grid height must be order $y^+ = 1$ and with low-Re number turbulence model. To calculate the first cell height for a desired y^+ the Reynolds number must be calculated using the following equation:

$$Re = \frac{\rho U d}{\mu} \quad (129)$$

where ρ and μ represents the density and the viscosity of the air, U the freestream velocity, and d the pipe diameter. For a given y^+ value the first cell height (Δy_1) can be calculated by:

$$y^+ = \frac{\rho h_0 \times U_\tau \times \Delta y_1}{\mu} \rightarrow \Delta y_1 = \frac{y^+ \times \mu}{\rho \times U_\tau} \quad (130)$$

where U_τ represents the frictional velocity given by:

$$U_\tau = \sqrt{\frac{\tau_w}{\rho}} \quad (131)$$

The wall shear stress (τ_w) is calculated based on the skin friction coefficient (C_f):

$$\tau_w = 0.5 \times C_f \times \rho \times U^2 \quad (132)$$

For an internal flow, the skin friction coefficient is given by:

$$C_f = 0.079 \times Re^{0.25} \quad (133)$$

For this mesh sensitivity study, the average air velocity is 1 m/s ($Re \sim 6920$) where the Δy_1 is equal to 0.00023 meters.

A1.2 Unstructured grid analysis

The first models used an unstructured grid due to the irregular connections between elements. However, at this stage, a semi-automatic mesh can be used as first approach. The first four models (CFX01 to CFX04) were developed to analyse the mesh density in the ground domain using hexahedra elements without considering Δy_1 . Four symmetric partitions around the heat exchanger were used in the ground domain to achieve better element symmetry. Inflation zones of 0.025 (5 layers) and

ANNEX A

Grid analysis and numerical convergence of EAHE CFD models

0.1 (10 layers) meters were used in air and ground domain, respectively. The number of air and pipe elements at this point was considered fixed and with values of 252000 and 38646, respectively. The second study consists of fixing the number of elements of the ground and pipes domains and by increasing the mesh density in the air domain. Four models (CFX05 to CFX08) were developed by increasing the number of air elements, and the Δy_1 was set to be equal to 0.00023 m. The number of elements for each model is present in Figure A.1.

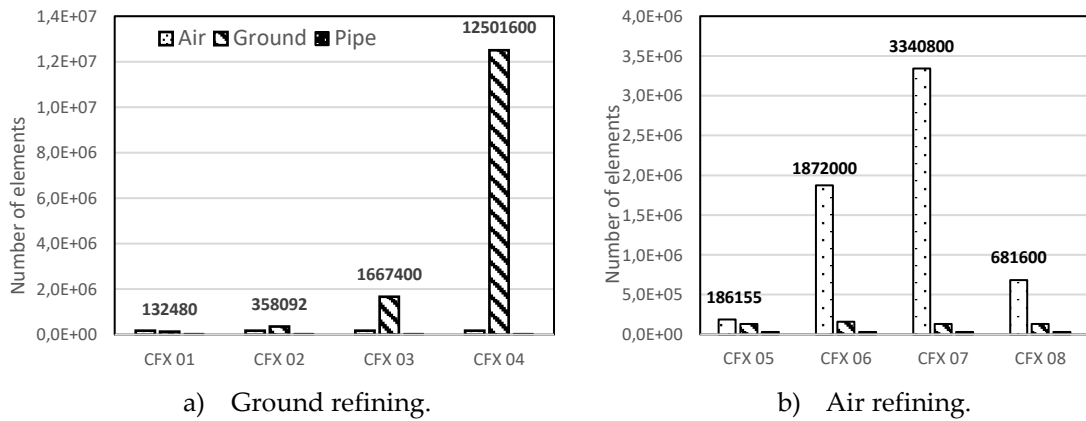


Figure A.1 – Number of elements with unstructured grid mesh.

The evaluation of mesh sensitivity in the ground domain was conducted monitoring the numerical results in one point at 0.5 meters distance (Sensor A) and checking the outlet air temperature. The values were evaluated after running the Steady-State model (initial condition or $t = 0h$) and for the maximum inlet air temperature in transient conditions ($t = 17h$). Results allow verifying that the number of elements in the ground domain does not have any significant influence on the numerical results.

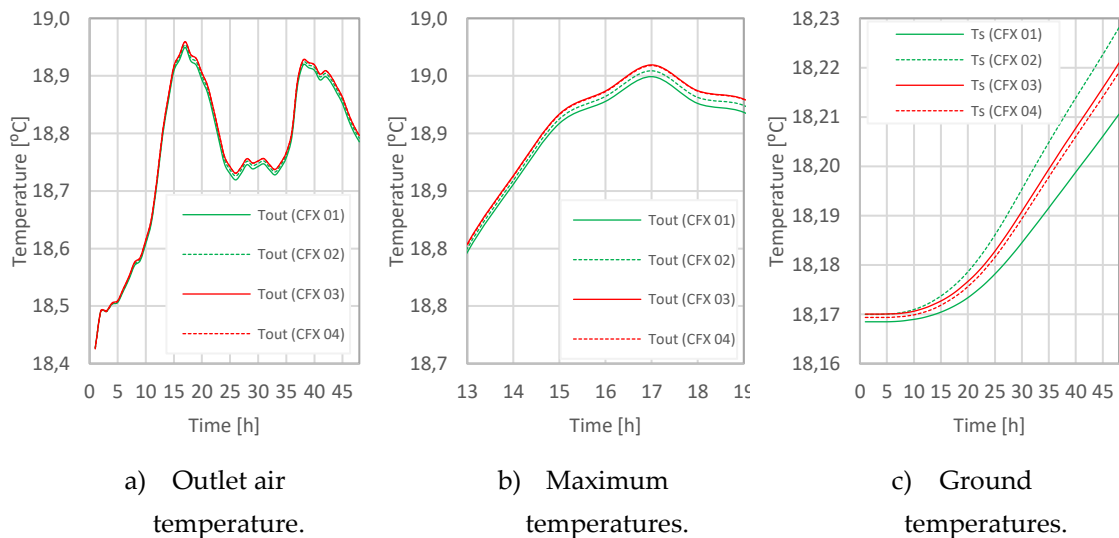
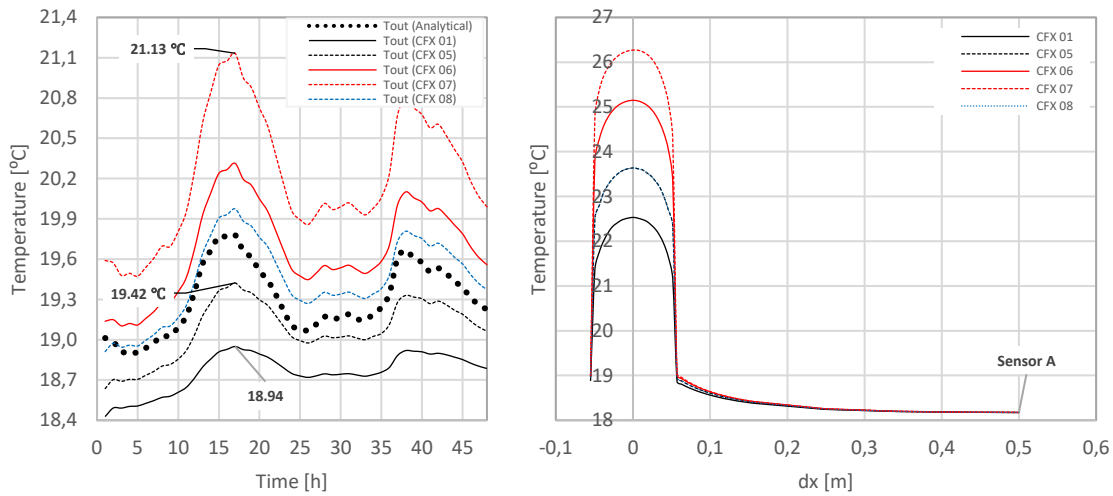


Figure A.2 – Numerical results for grid refining in ground domain.

After the mesh sensitivity study of the ground domain and using the same mesh of model CFX 01, the air domain was refined (Figure A.1 b) and the first cell height previously calculated was considered. Figure A.3a and b present the outlet air temperature and temperature distribution in a cross-section at 12 meters length (for $t = 17h$), respectively. The monitored points values did not converge well, as observed in Figure A.3. For instance, for the maximum outlet air temperature, the difference between model CFX05 and 07 was $1.71\text{ }^{\circ}\text{C}$ (tolerance $0.5\text{ }^{\circ}\text{C}$). An improvement of the meshing accuracy is present in the next section.



a) Outlet air temperature.

b) Cross-section temperature distribution.

Figure A.3 – Numerical results for grid refining in air domain.

A1.3 Hybrid grid analysis

To improve the mesh accuracy a hybrid grid was developed in this study (Figure A.4 a and b). The ground domain was divided into twelve solids in which ten of them have structured grids (quadrilateral/hexahedra elements). The solids near to the pipe have an unstructured grid with tetrahedrons elements. Therefore, considering a 3D space, the number of air/pipe and ground elements can be increased and decreased, respectively, without losing nodes connections. The partitions sizes and number of elements were design to achieved elements with 0.05 meters in the ground domain (structured grid) and different element sizes in the air/pipe domains. The air domain was also divided into five symmetric sections for better orthogonality and to have a structured mesh. These partitions allowed to the increase the number of elements and element dimensions in a tridimensional space. Four models were developed to analyse the mesh sensitivity in the air domain (Figure A.4 a). The difference between the models are: (1) refinement at the inlet boundary direction (x, y) and increase elements length (z) between model A4-2 and A4-3; (2) decrease the size in x and y

ANNEX A

Grid analysis and numerical convergence of EAHE CFD models

and increase element length (z) between model A4-4 and A4-5. The mesh/numerical convergence was analysed considering the residual values, domains imbalances and monitoring points. These values were analysed considering the computational effort and how fast it could be achieved the results without compromising their viability.

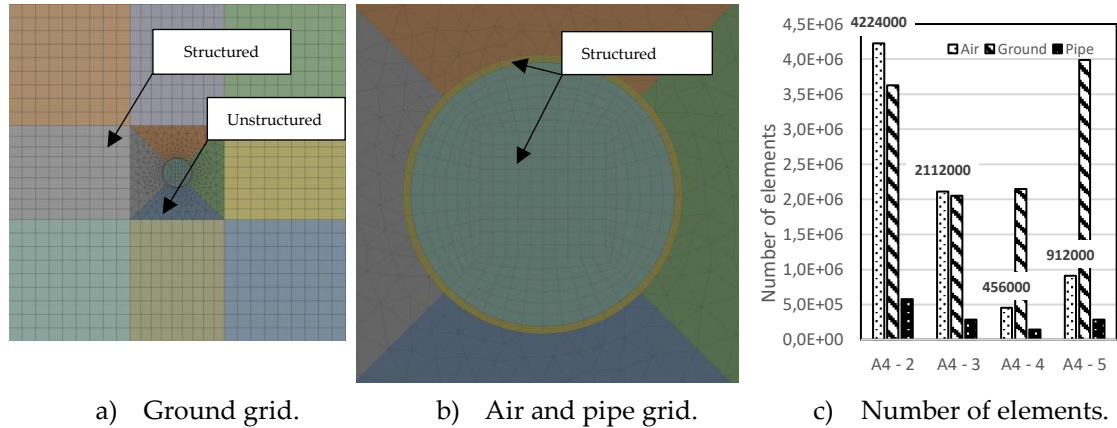


Figure A.4 – Hybrid grid in Ansys CFX.

A1.4 Numerical convergence control

The Steady-State/Transient simulations convergence was verified by observing the RMS values (lower than 10^{-4} or 10^{-5}) and domain imbalances (lower than 1%). Figure A.5 presents the numerical convergence of model A4-02 after running the steady-state model to achieve the initial conditions and the numerical convergence in transient conditions (for all time-steps and iterations). It was found residual values below the targets (10^{-4} and 10^{-5}) in Steady-State and Transient simulations. The steady-state model has higher residual values due to air physics (no air velocity/laminar flows which are harder to converge). The domain imbalances are always lower than 1%. Results show a good convergence of the numerical models.

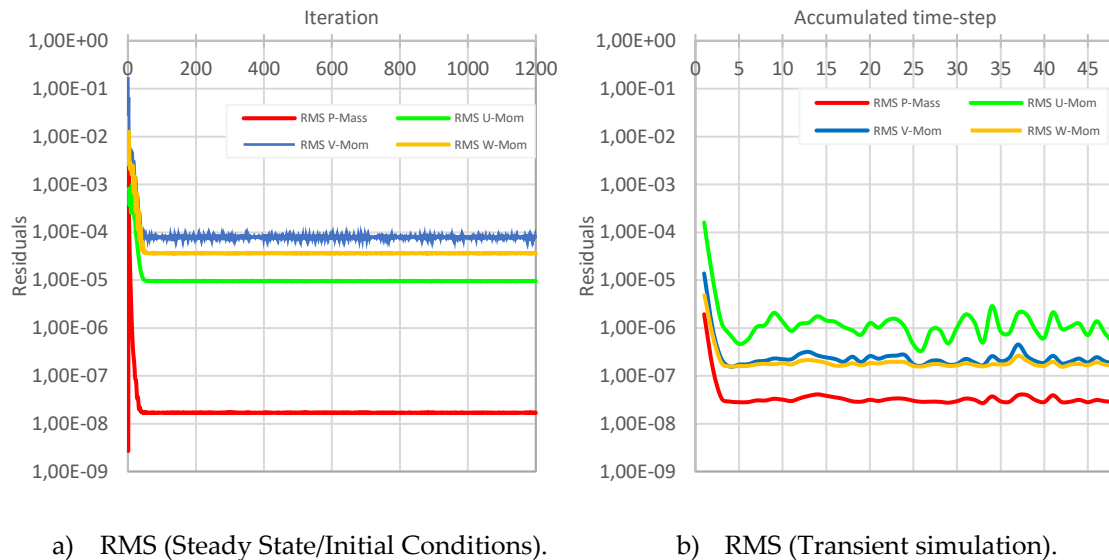


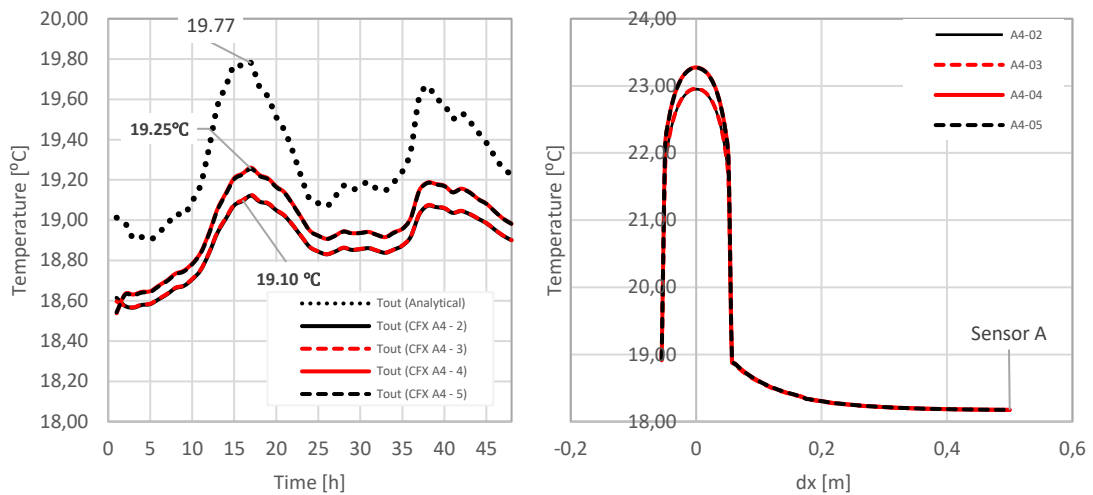


Figure A.5 – Numerical convergence.

The mesh sensitivity in the air domain with a structured grid was evaluated by monitoring the outlet BC and ground temperature at Sensor A. All the values were analysed at 0h and 17h (simulation time) in a cross-section at 12 meters length distance from the inlet boundary. Figure A.6a and b present the outlet air temperature of the heat exchanger and temperature distribution in a cross-section at 12 meters length for $t = 17h$, respectively. It can be observed a good mesh convergence with these models, where the major difference between the outlet air temperatures at 17h of simulation is 0.15 °C (tolerance 0.5 °C). As can be seen in Figure A.6 the air/pipe and ground temperature converged well. The initial time-steps convergence can be improved by increasing the mesh density and by decreasing the time-steps. However, this would lead to a higher computational effort which in this case is not necessary since the results are within the expected.

ANNEX A

Grid analysis and numerical convergence of EAHE CFD models

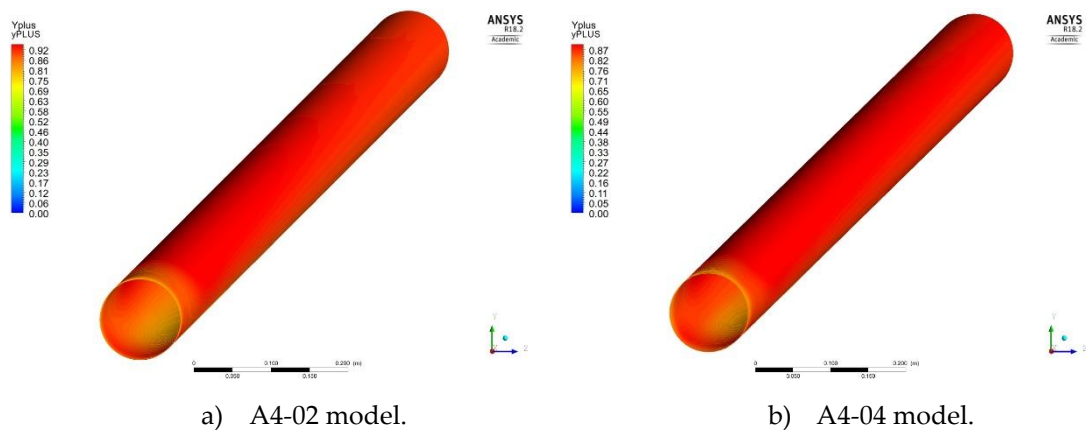


a) Outlet air temperature.

b) Cross-section temperature distribution.

Figure A.6 – Numerical results for grid refining in air domain.

Figure A.7a and b present the numerical results (at $t = 17$ hours of simulation) for the y^+ values between the model with the highest and lowest elements number. It was observed that model A4-02 and A4-04 achieved average y^+ values of 0.91 and 0.88, respectively. The lowest y^+ is achieved near to the inlet boundary (Figure A.7).



a) A4-02 model.

b) A4-04 model.

Figure A.7 – Yplus contour at 17 hours of numerical simulation.

Figure A.8a and b present the temperature contours for a cross-section at 12-meter length when the inlet temperature was higher. As observed in Figure A.8a and b, the temperature contours (ground and air temperatures) in both models have very similar patterns.

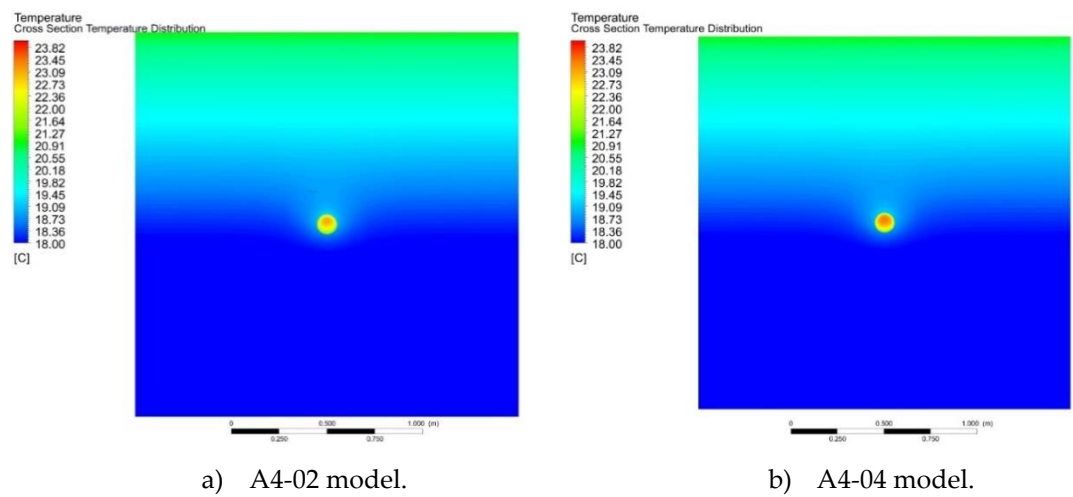


Figure A.8 – Temperature contour in transient conditions for t = 17 hours of simulation.